Microstructural Evolution in Fe-Cr-B based Alloy Powder and Thermally Sprayed Coatings and Their Wear Performance

Komsanti Chokethawai, MSc

Thesis submitted to the University of Nottingham

for the degree of Doctor of Philosophy

October 2010

Abstract

To date, the development of an amorphous alloy has concentrated entirely on a multi-component Fe-based amorphous alloy (Fe-Cr-B based alloy systems) containing boron and/or carbon. The major driving force behind these developments lies in the desire to produce an amorphous coating which exhibits both excellent thermal stability and wear performance, whilst achieving significant cost reductions over existing materials used in wear applications.

Three commercially available gas atomised Fe-Cr-B based alloy powders, namely Armacor M, Armacor C and Nanosteel SHS7170 and a locally designed powder (KC1) were employed in this study. High velocity oxy-fuel (HVOF) thermal spraying was used to deposit coatings of these multi-component Fe-based amorphous alloys, approximately 300 μm thick on a mild steel substrate. The microstructures of the feedstock powders and the coatings before and after heat treatment were investigated by means of X-ray diffraction (XRD), scanning electron microscopy (SEM), transmission electron microscopy (TEM) and differential scanning calorimetry (DSC).

The as-sprayed Armacor M, Armacor C and Nanosteel SHS7170 coatings are a mixture of amorphous and crystalline phases, whereas the as-sprayed KC1 coating is composed of only an amorphous phase. The fraction of amorphous phase decreases in the order KC1 >> Nanosteel SHS7170 > Armacor C > Armacor M.

The amorphous phase in these coatings crystallises on annealing at about 600-700°C and the crystallisation temperature depends on the content of solute elements (i.e. boron and carbon). Thermal stability of the amorphous phase containing boron and carbon is higher than those phases containing boron.

After heat treatment of the coatings above the crystallization temperature (~700°C) the amorphous phase in the coatings devitrified into a multiphase structure. In the KC1 coating, formation of a very fine mixed structure of α-Fe, carbide, borocarbide and/or boride by decomposition of the amorphous phase can be observed, bringing about a hardness of (~12.4-13.2 GPa). In contrast, the hardness of the Armacor M and Armacor C coatings, containing boron decreased when annealed at temperatures of 750°C or higher.

The wear performance of the sprayed SHS7170, Armacor C and Armacor M coatings was evaluated by sliding wear (ball-on-disc) testing under unlubricated conditions. The testing was performed with ceramic and steel counterfaces as a function of load and sliding distance. The results show that the SHS7170 coating, containing larger proportion of amorphous phase exhibits higher sliding wear resistance, compared with that of the Armacor M and Armacor C coatings. Wear mechanisms were investigated and related to properties (i.e. fracture toughness) and microstructures of the coating.

Acknowledgements

At this point I would like to thank all those who have helped me during my PhD period. First and foremost, I would like to express my appreciation to my supervisors Prof. D.G. McCartney and Prof. P.H. Shipway for their guidance and patience throughout the course of my PhD, and especially in the last few months of writing this thesis. They have given me a lot of help in my work and my life.

I also especially appreciate the help of Prof. Paul D. Brown for supervising the operation of the TEM and for discussing scientific phenomena. I would also like to thank the support staff within the School of M3, Keith Dinsdale, Martin Roe, Tom Buss, Dr. Nigel Neate, Graham Malkinson, Rory Screaton and Mark Daine. They are the best in the world and have always given me strong support whenever needed.

Thanks also to my colleagues Dr. Deen Zhang, Dr. Craig Degnan, Dr. Runglawan Somsunan, Dr. Michael Fay and Dr. Hannah Edwards for helping with my experiments and for discussions. I am also very grateful to Dr. David Weston for helping me many things.

I am highly grateful to Ministry of Science and Technology scholarship of Thailand for financial support towards the course. The material support from TWI Ltd (Cambridge, UK) is also gratefully acknowledged.

I specially thank my family for their support and for helping me overcome many difficulties in this period.

Contents

Chapter 1

Introduction

Thermal spraying is widely used to deposit coatings for many industrial applications, especially to protect components from wear and corrosion. High velocity oxy-fuel (HVOF) thermal spraying is one of the recent developments in thermal spraying techniques which is widely used for high quality coatings, due to its potential to produce dense deposits, with relatively low porosity and low oxide content. In the last decade, there has been a growing demand for the production of protective coatings with high wear and corrosion resistance, such as the wear resistant cermets WC-Co or the metallic alloy Inconel 625 (Ni-Cr based) for high corrosion resistance. Additionally, in some applications there is the special demand for improved coatings to protect components in aggressive operating conditions at elevated temperature for which NiCr-Cr_3C_2 can be used.

WC-Co coatings contain hard, brittle WC grains which are bonded strongly in the relatively ductile Co matrix phase and thus exhibit good wear resistance. However, they are limited to a maximum service temperature of 500°C as they oxidise rapidly above this temperature range (Berger et al., 1998; Laul, 2000; Somaraju et al., 2000; Koiprasert, 2004). NiCr-Cr_3C_2 coatings have better oxidation resistance and can be used up to 900°C (Wirojanupatump, 2001; Kamal et al., 2009; Guilemany, 2002; Ding, 2009). This is due to its low oxidation rate and the formation of uniform, protective and highly adherent oxide layer of on its surface. However, NiCr-Cr_3C_2 coatings have poorer wear properties than WC-Co coatings (Sahraoui et al., 2003; Sidhu, 2009). This is due to the lower hardness of the Cr_3C_2 phase in the cermet (14

GPa c.f. 22.0 GPa for WC) and the phase transformations of carbides from Cr_3C_2 to softer Cr_7C_3 and $Cr_{23}C_6$ during spraying (Murthy, 2006). Thus, there is a growing demand for the production of the coatings with good room temperature wear properties which can also be used at temperatures of between 500 and 900°C and/or in a highly corrosive environment. Materials proposed for these applications are Fe-Cr-B based alloys.

Fe-Cr-B based coatings are an attractive alternative to WC-Co and NiCr-Cr_3C_2 due to an abundance of the natural resource (Fe) and its low material cost and good chemical and physical properties, such as high hardness of borides, low density, and reasonable thermal stability at elevated temperatures (Branagan et al., 2005; Liu et al., 2009). These coatings contain an Fe-based matrix with a high chromium level to provide oxidation resistance as well as corrosion resistance whilst the ceramic phase (boride) is oxidation resistant and also exhibits high hardness which provides the wear resistance. Fe-Cr-B based alloys have been proposed for use for high temperature, wear resistance and corrosion resistance applications in various industrial fields such as aerospace industry, power generation industry, etc. (Pang et al., 2002, Branagan, 2004; Mellor, 2006).

A number of researchers have investigated the deposition, by thermal spraying of multi-component Fe-Cr-(B,C) based alloys which form an amorphous or partially amorphous structure when quenched from the melt at sufficiently high cooling rates (Kishitake et al., 1996; Pang et al., 2002; Farmer et al., 2009). Frequently, it has been found that when such alloys are deposited by the HVOF process the final coatings exhibit only a partially amorphous structure. This can be attributed to several factors.

Firstly, crystallization of materials due to reheating of splats by the deposition of subsequent layers and secondly, the presence of large unmelted powder particles in the coating with a crystalline structure due to incomplete amorphous phase formation in the original starting powder.

Over the last decade there have been attempts to study multi-component alloy systems with high glass forming ability (GFA) i.e. the ability to form an amorphous structure at cooling rates below 10^3 Ks^{-1}. Fe-based alloys have been developed and it has been found that these materials are suitable, in the form of gas-atomized powders, for HVOF spraying which can form amorphous coatings at low critical cooling rates in the range 10^1 to 10^3 Ks^{-1}. The coatings exhibit high glass transition and crystallization temperatures. With HVOF spraying, it is thus possible to make coatings with a large fraction of amorphous phase significantly greater than previously studied in alloys with low GFA (Kishitake et al., 1996).

In assessing the suitability for industrial applications of HVOF-sprayed protective coatings which are produced from high GFA alloys, an important issue to be addressed is their thermal stability. The thermal stability of an amorphous coating with respect to crystallization is an important property which must be considered when / before the protective coating is in service. There are two main reasons to be considered before applying the protective amorphous coatings into services. Firstly, the ability of materials to resist crystallisation at relatively low temperature when the coating is in service, which could be deleterious to its properties. Secondly, the ability to induce devitrification of the amorphous phase into the coatings by heat treatment

leading to the formation of a nanostructure (prior to entry into service). This could therefore enhance mechanical properties such as hardness and wear resistance.

In the light of these considerations, the two main aims of the work reported here were firstly to identify the microstructures formed in HVOF sprayed coatings using the commercially available alloy powders (Armacor M, Armacor C and Nanosteel SHS7170), based around an Fe-Cr-B composition as well as a specially designed Fe-Cr-B-C based alloy powder (given the code KC1) which is reportedly a high GFA alloy (Pang et al., 2002). The coating thermal stability was also investigated. The techniques of X-ray diffraction (XRD), scanning electron microscopy (SEM) utilizing an X-ray energy dispersive spectroscopy (EDS), transmission electron microscopy (TEM), microhardness testing and differential scanning calorimetry (DSC) were all employed to characterize powders and coatings before and after heat treatments in the temperature range up to 925°C.

The second aim was to investigate the unlubricated wear property of coatings produced from the commercial powders. The sliding wear tests of the coatings were performed using a ball-on-disc apparatus, with the ceramic balls (alumina and zirconia) and steel 440C ball being the counterface pin. The mechanisms of material loss in sliding wear were investigated and related to the coating microstructures, which are then related to the processes occurring during spraying and finally to the makeup of the powder feedstock.

Chapter 2

Literature Review

2.1 Surface engineering

Surface engineering involves the enhancement of certain properties of the surface of a component which are distinct from those of its bulk material. Wear and corrosion resistance are typical properties which can be improved by surface engineering (Mellor, 2006). There is a considerable effort on the part of research to develop techniques to impart improved wear and corrosion properties, to surfaces to improve component lifetimes resulting in less downtime for repair, thus it is cost effective. Surface engineering encompasses many and varied processes and techniques. These can be separated into three categories (Shipway, 2006).

(1) Processes that modify the existing surface without a change in composition (e.g. transformation hardening, shot peening and surface remelting).

(2) Processes that modify the existing surface by inducing a change in composition of the component, creating a surface engineered layer. Often this leads to a diffuse boundary between the substrate and the reaction layer, e.g. as in anodising, boronising and ion implantation.

(3) Processes which apply a new material, as a coating, to the surface, i.e. those processed which lead to the formation of a different phase with a distinct boundary between itself and the substrate. Weld hardfacing, electroplating, thermal spraying,

physical vapour deposition (PVD) and chemical vapour deposition (CVD) are examples of these processes.

Table 2.1 shows examples of common coating process and the desired property and certain features that are imparted by the technique on a typical application. In selecting a technique for a given application, however, many important aspects must be taken into account, including the resulting surface properties required, the thickness of the modified layer, the substrate temperature during treatment, as well as economic factors. For many engineering components the temperature during coating is an important factor for the mechanical and physical properties of the coating as well as the base material. Fig.2.1 summarizes the substrate temperature involved in coating processes and coating thicknesses ranges for the different respective processes (Schneider et al., 2006).

Of these three categories, only 3 techniques in the 3rd category have the capability of producing a thick coating in excess of 500 μm. Thick coatings are essential in some applications where high temperature, high wear resistance and/or corrosion resistance of components are of primary concern, such as landing gear, gas turbine components etc.

Weld hardfacing is a process that applies a coating material to a surface of a component by welding. Plasma-transferred arc is example of this process. It is normally used for refurbishment where significant wear resistance of the surface component is required, i.e. earth and rock engaging equipment. This process can produce extremely thick surface layers up to 100 mm or more in thickness. In

welding methods, the coating material in the form of a consumable electrode or rod is fed into the fusion zone and the substrate surface to be coated is also melted leading to good metallurgical bonding between the coating and substrate. Weld hardfacing has advantages as it is a line-of-sight process. However, as it involves high temperature welding processes, a dilution zone exists between the deposited material and substrate, thus affecting the properties of the deposited layer. In addition, the substrate also exhibits a heat-affected zone, leading to a change of the substrate properties, such as the formation of martensite in steels with high harden ability or the uncontrolled ageing of tool steels which results in high thermal stresses and cracking of deposit.

Electrodeposition is also known as electroplating. This process is typically restricted to an electrically conducting contact to the substrate surface. There are two technologies for plating, namely electroplating and electroless plating. In the electroplating process the substrate being coated is placed in a liquid solution (electrolyte) containing a solution of a salt of the meltal to be deposited, e.g. $NiSO_4/NiCl_2$ – Watts bath for nickel plating. Traditionally, hard chrome plating is for wear and corrosion resistant coatings, such as landing gear etc. When an electrical potential is applied between the substrate (cathode) and another electrode (anode), the metal ions in the bath are reduced at the cathode surface to form the required coating on the substrate. In the electroless plating process, a more complex chemical solution is used and both oxidation and reduction occur on the substrate being coated. So there is no requirement of any electrical potential contact to the substrate. However, hard chrome plating or other plating processes involve the use of

hazardous plating materials such as hexavalent chromium which is environmentally dangerous (Weston et al., 2009).

Thermal spray coatings have the potential to be alternative overlay-type coatings in a number of circumstances. Thermal spraying can produce a coating with a low oxidation level, a low porosity and good adhesion. The low residual thermal stress associated with this process mean that coatings can be sprayed to thickness of about 100-500 μm. In addition, large surface areas and complex shapes can be coated with composite microstructures to suit particular service needs. Also thermally sprayed coatings can usually be applied without heating the substrate excessively, thus avoiding formation of a heat affected zone. A more detailed description of the thermal spray process will be given in the following sections.

Considering all advantages and disadvantages among all surface treatments, thermal spray processes often offer the best solution and as it is the subject of this thesis thermal spraying methods will be reviewed in greater detail in the next section.

2.2 Thermal spraying

Thermal spraying is the terminology for a group of processes in which metallic or non-metallic materials, usually in the form of powder or wire, are deposited onto a substrate. It uses thermal energy deriving from combustion of a fuel or from an electrical discharge (arc or plasma) to melt or soften and accelerate molten or partially molten droplets to speeds in the range of 50 to more than 1000 m/s. The molten particles strike the surface, flatten and form thin lamellar splats which solidify at a cooling rate up to ~10^6 K/s (Moreau et al., 1991). The microstructure of the coatings deposited by thermal-spray processes can be generally described as a layered structure consisting of lamellar type splats, resulting from flattening of the molten/semi-molten droplets as they hit the surface. The splats can be surrounded by thin layers of oxide inclusions in metallic materials. The oxide inclusions form as a result of both surface oxidation of the molten metal droplets in-flight, and continued oxidation of the splats on the surface as they solidify. Some particles may not be melted, resulting in porosity or trapped unmelted particles with near spherical morphology as seen in Fig. 2.2 (Krepski, 1993). The degree of these coating features varies depending on the type of thermal spray process used, the operating conditions selected and the material being sprayed (Davis, 2004).

The following section outlines the various common thermal spraying techniques available for the production of cermet coatings.

Thermal spraying processes can be divided into three main categories, namely plasma spraying, combustion spraying and electric/wire arc spraying and these three classifications can be subdivided as shown in Fig. 2.3. In particular plasma spraying,

wire-arc spraying, flame spraying, D-gun spraying and high velocity oxy-fuel (HVOF) spraying will be discussed below. The comparison between HVOF spraying process and other spray systems is shown in Table 2.2 (Smith & Knight, 1995).

2.2.1 Wire-Arc Spraying (AS)

Wire-arc spray process is a form of thermal spraying in which the heat source for melting is produced by an electric arc between two electrically conductive wires of the desired material. An electric arc is created when both wires which act as electrodes are fed together and brought into close contact. The tips of the wires are melted and atomised by the stream of high velocity compressed air and propelled towards a prepared substrate. A schematic diagram of wire-arc spraying is shown in Fig.2.4 (Smith & Knight, 1995).

Electric arc spraying is generally the most economical method for applying protective metal coatings, such as aluminium, zinc, aluminium-zinc alloys for the application of corrosion resistant coatings. Lower energy costs and higher deposition rates of approximately 12 kg/hr, compared with those of competing methods such as wire flame spray are advantages of the arc spraying process. This method can be used to spray materials of much higher melting points than is possible by flame spraying (see section 2.2.4) and the coatings produced are also lower porosity and exhibit better adhesion to the substrate than flame sprayed coatings.

2.2.2 Atmospheric plasma spraying (APS)

In atmospheric plasma spraying (Fig.2.5) or air plasma spraying, an electric D.C. arc is generated between a water-cooled tungsten cathode and copper anode (which is

shaped as the nozzle). This arc ionises the plasma gases, normally Ar, He, H_2 and sometimes N_2, creating a free plasma jet with a temperature exceeding 25,000°C, significantly above the melting point of any known material. Powder feedstock, which is suspended in a carrier gas, is injected either internally through the nozzle or externally (radially across) and into the plasma jet, fused and accelerated toward the substrate being coated. Particle velocities can range from 100-300 m s^{-1} (Herman, 1996). A typical feedstock throughput can range from 3 to 9 kg/hr. The advantage of plasma spraying is that it can be used to apply surfacing materials that melt at very high temperatures such as ceramics like alumina or zirconia as thermal barrier coatings in the gas turbine aero-engine and a range of other materials (e.g. hard-facings WC-Co, nickel-based alloys and ferrous alloys).

2.2.3 Vacuum plasma spraying (VPS)

Vacuum plasma spraying (VPS) or low-pressure plasma spray (LPPS) is similar to the APS process, but VPS uses modified plasma torches in a chamber at low pressures. It is carried out in a controlled atmosphere to avoid oxidation of spraying materials which are prone to oxidation (e.g. WC-Co and NiCr-Cr_3C_2). In VPS (Fig.2.6) the reaction with air is reduced or eliminated, thus leading to an increase in diameter and length of the plasma jet and results in a particle velocity increases due to the absence of gas molecules. The absence of oxygen and the ability to operate with higher substrate temperatures produce denser, more adherent coatings with much lower oxide contents (Rickerby & Matthews, 1991).

Another advantage of VPS is the use of the reversed transferred arc to remove oxides on the surface of the component before spraying. This allows coating adherence on

clean surfaces. The main disadvantage of VPS, however, is the high cost associated with the equipment required to produce the necessary environment (vacuum systems, etc).

2.2.4 Flame Spraying (FM)

Flame spraying or combustion flame spraying is the oldest of the thermal spraying processes. It was first invented in 1910 by Schoop in Switzerland for depositing zinc on a steel substrate for the protection of steel against corrosion. This process uses combustion gases, commonly oxygen and propylene, for heating the materials and compressed air as the propellant gas. Fig.2.7 shows a schematic of a generic powder flame spray process. The feedstock materials in the form of wire or powder are fed into a combustion flame where they are melted and then compressed air surrounding the flame atomises the liquid metal (in the case of wire) and propels the droplets to the substrate. Flame temperatures and characteristics depend on the oxygen to fuel ratio and pressure. The flame spray process has advantages, including low cost investment, high deposition rates and efficiencies, and ease of operation and cost of equipment maintenance. However, flame sprayed coatings exhibit lower bond strengths, more porosity than most other thermal spray processes (Pawlowski, 1995).

2.2.5 Detonation-Gun Spraying (D-Gun^{TM})

Detonation spraying process was originally developed and patented in the United States by the Union Carbide Corporation in 1955 (now Praxair Inc.) and independently developed in 1969 at the Institute of Materials Science (Kiev, Ukraine) and then it was used in various industries, particularly in the aircraft industry. Detonation spraying is a coating technology using gas explosion energy to heat and accelerate powder particles. Among these three flame spraying processes, the detonation process offers highest particle velocity ~ 800-1200 m/s that is unattainable by the plasma and HVOF processes. Fig.2.8 shows a schematic diagram of the detonation spraying apparatus. This D-gun consists of a long water-cooled barrel with a spark plug and inlet valves for gases and powder. A mixture of oxygen and fuel gas (acetylene most commonly) is fed through a mixer into a barrel closed at one end along with a pulse of powder. The gas mixture is repetitively ignited by a spark plug inside a combustion chamber to produce detonation waves (Poorman et al., 1955). The high temperature and high pressure detonation wave moving down the barrel heats the powder particles and accelerates them toward the substrate surface being coated. After each detonation, the barrel is purged with nitrogen and the process is repeated at up to about 1-15 times per second (Walsh et al., 1995). A maximum temperature of 4500°C can be achieved when 45% acetylene is employed and particle velocity within the range of 500 to 1200 m/s. It is widely used to deposit high quality WC-Co and NiCr-Cr_3C_2 cermet coatings.

2.2.6 High Velocity Oxy Fuel Spraying (HVOF)

HVOF spraying is one of the more recent developments in thermal spraying techniques and was developed as an alternative to the D-Gun and flame spray. This

process differs from conventional flame spraying as the combustion process is internal and the gas flow rates and delivery pressures are much higher than those in the flame-spraying processes (Sturgeon, 1993). Gas velocity in the flame can reach up to 2000 m/s and particle velocities can range from 600-800 m/s.

In the HVOF process (Fig. 2.9), oxygen and liquid or gas fuel, are mixed in a mixer and the mixture burns in a combustion chamber. Hot exhaust gases expand at the exit of the nozzle with supersonic speeds, creating characteristic diamond shock waves. Powder is either fed axially into the combustion chamber or somewhere downstream depending on the design of the systems, using a carrier gas and is subsequently heated and accelerated. The molten or partially molten high velocity particles impinge on the substrate and form splats that rapidly solidify.

There are a numerous variations of the HVOF spray gun systems, but these may be divided by the type of combustion fuel used into two main groups; one using gas fuel (HVOGF) and the other liquid fuel (HVOLF). A range of gaseous fuels is currently used, including propylene, propane, hydrogen and acetylene and liquid fuel is normally kerosene. The maximum flame temperature (in the gun) for the HVOF process can reach up to about 3000 °C, but it depends on the fuel type and the fuel to oxygen ratio.

The first HVOF system utilizing a gas-fuel, known as Jet-Kote HVOF system, was invented by James A. Browning in 1992, for the production of carbide cermet coatings for wear resistance in gas turbine applications. Later on, a variety of different types of other gas-fuelled HVOF spray systems has been developed and

commercialized in thermal spraying (Schneider et al., 2006). However, presently the most popular and widely accepted by the market place systems are Diamond Jet (Sulzer Metco), HV2000 (Praxair) and Jet-Kote (Deloro Stellite). Most recently, HVOF spray systems utilizing a liquid fuel (kerosene) are currently available such as, JP5000 (Praxair-Tafa), WOKA Star^{TM}600 (Sulzer Metco) and Met-Jet II (Metallisation). Schematic diagrams of a variety of HVOF spray guns are shown in Fig.2.9.

Although, they are very similar in principle, there are potentially significant detailed differences between each system, such as powder feed position, type of fuel, gas flow rates and oxygen to fuel ratio. In the Top Gun and HV2000 systems, the powder is fed axially into the combustion chamber, whereas in the Jet-Kote and Diamond-Jet systems the point of powder entry is further down the exhaust barrel at a different distance from the chamber (Harvey, 1996). In the case of the Met Jet and JP5000 guns the powder is fed radially, downstream of a converging-diverging section. This is experiences lower temperature high velocity exhaust gas conditions. It is clearly demonstrated that feeding powder into the combustion chamber where the gases have low velocity results in high heat transfer to the particles as in the Top Gun and HV2000 systems, but in contrast, feeding powder into the nozzle where the gas velocities are higher results in less heat transfer to the particles in the JP5000 and Met Jet. The capability of the gun is dependent upon the type of fuel used and the combustion chamber design. A liquid fuel (kerosene) HVOF system is capable of much higher deposition rates than the conventional gas-fuelled units.

2.2.7 Advantages of HVOF Process over APS

As mentioned previously in the section 2.2.6, HVOF spraying was invented to compete with D-gun spraying, flame spraying and plasma spraying. Cermet coatings (such as WC-Co and Cr_3C_2-NiCr) have commonly been sprayed with the D-gun, HVOF and plasma spraying. There are many researches addressing the microstructural characterisation of WC-Co coatings deposited with HVOF and plasma spray systems and reported the mechanical properties of the coatings. It is generally reported that cermet coatings sprayed with HVOF systems exhibit lower porosity, higher hardness and higher bond strength than coatings deposited by plasma spraying. In HVOF spraying, particles have a higher kinetic energy than in plasma spraying this produces WC-Co coatings with low porosity (typically lower than 1 %) and reduces the amount of oxidation of particles during their residence time in the hot flame temperature. With higher kinetic energy and lower thermal energy input, HVOF spraying generates more plastic deformation resulting in a lower coating porosity and high adhesive strength between coating and substrate (Sturgeon, 1992). As a result of high degree of decarburisation and oxidation involved in plasma spraying, the coatings are usually highly degraded and contain complex carbides such as W_2C, $Co_xW_yC_z$ and metallic tungsten in plasma sprayed WC-Co coatings (Fincke et al., 1994). It also has been reported that a higher degree of decarburisation reduces wear resistance of the coatings (Liao et al., 2000). Therefore, HVOF spraying has been used increasingly to spray WC-Co coatings to achieve desirable engineering properties.

It can be noted that HVOF spraying system shows more advantages in terms of velocity, temperature approach as well as a relatively lower costs compared to plasma spraying process as shown in Fig. 2.10 (Rickerby & Matthews, 1991).

2.2.8 Materials for thermal spraying

Metals or non-metallic materials in the form of wire, rod or powder are usually used to deposit onto a substrate by thermal spraying processes. The materials in form of wire are used in the wire-flame spray process and arc spray process. While the materials in form of powder are used in the plasma spray processes, powder-flame spray process, detonation gun and HVOF process.

In HVOF thermal spray process, a suitable powder size is usually in the range of 15 to 45 μm, whereas in other techniques such as APS, the powders can be coarser. Smaller powder particle may be vaporized, burn or oxidized completely during spraying process, while a larger power particle size may remain as unmelted particles in the structure of the deposited layer (Harvey, 1996; Mellor, 2006). The morphology of powder can affect the spray parameters such as, powder feed rate, a dwell time in the flame, etc. Rounded powder particles exhibit a high flow-ability during spray process and are usually preferred over angular particles.

2.3 Cermet coatings and their limitations

Thermally sprayed WC-Co, NiCr-Cr_3C_2, and NiCr-TiC cermet coatings are widely used to enhance the wear resistance of many types of engineering components such as aeroplane landing gear, gas turbine engines etc. These are composite materials containing ceramic particles in a metal matrix, e.g., WC in a metal matrix. They typically have a combination of high hardness (~1200 kgf/mm^2), high adhesive strength (~70 MPa) and high Young's modulus (~350 GPa). Many studies have been conducted to examine the wear behaviour of thermally sprayed WC-Co coatings (e.g. sliding wear, abrasive wear, erosive-corrosive wear). It was reported that WC-Co coatings show the highest sliding wear resistance at ambient temperature (Yang et al., 2003; Sidhu et al., 2010; Wood, 2010), or even at moderately elevated temperatures up to 400°C (Yang et al., 2006). However, they are limited to a maximum service temperature of 500°C as they oxidise rapidly above this temperature range (Berger et al., 1998; Laul & Dorfman, 2000; Somaraju et al., 2000; Koiprasert, 2004).

NiCr-Cr_3C_2 coatings have excellent oxidation resistance and can be used up to 900°C (Wirojanupatump, 2001; Kamal et al., 2009; Guilemany, 2002; Kaur et al., 2009; Ding, 2009). This is due to its low oxidation rate and the formation of a uniform, protective and adherent Cr_2O_3 layer of on its surface. However, NiCr-Cr_3C_2 coatings have poorer wear properties than WC-Co coatings (Sahraoui et al., 2003; Sidhu, 2009). This is due to the lower hardness of the Cr_3C_2 phase in the cermet (14 GPa compared with 22.0 GPa for WC) and the phase transformations of carbides from Cr_3C_2 to softer Cr_7C_3 and $Cr_{23}C_6$ during spraying (Ding, 2009; Murthy, 2006). Therefore, there is a demand for the development of a material that can operate at

temperatures of between 500 and 900°C with comparative, if not better, wear properties than WC-Co and NiCr-Cr_3C_2 coatings. Cermet materials proposed for this application are Fe-Cr-B based alloys.

Fe-Cr-B based coatings are an attractive alternative to WC and Cr_3C_2 due to their high hardness, low density, and reasonable thermal stability at elevated temperatures (Branagan et al., 2005; Liu et al., 2009). These coatings contain an Fe-based matrix with a high chromium level to provide oxidation resistance as well as corrosion resistance whilst the ceramic phase (boride) is oxidation resistant and also exhibits high hardness which provide the wear resistance. Fe-Cr-B based alloys are being considered for high temperature, wear resistance and corrosion resistance applications in various industrial fields such as aerospace industry, power generation industry, etc.

To date, various modifications have been made to the boride and the matrix phases of Fe-Cr-B based powders in an attempt to optimise the performance of the final thermally sprayed coating, but with varying degrees of success. A major limitation has been a lack of systematic detailed study of the linkages between the powder structure, spray process conditions, coating microstructure and coating performance.

Therefore, the present research focuses on the manufacture of wear resistant Fe-Cr-B coatings by the HVOF thermal spray technique. The main theme of this thesis is focused on an understanding of the microstructure of high velocity liquid fuel (HVOLF) thermally sprayed coatings and their relationship with the coating

properties. In order to understand the development of the coating microstructure, the associated phase relationships will be reviewed in the following section.

2.4 Constitution of binary and ternary based transition metal systems

2.4.1 Fe-B phase diagram (amorphous phase)

The phase diagram of Fe-B based alloys system has been established, as shown in Fig.2.11 (Liao & Spear, 1986). According to the diagram proposed, the system Fe-B contains two borides: Fe_2B and FeB. At the eutectic temperature 1174°C of the reaction L = γ-Fe + Fe_2B, the solubility of B in Fe-B liquid phase is up to 17 at% B. The eutectic point at 1500°C corresponds to the reaction of L = FeB + B. Also there is a peritectic reaction, L + FeB = Fe_2B at temperature 1389°C (Massalski, 1990).

2.4.2 Cr-B phase diagram

In the Cr-B system shown in Fig. 2.12, the system contains six borides: Cr_2B, Cr_5B_3, CrB, Cr_3B_4, CrB_2, CrB_4. The simple eutectic point at 1630°C corresponds to the reaction L = α-Cr + Cr_2B, the solubility of B in B-Cr liquid phase is 13.5 at% B at 1630°C. The eutectic point at 2050°C corresponds to the reaction of L = CrB + Cr_3B_4. There are two peritectic reactions, L + CrB = Cr_5B_3, and L + CrB_2 = Cr_3B_4 at temperature 1900°C and 2070°C, respectively (Liao and Spear, 1986; Gigolotti et al., 2008). There is also a peritectic at 1870°C, L + Cr_5B_3 = Cr_2B.

2.4.3 Fe-Cr phase diagram

The iron-chromium binary phase diagram is given in Fig.2.13. Three important features can be seen from the diagram consisting of the γ-loop separating the ferrite (α) and austenite (γ) fields, the formation of σ phase region below 820°C and decomposition reaction of the α and ά at low temperature. Fig. 2.13 shows that there is a narrow (α + γ) range between 12% and 13% Cr and chromium restricts the occurrence of the γ-loop to the extent that above 13% Cr the binary alloys are ferritic over the whole temperature range above 820°C and below 1507°C.

2.4.4 Fe-Cr-B system

The ternary Fe-Cr-B system is the important system for the iron-based alloys which are reinforced by boride particles. Knowledge of phase equilibria of this system at the temperatures of use is required in order to control the microstructure of these alloys. A partial liquidus projection of the Fe-Cr-B ternary phase diagram is shown in Fig. 2.14 and the calculated isothermal sections of this ternary system at 700°C, 900°C, 1100°C and 1250°C are shown in Figs. 2.15-2.18, respectively. This system consists of the following seven phases: the α-Fe phase, γ-Fe phase and five borides; M_2B, MB, γM_2B, δM_5B_3, εMB in which M corresponds to Fe and Cr. In M_2B, MB, γM_2B, δM_5B_3, εMB, Fe and Cr can be substituted for each other (Veshchunov, 1995; Bondar, 2008).

2.4.5 Crystal structure of boride phases e.g. Cr_2B, Fe_2B

This section illustrates four kinds of borides which are relevant to the present work, consisting of two kinds of M_2B (viz., a Cr_2B based one with a fraction of Cr substituted by Fe and an Fe_2B based one with a small fraction of Fe substituted by Cr), M_3B_2 and $M_{23}B_6$. Their crystal structure parameters are summarized in Table 2.3 (Yijian et al., 1990). The mechanical and physical properties of these borides are shown in Table 2.4 in comparison to ceramic phases (e.g. Cr_3C_2 , WC) (Culter, 1991; Berger, 1996).

Chromium diboride (Cr_2B) and iron diboride (Fe_2B) are a transition metal-based refractory ceramics that have a low density, high hardness, high melting point, wear resistance and corrosion resistance and makes it a suitable material for use in high temperature and high wear conditions. Cr_2B has an orthogonal crystal structure while Fe_2B has a body-centered tetragonal (bct) crystal structure. Fe_2B is more stable at medium temperature range (melting point, 1391°C), while Cr_2B is more stable at higher temperature (melting point, 1873°C). At high temperature, the transformation from Fe_2B to Cr_2B may occur through atom substitution of Cr atoms for Fe in Fe_2B. This results in a coexistence of Fe_2B and Cr_2B and the remaining Fe_2B may be sandwiched in the form of thin slices between (100) faces of Cr_2B as stacking faults. However, at lower temperature, the boride M_2B may exist in the form of Fe_2B instead of Cr_2B due to low solubility of Cr (less than 16 at. %) in Fe_2B but that of Fe in Cr_2B is much higher (Yijian and Jian, 1991; Goldfarb et al., 1995). Fig.2.19 shows that in a single Cr_2B cell (Fig. 2.19a), it consists of four sections of A, B, C and D, aligned along the *a*-axis, while the Fe_2B cell (Fig. 2.19b) can be regarded as a combination of sections A and C. When comparing their lattice parameters, it found

that $C_{Cr_2B} = C_{Fe_2B}$, $b_{Cr_2B} = \sqrt{2}\, b_{Fe_2B}$ and $a_{Cr_2B} = 2b_{Fe_2B}$, this means only four Fe_2B cells can be put in a single Cr_2B cell.

M_3B_2 has a tetragonal crystal structure with lattice parameters a = 0.5665-0.5736 nm and c = 0.3078-0.3112 nm. It was reported that M_3B_2 can precipitate from the supersaturated α-Fe solid solution of the melt-quenched $Fe_{70}Cr_{18}Mo_2Si_1B_9$ ribbon during annealing at temperature between 700-1150°C (Yijian and Jian, 1991).

Fig.2.20 illustrates the volume percentages of different phases formed (including Fe_2B, M_3B_2 and Cr_2B) in the melt-quenched $Fe_{70}Cr_{18}Mo_2Si_1B_9$ ribbon under different annealing regimes. It shows that only Fe_2B was found to precipitate after annealing at 700°C for 0.5 h. As the annealing temperature was raised, the content of Fe_2B was gradually transformed into M_3B_2 and Cr_2B and Fe_2B became unable to be detected after annealing at or above 900°C. Meanwhile, the content of M_3B_2 increased continuously to a peak at about 900°C and then decreased, but Cr_2B increase monotonously with increase of annealing temperature up to 1150°C.

$M_{23}B_6$ has a face centered cubic crystal structure with a lattice parameter a = 1.062 nm. In general, $M_{23}B_6$ can be found within a narrow temperature range under the condition of co-existence of Fe, Cr, Mo and Si. For example, during annealing of the melt-quenched $Fe_{70}Cr_{18}Mo_2Si_1B_9$ ribbon at temperature 950°C, $M_{23}B_6$ was found to nucleate at the interface between Cr_2B and α-Fe (Yijian and Jian, 1991).

2.5 Amorphous alloys and high glass forming ability (GFA) alloys

In the last ten years, Fe or Fe-Cr based cermets are increasingly becoming more popular as wear resistant materials because they retain high hardness, strength and wear resistance. Particularly, when B (12 to 25 at%, closely to the eutectic point in the binary Fe-B phase diagram) is added to Fe or Fe-Cr alloys, the critical cooling rate ~ 10^6 K/s can be reached (Greer et al., 2002 ; Branagan et al., 2001) and it is possible to suppress crystallization during continuous cooling. For this reason, the amorphous or partially amorphous Fe-Cr-B based alloys with exhibit a high glass forming ability (GFA) can be made. Thus in studying the structures of Fe-Cr-B materials the possibility of amorphous phase formation needs to be considered.

2.5.1 Definition of amorphous alloys

Amorphous alloys, also known as metallic glasses, differ from conventional metal alloys in that they have a non-crystalline structure. Many common materials, including oxide glasses and many polymers, can be amorphous (Johnson, 1990). Amorphous alloys can have more advantageous mechanical properties and corrosion resistance due to their lack of long-range crystalline order and grain boundary which are features of crystalline metals and alloys.

The differences between amorphous and nanocrystalline alloys are shown in Table 2.5 in terms of their short-range order (SRO), long-range order (LRO) and the length scales. It is noticed that amorphous alloys have no long-range atomic order (LRO)

and only have a short-range atomic order (SRO) with a structural correlation length (the grain size) in the order of atomic distances. Whereas nanocrystalline alloys have a limited long-range atomic order which is the same as the short-range atomic order (with a structural correlation length on the nanometre scale) (McHennry et al., 1999).

2.5.2 Production of amorphous alloys

Amorphous alloys or metallic glasses are often produced by a liquid quenching method which requires high cooling rates (Greer, 2001a). The basic theory of this method can be described in Fig.2.21. Crystallization occurs when the temperature is lowered below the liquidus temperature of the alloy, $T_{liq.}$ However, this crystallization can be avoided when the cooling rate is sufficiently high (Busch, 2000). The result is that an amorphous alloy can be formed at such a cooling rate. For amorphous alloys or metallic glasses, the critical cooling rates are generally high in order of 10^5 K/s.

To achieve a high cooling rate, the heat of the melt must be transferred rapidly to the substrate or the surrounding environment (Johnson, 1990). Thus, the dimension of the molten sample must be considered and corresponds to such cooling rates as following.

Cooling a molten sample, dimension R from the initial temperature T_m (the melting point of the materials) to ambient temperature require a total cooling time τ

$$\tau \sim (R^2 / \kappa) \qquad (2.5.1)$$

where

κ is thermal diffusivity of the metal (m^2/s) and $\kappa = K/C$

K is the thermal conductivity W/(m-K)

C is the volumetric heat capacity (J/(m^3-K)

Thus, the cooling rate (dT/dt) can be written in term of

$$dT/dt = T_m / \tau = (K T_m / CR^2) \quad (2.5.2)$$

For a typical of a molten metal

$K \sim 100$ W/(m-K), $T_m \sim 1000$ K and C ~ 2 x 10^6 J/(m^3-K)

Thus,

$$dT/dt = (500 / R^2) \quad (2.5.3)$$

It can be considered from Eq.2.5.3 that to achieve a high cooling rate ~ 10^6 K/s, the dimension of the sample must be in the order of 100 μm or less.

Such high cooling rates can be achieved when the liquid samples are in contact with a cold, highly conductive surface allowing rapid heat extraction. These factors were considered for the design of methods to produce amorphous alloys at high cooling rates. The production of amorphous alloys by various techniques will be described in the following section.

The method to provide such high cooling rates was first discovered by Pol Duwez and his colleagues in 1959. In this technique, a liquid droplet is melted and then accelerated to impact on a cold copper surface. The droplets spread on the copper surface and solidify with high cooling rates in order of 10^6 to 10^8 K/s. A schematic of this method is shown in Fig.2.22. This method, known as gun quenching was used for studying solidification of metals at high cooling rates. The first amorphous alloy was produced in the gold-silicon binary system by this method.

By 1960, Duwez group developed a new version of previous method as named the piston and anvil technique. By this method, a thin foil sample with thickness ranging from 30 to 50 μm can be produced. The cooling rates of this method are in the order of 10^5 to 10^6 K/s.

However, the metallic glasses produced by these method (gun quenching and the piston and anvil technique) can not meet the needs of industries, because of a limitation of making a large sample quantities. Several researchers tried to develop a method, which can provide this need.

In 1970, melt spinning or the continuous casting processes was developed to produce larger quantities of metallic glasses. In these processes, the liquid metal steam is injected continuously onto the surface of rotating wheel. This steam spreads onto the substrate and solidifies. The ribbon of metallic glass is drawn out by the rotating wheel.

Furthermore, a uniform sheet of metallic glass was produced by the planar-flow casting technique (Johnson, 1990). In this technique, a steam of molten metal is dropped continuously onto the rotating wheel and the thin sheet of metallic glass is thrown from the rotating wheel. This method can produce a broad sheet of metallic glass with a thickness of about 15 to 150 μm, widths up to 1 m, and unlimited length.

To avoid crystallization during the quenching of the melt the conditions shown in Fig. 2.21 must be met. The maximum rate of crystallization relates to the ratio T_g / T_m and depends strongly on the value of T_g more than an T_m. As shown in Fig.

2.23, when the ratio T_g / T_m is relatively small ~ ½, a maximum rate of nucleation (N) ~ 10^8 nuclei/$cm^3.s^{-1}$, while the maximum rate of nucleation is only about 10^{-30} nuclei/$cm^3.s^{-1}$ when the ratio T_g / T_m is larger than ~ 2/3. This indicates that the crystallization can be more easily avoided, when the ratio T_g / T_m is large enough.

Additionally, the maximum sample thickness for glass formation (t_{max}) will be increased dramatically when the critical cooling rate for avoiding nucleation (R_c) decreases (Inoue, 2000). This observation led to the search for alloys with a high T_g / T_m. It was found that the critical cooling rate (R_c) of Fe-based alloys containing metalloid elements (i.e., $Fe_{80}P_{13}C_7$) is around 10^4 K/s and the maximum sample thickness (t_{max}) is about 0.2 mm, as shown in Figs.2.24 and 2.25. New multi-component Fe-based amorphous alloys, such as Fe-Al-Ga-P-C-B and Fe-Co-Zr-Nb-B have been found to have lower critical cooling rate (~10^2 K/s) compared to $Fe_{80}P_{13}C_7$ and their maximum sample thickness are as large as 5 mm. The large sample thickness for glass formation indicates a high glass forming ability (GFA) of these amorphous alloys. Such high GFA alloys are now termed bulk metallic glasses. The GFA of amorphous alloys can be characterized by the critical cooling rate (R_c) and the most often used parameters, such as the supercooled liquid region ΔT_x (= T_x – T_g) and reduced glass transition temperature T_g / T_m or sometimes T_g / T_l (where T_g is the glass transition temperature, T_x is the crystallization onset temperature during heating, T_m is the melting onset temperature and T_l is the liquidus temperature of the alloy). However, in the case where T_g can not be detected (for example in binary $Fe_{80}B_{20}$ amorphous alloys), the parameter T_x / T_m can be used as an alternative. Thermal parameters of Fe-based amorphous alloys are listed in Table 2.6.

The reason for the increase of GFA of amorphous alloys can be understood in the framework of the three empirical rules for achievement of large GFA which are (1) multicomponent alloy systems consisting of more than three elements; (2) the main constituent elements have significantly different (>12%) atomic sizes; and (3) negative heats of mixing among the elements (Ma & Inoue, 1999).

2.5.3 Fe-B based alloys and Fe-Cr-B based alloys

For Fe-B based alloys, it was reported that Fe-B based amorphous alloys were formed in the composition range $Fe_{100-x}B_x$ where x = 12 to 25. Fe-B based alloys with these compositions are referred as alloys with trough deep eutectic, see Fig. 2.11. It was reported that for $Fe_{83}B_{17}$ (roughly centred on the eutectic point in the binary Fe-B phase diagram, Fig.2.11), the critical cooling rate is about $2x10^6$ K/s (Comlam and Carr, 1985). However, they have been mainly fabricated only in the form of melt-spun ribbons because of their low GFA. The limitations of size and shape have prevented a further extension of their application fields.

Recently, new multi-component Fe-based alloys containing glass-forming metal elements such as Al, Ga, Zr, Nb, Ta and Y have been developed in Fe-(Al, Ga)-(P, C, B, Si) (Inoue, 1997a), Fe-(Co, Ni)-(Zr, Nb, Ta)-B (Inoue et al., 1997b), Fe-Ni-P-B (Shen & Schwarz, 2001) and Fe-Si-B-C (Inoue & Wang, 2000) systems. These amorphous alloys exhibit high GFA and can be prepared in a bulk glassy form by casting into a mould with a maximum thickness of 2-6 mm exhibiting good mechanical properties, thermal stability and soft magnetic properties. However, there has been no data on wear resistance of these Fe-based bulk amorphous alloys.

For this reason, Fe-Cr-B based alloys are the most attractive for forming an amorphous phase due to the abundance of the natural resources (Fe and Cr), the low material cost and their unique properties. It has been reported that Fe-Cr-B based alloys with chromium and boron contents can provide high wear resistance, high corrosion resistance, high thermal stability and other properties required, better than those of Fe-Al-Ga-P-C-B, and Fe-Co-Zr-Nb-B alloys and also Fe-B based alloys (Pang et al., 2002).

In the present study, multicomponent alloys in the Fe-Cr-B system were investigated in detail with the partial aim of finding new Fe-Cr-B based alloys which are expected to have high thermal stability and high wear resistance. This work intends to examine the composition range in which crystalline and/or amorphous phase (single phase) is formed in Fe-Cr-B alloys and to investigate the composition dependence of microstructure, thermal stability and hardness. The compositions of Fe-Cr-B based alloys used in this work will be presented in chapter 3. This work also reports the wear behaviour of the present Fe-Cr-B based alloys. The microstructure and wear resistance for the Fe-Cr-B based alloys are further discussed in chapter 8.

2.5.4 Properties of amorphous alloys

2.5.4.1 Magnetic properties

Amorphous alloys have low magnetic losses and high permeability, because of their lack of long range order. Ferromagnetic amorphous alloys containing Fe and Co have excellent soft magnetic properties equivalent to those of conventional materials (Greer, 2001a).

2.5.4.2 Mechanical properties

Bulk amorphous alloys offer higher tensile strength and lower Young's modulus when compared with the corresponding crystalline phase. It has been reported that amorphous alloys have high strength and extremely high hardness which suggests a good resistance to sliding and/or abrasive wear (Greer 2001). In addition, the hardness of amorphous alloys can be significantly improved when they are annealed to form a nanophase composite structure. A mixed amorphous–nanocrystalline structure has superior sliding/abrasive wear resistance to both the amorphous and fully crystallized structures (Anis et al., 1994; Wang et al., 2000; Greer et al., 2002).

2.5.4.3 Chemical properties

Amorphous alloys have excellent corrosion resistance, due to their lack of grain boundaries (Inoue, 2000). The corrosion behaviour of melt-spun amorphous alloys in Zr-TM-Al-Ni-Cu (TM = Ti, Cr, Nb, or Ta) systems was examined in HCl and NaCl solutions at room temperature. It was revealed that the Nb- and Ta-containing amorphous alloys exhibit high corrosion resistance in their solutions.

2.6 Structure and properties of Fe-Cr-B based alloys for thermally sprayed coatings

Purpose of this section is to give specific details of work done previously on this family of materials.

2.6.1 Alloy compositions which have been developed and patented

Scruggs (1988) worked on a variety of compositions based around a glass-forming composition. The preferred amorphous materials consist essentially of three components:

1. 40-70 wt% of the component selected from Fe, Co and combinations of these.
2. 20 wt% of the component selected from Cr, Mo, W, Nb, V, Ti and combinations thereof.
3. 2-6 wt% of the component selected from B and C and combinations of these.

Elevated temperature wear resistance of the coatings can be achieved by addition of Mo, Nb or W in place of Cr, or in combination with Cr. The corrosion resistance can be improved by increasing the content of Co in place of Fe, or in combination with Fe.

Scruggs (1988) also stated that the composition of alloys which can be readily transformed to the amorphous state under frictional or wear forces, consists essentially of about 59Fe, 36Cr, and 5B (in wt%).

Coatings of such alloys were prepared by a variety techniques, including plasma spraying, laser cladding, and electron beam melting. Abrasive wear testing using the

ASTM G-65 standard practice was carried out to provide wear data. The coatings were exposed to wear, and worn by unlubricated abrasive wear. It was found that only a portion of the outermost layer of the coatings can be an amorphous structure, after explosive of the coatings to wear-inducing environment.

The frictionally transformable materials were used in a wide range of machinery applications such as in seals, valve, bearing surfaces and the cutting tools.

More recently, particular compositions of an alloy which can lead to metallic glass formation have been developed by Branagan (2004). In this invention, the alloy consists of a steel composition, containing at least three elements

1. at least 50%Fe.
2. at least one element selected from Ti, Zr, Hf, V, Nb, Ta, Cr, Mo, W, Al, La, Ce, Pr, Nd, Sm, Eu, Gd, Th, Dy, Ho, Er, Tm, Yb and Lu.
3. at least one element selected from B, C, N, O, P and S.

The preferred alloy composition in this invention was represented by the formula of Fe (100-x-y)M(x)B(y) (atomic percent), where M represents at least one element selected from Ti, Zr, Hf, V, Nb, Mo, Ta, Cr, W and Mn and wherein (x=15-24), (y=2-25) and (x+y=7-35). The alloys can consist of fewer than eleven elements, seven elements and five elements. However, the alloys having a few elements can be easier to reproduce a material. A variety of alloys used in this inventory along with their hardness value before and after heat treatment at temperature of 700°C and 800°C as well as the peak temperature, T_p are shown in the Table 2.7.

The addition of Cr to alloys provides improved corrosion resistance. Mo and W can be included to promote the hardness. Moreover, B and/or P can be included to generate a particular glass transition temperature and promote formation of an amorphous phase

From Table 2.7, it is seen that the hardness of Fe_{63} Cr_8 Mo_2 B_{17} C_5 Si_1 Al_4 alloy (DAR1) was as high as 15.5 GPa, which is greater than commercial steel such as, Cr-Ni austenitic stainless steel (1.5 GPa), 0.74%C plain carbon steel (4.9 GPa), 4340 ultra high strength steel (5.5 GPa), T5 W tool steel (7.5 GPa), and also WC cermet carbide (10.1 GPa).

However, the alloy DAR1 has a disadvantage, due to it composed of numerous elements. Therefore, the preferred materials (DAR2 to DAR19) which contain a few components have been developed by generating data of DAR1, Fe_{63} Cr_8 Mo_2 B_{17} C_5 Si_1 Al_4.

The alloys DAR2 to DAR19 have hardness values in a range between 9.61 GPa to 11.61 GPa, depending on alloying elements. After heat treatment these alloys at temperature of 700°C, their hardness were improved significantly, for example in as-spun ribbon DAR17 $(Fe_{0.8}Cr_{0.2})_{79}B_{17}W_2C_2$) the hardness can be significantly increased from 11.02 GPa to 16.21 GPa. However, samples heat treated at 800°C, their hardness were found to decrease gradually, in most cases their hardness were well below the hardness in the as-spun ribbons.

The detailed work on the alloys described above and in Table 2.7 led to the development of commercial alloy products manufactured under the trade name Nanosteel. One of the earliest paper about the formation of mixed amorphous/nanocrystalline Fe-based coatings using thermal spraying is that by Branagan et al. (2001).

2.6.2 Previous work on Armacor M, Armacor C, Nanosteel and other related alloys based on Fe-Cr-B, Fe-Cr-C/P, Fe-Cr-(B,C,P) or similar systems.

Manna et al. (2008) have examined two commercially available gas atomized Fe-Cr-B based alloy powders with different binder (e.g. Cr, Ni) and B contents namely Armacor M (compositions in wt% Fe-balance, 50%Cr-8.0%B-0.17%C-3.0%Si) and Armacor C (Fe-balance, 32.0%Cr-19.0%Ni-9.0%Co-4.0%Mo-2.4%Cu-4.0%B-0.12%C-1.4%Si in wt.%). These alloys are commercially available from Liquidmetal Inc. It was reported that the Armacor M powder contained boride ($Cr_{1.65}Fe_{0.35}B_{0.96}$) and ferrite matrix phases whilst the Armacor C powder contained boride ($Cr_{1.65}Fe_{0.35}B_{0.96}$) and austenite matrix phase. This indicated that powders with different binder contents contain different matrix phase. However, the different B contents does not influence on the type of boride phase.

Similar work by Dent et al. (1997), the Armacor M^{TM} (with compositions Fe-balance, 42.0%Cr-2.2%Si-6.1%B in wt.%) and Armacor C^{TM} (with compositions 25.2%Fe-Cr balance-28.2%Ni-3.2%Cu-4.4%Mo-1.5%Si-4.3%B in wt.%) were analysed using XRD for both as received powders and as-sprayed coatings. It is reported that the Armacor M^{TM} powder consists of α-Fe, Fe(Cr) solid solution matrix phase and Cr-rich metal boride $Cr_{1.65}Fe_{0.35}B_{0.96}$. The as-sprayed Armacor M^{TM} coating has retained an α-Fe, Fe(Cr) solid solution matrix phase and Cr-rich metal boride $Cr_{1.65}Fe_{0.35}B_{0.96}$ but some oxide Fe_2O_3 inclusions were also present. The Armacor C^{TM} powder consists of γ-Fe and Cr-rich metal borides such as Cr_2B and Cr_5B_3, the as-sprayed Armacor C^{TM} coating contain matrix materials with two phase

γ-Fe/α-Fe structure and boride Cr_5B_3 but Cr_2B has disappeared as well as the oxide $FeCr_2O_4$.

The as-sprayed Armacor M™ coating shown a higher hardness (6.49 GPa to 9.96 GPa) while the as-sprayed Armacor C™ coatings had a hardness (6.14 GPa to 7.54 GPa). This suggests a superior wear resistance of the as-sprayed Armacor M™ coating.

Kim et al. (1999a) have characterised the microstructure of the Armacor M coating. A commercial Fe-Cr-B based alloy; Armacor M was used to deposit the coatings using the HVOF spraying process. The chemical composition of Armacor M was 47.4%Fe-44.5%Cr-5.9%B-2%Si-0.2%S (in wt.%). The microstructure of the cross-section of the coatings was revealed by SEM. Using backscattered electron imaging, two different phases present were seen as different contrast levels. Those phases were then identified as Fe-rich, Fe-Cr solid solution (the bright contrast area) and Cr-rich, chromium-iron boride (the dark contrast area). The boride phase was homogeneously distributed in Fe-based matrix. The size of the boride phase in the coating was smaller than those found in the feed stock powder. This is explained by the authors as the same phenomenon in decarburizing during spraying.

The XRD pattern from the as-sprayed Armacor M coating revealed the presence of Cr_2B and $Cr_{1.65}Fe_{0.35}B_{0.96}$ boride phases as well as a broad diffusion peaks at $2\theta \approx 44°$. These indicated that the Armacor M coating comprised of a partially amorphous structure. However, oxide phase (Fe_2O_3) was not detected in both XRD and microstructural analyses.

The microhardness measurement was conducted on mounted cross-sections using a 500 g. load. The as-sprayed Armacor M coating shows a high hardness 9.73 GPa (8.96-10.89 GPa).

Kim et al., (1999b) also studied the effect of heat treatment on properties of the HVOF-sprayed Armacor M coating. The heat treatments were done in a vacuum furnace for an hour at temperature 700°C, 800°C, 900°C and 1000°C. The results shown that there was no change in phase after heat treatment and its hardness decreased as compared to that of the as-sprayed coating.

Wu et al. (2009) examined microstructure and microhardness of Fe-based alloy (Fe-balance, 44.7%Cr-5.8%B-1.98%Si in wt.%) coating deposited by HVOF thermal spraying on stainless steel substrate. They examined by SEM, the deposited layers which were found to contain fine boride precipitates within the metallic matrix phase and TEM results indicated that the main types of borides were Cr_2B, CrB, $Fe_{1.1}Cr_{0.9}B_{0.9}$ and FeB.

The average Vickers microhardness of the coating was 9.9 GPa. The high microhardness value of the coating was thought to be due to the effects of grain boundary strengthening, dispersion strengthening and solid solution strengthening (Wu et al., 2009).

Branagan, et al. (2004) have characterised the microstructure of the Nanosteel SHS7170 coating (compositions in wt%, 25%Cr-10%Mo-10%W-10%B-5%C-5%Si-5%Mn and the balance Fe) deposited by a twin-roll wire arc spraying using a Praxair

Tafa 8835 arc gun. TEM analysis revealed that the as-sprayed SHS7170 wire-arc coatings contained three phases, consisting of an α-Fe amorphous matrix, a boride $(Fe\text{-}Cr\text{-}W\text{-}Mo)_{23}C_6$-type phase and a $(Fe\text{-}Cr\text{-}W\text{-}Mo)_3B$-type phase. Following heat treatment at 700°C for 10 min, the amorphous phase in the coating was devitrified to a multiphase nanoscale composite microstructure giving a high hardness value ~11.87 GPa, compared with ~10.84 GPa for the as-sprayed condition.

Alloy powders of $Fe_{63}Cr_8Mo_2B_{17}C_5Si_1Al_4$ (in at %) were sprayed by the high velocity oxy-fuel (HVOF) and plasma spray process (Branagan et al., 2001). HVOF spraying was performed using a Tafa/Praxair JP-5000 gun and plasma spraying was done using a Praxair SG-100 plasma arc spray gun with cooling the substrates and coatings by argon jets. The XRD results of both as-sprayed HVOF and plasma-sprayed coatings showed significant broad diffusion peaks of primarily amorphous structures.

After heat-treatment of the as-sprayed HVOF coatings at 750°C for 1 hour, the crystalline structure with grain sizes ranging from 75 to 125 nm and 20 nm second phase precipitations at grain boundaries was found by TEM analysis.

Vickers microhardness tests were carried out to determine the hardness of the as-sprayed and heat-treated coatings. The hardness of the as-sprayed plasma sprayed coating was 10.7 GPa and increased to 12.8 GPa after heat treatment at 800°C for 1 hour. Whereas the hardness of the as-sprayed HVOF coating was 10.2 GPa and increased to 11.4 GPa after heat treatment at 750°C for 1 hour.

Branagan et al. (2006) also investigated microhardness values of the Fe-Cr-B based alloy coatings with composition of $Fe_{49.7}Cr_{17.7}Mn_{1.9}Mo_{7.4}W_{1.6}B_{15.2}C_{3.8}Si_{2.4}$ (in at %) sprayed by the HVOF JP5000 system. It was found that the coatings had hardness values ranging from 9.62 to 10.42 GPa (981 to 1062 kg/mm^2) and the hardness increase significantly up to 11.55 to 12.68 GPa (1178 to 1293 kg/mm^2) after heat treatment at 700°C for 10 minutes.

Alloys of Fe-10Cr-10Mo containing a large amount of carbon and/or boron were sprayed by low pressure plasma spraying (LPPS) and high energy plasma spraying (HPS). The as sprayed coatings obtained by the LPPS process are composed of only amorphous phase as revealed by broad diffusion peaks on the XRD patterns, whereas as-sprayed coatings obtained by the HPS process are a mixture of amorphous and crystalline phases (Kishitake et al., 1996).

After heat-treatment of these coatings at 600°C for 1 hour, the amorphous phase in the coatings crystallizes into a very fine mixed structure of ferrite and carbide, borocarbide or boride, bringing about a hardness of 11.77 to 13.73 GPa (Kishitake et al., 1996).

The microstructure of the Fe-Cr-P-C alloys coatings were studied by XRD, SEM and TEM technique (Shmyreva and Knapp, 2003). The Fe-Cr-P-C alloys coatings were very dense and showed lamellar splats. The Fe-Cr-P-C alloys coatings consisted of an amorphous and/or nanocrystalline structure. The XRD pattern showed broad peaks between $2\theta \sim 35°$ to 55° and 70° to 90°.

Vickers microhardness data of Fe-Cr-P-C alloy coatings were obtained and compared with stainless steels and Ni/Co based alloys. The Fe-Cr-P-C alloys coatings showed a significantly higher hardness 8.34-9.32 GPa (850-950 kg/mm^3) than that of stainless steels 2.94-3.92 GPa (300-450 kg/mm^3), Ni-based alloys 2.45-4.41 GPa (250-450 kg/mm^3) and Co-based alloys 2.75-4.61 GPa (280-470 kg/mm^3) (Shmyreva & Knapp, 2003).

2.6.3 Corrosion resistance of Fe-Cr-B based alloy coatings

Dent et al. (1997) have investigated corrosion resistance of Armacor M^{TM} and Armacor C^{TM} coatings deposited by a Miller Thermal/UTP HVOF spray system with hydrogen as a fuel gas. Potentiodynamic corrosion tests of anodically polarised samples of each coating were carried out in 1N sulphuric acid according to the ASTM G5-94 standard procedure. The results shown that both of the deposits exhibit a distinct passivation zone, but the Armacor M^{TM} coating is greater in terms of the voltage range of passivation (between ≈ 0-1 V) and the lower current density whereas the Armacor C^{TM} coating passivated between ≈ 0.45-0.95 V and the higher current density of 1 mA/cm^2. A high corrosion resistance of the Armacor M^{TM} coating was associated with a greater amount of amorphous phase in the coating which is thought to be a contributing factor to the resistance of the passive film which forms on the Armacor M^{TM} coating.

The corrosion behaviour of Fe-Cr-P-C alloys coatings and stainless steels for use in medical applications has been studied (Shmyreva & Knapp, 2003). The Fe-Cr-P-C based eutectic alloys were deposited on the substrates using the Super D-Gun^{TM}

process. The amorphous Fe-Cr-P-C alloy coating exhibited good corrosion resistance to 1N sulphuric acid when compared to 430 stainless steel. The Fe-Cr-P-C alloy coatings had significantly lower corrosion current density $1.5x10^{-4}A/m^2$ (I_{corr} = $1.5x10^{-8}A/cm^2$), than the stainless steel 2.2 A/m^2 (I_{corr} = $2.2x10^{-4}A/cm^2$).

Ni, H.S. et al. (2009) studied corrosion behaviour of HVOF Fe-based coating $Fe_{48}Cr_{15}Mo_{14}B_6C_{15}Y_2$ (in at%) in the 1 M HCl aqueous solution. The potentiodynamic polarization curves of the coatings in comparison with the corresponding rod, the stainless-steel substrate and electroplated Cr. The coating exhibits a low passive current density and a wide passive region. It was found that the coating shows a superior corrosion resistance to the electroplated Cr. The passive current density of the coatings is as low as 3 A/m^2 whereas that of the rod and electroplated Cr is 0.05 A/m^2 and 400 A/m^2, respectively. This indicates the ability to resist localized corrosion. Additionally, the coating has a wide passive region (1.4 V similar to transpassive potential of the rod) which is larger than the transpassive potential of the Ni-based amorphous coatings prepared by kinetic metallization, which implies a weakened ability for Ni-based coatings to resist localized corrosion.

2.7 Wear mechanism

Wear is unwanted material removal through a relative motion of a solid with respect to another. Its effect is significant to the functions of many kinds of artificial and natural joining mechanisms. The gradual removal of material from one or both surfaces in contact increases the clearance between the surfaces. This spatial freedom may induce a vibration that often leads to fatigue failures of machinery components. In many cases, the presence of a wear product (known as wear debris) may cause further problems. In the case of body prosthetics, the debris may cause severe pain and leads to the failure, e.g. of total hip or knee prostheses. Therefore, a relatively small amount of material by wear can cause the failure of large and complex devices (Ludema, 1992).

2.7.1 Types of wear

There are several distinct types of wear which generally fall into six main categories:

1. Adhesive wear
2. Abrasive wear
3. Erosive wear
4. Fretting wear
5. Fatigue and delamination wear
6. Chemical wear and oxidation wear

Generally, more than a single mechanism occurs at the same time. However, there is always a primary mechanism that governs the material removal rate. Whenever there is a possibility of abrasive wear, it is the most important problem to be solved (Neale

et al., 2000). The wear rate of abrasive wear is at least one to two orders of magnitude larger than those of other mechanisms.

The type of wear encountered in a particular application is an important factor that influences the selection of a wear-resistant material. The mechanisms of various types of wear that occur in industry applications is shown in Fig.2.26.

2.7.1.1 Adhesive wear

Of the major types of wear, adhesive wear is perhaps the most complex, not in concept, but in the way different materials respond to sliding conditions. Adhesive wear is a possibility whenever two solid surfaces are loaded together and moved relative to one another. The chances of damage by adhesive wear are increased markedly if the two surfaces have similar crystal structure, and if there is little or no lubrication present (Greer et al., 2002). Under some conditions, adhesive wear can generate debris which then causes further wear by abrasion (Hutchings, 1992). Wear debris generated under the conditions of high loads and high speeds will appear as large particles. In contrast, under low loads and low speeds, fine oxide wear debris can be observed.

2.7.1.2 Abrasive wear

Abrasive is encountered when hard particles or hard projections (on a counter-face) are forced against, and moved along a solid surface forming scratches and grooves. Abrasion can be classified in terms of the amount of abrasive fragmentation occurring in the system. The terms high and low stress abrasion relate to the condition of the abrasive medium (be it hard particles or projections) after interaction

with the surface. If the abrasive medium is crushed, then the high stress condition is said to prevail. If the abrasive medium remains intact, the process is described as low stress abrasion (Hutchings, 1992; Wood, 2006). Typically, high stress abrasion results from the entrapment of hard particles between metallic surfaces in relative motion, while low stress abrasion is encountered when moving surfaces come into contact with packed abrasives, such as soil and sand.

Abrasion can be further classified into two groups in terms of the types of contact, namely two-body and three-body abrasion. Two-body abrasion occurs when an abrasive slides along a surface and is not free to roll between the surfaces. Whereas, three-body abrasion occurs when the abrasive is free to rotate between them. Cutting on the worn surface occurs more often rather than indentation and ploughing if the abrasive is fixed and not free to roll as in two-body abrasion. It has been estimated by Tylczak (1992) that 50% of all wear problems in industry are due to abrasion and a two-body system experiences from 10 to 1000 times as much material loss as a three-body system for a given load and path length of wear.

2.7.1.3 Erosive wear

Erosive wear is the removal of material by impingement of solid particles or liquids onto the surface. It normally occurs by a combination of two mechanisms namely: abrasion and deformation. The deformation of metals involves plastic flow, but brittle and less ductile materials may wear by fracture. Two types of erosion are defined depending on impact angle: abrasive erosion occurs when the impact angle is very shallow or nearly parallel to the solid surface. In contrast, if the impact angle is nearly normal to the solid surface, it is called impact erosion. Nevertheless, it is

necessary to consider both the influence of impingement angle and particle velocity on the rate of erosion (Hutchings, 1992). Erosion wear is a problem for many components such as turbine blades, propulsors, pipelines and fluidized-bed combustion systems. However, erosion can be advantageous, notably for cleaning and preparation of surfaces for subsequent coating by grit blasting and cutting through steel using abrasive water jets.

2.7.1.4 Fretting wear

Fretting wear is a result of vibration or small amplitude oscillatory motion, usually tangential, between two contacting surfaces (Wood, 2006). It is one of the major causes of failure in many contacting machine components, such as the blade and disc contact of turbine engines (which are subjected to a wide range of vibrations), splined couplings (methods of connecting elements in rotating machinery), in riveted or bolted joints, in oscillating bearings, in press fits on shafts, in universal joints, base plates, shackles and orthopaedic implants (Davis, 2001). Fretting wear can generate an accelerated failure if it becomes abrasive wear or promotes another type of damage. For example, crack nucleation and crack propagation driven by fatigue loading (in Ti-6Al-4V fretting damage) may result from fretting damage. Oxidised debris formed during fretting wear can accelerate wear rate of the components.

2.7.1.5 Fatigue and delamination wear

Fatigue wear is observed during repeated sliding or rolling over a solid surface, for example in cams, tappets and gears. The repeating loading and unloading cycles may induce the formation of surface or subsurface cracks which eventually result in the

break up of the surface. This leads to the formation of large fragments which are subsequently removed to leave pits in the surface.

Delamination wear is a particular kind of fatigue wear in which material is lost in the form of thin flake-like sheets, caused by the subsurface crack nucleation and propagation nearly parallel to the surface. The delamination wear theory was developed and has been described in detail by Suh (1973). This theory was based on the behavior of dislocations near and at the surface. Movement was thought to nucleate subsurface cracks and voids due to plastic deformation of the surface layer and subsequent joining of cracks by shear deformation of the surface and by crack propagation. The cracks tend to propagate parallel to the surface, resulting in the eventual removal of material in the form of thin, delaminated sheets. This delamination theory of wear is widely accepted as the first major development in wear theory since Bowden and Tabor in 1950. In fact, the adhesive-induced delamination wear dominated at low sliding speeds, while abrasive-induced delamination wear dominated at high speeds.

2.7.1.6 Chemical wear and oxidation wear

Chemical or tribochemical wear occurs by detrimental chemical reactions within the contact, initiated by the influence of the environment, and in combination with mechanical contact damage (Wood, 2006). Contact between sliding surfaces can accelerate chemical reactions and material removal. Rubbing contacts result in increased temperatures at the surface and can induce surface cracks which are favourable for more chemical reactions to take place.

Oxidation wear is the most common chemical wear process. The presence of thin oxide layers forming on contacting metal surfaces often inhibits wear and catastrophic failures by seizure. Formation of oxide on the steel surface is example for this kind of behaviour. The mechanism of oxidation wear has been extensively studied and has been described by several authors (Quinn, 1983; Quinn & Winer, 1985; So, 1995; So et al., 2002). The formation of iron oxide, such as α-Fe_2O_3 on steel rubbing surfaces during sliding wear is an example of oxidation wear (Edrisy et al., 2005). The protective oxides formed can act as a barrier between the real areas of contact and can support the load during sliding wear, thus lowering the wear rate. However, if the oxide growths and reaches a particular thickness, called the critical oxide thickness, the oxide becomes too weak to withstand the frictional shear or the load imposed and that can break off as oxide debris. In some cases, it may be trapped and cause abrasion of the substrate. However, in some cases, a protective layer may be formed by the compaction of oxide wear debris into a crystalline glaze and that reduces metal-metal contact and leads to a reduced wear rate.

2.7.2 Friction

2.7.2.1 Introduction

Friction is defined as the resistance to motion which exists when a solid object is moved tangentially with respect to the surface of another object against which it is loaded. In sliding, a tangential force, F, is needed to move the upper over the stationary counterface, as illustrated in Fig.2.27 (Basu et al., 2005).

The ratio between this frictional force and the normal load, W, is recognised as the coefficient of friction, and is usually indicated by the symbol, μ. According to the empirical study by Bowden and Tabor (1950), the laws of friction state that;

a) In sliding, the friction force, F is directly proportional to the normal load, W
b) In sliding, F is independent of the area of contact.
c) In sliding, F is independent of the sliding velocity.

The first two laws of friction are generally well obeyed for sliding metallic surfaces with very few exceptions. However, the third law is less well founded for metallic surfaces. It is commonly observed that the frictional force required to start sliding is usually larger than that necessary to maintain it. Thus, it follows that the coefficient of static friction is usually greater than the coefficient of dynamic friction. Nevertheless, once sliding is established, the friction which is found for most systems is linearly independent of sliding velocity (Hutchings, 1992).

2.7.2.2 The origin of the frictional force and its effect on wear

It is generally accepted by many researchers (Bowden & Tabor, 1964; Rabinowicz, 1965) investigating wear phenomena that friction is its primary cause by adhesion of asperities (Fig. 2.28). Hence, asperities of the sliding surfaces coming into contact and forming micro-welded junctions have to be sheared if sliding is to continue. Recent theories accept that localised asperity welding is an important factor in the origin of friction but also propose that other equally or more important factors are present. The frictional force between sliding surfaces is considered to be due to the various combined effects of adhesion between asperities, ploughing of surfaces by wear particles and hard surface asperities, and asperites deformation (Suh, 1986). The relative contribution of these components depends on various factors; for instance, surface topography, type of materials used, and environmental conditions.

Suh (1986) has characterised these effects with relation to sliding distance/sliding time. In addition, he has divided frictional behaviour into six distinct stages by experimental observation, see Fig.2.29.

Stage I: In this initial stage, the coefficient of friction is largely dictated by ploughing of the surface by asperities; the coefficient of friction is largely independent of material combinations, surface conditions and environmental conditions.

Stage II: In this stage, the value of friction is beginning to rise slowly. It can be increased more rapidly if wear particles generated by asperity deformation and fracture become trapped.

Stage III: The swift increase in the number of wear particles entrapped between the sliding surfaces gives the friction curve a steep slope during this stage. Adhesion is also increased due to rapid increase of clean surfaces.

Stage IV: Friction remains constant during this stage as adhesion and asperity deformation are now constant, as is the number of trapped wear particles.

Stage V occurs if one member of the sliding couple is significantly harder than the other then the asperities of the hard surface are gradually removed, creating a mirror finish of the hard surface. During this stage friction decreases, due to the decrease in asperity deformation and ploughing.

Stage VI the hard surface is mirror smooth, the softer surface also acquires a mirror finish and the value of the friction levels off.

2.7.3 The origin of Archard's equation

A simple model for the wear of sliding surfaces has been proposed by Archard (Archard, 1953; Hutchings, 1992). His theory postulates that wear volume is a linear function of sliding distance at a constant speed and that the wear rate is proportional to the applied load (Wood, 2006). This relationship can be derived by first examining the behaviour of a single asperity, and assuming that a single asperity contact has a circular cross-section with a radius a. The model is described in Fig.2.30. When this asperity contact reaches a maximum at stage c (Fig. 2.30c), the load supported by this contact, δW is given by

$$\delta W = P\pi a^2 \qquad (2.7.1)$$

where P is the yield pressure for the plastically deforming asperity and a is the radius of contact area.

Assuming that the volume of wear particles removal by wear, δV are hemispherical in shape with the same radius a as the contact areas and thus δV is given by

$$\delta V = \frac{2\pi a^3}{3} \qquad (2.7.2)$$

It is assumed that there is a fraction K of asperity contact points which result in a wear particle. Thus the average volume of material removal per unit of sliding distance or wear rate δQ due to a pair of asperities sliding through a distance of $2a$ is given by;

$$\delta Q = \frac{k\delta V}{2a} \qquad (2.7.3)$$

From above equation (7.2) and (7.3)

$$\delta Q = \frac{k\pi a^2}{3} \qquad (2.7.4)$$

The overall wear rate (Q) arising from all the asperity contacts is given by

$$Q = \sum \delta Q = \frac{k}{3}\sum \pi a^2 \qquad (2.7.5)$$

Likewise, the total normal load W is given by

$$W = \sum \delta W \qquad (2.7.6)$$

Substituting for δW

$$W = P\sum \pi a^2 \qquad (2.7.7)$$

From equation (7.5) and (7.7)

$$Q = \frac{kW}{3P} \qquad (2.7.8)$$

By assuming that $P \approx H$, where H is the indentation hardness of the counterface, the total volume removed by wear per unit sliding distance, Q is given by,

$$Q = \frac{KW}{H} \qquad (2.7.9)$$

Where $k = 3K$.

or this can be write in term of $V_{w,}$

$$V_w = K\frac{SW}{H} \qquad (2.7.10)$$

Where V_w is the total volume of material removed by wear, S is the total relative sliding distance, W is the normal load, H is softer surface hardness and K is the wear coefficient.

This is known as the Archard wear equation, which indicates that for a system with a constant K, the wear rate is directly proportional to the normal load, but inversely proportional to the surface hardness. In general, this equation is used to describe sliding wear and is based around the theory of asperity contact. However, an equation with exactly the same form was developed for abrasive wear, i.e. two-body abrasive wear involving plastic flow, in which hard angular particles are dragged by one body over the counterface (Rabinowicz, 1965). For the steady state, in sliding wear, V_w is proportional to S and the other dependences follow from considering the area of contact, but in abrasive wear, V_w depends on the normal load and the hardness and is related to the depth of the particle indentation.

The dimensionless wear coefficient K in equation (2.7.9) is of fundamental interest in indicating the severity of the wear of the same material under different conditions and to compare the wear resistance of materials under similar conditions. The larger value of wear coefficient, the more severe the wear for that system could be. Typically for mild wear, $K \approx 10^{-8}$, whereas for severe wear, $K \approx 10^{-2}$. The value of

the wear coefficient is strongly dependent on both the choice of material and the tribological system used. Table 2.9 shows typical values of K for sliding wear (both unlubricated and lubricated in various ways), for abrasion and for erosive wear (which results from hard particles impinging the surface). It is indicated that typical values of K in two-body abrasion of metals are within the range of 5 x 10^{-3} and of 50 x 10^{-3} and in the range of 0.5 x 10^{-3} and of 5 x 10^{-3} for the three-body abrasion (Hutchings, 1992). It is particularly useful to define a normalized wear rate or the dimensional wear coefficient k (= K/H = V_w/SW) when comparing the wear rates between different materials. This represents the volume of material removed by wear per unit normal load per unit sliding distance and values are often quoted as $mm^3\ N^{-1}\ m^{-1}$ or $m^2\ N^{-1}$ (1 $mm^3\ Nm^{-1} = 10^{-9}\ m^2\ N^{-1}$).

2.7.4 Wear resistance of amorphous alloys and related materials

Wear resistance is not an intrinsic property of a material. Wear resistance will depend not only on the properties of the components involved in the wear couple, but also on external variables. In the following section the effects of sliding distance, load, sliding speed, surface chemistry and hardness on the wear rate of amorphous alloys and other related materials will be reviewed (Greer et al., 2002).

2.7.4.1 Dependence on sliding distance

The wear volume V_w varies linearly with sliding distance S. Fig. 2.31 shows the result of micro-scale abrasion tests, for four bulk metallic glasses ($La_{60}Al_{20}Ni_{10}Co_5Cu_5$, $Mg_{65}Ni_{20}Nd_{15}$, $Pd_{40}Ni_{10}Cu_{30}P_{20}$, $Zr_{55}Al_{10}Ni_5Cu_{30}$). The wear volume of four bulk metallic glasses (Greer and Myung, 2001) increases linearly with sliding distance S and obeys equation (2.7.10).

Nevertheless, there maybe a substantial change of wear regime as a function of sliding distance during initial running-in period, usually in the direction from severe to mild wear as can be seen in Fig.2.32. The result indicates that there was initial rapid wear at the start of the test before the steady state caused by oxidation of the accumulation of wear debris (Fu and Rigney, 1999).

2.7.4.2 Dependence on normal load

For amorphous alloys, there is a linear variation between the wear rate and normal load for both abrasive and dry sliding wear tests. Wong and Li (1984) found that the abrasive wear of $Fe_{81}B_{13.5}Si_{3.5}C_2$ amorphous alloy varies linearly with normal load N as shown in Fig.2.33.

2.7.4.3 Dependence on sliding speed

The correlation between the dimensional wear coefficient, *k* and sliding speed during wear of amorphous alloys has revealed a complex picture as shown in Fig.2.34 (Li and Wang, 1991). It was noticed that two Co based amorphous alloys show their maximum wear coefficient at different speeds caused by the transitions between mild and severe wear arising from the competition between the rate of oxidation and the rate of surface removal.

2.7.4.4 Dependence on alloy and surface chemistry

The wear resistance of amorphous alloys depends on their composition. Whang and Giessen (1982) found that the different compositions of amorphous alloys can provide different wear resistance (in terms of wear coefficient) related to friction coefficient, as shown in Fig.2.35. Moreover, oxidation and other surface chemistry effects involved in the ambient testing conditions can influence the mechanism of wear (Miyoshi and Buckley, 1986).

2.7.4.5 Wear resistance as function of hardness

Whang and Giessen (1982) found that the wear rate of amorphous alloys with similar chemistry varies inversely with hardness as can be seen in Fig.2.36. Similar behaviour has been demonstrated for abrasive wear for four bulk amorphous alloys $La_{60}Al_{20}Ni_{10}Co_5Cu_5$, $Mg_{60}Ni_{20}Nd_{15}$, $Pd_{40}Ni_{10}Cu_{30}P_{20}$, and $Zr_{55}Al_{10}Ni_5Cu_{30}$ by SiC particles as shown in Fig.2.37, which shows a linear correlation between wear resistance and hardness for these four bulk amorphous alloys (Rutherford and Hutchings, 1996). However, there is no simple correlation between wear resistance and hardness because of the chemical effects as shown in Fig.2.38 (Moreton and Lancaster, 1985).

The wear rate of the components can generally be reduced by making them harder. However, very hard materials tend to be brittle, and components made from them tend to be less robust. For this reason, the hardness and toughness should be considered. Thus make materials harder does not necessarily result in reduced wear rates. Surface coatings are widely used to achieve harder materials with very high wear resistance (Neale and Gee, 2000).

2.7.5 Wear of Fe-Cr-B based alloy coatings

Kim et al., (2001) have investigated wear behaviour of Armacor M coatings and Armacor C coatings deposited by a plasma transferred arc weld-surfacing process. Pin-on-disc dry sliding wear tests were carried out using the pins of the Armacor M and Armacor C coatings against the disc made from SUJ2 steel with hardness of 2.01 GPa at a sliding speed of 0.8 m/s and total sliding distance 9048 m. It was reported that the plasma sprayed Armacor M coating had a higher wear resistance than the Armacor C coating. The high wear rate of the Armacor C coating was associated with a high friction coefficient. They also showed that the wear rate and the coefficient of friction of both the Armacor M and Armacor C coatings increased with the increasing applied load.

Dent et al (1997) have characterised the wear behaviour of Fe-Cr-B based alloys systems. The Armacor M^{TM} and the Armacor C^{TM} coatings were deposited on the substrates using a Miller thermal/ UTP HVOF spray system. An abrasive wear test was employed using a rig based on the ASTM standard G65-91. The as-sprayed Armacor M^{TM} coating had a higher hardness (6.5 to 9.96 GPa) than that of the Armacor C^{TM} coatings (6.14 to 7.54 GPa). The as-sprayed Armacor M^{TM} and the Armacor C^{TM} coatings exhibited excellent wear resistance as compared with HVOF sprayed Inconel 625 coatings. The wear rate of the as-sprayed Armacor M^{TM} and the Armacor C^{TM} coatings was similar to Ni/Cr-Cr_3C_2 coatings, but higher than that of WC-Co coatings.

A comparison of the wear behaviour of the Armacor M coating and the Armacor C coating which were sprayed with the high velocity oxy-fuel spraying using a TAFA

JP5000 gun on mild steel substrates was reported by Manna et al. (2008). A ball-on-plate test was employed using alumina and hardened 100Cr6 balls. The high friction coefficient (1.00 against alumina ball and 0.97 against 100Cr6 ball) observed for the Armacor C coating was associated with a high wear coefficient.

Branagan et al. (2002) have characterised the wear behavior of the as-sprayed $Fe_{63}Cr_8Mo_2B_{17}C_5Si_1Al_4$ (in at %) and heat treated plasma deposited coatings using a two-body abrasive wear test (ball-on-disk). A Si_3N_4 ball with a diameter of 0.5 in. and hardness of 15.4 GPa, was loaded against the coating with a sliding speed of 0.106 m/s. The investigations showed that no wear was found on both the as-sprayed and heat treated plasma deposited coatings.

The wear performance of the as-sprayed and heat-treated HVOF coatings was conducted using a three-body wet sand rubber wheel wear test (Branagan et al., 2002). The as-sprayed HVOF coatings exhibited high resistance to wear (weight loss of 0.0795 g.) similar to that of the 1090N steel and after heat treatment, the coatings exhibited improved wear resistance (weight loss of 0.0201 g). However, the wear resistance of the as-sprayed and heat treated HVOF coatings were lower than that of the as-sprayed HVOF WC-12%Co coatings (weight loss of 0.0082 g).

Ni et al. (2009) studied wear behaviour of HVOF Fe-based coating $Fe_{48}Cr_{15}Mo_{14}B_6C_{15}Y_2$ (in at%). The wear tests were carried out using sliding wear ball-on disk testing. The counter ball was GCr15 steel. The value of wear resistance can be calculated using the Rabinowitz relationship $R_w = S \times N/V_w$. The wear resistance of an HVOF Fe-based coating $Fe_{48}Cr_{15}Mo_{14}B_6C_{15}Y_2$ (in at%) was found to

be in correlation with their microhardness. It was found that the wear resistance of Fe-based alloy coatings is several times larger than that of the substrate, electroplated Cr specimens and the Ni-based amorphous coating sprayed by HVAF. The high wear resistance of the coating was thought to be due to the absence of grain boundaries and easy crystal slip mechanisms in metallic glasses as well as the improvement of hardness of the coating caused by the addition of Mo.

Kim et al. (2007) have studied the wear behaviour of Fe-based alloy (49.03%Fe-48.24%Cr-0.63%Ni-0.32%Co-0.12%Mo-1.66%Si in wt.%) coatings deposited by flame spraying process on a carbon steel substrate. Dry sliding wear tests (ball-on-disc) were carried out using AISI 52100 balls with diameter of 8mm as a counterface under the sliding speeds of 0.4 and 0.8 m/s and the applied loads of 3 and 6 N. It was found that the wear rate of the coatings increases when the sliding speed and the applied load increase. The wear rates of coatings under various conditions are shown in Fig. 2.39. They also concluded that the main wear mechanism of Fe-based alloy coating was delamination of coating layers, which is a typical wear mechanism for thermally sprayed coatings. This can be seen in SEM of the worn surfaces of the coating layers at the sliding speed of 0.8 m/s and the applied load of 3 N (Fig.2.40a) and the sliding speed of 0.4 m/s and the applied load of 6 N (Fig.2.40b).

Table 2.1 Coating processes and typical properties (courtesy of Sulzer Metco).

Coating process	*Typical coating thickness (μm)*	*Coating material*	*Properties*	*Examples*
PVD	1–5	Ti (C, N)	Wear resistant	Tools
CVD	1–50	SiC	Wear resistant	Fibre coating
Paint	1–10	Polymere	Corrosion resistant esthetical	Automotive
Thermal spraying	40–3000	Ceramic and metallic alloys	Wear resistant corrosion resistant thermal protection	Bearing Turbine blades
Hard chromizing	10–100	Chromium	Wear resistant	Rolls
Weld cladding	0.5–5	Steel, stellite	Wear resistant	Valves
Zinc galvanize	1–5	Zinc	Corrosion resistant	Steel plates
Braze cladding	10–100	NiCrBSi alloy	Hard and dense	Shafts

Table 2.2 Characteristics of thermal spray processes (Sturgeon, 1993)

Deposition processes	Heat source	Feedstock	Typical temperature in gun (°C)	Powder velocity (m/s)	Deposition rates (kg/hr)	Coating porosity (% by volume)
Arc spraying	Electric arc	Wire	6,000	100	12	12
Air plasma spraying	Plasma arc	Powder	12,000	100-300	3-9	3-9
Vacuum plasma spraying	Plasma arc	Powder	12,000	400	3-9	3-9
Flame spraying	Oxy-acetylene Oxy-hydrogen	Wire or powder	3,000	50	2-6	2-6
Detonation-Gun spraying	Oxy-acetylene nitrogen gas detonation	Powder	4,500	800	0.5	0.5
HVOF spraying	Oxy-fuel	Powder	3,000	400-600	2-4	2-4

Table 2.3 Structure unit cell parameters of borides (Yijian, 1990)

Boride	Crystal system	Lattice parameters (nm)	B atom fraction	Major constituent
Fe_2B	b.c.t.	a = 0.5099 c = 0.4240	4/11	$(Fe,Cr)_2B$ Cr<16%
Cr_2B	f.c. ortho.	a =1.457 b = 0.732 c = 0.422	16/48	$(Cr,Fe)_2B$
M_3B_2	tetra.	a = 0.5665-0.5734 c = 0.3078-0.3112	4/10	$Mo_{1+x}(Fe,Cr)_{2-x}B_2$ $(0\leq x\leq 1)$
$M_{23}B_6$	f.c.c.	a = 1.062	24/116	$(Fe,Cr,Mo)_{23}B_6$

(where M is metal)

Table 2.4 Properties of borides and carbides (Culter, 1991, Berger, 1996)

Boride	Crystal structure	Density (g/cm^3)	Melting point (°C)	Hardness (GPa)
Fe_2B	Tetragonal	7.34	1410	13.1-17.7
FeB	Orthorhombic	6.73	1650	16.2-18.6
Cr_2B	Orthogonal	6.58	1870	13.2
CrB	Tetragonal	6.14	-	11.8-12.7
Mo_3B_2	Tetragonal	9.07	2070	-
$Fe_{23}B_6$	Cubic	7.38	-	-
TiB_2	Hexagonal	4.52	3225	36
Cr_3C_2	Orthorhombic	6.68	1810	14
WC	Hexagonal	15.72	2776	22.0

Table 2.5 Classification of materials by range and type of atomic order (McHennry et al., 1999)

SRO	Range of SRO	LRO	Range of LRO	Materials classification
Crystalline	>10 μm	Crystalline	>10 μm	Macrocrystal
Crystalline	>100 nm <10 μm	Crystalline	>100 nm	Microcrystal
Crystalline	<100 nm	Crystalline	<100 nm	Nanocrystalline
Near crystalline	~ 1 nm	No LRO		Amorphous I
Non crystalline	~ 1 nm	No LRO		Amorphous I I
Non crystalline		Quasiperiodic	~ 1 nm	Quasicrystal

(Note: SRO = short-range order, LRO = long-range order, and the length scales)

Table 2.6 T_g, T_x, ΔT_x and T_g / T_m of Fe-based amorphous alloys

Alloys	T_g (K)	T_x (K)	T_m (K)	ΔT_x (K)	T_l (K)	T_g/T_m	T_g/T_l	Ref.
$Fe_{80}B_{20}$	-	745.7		-				Ma & Inoue,1999
$Fe_{46}Cr_{16}Mo_{16}C_{18}B_4$	862	915	1389	53		0.62		Pang et al.,2002
$Fe_{44}Cr_{16}Mo_{16}C_{18}B_6$	870	932	1414	62		0.62		Pang et al.,2002
$Fe_{42}Cr_{16}Mo_{16}C_{18}B_8$	887	947	1405	60		0.63		Pang et al.,2002
$Fe_{52.3}Cr_{19}Mn_2Mo_{2.55}W_{1.7}B_{16}C_4Si_{2.5}$	841-847	896	1383	49-55	1611	0.61	0.53	Farmer et al.,2006
$Fe_{48}Cr_{15}Mo_{14}B_6C_{15}Y_2$	857	926	1394	69	1563	0.61	0.55	Farmer et al.,2006

Table 2.7 Alloy compositions and the hardness before and after heat treatment (Branagan, 2004)

Alloy	Composition	Hardness (GPa)			T_p(°C)
		As-spun	700 °C	800 °C	
DAR1	$Fe_{63}Cr_8Mo_2B_{17}C_5Si_1Al_4$	15.5			568
DAR2	$(Fe_{0.85}Cr_{0.15})_{83}B_{17}$	9.77	8.19	8.47	480
DAR3	$(Fe_{0.8}Cr_{0.2})_{83}B_{17}$	10.28	9.17	8.53	492
DAR4	$(Fe_{0.75}Cr_{0.25})_{83}B_{17}$	10.45	9.91	8.71	506
DAR5	$(Fe_{0.8}Mo_{0.2})_{83}B_{17}$				535
DAR6	$(Fe_{0.6}Co_{0.2}Cr_{0.2})_{83}B_{17}$	9.61	10.97	9.65	507
DAR7	$(Fe_{0.8}Cr_{0.15}Mo_{0.05})_{83}B_{17}$	10.41	15.43	8.83	552
DAR8	$(Fe_{0.8}Cr_{0.2})_{79}B_{17}C_4$	10.82	12.91	11.71	523
DAR9	$(Fe_{0.8}Cr_{0.2})_{79}B_{17}Si_4$	10.75	11.28	8.67	554
DAR10	$(Fe_{0.8}Cr_{0.2})_{79}B_{17}Al_4$	10.32	10.97	9.28	522
DAR11	$(Fe_{0.8}Cr_{0.2})_{75}B_{17}Al_4C_4$	10.76	13.53	11.37	548
DAR12	$(Fe_{0.8}Cr_{0.2})_{75}B_{17}Si_4C_4$	11.61	14.80	12.21	580
DAR13	$(Fe_{0.8}Cr_{0.2})_{75}B_{17}Si_4Al_4$	10.42	12.42	10.34	557
DAR14	$(Fe_{0.8}Cr_{0.2})_{71}B_{17}Si_4C_4Al_4$	10.72	13.49	11.12	555
DAR15	$(Fe_{0.7}Co_{0.1}Cr_{0.2})_{83}B_{17}$	10.22	11.13	8.68	502
DAR16	$(Fe_{0.8}Cr_{0.2})_{76}B_{17}Al_7$	10.08	14.13	8.51	536
DAR17	$(Fe_{0.8}Cr_{0.2})_{79}B_{17}W_2C_2$	11.02	16.21	11.99	543
DAR18	$(Fe_{0.8}Cr_{0.2})_{81}B_{17}W_2$	10.31	15.34	10.79	540
DAR19	$(Fe_{0.8}Cr_{0.2})_{80}B_{20}$	10.72	10.24	9.47	480

Table 2.8 Summary of the microhardness values and phases present in Fe-Cr-B coatings sprayed with various spray systems.

Investigator	powders	Spraying system	Microhardness (GPa)	Present phases
Dent et al. (1997)	Armacor M Armacor C	HVOF (Top gun)	6.49-9.96 6.14-7.54	α -Fe , $Cr_{1.65}Fe_{0.35}B_{0.96}$, Fe_2O_3 γ–Fe/α –Fe, Cr_5B_3, Cr_2B, $FeCr_2O_4$
Kim et al. (1999a)	Armacor M	HVOF (JP-5000)	~9.73	Fe-rich matrix,Cr_2B, $Cr_{1.65}Fe_{0.35}B_{0.96}$,
Kim et al. (1999b)	Armacor M	HVOF (JP-5000)	~ 9.8	α –Fe, Cr_2B, $Cr_{1.65}Fe_{0.35}B_{0.96}$
Burkle et al. (2002)	Armacor M Armacor C	HVOF (JP-5000)	~12 ~7	α - Fe, $Cr_{1.65}Fe_{0.35}B_{0.96}$ α –Fe, γ-Fe, Cr_2B
Branagan et al. (2004)	Nanosteel SHS7170	Wire-arc spraying	~ 10.84	α –Fe, $M_{23}C_6$, M_3B (where M= Fe-Cr-W-Mo)
Manna et al. (2008)	Armacor M Armacor C	HVOF		α , $Cr_{1.65}Fe_{0.35}B_{0.96}$ γ , $Cr_{1.65}Fe_{0.35}B_{0.96}$
Branagan et al. (2001)	$Fe_{63}Cr_8Mo_2B_{17}C_5Si_1Al_4$ (in at %)	HVOF (JP-5000) Plasma spraying	~10.2 ~10.7	
Branagan et al. (2006)	$Fe_{49.7}Cr_{17.7}Mn_{1.9}Mo_{7.4}W_{1.6}B_{15.2}C_{3.8}Si_{2.4}$ (in at %)	HVOF (JP-5000)	9.62-10.42	
Wu et al. (2009)	44.7 wt% Cr-5.8 wt% B-1.98 wt% Si (balance Fe)	HVOF	~9.9	matrix, CrB, FeB, Cr_2B, $Fe_{1.1}Cr_{0.9}B_{0.96}$

Table 2.9 Typical values of dimensionless wear coefficient K for different types of wear (Hutching, 1992)

Types of wear	*K* (dimensionless)
Sliding wear: metals and ceramics	
lubricate: full fluid film	$< 10^{-13}$
lubricated: elasto-hydrodynamic	$10^{-13} - 10^{-9}$
lubricated: boundary	$10^{-10} - 10^{-6}$
lubricated: solid lubricant	10^{-6}
unlubricated: mild wear	$10^{-6} - 10^{-4}$
unlubricated: severe wear	$10^{-4} - 10^{-2}$
Abrasive wear: metals	
Three body	$5 \times 10^{-4} - 5 \times 10^{-3}$
Two body	$5 \times 10^{-3} - 5 \times 10^{-2}$
Erosive wear: metals	$5 \times 10^{-3} - 10^{-1}$

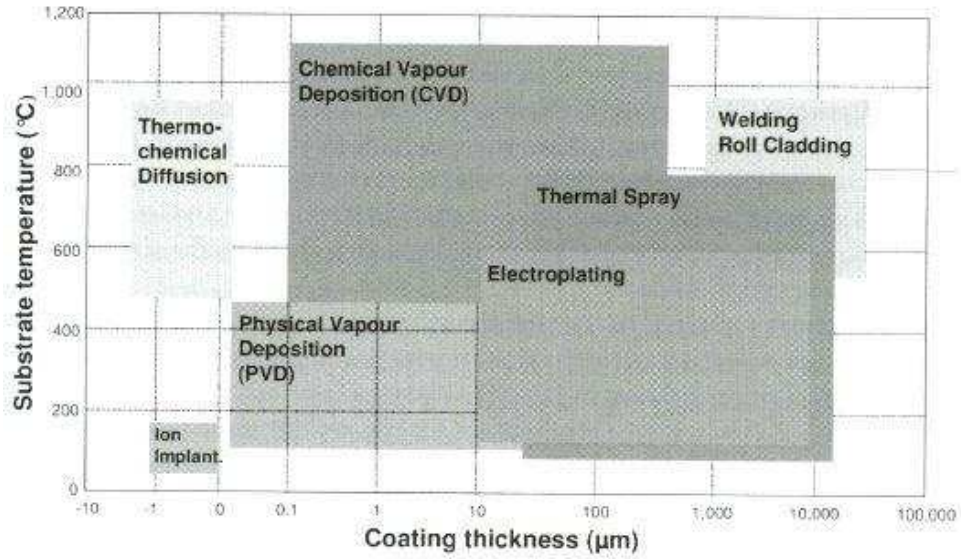

Fig. 2.1 Typical ranges for depths of surface modification and thickness of coatings and processing temperatures for surface technologies (courtesy of Sulzer Metco).

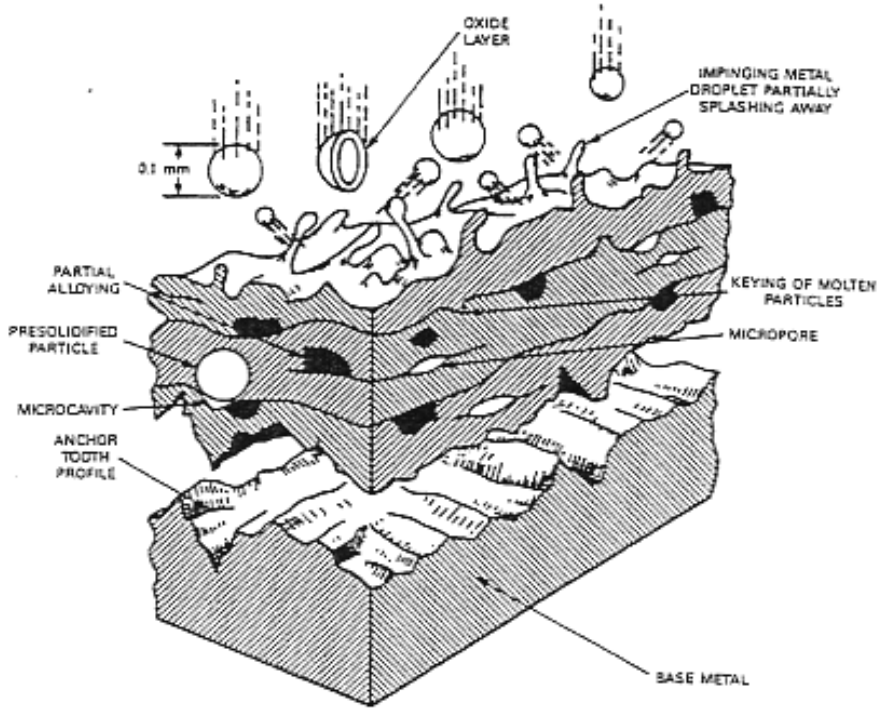

Fig.2.2 Schematic overview of coating process illustrating the possible formation of phases and microstructural features (Krepski, 1993).

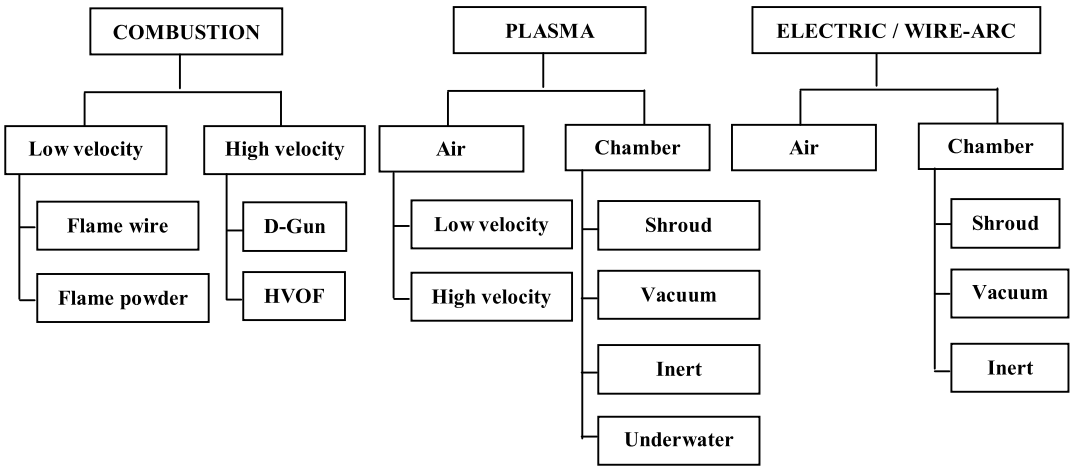

Fig.2.3 Classification of thermal spray processes (Smith & Knight, 1995).

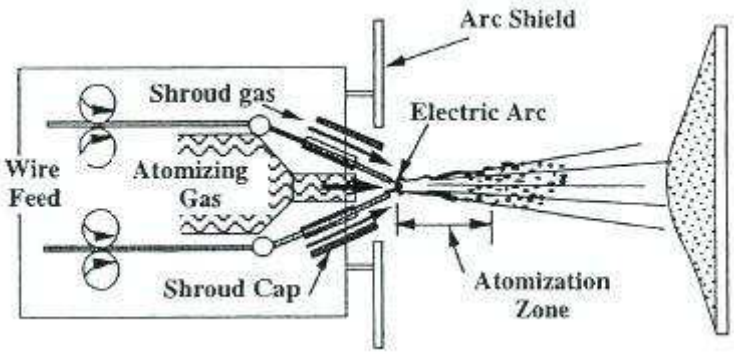

Fig. 2.4 Schematic of wire-arc spraying system

(Smith & Knight, 1995).

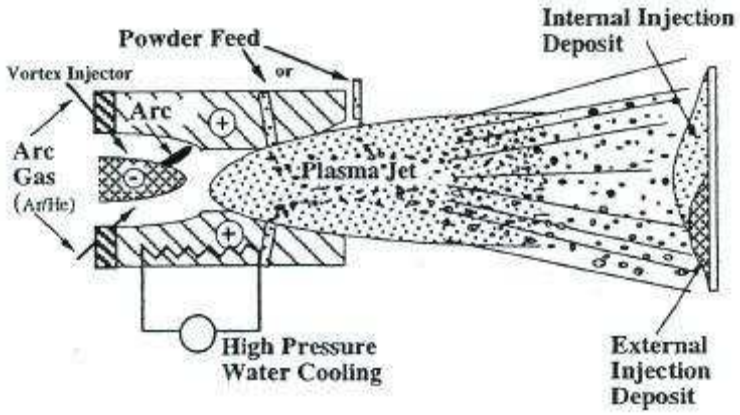

Fig.2.5 Schematic of atmospheric plasma spraying system

(Smith & Knight, 1995).

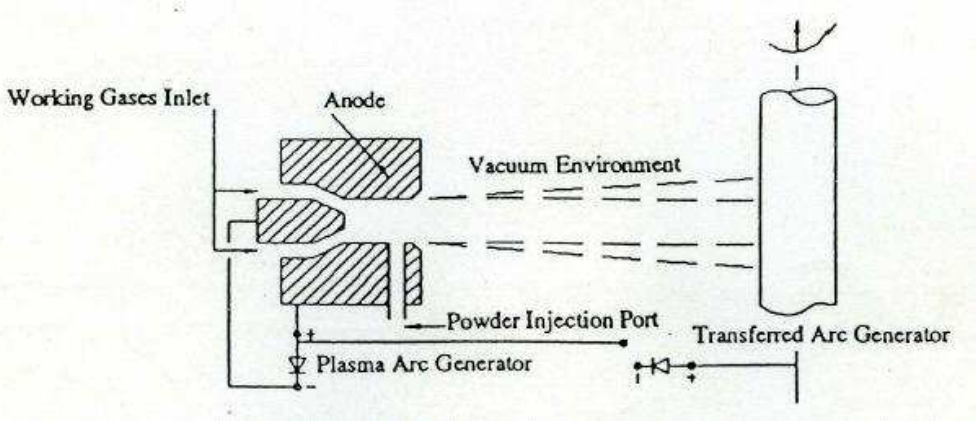

Fig. 2.6 Schematic of vacuum plasma spraying system

(Rickerby & Matthews, 1991).

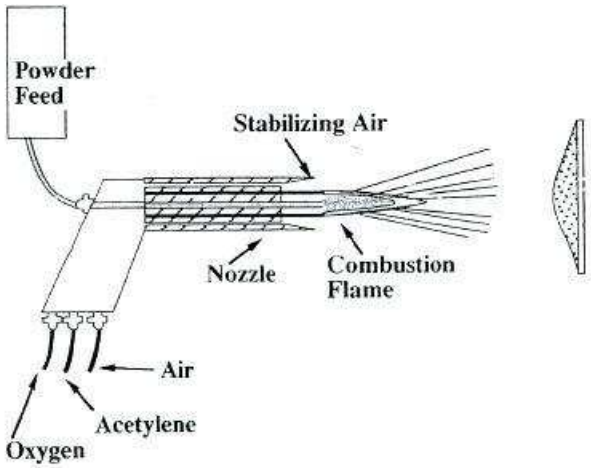

Fig. 2.7 Schematic of combustion flame spraying system

(Smith & Knight, 1995).

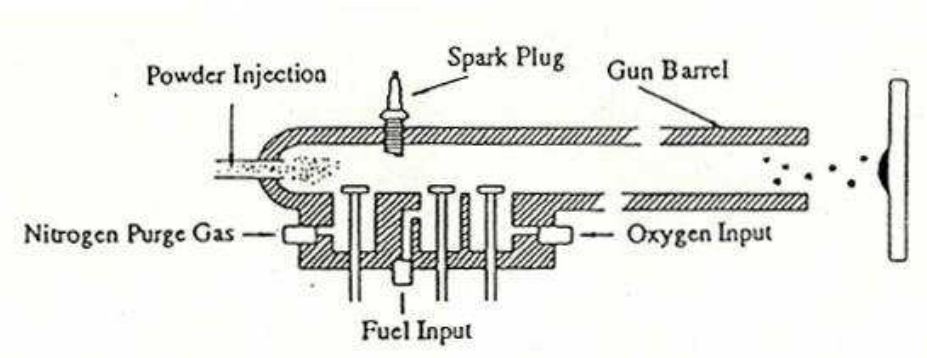

Fig. 2.8 Schematic diagram of the detonation spraying apparatus

(Pawlowski, 1995).

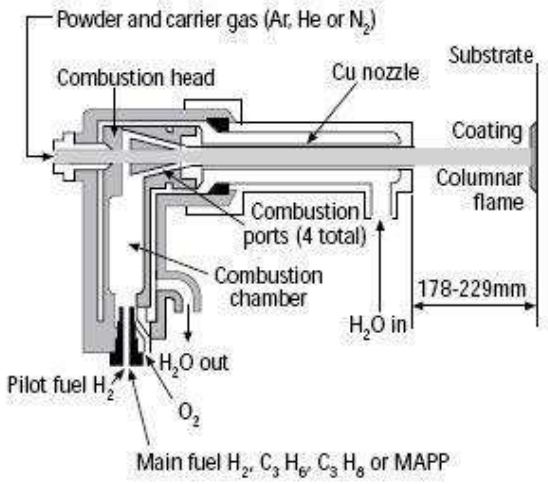

(a) Jet-Kote spraying system (Harvey, 1996)

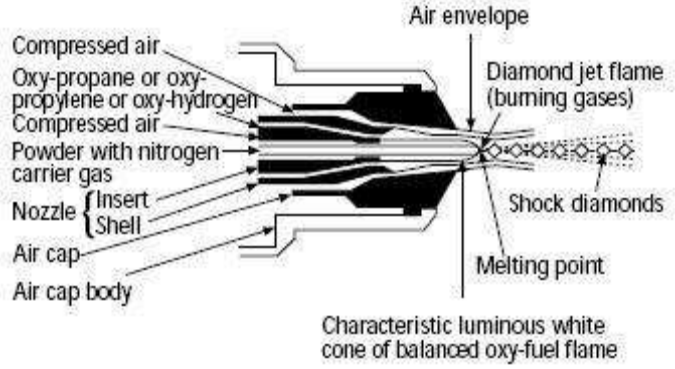

(b) Diamond Jet spraying system (Harvey, 1996)

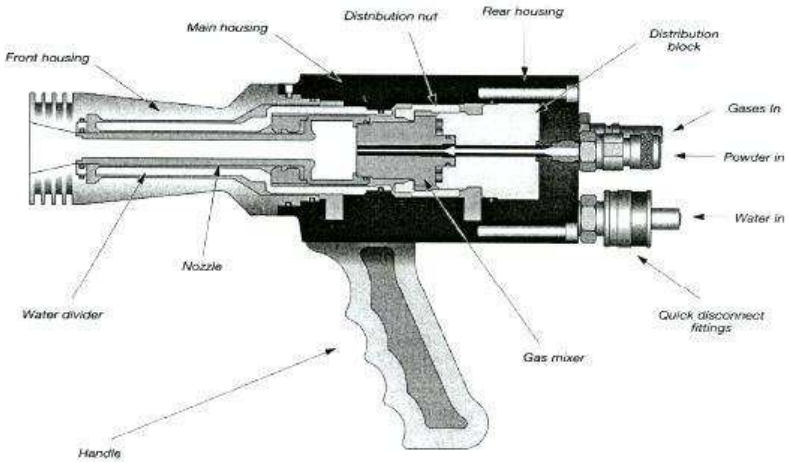

(c) HV-2000 (Praxair Surface Technologies, Inc., 1997)

Fig.2.9 Schematic diagrams of the HVOF thermal spray guns:

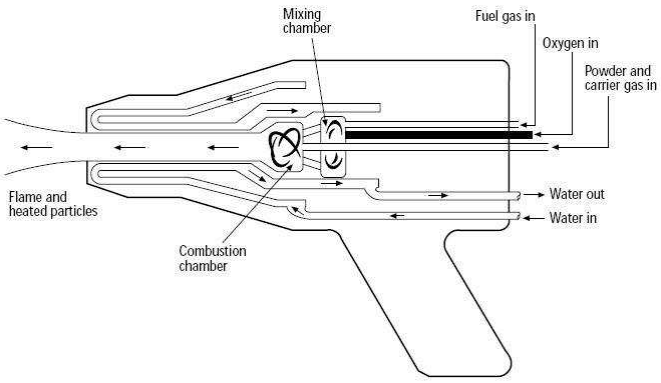

(d) Top Gun HVOF spray gun system (Harvey, 1996).

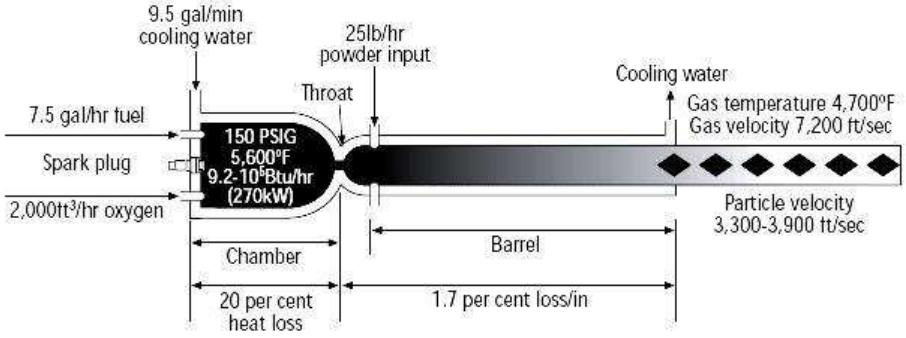

(e) Liquid fuel combination HVOF system, Model JP-5000 (Harvey, 1996).

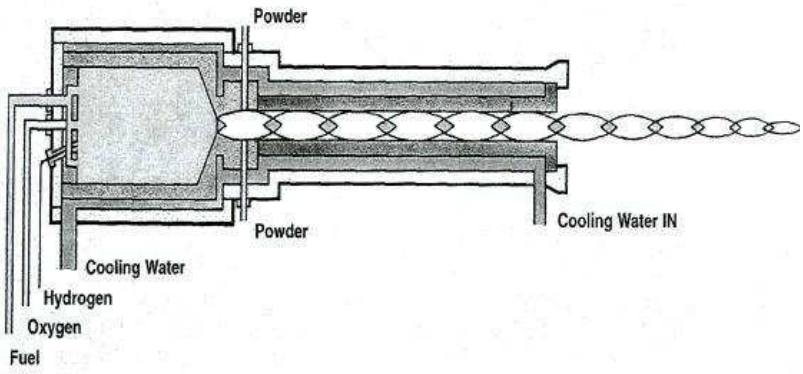

(f) Met-Jet (Metallisation, Ltd.)

Fig.2.9 (continued) Schematic diagrams of the HVOF thermal spray guns:

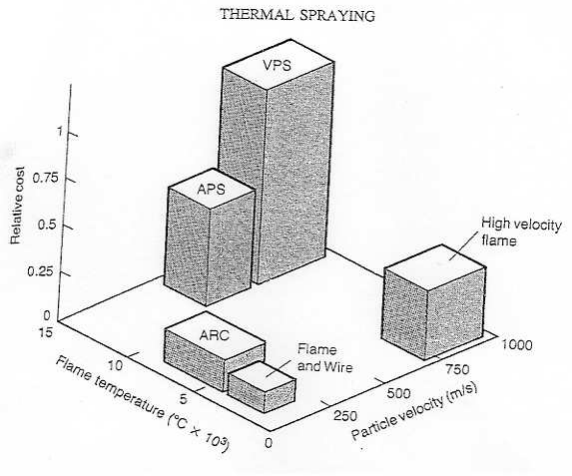

Fig. 2.10 Comparison of the relative flame temperatures, particle velocities and costs associated with the major thermal spray processes (Rickerby & Matthews, 1991)

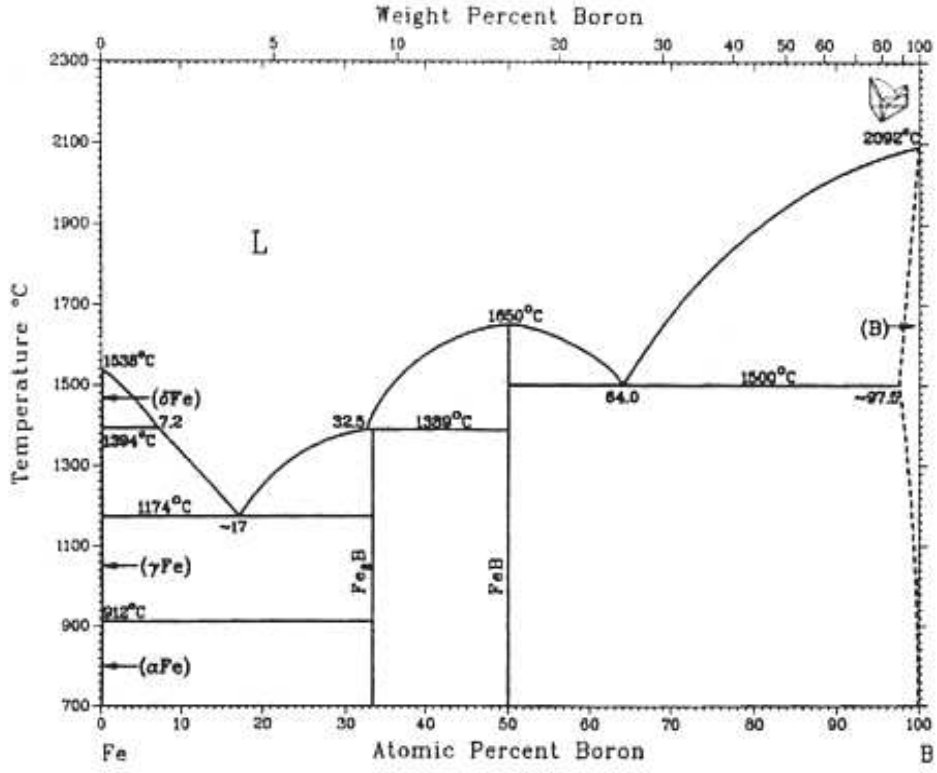

Fig.2.11 The phase diagram of Fe-B based alloys system (Liao & Spear, 1986).

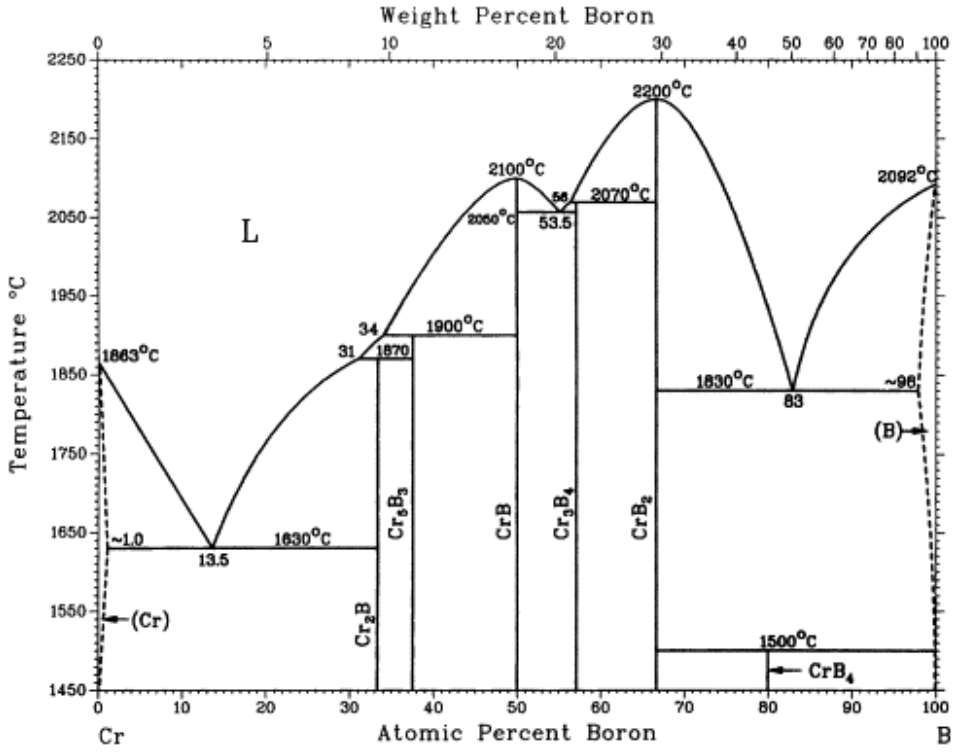

Fig.2.12 Cr-B phase diagram considered by Liao & Spear (1986) in (Massalski,1990).

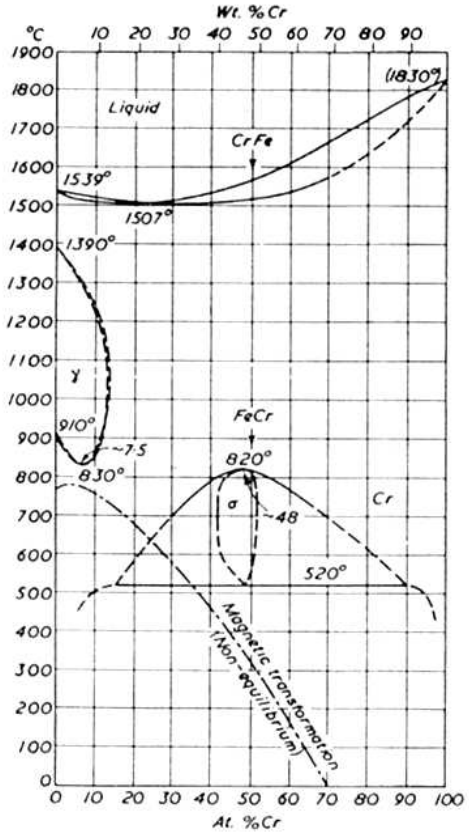

Fig.2.13 The phase diagram of Cr-Fe based alloys system (Baker, 1992).

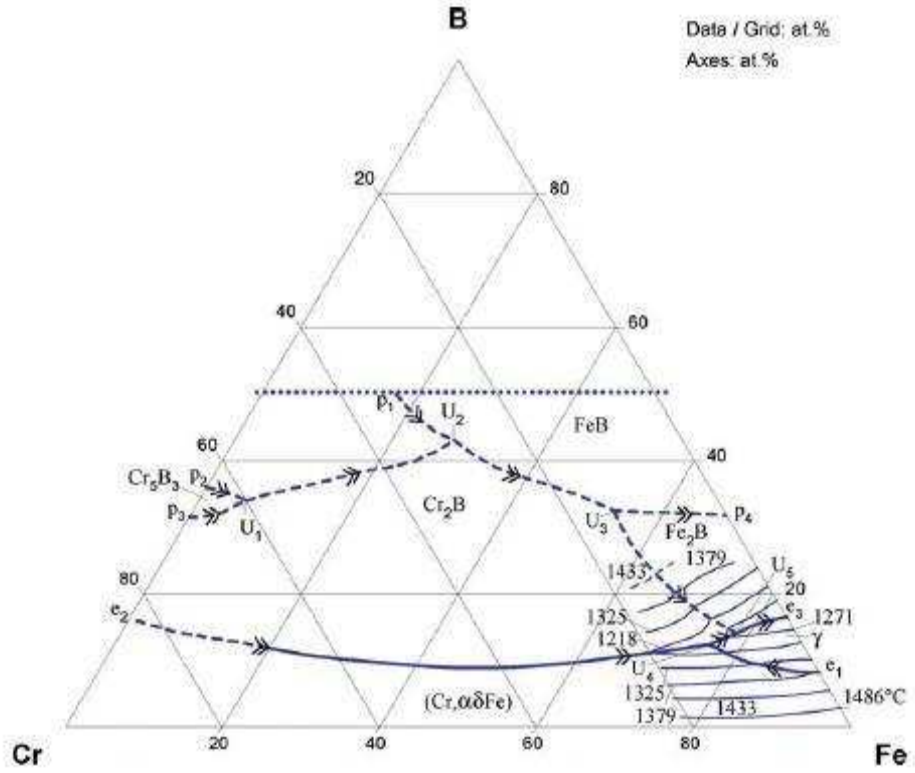

Reaction Scheme

Reaction	T [°C]	Type	Phase	Composition (at.%)		
				Cr	Fe	B
L + CrB ⇌ FeB	1960	p_1	L	33	17	50
			CrB	45.5	4.5	50
			FeB	40	10	50
L + Cr_5B_3 ⇌ Cr_2B + CrB	~1850	U_1	L	60	6	34
L + CrB ⇌ Cr_2B + FeB	~1700	U_2	L	28	29	43
L + FeB ⇌ Cr_2B + Fe_2B	~1350	U_3	L	14	53,5	32,5
L + (Cr,αFe) ⇌ (γFe) + Cr_2B	1270	U_4	L	17.3	71.1	11.6
	1270			14.7	73.8	11.5
	1230			11.9	75.7	12.4
L + Cr_2B ⇌ (γFe) + Fe_2B	1226	U_5	L	10.4	75.2	14.5
	1201			7.5	78.4	14.1
Cr_2B + (γFe) ⇌ (Cr,αFe) + Fe_2B	~1150	U_6	No data	-	-	-

Fig. 2.14 Fe-Cr-B ternary diagram (after Bondar, 2008).

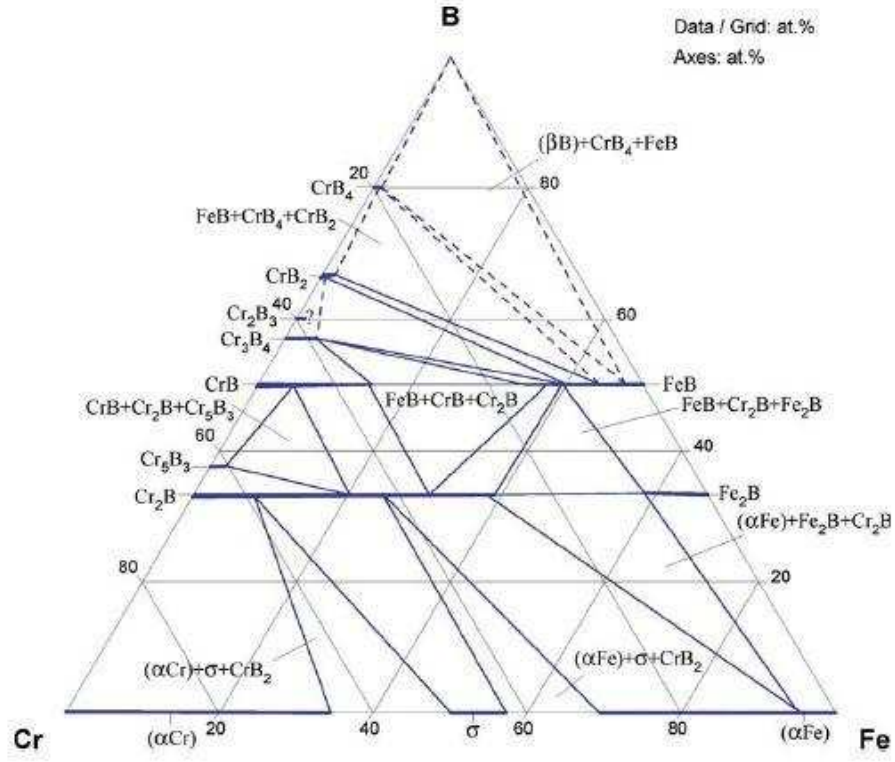

Fig. 2.15 Fe-Cr-B Isothermal section at 700°C (Bondar, 2008).

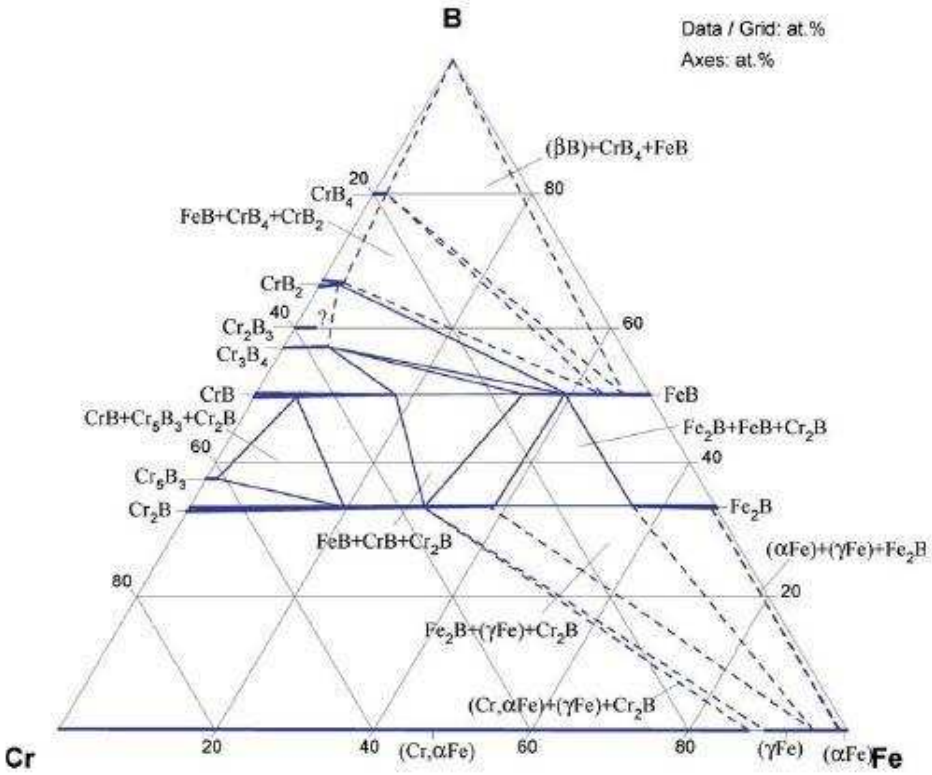

Fig. 2.16 Fe-Cr-B Isothermal section at 900°C (Bondar, 2008).

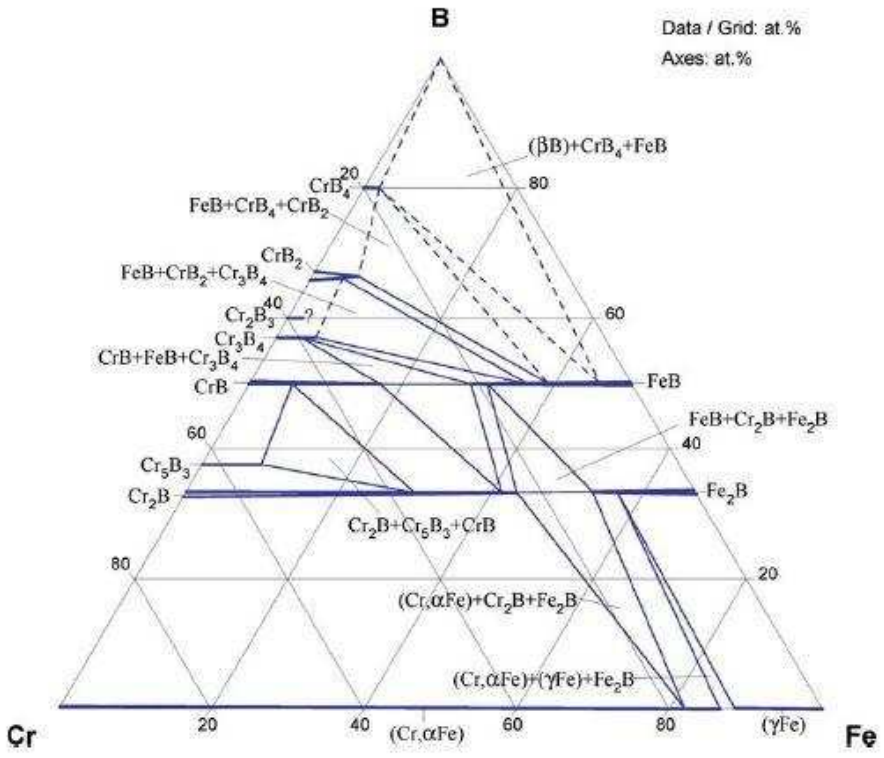

Fig. 2.17 Fe-Cr-B Isothermal section at 1100°C (Bondar, 2008).

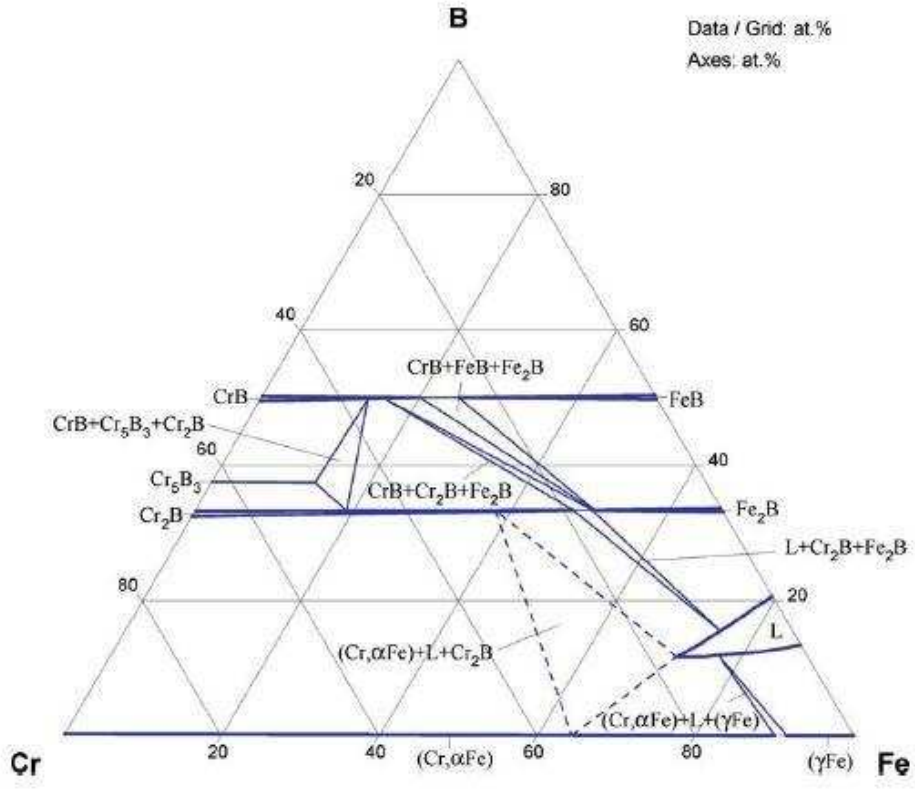

Fig. 2.18 Fe-Cr-B Isothermal section at 1250°C (Bondar, 2008).

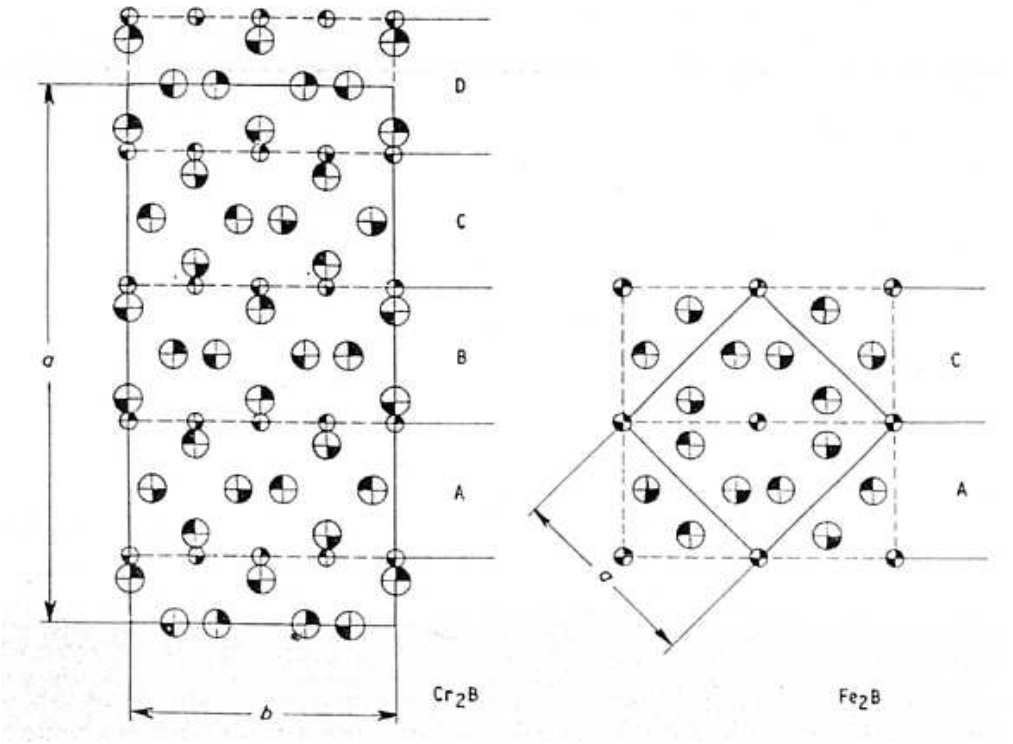

Fig. 2.19 A comparison between crystal structures of (a) Cr_2B and (b) Fe_2B where the larger atoms are Cr and Fe and smaller atoms are B (Yijian and Jian, 1991).

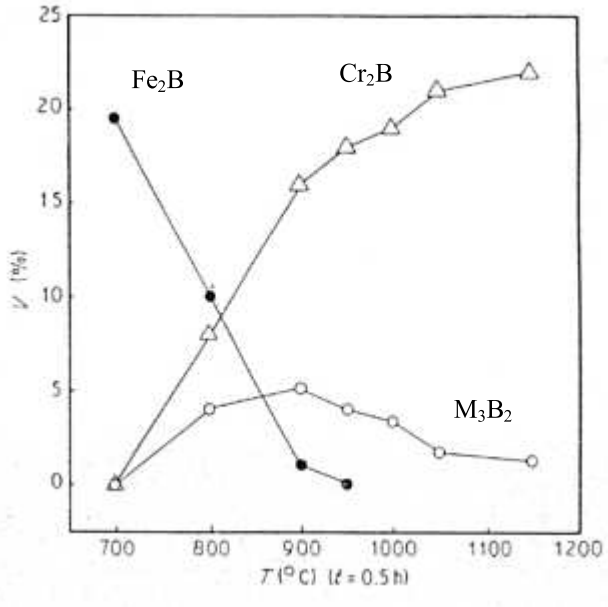

Fig.2.20 The relation between the volume fractions of borides and the annealing temperature, (Δ) Cr_2B, (○) M_3B_2, (●) Fe_2B (Yijian and Jian, 1991).

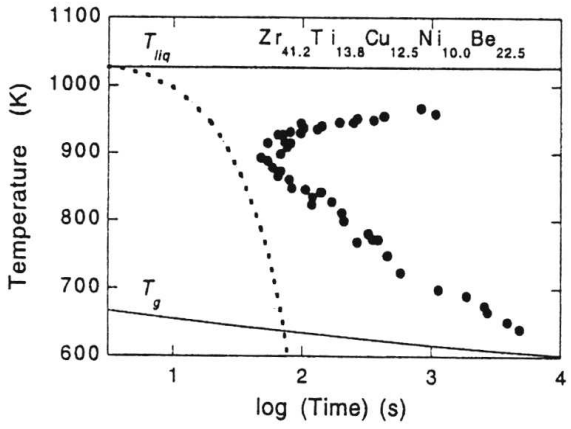

Fig.2.21 Isothermal transformation diagram for the onset (10^{-4} fraction transformed) of primary crystallization of the bulk metallic glass-former vitreloy1. Crystallization occurs between the liquidus T_{liq} and the glass transition temperature T_g, and can be avoided by sufficiently rapid quenching of the liquid (dotted line) (Busch, 2000).

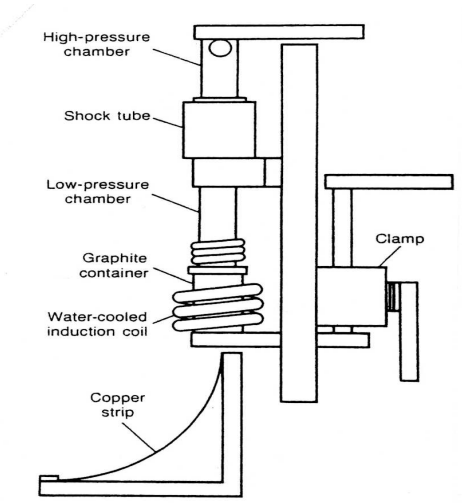

Fig.2.22 Schematic showing the gun quenching apparatus used by Dewiz et al. to carry out rapid solidification experiments (Johnson, 1990).

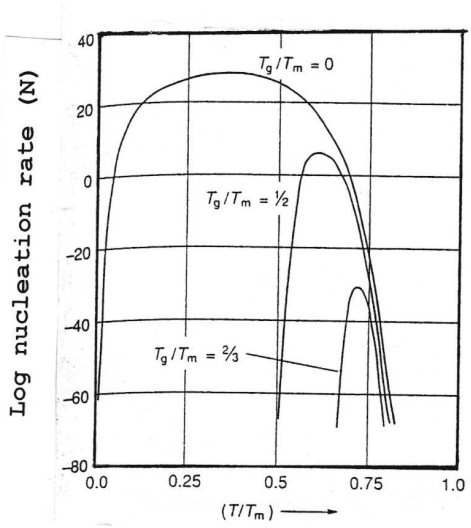

Fig.2.23 The nucleation rate (N) in an undercooled melt as a function of the ratio T_g/T_m (Johnson, 1990)

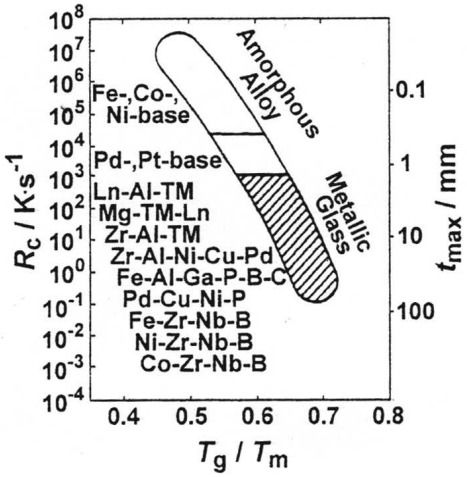

Fig.2.24 Relation among the critical cooling rate for glass formation *(R_c)* t_{max} and T_g /T_m (Johnson, 1990).

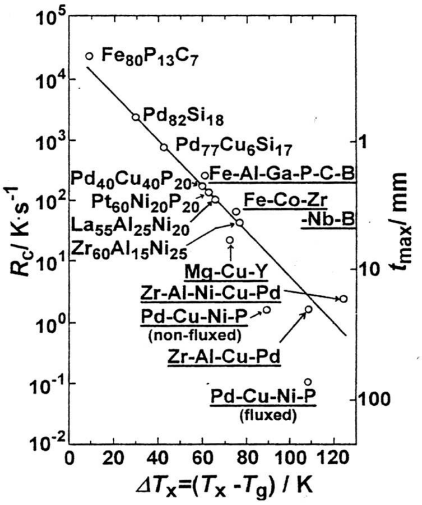

Fig.2.25 Relation among formation (R_c), t_{max} and ΔT_x ($=T_x - T_g$) (Johnson, 1990).

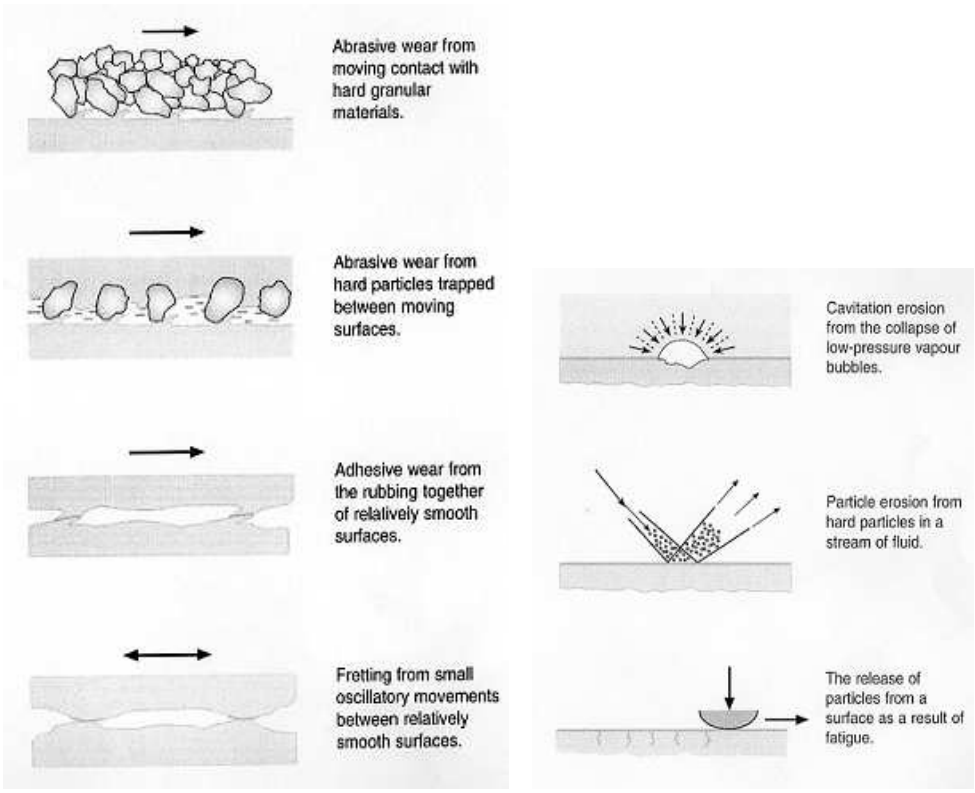

Fig. 2.26 The types of wear that occur in industial machines (Neale et al., 2000).

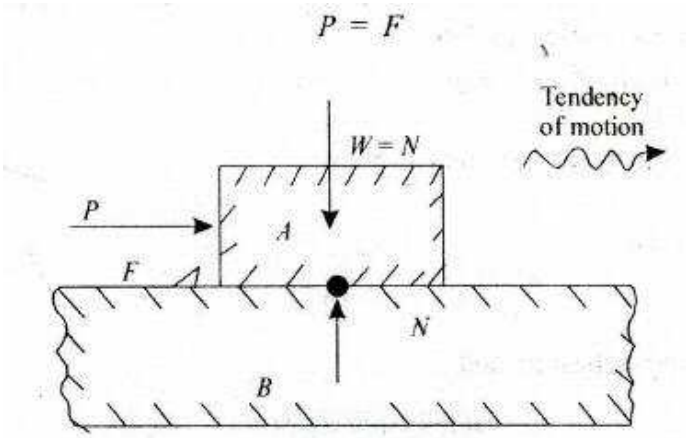

Fig. 2.27 shows a sliding pair A and B, where F is the frictional force causing a tendency to slide. Note that for sliding conditions (Basu et al., 2005).

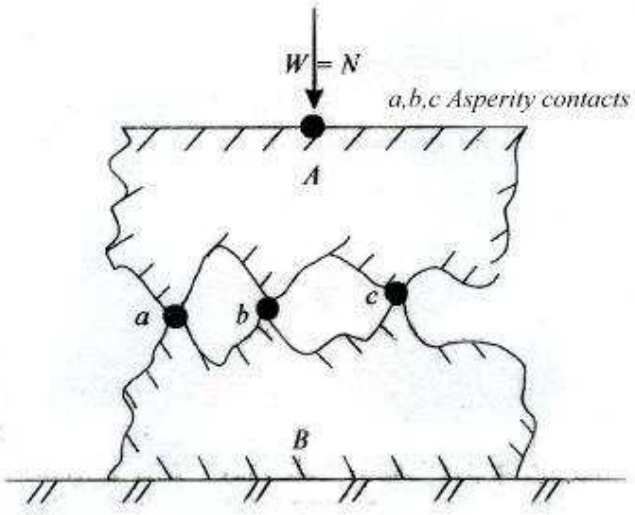

Fig. 2.28 shows two surfaces (A and B) comes in contact, only the high spots (a, b and c) called asperities touch each other (Basu et al., 2005).

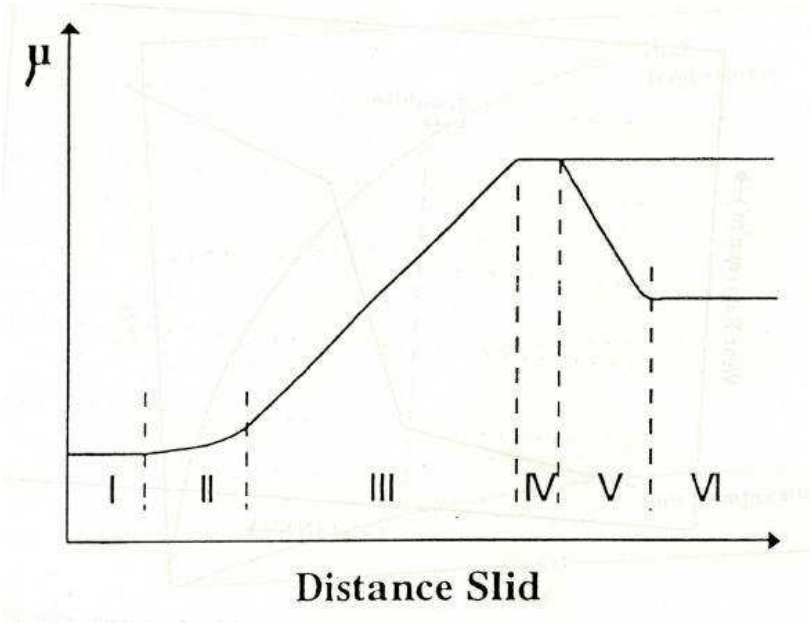

Fig. 2.29 Six stages in the frictional force versus distance slid relationship (Suh, 1986).

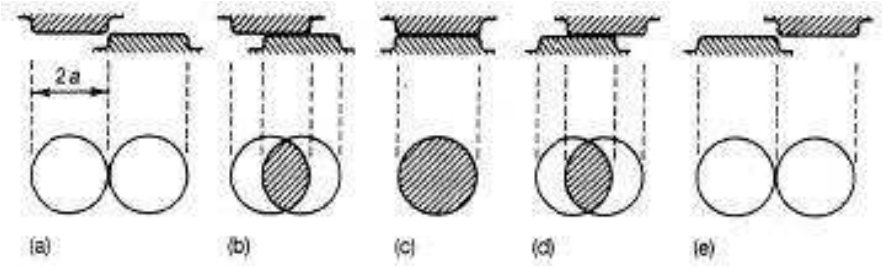

Fig. 2.30 Schematic diagram showing the evolution of a single contact patch as two asperities move over each other (Archard, 1953).

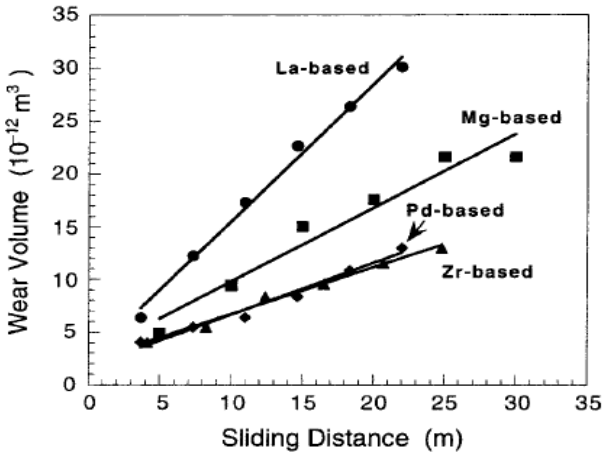

Fig.2.31 Volume of wear scars in four bulk metallic glasses ($La_{60}Al_{20}Ni_{10}Co_5Cu_5$, $Mg_{65}Ni_{20}Nd_{15}$, $Pd_{40}Ni_{10}Cu_{30}P_{20}$, and $Zr_{55}Al_{10}Ni_5Cu_{30}$) as a function of sliding distance S during three-body abrasive wear in micro-scale abrasion test (Greer and Myung, 2001).

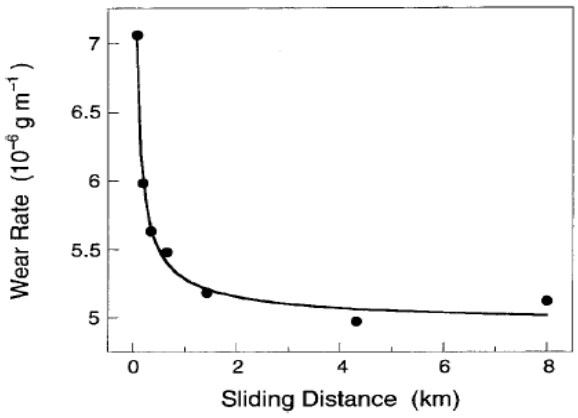

Fig.2.32 Wear rate of bulk metallic glass ($Zr_{41.2}Ti_{13.8}Cu_{12.5}Ni_{10.0}Be_{22.5}$), Disc sliding against pin of same material in air (Fu and Rigney, 1999).

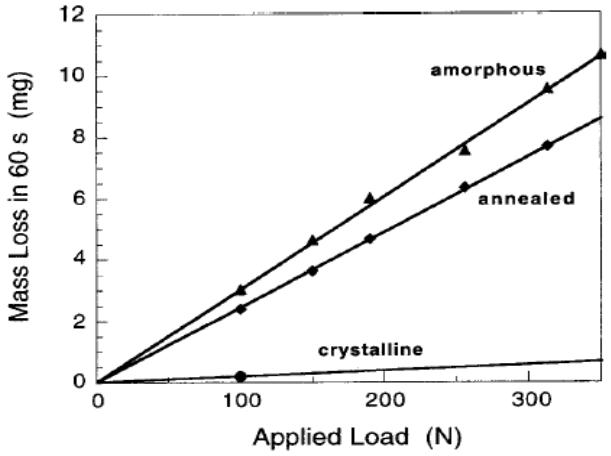

Fig.2.33 Mass lost in 60s as function of normal load N during dry two-body abrasive wear (on 8 μm grade WC rolls) of $Fe_{81}B_{13.5}Si_{3.5}C_2$ at sliding speed of 37.5 mms^{-1} for material tested in three conditions; as quenched, annealed to induce structural relaxation, and crystallised (Wong and Li, 1984).

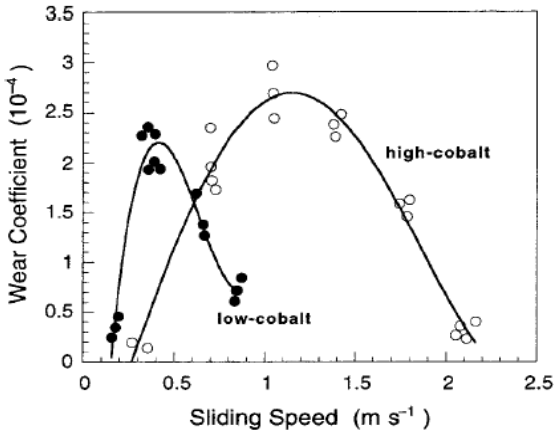

Fig.2.34 Wear coefficient K of two Co based amorphous alloys under dry sliding wear as function of sliding speed (Li and Wang, 1991).

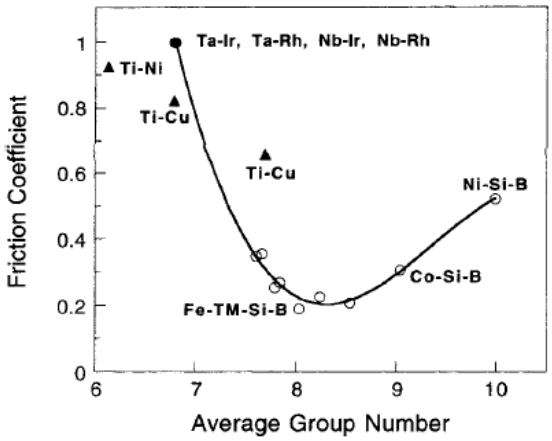

Fig.2.35 Friction coefficient as function of average Mendeleev group number in periodic table for various amorphous alloys (Whang and Giessen, 1982).

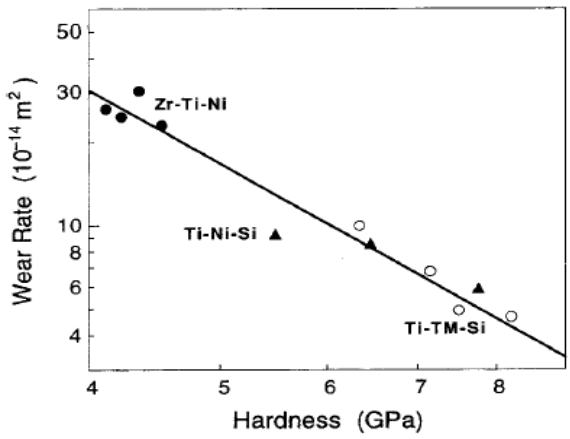

Fig.2.36 Log-log plot showing that wear rate Q decreases with increasing hardness H for ternary Ti or Zr based amorphous alloys (Whang and Giessen, 1982).

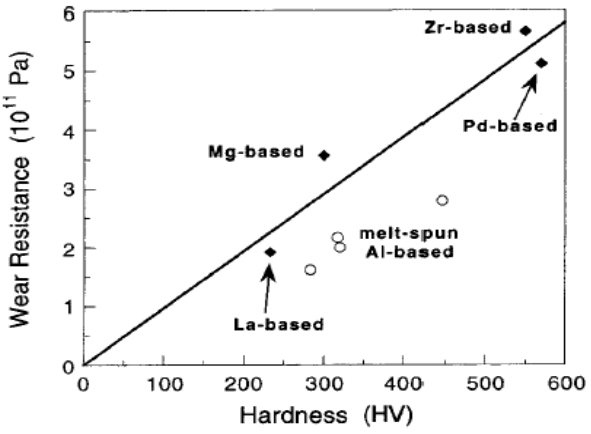

Fig.2.37 Correlation of wear resistance (under three-body abrasion) with hardness for four bulk metallic glasses (Fig.2.31) (Rutherford and Hutchings, 1996) and also shown a data for rapidly quenched ribbons of Al based metallic glasses (Greer, 1997; Gloriant, 1998).

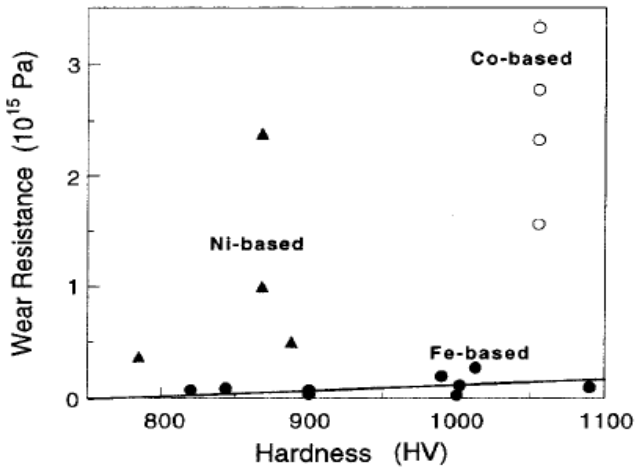

Fig.2.38 Correlation of wear resistance with hardness for like-on-like sliding wear of various Fe, Ni, and Co based amorphous alloy (Moreton and Lancaster, 1985).

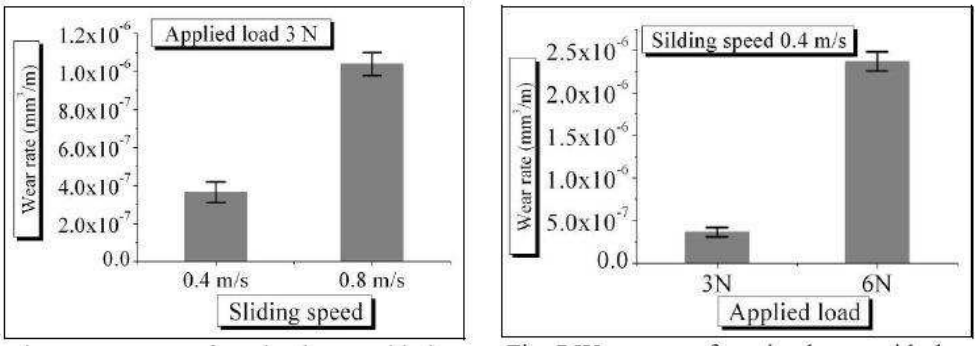

(a) (b)

Fig. 2.39 Wear rates of coating layers with the sliding speed at the applied load of 3 N (a) and with the applied load at the sliding speed of 0.4 m/s (b), (Kim et al., 2007).

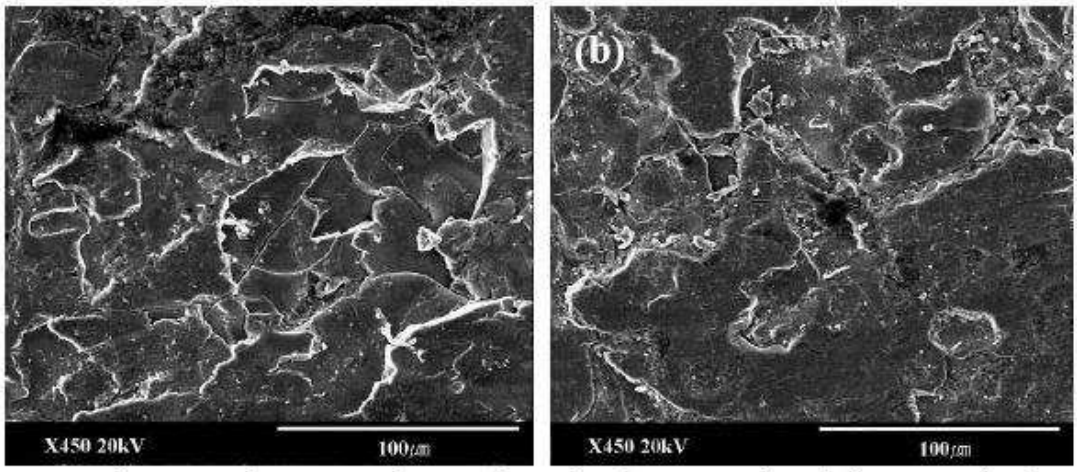

(a) (b)

Fig. 2.40 SEM images of the worn surfaces of the coating layers at the sliding speed of 0.8 m/s and the applied load of 3 N (a) and the sliding speed of 0.4 m/s and the applied load of 6 N (b), (Kim et al., 2007).

Chapter 3

Experimental Procedures

The aim of this chapter is to provide a generalized introduction to the characterisation techniques used in this work. The principal concept of particle size analysis of powders using a Malvern Mastersizer S is presented first. A number of microstructural characterisation techniques, such as X-ray diffraction (XRD), scanning electron microscopy (SEM), energy dispersive X-ray (EDX) analysis, transmission electron microscopy (TEM) and differential scanning calorimetry (DSC) are then presented. The assessment of microhardness of coatings and the procedure of heat treatment are briefly described. In addition, the procedure for dry sliding wear testing is given in section 3.6.

3.1 Materials

Three commercially available gas atomised Fe-Cr-B based alloy powders (Armacor M, Armacor C and SHS7170) and a powder composition designed during this study (given the code KC1) were employed in this work. The Armacor M and Armacor C powders were supplied by Liquidmetal Company, Texas, CA, USA. The SHS7170 powder was supplied by Nanosteel Company Inc, Providence, Rhode Island, USA and the gas atomised powder KC1 was made at University of Birmingham, UK. In addition, WC-Co-Cr powder (with the nominal composition in wt%, 86WC-10Co-4C) was obtained from Praxair Inc., and was used as a feedstock to spray a reference coating for the sliding wear testing.

3.2 Thermal Spraying and Heat Treatment

3.2.1 Substrate Preparation

The substrates used in this work were mild steel (BS08015). Discs of diameter 40mm with thickness of 6mm were used for dry sliding wear testing and substrate of 25 x 59 x 2 mm were used for characterisation of the coatings. The substrates were degreased and grit-blasted with alumina before spraying to provide a roughened surface to enhance the bonding of the coatings.

3.2.2 Deposition Procedure

High-velocity oxy-fuel (HVOF) thermal spraying was carried out using a Metallisation Met-Jet II spray system (Metallisation Ltd., Dudley, UK) as shown in Fig. 3.1. Liquid kerosene was used as a fuel which is combusted with pure oxygen at a pressure of around 8 bar in the combustion chamber of the gun. The combustion products flow through a converging-diverging nozzle and powder is injected, downstream of the throat through two radial ports, into the hot, high-speed gas. The powder is then accelerated and heated by the gas stream as it flows along a parallel-sided barrel. Coatings, typically of thickness 300-400 μm, were deposited onto flat, grit-blasted and degreased mild steel substrates which were mounted on a turntable and rotated while the spray gun traversed vertically with a speed ~ 1 ms^{-1}. Samples were cooled during and after spraying using compressed air jets to keep the temperature below 200°C. Spray parameters selected were optimised to minimise both the deposit porosity and degree of oxidation of the particles during spraying. The operating parameters of the Met-Jet II spray system for deposition of the various coating types are shown in Table 3.1.

Table 3.1 Parameters used in the deposition of the Fe-Cr-B based alloy powders using a Met Jet II gun

Parameter	Armacor M	Armacor C	SHS7170	KC1
Kerosene flow rate (l min^{-1})	0.44	0.44	0.39	0.33
Oxygen flow rate (l min^{-1})	791	743	897	915
Carrier gas flow rate (l min^{-1})	7.5	7.5	7.5	7.0
Spraying distance (mm)	355	355	355	355
Nozzle length (mm)	100	100	100	100

(WC-Co-Cr coating was supplied by TWI company and spray parameter is not shown here).

Fig. 3.1 The set up of the high-velocity oxy-fuel (HVOF) thermal spraying system using a Metallisation Met-Jet II spray system

3.2.3 Heat Treatment of powders and coatings

The heat treatments were carried out in a furnace with an argon atmosphere to prevent oxidation of both the powder and coating. The powder and coating were heated from room temperature to the heat treatment temperature at a heating rate 20 K min^{-1} and were then held for the appropriate time before being furnace cooled down to room temperature. One set of heat treatments was performed for a fixed time of 60 minutes at the following temperatures: 550, 650, 750 and 925°C. A second set of heat treatments was performed at only two temperatures, namely 650 and 750°C, with holding times of 60 to 3900 minutes at 650°C and 20 to 120 minutes at 750°C. This choice of temperatures was based on results obtained relating to the crystallization behaviour of amorphous material within powders and coatings.

3.3 Microstructural Characterisation of Materials

3.3.1 Size Distributions of powders

A Malvern Mastersizer S (Malvern Instruments Ltd, Malvern, UK) was used to measure the particle size distribution of the feedstock powders by laser granulometry, using Masterizer-s (V 2.18) software for analysis. The Fraunhofer diffraction model, assuming a standardized spherical shape, was used to analyze all samples. The powders were dispersed and circulated in 2-propanol. When the particles passed through the laser beam, the light was scattered, and collected by annular detectors. The angles and intensity of the scattering of the light beam enabled the equivalent powder diameter to be calculated.

3.3.2 Chemical Analysis of powders

The chemical compositions of the three powders (Armacor M, Armacor C and SHS7170) were analyzed by inductively coupled plasma (ICP) spectroscopy, X-ray fluorescence spectrometry (XRF) and a combustion method for carbon and sulphur analysis at London & Scandinavian Metallurgical (LSM) Co Limited, England. The chemical composition of the KC1 powder was analyzed by SEM/EDX analysis for Fe, Cr, Mo, Si while B and C are nominal values. The results are shown in Table 3.2.

Table 3.2 The composition of the four Fe-Cr-B based feedstock powders used in weight % and atomic%.

	Composition wt%											
Element	Fe	Cr	B	Si	Mo	Mn	Ni	Cu	Co	W	C	S
Armacor M	Bal	44.1	5.6	4.7	-	-	-	-	-	-	0.1	0.005
Armacor C	Bal	30.4	3.5	3.1	3.6	-	20.3	2.7	8.7	-	0.1	0.006
Nanosteel	Bal	20.3	3.6	1.6	4.8	2.1	-	-	-	6.3	1.0	-
KC1	Bal	17.1	2.1	0.5	32.5	-	-	-	-	-	3.6	-

	Composition atom%											
Element	Fe	Cr	B	Si	Mo	Mn	Ni	Cu	Co	W	C	S
Armacor M	Bal	35.9	22.0	7.1	-	-	-	-	-	-	0.4	0.01
Armacor C	Bal	27.9	15.4	5.3	1.8	-	16.5	2.0	7.1	-	0.4	0.01
Nanosteel	Bal	18.9	16.2	2.8	2.4	1.8	-	-	-	1.7	4.1	-
KC1	Bal	16.7	10.0	0.9	17.2	-	-	-	-	-	15.0	-

3.3.3 X-Ray Diffraction of powders and coatings

X-ray diffraction is commonly used for the assessment of powder and coating phase analysis. The basic principles associated with diffraction are presented here regarding to X-ray scattering and interference.

In XRD, an X-ray wave may be described as an electromagnetic field which when interacting with an atom can cause the atom to oscillate and emit an electromagnetic wave, being coherent with the incident X-ray wave. This process is known as Rayleigh scattering. In a crystal, there will be three dimensional planes of atoms which can act as diffraction gratings for radiation having a wavelength comparable in size to the spacing between the atomic planes. A simple description of diffraction process can be explained by using Bragg's law as shown in Fig. 3.2. The condition for constructive interference is satisfied when the difference in path length between the incident and scattered waves is equal to a whole number (n) of wavelengths. That is:

$$n\lambda = 2d \sin\theta \qquad (3.1)$$

where n is an integral number, d is the lattice spacing, λ is the X-ray wavelength and θ is the incident Bragg angle (Culity & Stock, 2001; Hammond, 2001; Chamness, 2001). Equivalently this can be written as $\lambda = 2d_{hkl} \sin\theta$ where $(\frac{d}{n})$ is taken to be d_{hkl}.

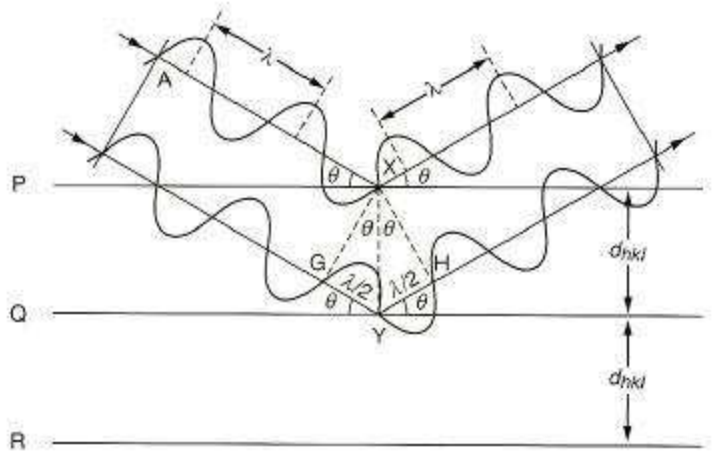

Fig. 3.2 Bragg's diffraction condition is satisfied when the difference in path length between the incident and scattered waves is equal to a whole number (n) of wavelengths. P, Q and R are three lattice planes (hkl) of spacing d_{hkl} in a crystal. The incoming radiation of wavelength λ incident at a glancing angle θ is diffracted at the same angle. Constructive interference is obtained when the Bragg equation is satisfied (Champness, 2001).

Fig. 3.3 shows a schematic diagram of a typical powder XRD set up for a polycrystalline material. In XRD, the sample is rotated at a constant angular velocity and when Bragg's diffraction condition is satisfied (see equation 3.1), a corresponding x-ray diffraction (constructive interference) would occur at an angle of 2θ. The positions and the intensities of the peaks give information that can be used to determine the lattice parameters of the unit cell and the atomic positions within the unit cell, respectively. Each peak present in the pattern has its own set of indices (hkl).

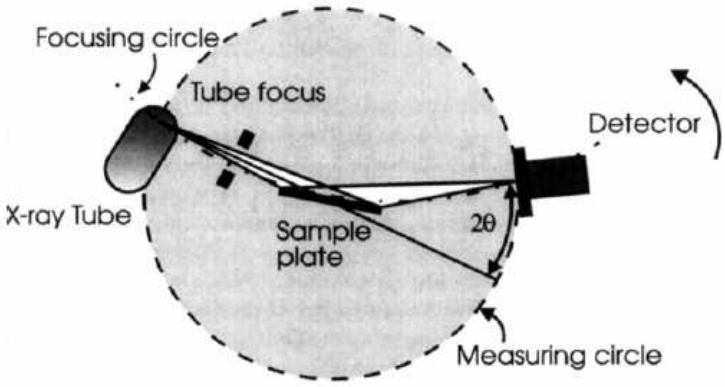

Fig. 3.3 Schematic diagram of a typical powder XRD set-up (Cullity & Stock, 2001).

By comparing the pattern with standard database which holds a record of the indices of each diffraction peak, such as the Joint Committee for Powder Diffraction Standards (JCPDS) etc., it is possible to identify specific phases. The process of determining the (hkl) associated with an individual peak is known as indexing the pattern. An example of indexing of the pattern of as-received Armacor M powder is given in table 3.3-3.5 and comparison of the experimental XRD pattern with JCPDS files of borides $Fe_{1.1}Cr_{0.9}B_{0.9}$ and Cr_2B is shown in Fig. 3.4a-3.4b.

Table 3.3 XRD 2θ and intensity data for as-received Armacor M powder compared with JCPDS 72-1073 for boride $Fe_{1.1}Cr_{0.9}B_{0.9}$.

hkl reflection	JCPDS 72-1073 $Fe_{1.1}Cr_{0.9}B_{0.9}$ 2θ	Intensity	Data observed 2θ	Intensity	DATA calculated 2θ	Difference 2θ
311	30.582	130	30.611	3.0	30.560	0.022
511	39.515	664	39.513	10.1	39.465	0.050
131	43.244	999	43.263	21.4	43.216	0.028
202	44.677	778	44.833	100.0	44.787	0.110
620	44.752	901				
331	46.865	287	46.751	7.4	46.706	0.159
022	49.845	88	49.840	8.4	49.797	0.048
711	50.41	397	50.350	8.8	50.307	0.103
422	56.261	350	56.233	18.9	56.193	0.068
911	62.716	33	62.538	2.6		
822	73.317	105	73.235	7.8	73.207	0.110
			76.042	3.5		
133	78.735	169	78.658	8.1	78.635	0.100
642	79.756	160				
1002	79.945	129				
751	83.93	76	82.529	22.0	82.509	1.421
1131	86.697	90	86.394	4.0	86.378	0.319

Table 3.4 XRD 2θ and intensity data for as-received Armacor M powder compared with JCPDS 38-1399 for boride Cr_2B.

hkl	JCPDS 38-1399 Cr_2B 2θ	Intensity	Data observed 2θ	intensity	DATA calculated 2θ	Difference 2θ
131	30.307	14	30.611	3.0	30.560	0.253
151	39.14	57	39.513	10.1	39.465	0.325
311	42.746	55	43.263	21.4	43.216	0.470
022	44.334	100	44.833	100.0	44.787	0.453
331	46.354	16	46.751	7.4	46.706	0.352
080	49.538	10	49.840	8.4	49.797	0.259
171	49.883	38	50.350	8.8	50.307	0.424
440	55.503	19				
242	55.734	26	56.233	18.9	56.193	0.459
282	72.565	8	70.951	1.6		
551	75.12	10	73.235	7.8	73.207	1.913
313	77.949	11	76.042	3.5	76.016	
462	78.815	14	78.658	8.1	78.635	0.180
			82.529	22.0	82.509	
3111	85.625	10	86.394	4.0	86.378	0.753

Table 3.5 XRD 2θ and intensity data for as-received Armacor M powder compared with JCPDS 06-0696 for α-Fe (bcc).

hkl reflection	JCPDS 06-0696 Fe (BCC) 2θ	Intensity	Data observed 2θ	intensity	DATA calculated 2θ	Difference 2θ
			24.458	10.2	24.405	
			30.611	3.0	30.560	
			39.513	10.1	39.465	
			43.263	21.4	43.216	
110	44.674	100	44.833	100.0	44.787	0.113
			46.751	7.4	46.706	
			49.840	8.4	49.797	
			50.350	8.8	50.307	
			56.233	18.9	56.193	
			62.538	2.6		
200	65.023	20	65.211	10.1	65.177	0.154
			70.951	1.6		
			73.235	7.8	73.207	
			76.042	3.5		
			78.658	8.1	78.635	
211	82.335	30	82.529	22.0	82.509	0.174
			86.394	4.0	86.378	

From Table 3.3-3.4, it can be seen that pattern of boride $Fe_{1.1}Cr_{0.9}B_{0.9}$ (JCPDS 72-1073) gives a better fit to the peak positions of the as-received Armacor M powder in comparision to boride Cr_2B (JCPDS 38-1399) and from Table 3.5, the pattern of α-Fe (JCPDS 06-0696) shows a well defined of the main peaks with 2θ difference of less than 0.200. Therefore, the determination of the (hkl) associated with an individual peak of the XRD pattern of the as-received Armacor M powder is shown in Fig. 3.4a.

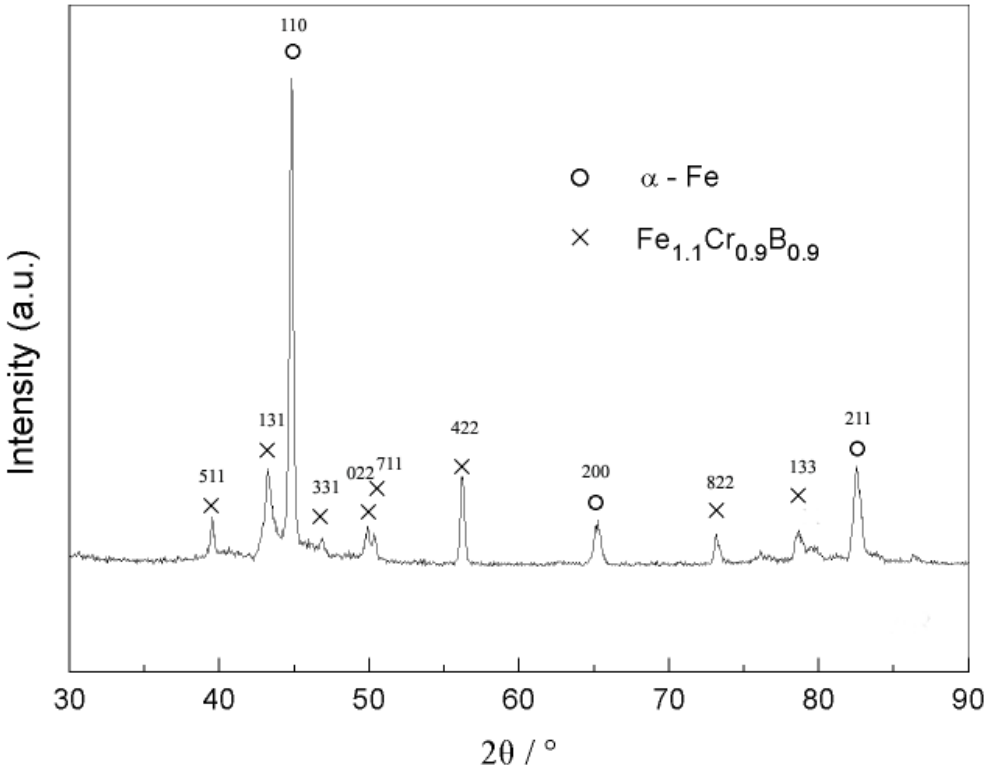

Fig. 3.4(a) XRD pattern of the as-received Armacor M powder.

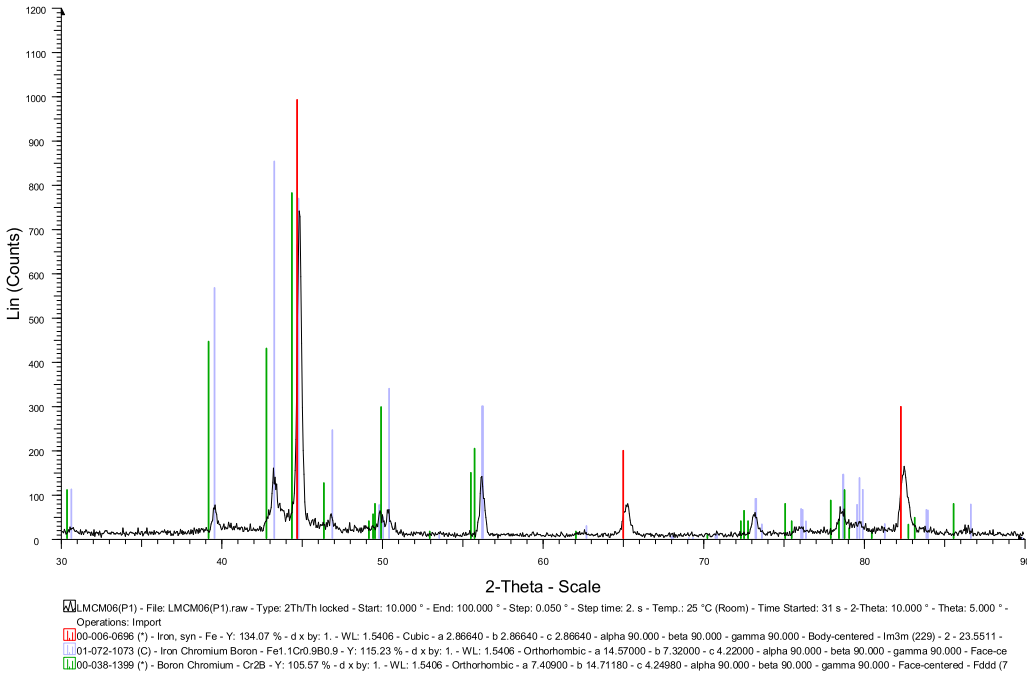

Fig. 3.4(b) Comparison of experimental XRD pattern with JCPDS files for Cr_2B (green line), $Fe_{1.1}Cr_{0.9}B_{0.9}$ (blue line) and α-Fe (red line).

In this work, X-ray diffraction (XRD) of the powders and as-sprayed coatings was carried out using a Siemens Kristalloflex diffractometer operating with Cu-Kα radiation (λ = 1.5406 Å). This was used to identify the phases present in the powders and the coatings. The diffractometer was operated at 40 kV and 20 mA with a diffraction angle (2θ) ranging from 30°- 90°, 0.05° step size and a 2 second dwell time per step were employed. Phases present were identified with the aid of JCPDS diffraction files. The preparation method for the powders was to sprinkle them on to an adhesive tab mounted on the sample holder. Coatings were prepared by grinding the top surface down to a 1μm finish. Before analyses of the sample, a small amount of pure silicon powder (whose d_{hkl} are known) was used to check the calibration of the diffractometer. The curve of the XRD calibration data with silicon is shown in Fig. 3.5 as a plot of Δ(2θ) versus 2θ. By using this curve, a series of XRD peaks of the samples can be corrected for instrumental error before the XRD patterns were indexed. The positions of the lines of the compound being studied are refined by interpolation with those of the standards.

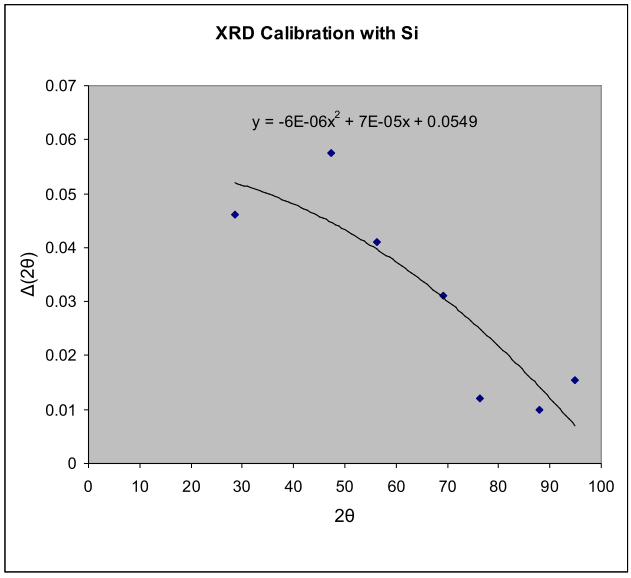

Fig. 3.5 Plot of Δ(2θ) versus 2θ where 2θ is the measured diffraction angle and Δ(2θ) is the difference between measured and known.

3.3.4 Electron microscopy of materials

Electron microscopy uses a high energy electron beam to examine objects on a very fine scale, generating a variety of information on surface morphology, elemental composition and sample crystallography, etc. This section starts with the basic properties of high-energy electrons and the interactions between electrons and matter, and then focuses on scanning electron microscopy (SEM) and transmission electron microscopy (TEM) based characterisation techniques such as selected area electron diffraction (SAED) etc.

3.3.4.1 Interaction of an electron beam with matter

The basic principles of electron beam interaction with matter are included in order to help understand the characterisation methods used for example in SEM and TEM. When the primary electron beam interacts with matter, various signals are created such as characteristic X-rays, secondary electrons (SE), back scattered electrons (BSE) and elastic or inelastic scattered electrons, but these depend on the thickness of the sample. Fig. 3.6 shows signals generated when a high energy beam of electrons interacts with a thin specimen (Brydson, 2001).

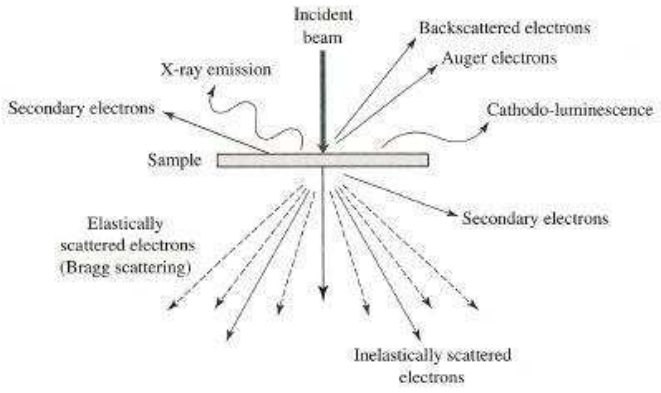

Fig. 3.6 Signals generated when a high-energy beam of electrons interacts with a specimen (Brydson, 2001).

In general, the samples for SEM are very thick, thus secondary electrons or backscattered electrons are generated and used to form an image. In contrast, the TEM samples are very thin, elastically scattered electrons are produced and used to form bright field, dark field images and diffraction patterns. More details of TEM sample preparation and TEM observation of coatings are given in section 3.3.4.3.

3.3.4.2 Scanning Electron Microscopy (SEM)

The external morphology and cross-section of powders were investigated using a Philips FEI XL30 scanning electron microscopy (SEM). A schematic diagram of a typical SEM set-up is shown in Fig. 3.7.

Powders were sprinkled on to a carbon tab (attached to an aluminium stub) which was then sputtered with gold to allow examination of their morphology. Cross-sections of the powders were prepared by mounting the powder in conductive epoxy mounting resin. The samples were then ground with SiC paper (240, 400, 800 and 1200 grit size), and diamond polishing to a 6μm and 1μm finish.

The cross-sections of the coatings were prepared by sectioning normal to the coating by a precision diamond blade on an automatic precision cut-off machine (Accutom-5) operating at 3000 rpm and a cutting rate of 0.01-0.02 mm s^{-1}. After cutting, the specimens were cleaned and then mounted in conductive epoxy mounting resin. The samples were then ground with SiC paper (240, 400, 800 and 1200 grit size), and diamond polished to a 6μm and 1μm finish. In addition, the coatings were etched for 10-30 seconds with reagent consisting of 1 part H_2O, 1 part HCl and 1 part HNO_3.

The external morphology of powders was investigated using secondary electron (SE) imaging in the scanning electron microscope whilst the cross-sections of the powders and the coatings were examined using the back scattered electron (BSE) imaging mode. Quantitative energy dispersive X-ray (EDX) analysis was also utilised to aid phase identification.

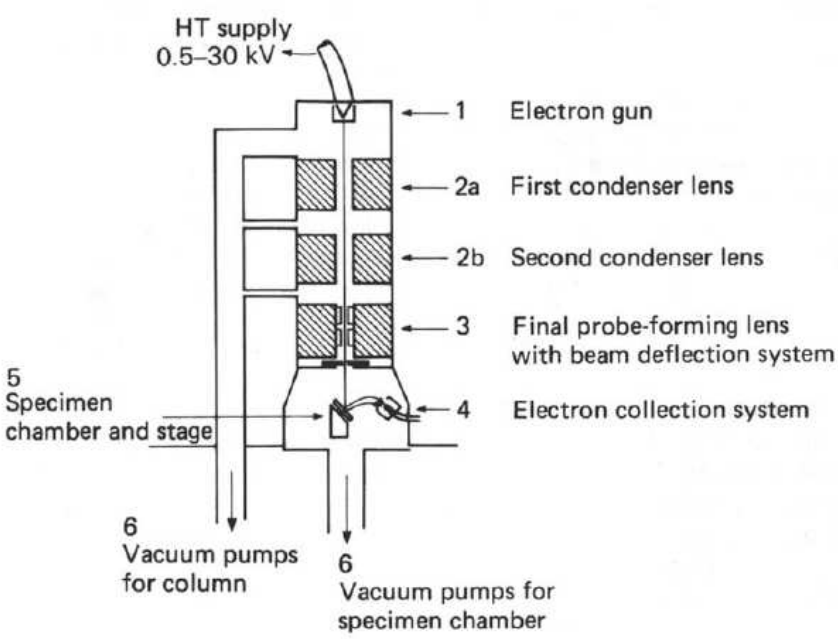

Fig. 3.7 Schematic diagram of the basic components of a SEM (Watt, 1997).

3.3.4.3 EDX analysis

Energy dispersive X-ray spectroscopy (EDX) is sometimes referred to as EDS or EDAX). It is a standard method used for identifying and qualifying the element composition of the specimen. When an electron beam interacts with a material in the SEM or TEM, the incident electron may inelastically scatter from an inner shell electron of one of the component atoms. As result of this inner shell scattering, the target atom is left in an excited state. The ionized atoms can relax by electron shell-to-shell transitions giving a characteristic X-ray as shown in Fig. 3.8. The X-ray emitted will have an energy that is characteristic of the transition between the two shells and can therefore be used to identify the atomic number of the target and also provide compositional information on the sample which is then used to form the X-ray energy-dispersive (EDX) spectra (Williams & Carter, 1996).

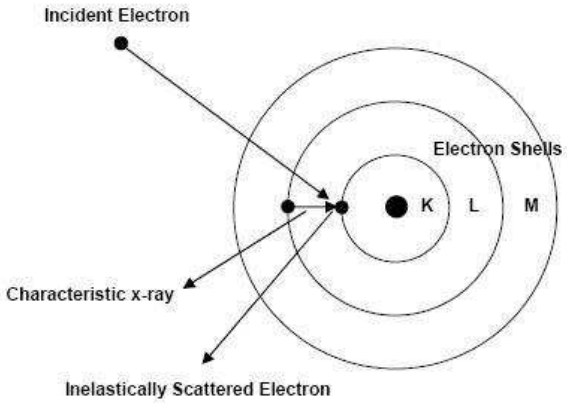

Fig. 3.8 The production of characteristic X-rays which are recorded in EDX analysis (i.e. Kα X-rays).

3.3.4.4 Transmission Electron Microscopy (TEM)

Fig. 3.9 shows a schematic diagram of the basic components of a conventional TEM. It consists of a number of electron optical components, e.g. electron gun, condenser lens, semi-transparent specimen, objective lens, projective lens and projection screen (Brydson, 2001). Electron gun produces a stream of electrons which are accelerated through the anode achieving the final beam energy, typically ~ 100 to 400 keV. The first condenser lens (C1) largely determines the spot size and the second condenser lens (C2) changes the size of the spot across the sample to provide appropriate illumination conditions. The condenser aperture filters out high angle electrons (those far from the optic axis). The thin foil specimen, typically <100 nm, is inserted close to the front focal plane of the objective lens. The contrast of the TEM image can be enhanced by inserting an objective aperture which restricts transmitted electrons with large diffraction angle (bright field imaging). The TEM can work in two modes, namely image mode and diffraction mode as shown in Fig. 3.10 (Williams & Carter, 1996). In the diffraction mode, the diffraction pattern can be obtained on the screen by taking the back focal plane of the objective lens as the objective plane of the intermediate lens and projector lens (the objective aperture is removed and a selected area aperture is inserted into the intermediate image plane). Whereas in the image mode, the image are formed on the screen, by taking the image plane of the objective lens as the objective plane of the intermediate lens and projector lens.

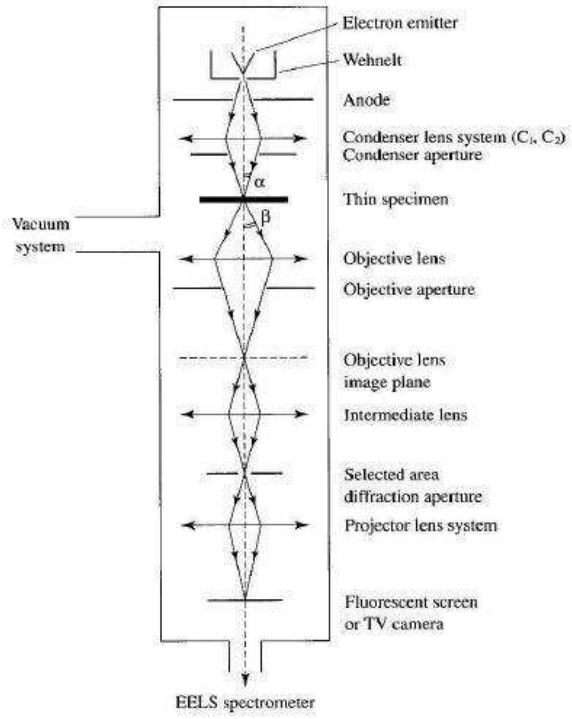

Fig. 3.9 Schematic diagram of the basic components of a TEM (Brydson, 2001).

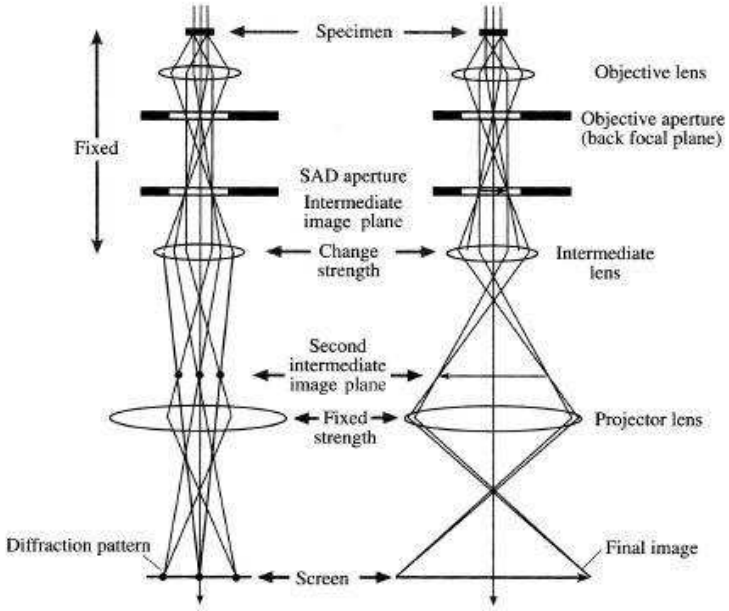

Fig. 3.10 Schematic diagram showing the optics for the formation of electron diffraction patterns and images within a TEM (Williams & Carter, 1996).

A selected area electron diffraction pattern can also be obtained from very small sample region by inserting a selected area diffraction aperture in the intermediate image plane (Hammond, 2001; Champness, 2001). Because the electron wavelength is much smaller than typical interplanar spacing, the diffraction angles will be very small (<3°), so the Bragg's equation can be simplified as follows.

$$\lambda = 2d_{\mathrm{hkl}}\,\theta \qquad (\sin\theta \approx \theta) \qquad (3.2)$$

From Fig. 3.11, the eq. 3.2 can be written as

$$\tan 2\theta = \frac{R_{hkl}}{L} \approx 2\theta = \frac{R_{hkl}}{L} \qquad (3.3)$$

where R_{hkl} is the distance between a central spot and a diffracted spot, L is a camera length and R_{hkl} << L. From eq. 3.2 and eq. 3.3, the following equation is obtained.

$$\lambda L = R_{\mathrm{hkl}}\, d_{\mathrm{hkl}} \qquad (3.4)$$

λL is known as the camera constant and can be determined using a standard sample of known lattice parameters, e.g. aluminium and GaAs. By measuring spot spacings or ring radii (R_{hkl}), the interplanar spacing (d_{hkl}) can be obtained by using eq. 3.4, an unknown material may be identified.

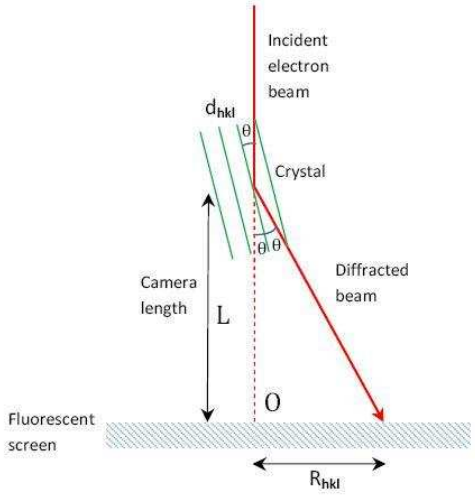

Fig. 3.11 Schematic diagram showing the formation of reflection electron diffraction patterns where R_{hkl} is the distance between the central spot and the diffraction spot and L is the camera length.

In this work, the microstructure and crystallography of phases present in coatings were investigated using a JEOL 2000-FX-II TEM operating at 200 kV with a LaB_6 thermal electron source. Bright field (BF) imaging and selected area electron diffraction (SAD) techniques were employed. TEM samples were prepared from thin sections of the coatings, 3x3 mm (for the disc) and about 300 μm thick which were then ground and polished with SiC papers down to a thickness of 100 μm. The disc samples 3mm in diameter, were mounted on copper washers and mechanically ground using a tripod polisher. Samples were then polished on both sides using diamond polished down to a 0.5 μm finish. Low angle ion beam milling was then performed using a Fishione 1010 Ion Mill operated at 6 kV and an incidence angle of 15° until the sample penetrated, leaving a significant thin area for TEM examination. The TEM sample was then introduced onto the specimen holder and was inserted into the vacuum chamber of microscope. The samples were then observed at varying magnifications.

3.4 Microhardness and Roughness Measurements

Vickers microhardness measurements of the coatings were carried out using a Leco M-400 instrument under a load of 200 g with a dwell time of 15 seconds. The average value of 10 measurements was quoted as the hardness of the sample. The hardness of the coatings was measured along the middle of the cross-sections of the coatings (parallel to the coating-substrate interface).

Profilometry and roughness measurements of the as-sprayed top surfaces were performed using a Talysulf CLI 1000 profilometer (Taylor Hobson, Leicester, UK). A diamond stylus was transversed across the coating with a tracing speed of 0.3 mm

s^{-1}, a cut off of 0.8 mm and a transverse length of 5 mm. Each sample was measured at five random locations with the average and standard error of the Ra values being quoted.

3.5 Thermal Analysis (DSC)

In general, the thermal properties of powders and coatings are analysed using differential scanning calorimetry (DSC). A schematic of a DSC instrument is shown in Fig. 3.12. In this method, the sample and a reference are subjected to identical temperatures and heated at a controlled rate. The temperature difference between the sample and reference as a function of time or temperature is recorded. This is then used to calculate the differential rate of heat flow associated with the sample which is usually expressed in W/g. Fig. 3.13 shows a typical DSC curve obtained for an amorphous sample.

Amorphous material is a non-crystalline, as the temperature increases the amorphous part changes from a glassy phase to a crystalline phase. The temperature at which this transition occurs is known as the crystallisation temperature (T_x). There are changes in the properties of sample at this temperature such as hardness, stiffness etc.

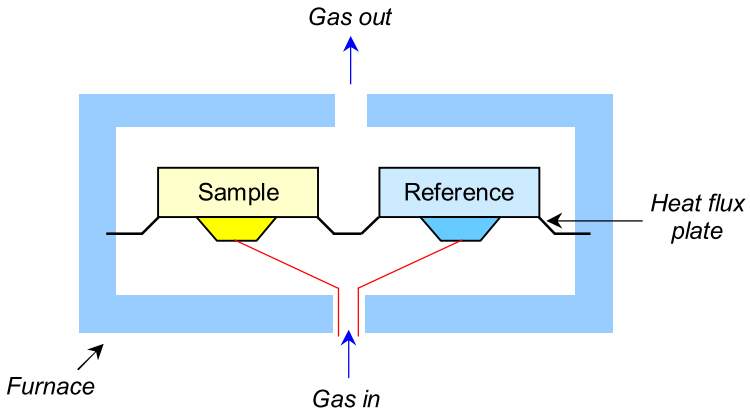

Fig. 3.12 The schematic of the differential scanning calorimetry.

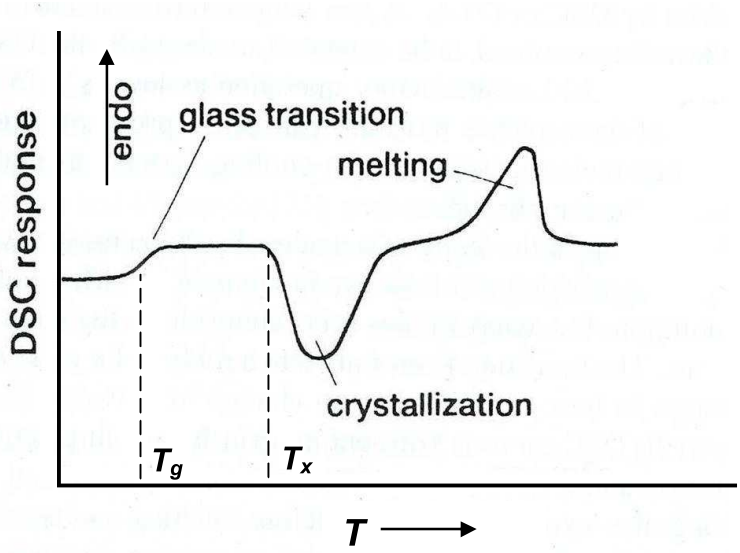

Fig. 3.13 A typical DSC curve obtained for an amorphous sample (modified from Brown, 1988) where the DSC response is W/g. T_g is the glass transition temperature and T_x is the onset of crystallization temperature during heating.

In this work, differential scanning calorimetry (DSC) was conducted using a TA Instruments Model SDT-Q600 under an argon atmosphere to prevent the oxidation of the samples. Temperature and energy calibrations of the instrument were performed

using the well-defined melting temperatures and melting enthalpies of high purity aluminium and gold supplied with the instrument. Coating samples for DSC analysis were obtained by carefully removing small areas of the coating from the substrate to obtain specimens approximately 4 mm in diameter by approximately 0.3 mm (300 μm) thick, with a sample weight of typically 60 mg. DSC analysis of powder samples was performed by filling the alumina sample pan with approximately 60 mg of loose powder. Empty Al_2O_3 pan was used as reference pan.

All runs were performed under a purified argon gas atmosphere (flow rate ~ 100 ml min^{-1}). A series of DSC experiments was carried out on powders and coatings with continuous heating rates in the range of 10-50 K min^{-1} and all traces were corrected by subtracting the instrumental baseline (obtained from a DSC run with two empty pans) such that the DSC curves presented reflect the heat flow due to transformations in the sample. The on-set of crystallization temperature and peak crystallization temperature were then determined using TA universal analysis software. The apparent activation energies of reactions were determined using Kissinger method by measuring the on-set of crystallization temperatures, T_x or peak crystallization temperature, T_p as a function of heating rates. The Kissinger's equation is expressed as following equation 3.5 (Kissinger, 1957)

$$ln(\beta/T_p^2) = - E_a / RT_p + \text{constant} \qquad (3.5)$$

where β is the heating rate, T_p is the peak temperature of crystallization, E_a activation energy for crystallization and R is the ideal gas constant, 8.3145 J/mol K.

Thus, by plotting $\ln(\beta/T_p^2)$ as a function of $1/T_p$, the activation energy, E_a can be determined from the slopes of the straight lines of this plot.

3.6 Sliding Wear Testing (Ball-on-Disc)

3.6.1 Wear Test Procedure

Sliding wear tests on the coatings were performed using a ball-on disc apparatus, shown schematically in Fig. 3.14. The ball-on-disc test was carried out at room temperature without lubrication. Both ball and disc samples were cleaned with ethanol and dry compressed air before and after testing. The load between the ball and disc was varied by application of heights to the hanger. The radius of sliding was 12-16 mm and the rotational velocity was 180 rpm, giving a sliding velocity of 0.302 m/s.

3.6.2 Ball Material

Sintered alumina balls (Al_2O_3), yttria stabilized zirconia (ZrO_2) balls and steel 440C balls with diameter 9.523 mm (supplied by Dejay Distribution Ltd., UK) were used as counterface materials. The alumina ball was chosen as a counterface material due to its high hardness and high wear resistance. The zirconia ball was selected since it has higher fracture toughness but lower hardness than the alumina ball. Table 3.6 shows the properties of ball materials used.

Table 3.6 The properties of the ball materials

Ball	Density (kg /m^3)	Hardness (GPa)	Fracture toughness (MPa m$^{1/2}$)	Thermal conductivity (W/mK)
Al_2O_3	3860	17.5	3-4	6.9
ZrO_2	6100	13.2	6-10	2.15
Steel 440C	7650	9.0	23.7	24.2

Note: Density and hardness of the balls were measured in this work, but fracture toughness and thermal conductivity data are obtained from references (Qu et al., 2005; Bansal & Zhu, 2005; Gautier & Kato, 1993).

3.6.3 Disc Preparation

HVOF coatings were sprayed onto mild steel discs of 40mm diameter and 6 mm thickness for the sliding wear tests. The coated discs were prepared by grinding and polishing of the coating top surface by a lapping procedure as follows. Specimens were ground and polished on a Struers LaboPol-5 equipped with a LaboForce-3 power head. Grinding can be classified as 2 steps: plane grinding (PG) and fine grinding (FG). In the PG step, a diamond grinding disc was employed to remove the roughness of the as-sprayed surface. A Struers MD-Allegro disc was used in the FG step to eliminate damage introduced during the PG step. The polishing comprised two steps: diamond polishing 1 (DP1) using a Struers MD-Pan disc (abrasive size, 6 μm) and diamond polishing 2 (DP2) using a MD-Mol disc (abrasive size, 1 μm).

3.6.4 Friction Measurement

The frictional force was measured via the deflection of a load beam (since the main arm which held the sample holder was freely pivoted in the horizontal plane). Deflection of the load beam was measured using an LVDT. The LVDT was calibrated via dead weight loading of the beam. The coefficient of friction, at any given time during the wear test could be calculated using the equation

$$\text{The coefficient of friction, } \mu = \frac{F}{W} \qquad (3.6)$$

Where F is the frictional force and W is the normal load applied at the ball.

3.6.5 Scope of Experiments

Tests were undertaken in which various variables, which were known to influence wear rate, were controlled independently. The purpose of these tests was firstly to

compare the wear performance of the HVOF thermally sprayed Fe-Cr-B based alloy coatings, in relation to each other and also against the mild steel substrate and a commercially available WC-Co-Cr coating. The variables chosen to be investigated in these experiments were as following;

1) The influence of load: tests were performed on the various coatings in which the load was varied over the range 5.8 to 70 N. Sliding distance and sliding speed were kept constant throughout the tests at 1000 m and 0.3 m s^{-1} respectively.

2) The influence of sliding distance: tests were performed on the various coatings in which the sliding distance was varied over the range 1,000 m to 10,000 m. Load and speed were kept constant at 23.3 N and 0.3 m s^{-1} respectively.

3.6.6 Investigation of Worn Surface and Debris

Optical and scanning electron microscopy were used to examine worn ball surfaces, cross-sections through worn surfaces and wear tracks on the coating disc material. The techniques employed during these examinations are detailed in section 3.3.4.2. The EDX facility available on the scanning electron microscope was also utilised in the examination of the worn ball and discs.

3.6.7 Calculation of Volume Loss of Discs and Balls

The wear track of the disc was measured using a Talysulf CLI 1000 profilometer (Taylor Hobson, Leicester, UK) to obtain the overall volume loss of the disc. This was obtained by measuring the average cross-sectional area of the track along 4 traces of the wear track. The volume loss of the disc was obtained by calculating;

$$V = 2\pi r \times A \qquad (3.7)$$

Where r = the average radius of wear scar of a disc measured from the middle of wear scar and A = the average cross-sectional area for 4 traces of the wear track with a profilometer.

The wear of the ball resulted in a near circular flat being formed, which it was assumed, represented the removal of a spherical cap of material. The diameter of the worn surface of the ball was measured by profilometry technique. The volume loss of the ball was calculated by the following equations (Shipway, 1999). A diagram of a ball worn corresponding to the equations is shown in Fig. 3.15. The average wear rate of the ball was calculated by dividing the total volume loss by the total distance slid.

$$V = \pi d^2 (r - \frac{d}{3}) \qquad (3.8)$$

$$d = \mathrm{r} - \sqrt{(r^2 - a^2)} \qquad (3.9)$$

Where d = the depth of wear scar, r = the radius of the ball, a = the radius of the scar and V = the volume loss of the ball.

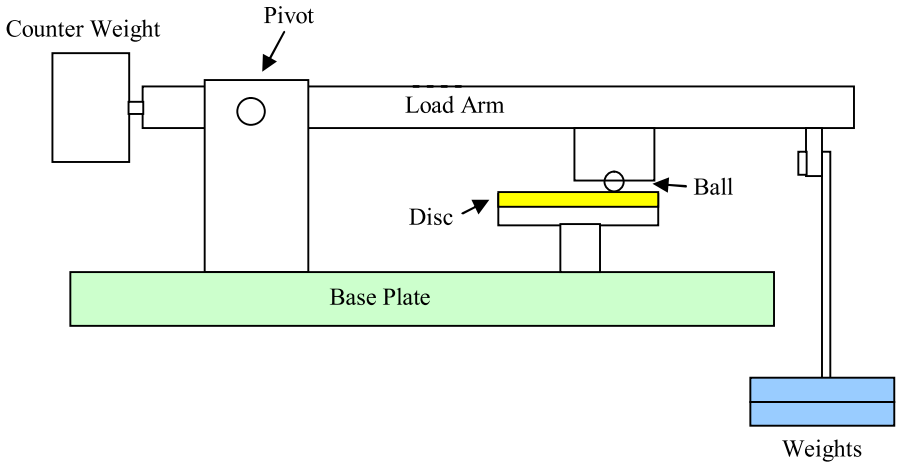

Fig. 3.14 The set up of the sliding wear machine.

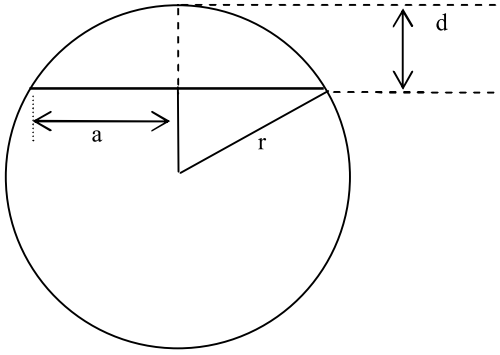

Fig. 3.15 A diagram of a ball worn shows the depth of wear scar (d), the radius of a ball (r) and the radius of a scar (a).

3.7 Summary

Characteristics of the gas atomised powder particles of different chemical compositions have been conducted. Then, the parameters for the thermal spraying of the coatings supplied by the manufacture have been introduced. The principles of the characterisation techniques of XRD, SEM, TEM, EDX and DSC have also been introduced. In addition, the annealing conditions of the powders and coatings have been introduced by using information from DSC data. In addition, microhardness measurement has been introduced in order to assess of coating properties. Finally, dry sliding wear ball-on-disc testing has been conducted to study wear behaviour of the coatings.

Chapter 4

Results: Microstructure evolution of Fe-Cr-B based alloy powders and coatings (Armacor M and Armacor C)

In this chapter, the microstructure of gas atomised Armacor M and Armacor C powders (based on Fe-Cr-B system), used as feedstock for HVOF spraying, and as-sprayed coatings are reported. The microstructure of the powders (small particles and large particles) and the coatings were characterised by X-ray diffraction (XRD), scanning electron microscopy (SEM), utilising energy dispersive X-ray spectroscopy (EDS) and transmission electron microscopy (TEM). Differential scanning calorimetry (DSC) was conducted to analyse the thermal stability of the samples. The microhardness of the coatings was investigated by mean of Vickers microhardness testing and is related to their microstructural development.

4.1 Armacor M

4.1.1 Powder size and composition

A commercially available powder, Armacor M, was obtained from the Liquidmetal company (Texas, CA, USA). It had a chemical composition, determined by X-ray fluorescence spectrometry (XRF), inductively coupled plasma (ICP) spectrometry and a combustion method, that is given in Table 4.1. It had a nominal size range +15 to 53 μm. The actual size distribution was obtained by laser diffractometry and is shown in Fig. 4.1. It is indicated that 10% of the powder was above 60 μm, and 10% below 27 μm with a d_{50} of 40 μm. Prior to spraying, the powder was sieved with a 53 μm sieve and after sieving the d_{10}, d_{50} and d_{90} values were 24 μm, 35 μm and 51 μm, respectively. Following sieving, the volume mean particle diameter was 38 μm. The external morphology of the powder is shown in the SEM image of Fig. 4.2. It is clear that the morphology was largely spherical and some particles with satellites also present. This is consistent with manufacture by the inert gas atomisation process.

Table 4.1 The composition of the Armacor M powder (as determined by XRF, ICP and a combustion method)

Element	Fe	Cr	B	Si	C
wt.%	Bal.	44.1	5.6	4.7	0.15
atom.%	Bal.	35.9	22.0	7.1	0.5

4.1.2 Characterisation of the as-received powder

XRD analysis

The phases present in the powder were determined by X-ray diffraction. The XRD traces from the as-received powder in Fig. 4.3(a) show the presence of a bcc phase with a lattice parameter close to α – Fe (JCPDS file # 006-0696) and the boride

phase $(Fe_{1.1}Cr_{0.9})B_{0.9}$ (JCPDS file # 072-1073). Figs. 4.3(b)-(c) compare indexing of the pattern with lines for Cr_2B (JCPDS file # 038-1399) and $(Fe_{1.1}Cr_{0.9})B_{0.9}$ (JCPDS file # 072-1073). The latter phase gives a better fit to peaks at 2θ = 39.4°, 43.2°, 46.9°, 50.4°, 56.2°, 73.1°, 79.8° and so is most probably the boride phase in the sample.

SEM analysis

When powder particle cross-sections were examined using BSE imaging it was found typically that small particles, Fig. 4.4(a) show varying contrast suggesting a multiphase structure, similar features can be observed from larger particles, Fig. 4.4(b). Bright areas indicate a higher mean atomic number and dark contrast needles or plates have a lower mean atomic number. A higher magnification BSE image of small particles Fig. 4.4(c) shows clearly a different contrast between two phases and more detail of the dark contrast needles or plates ~ 2 μm wide can be observed. At a higher magnification the BSE image of large particles Fig. 4.4(d) shows again a different contrast between two phases, but with larger dark contrast needles ~ 3 μm in width. EDX analysis of a bright area and a darker area are shown in Fig. 4.4(e) and Fig. 4.4(f), respectively. It can be seen that the bright area shows a higher Fe/Cr ratio, whilst a darker area shows a lower Fe/Cr ratio. Precise compositions of each phase can not be found due to the spatial resolution of the SEM. The peak ratio of Fe to Cr for each phases were calculated from the measured intensities of EDX spot analysis and the values were obtained for comparison. It was found that the Fe/Cr peak ratio for a bright area is 0.98, whereas the Fe/Cr peak ratio for a darker area is 0.37. This suggests that the bright matrix was the metallic bcc phase and the dark needles were the boride phase.

4.1.3 Characterisation of Slow Cooled Solidified Powder

To help understand the development of the microstructure, the melting and solidification behaviour of the Armacor M powder was studied by continuous heating, and cooling DSC experiments at relatively low rates in which the powder was melted, as shown in Fig. 4.5.

The DSC trace shows no peak that could be due to crystallization of an amorphous phase. On further heating, however, a wide endothermic peak was observed at an onset temperature of 1254°C, This could be due to the melting of α – Fe and possibly, the dissolution of boride phase. The critical temperatures are listed in Table 4.2.

Table 4.2 The melting temperature T_m , the liquidus temperature T_{liq} obtained from a DSC curve of the Armacor M powder at a scanning rate of 20 K/min.

Heating rate	T_m (°C)	T_{liq} (°C)
20 K/min	1254	1309

During cooling, also at 20 K/min only one major exothermic peak was observed as shown in Fig. 4.5(b), a large peak just below 1286°C was observed on the DSC scan with a relatively high enthalpy of reaction. This single exothermic peak during cooling of the melt suggests that the Armacor M sample has an eutectic composition.

Fig. 4.6 shows regions the DSC sample at increasing magnification. At low magnification Fig. 4.6(a) – 4.6(c) there are 30 μm size dark plates in a matrix. At the highest magnification, Fig. 4.6(d) all the phases are visible and are labelled A and B. EDX analysis was performed on these phase regions and EDX spectra are shown in

Fig. 4.7. Table 4.3 shows quantitative EDX analysis data for elements present (excluding the low atomic number elements boron and carbon).

Table 4.3 EDX analysis data for the elements present in the different regions in Fig. 4.6(d) (excluding B and C)

	Element (wt%)		
Regions	Fe	Cr	Si
(A) dark	30.4	69.6	0.1
(B) light grey	71.8	23.4	4.8

The dark regions arrowed (A) probably correspond to the boride phase whilst the bright regions arrowed B, of image Fig. 4.6(d) correspond to α – Fe (high Cr) phase. Therefore from the DSC trace, Fig. 4.5 and the SEM/EDX observations the following possible solidification sequence when cooling at 20 K/min is proposed

$$L \longrightarrow \alpha - Fe + (Fe_{1.1}Cr_{0.9})B_{0.9}$$

which starts at 1286 °C and ends at 1241°C.

4.1.4 Characterisation of heat treated powder

XRD analysis

Fig. 4.8 shows the XRD traces for the as-received powder (AR) and samples heat treated for 1 hour at 550°C, 750°C and 925°C. It was found that there is no phase change of the powder after heat treatment at temperatures of 550°C as shown in Fig. 4.8(b).

On further heating of the powder at a temperature of 750°C, led to small increase in the intensities of α-Fe peaks and the intensities of peaks from other phases (the boride phase, $Fe_{1.1}Cr_{0.9}B_{0.9}$) remained almost unchanged as shown in Fig. 4.8(c).

Additionally, when the powder was heated to a temperature of 925°C, the intensities of α-Fe peaks and the intensities of peaks from other phases (the boride phase, $Fe_{1.1}Cr_{0.9}B_{0.9}$) increased somewhat as shown in Fig. 4.8(d) and the peaks became a little sharper and less broad.

SEM analysis

The microstructure of the Armacor M powder was investigated using BSE imaging and EDX analysis. Heating the sample to a temperature of 925°C for 1 hour, there is no microstructural change that can be observed. Fig. 4.9(a) is a low magnification BSE image showing of a small particle and large powder particles in Fig. 4.9(b) show a different contrast between a matrix phase and dark contrast of boride needle. A higher magnification BSE image of small particles Fig. 4.9(c) shows boride needle grains with somewhat rounded edges and similar result can be observed at higher magnification BSE image of large particles, Fig. 4.9(d).

4.1.5 Characterisation of as-sprayed coating

XRD analysis

The phases present in the as-sprayed coating were determined by X-ray diffraction. There is no evidence for an oxide phase being present following spraying. The XRD trace from the as-sprayed coating, Fig. 4.10(a) shows the presence of a bcc phase with a lattice parameter close to α-Fe (JCPDS file # 006-0696) and the boride phase

of $(Fe_{1.1}Cr_{0.9})B_{0.9}$ (JCPDS file # 072-1073). The α-Fe peaks are significantly broadened as compared with that of the as-received powder. Figs. 4.10(b)-(c) compare indexing of the pattern of the Armacor M coating with lines for Cr_2B and $Fe_{1.1}Cr_{0.9}B_{0.9}$. The latter phase gives a better fit to peaks at 2θ = 39.4°, 43.2°, 46.9°, 50.4°, 56.2°, 73.1°, 76.1°, 79.8° and so is most probably the boride phase in the sample.

SEM analysis

The HVOF coatings in the as-sprayed condition were characterised by SEM using BSE imaging. Fig. 4.11(a), a low magnification unetched cross-section, reveals the microstructure of the as-deposited coating. The coating is seen to be around 260 μm thick with an irregular top surface. The rough interface between the coating and mild steel substrate is due to the grit blasting of the latter prior to coating deposition.

At higher magnification, the cross-section of the coating imaged in the BSE mode of the area (b) in Fig. 4.11(a), is shown in Fig. 4.11(b) and (c). The coating exhibits characteristic lamellar microstructures, with the splat layers parallel to the substrate surface and also a proportion of unmelted particles with a deformed spherical shape.

A BSE image of a typical region P from a cross-section of coating is shown in Fig. 4.12(a). This reveals a near- spherical morphology of an unmelted particle, labelled P in the coating and some porosity is visible as a very dark contrast region, generally outside the region P. Porosity of the coating producing by this HVOF thermally spray process is relatively low.

Fig. 4.12(a)-(b) show a lamellar splat like features with fine scale borides (eg F). This suggests near complete melting of the original particle and the re-precipitation of borides. The near-spherical region (e.g. P) corresponds to an original powder particle judging from the size of the boride phase within it. Such particles are either unmelted or heated only just above their onset of melting temperature. The EDX spectra and analysed data of the arrowed regions C and D of image Fig. 4.12(b) are shown in Fig. 4.12(c) and Fig. 4.12(d), respectively. Fig. 4.12(e) and (f) show boride phase clearly following etching in a solution of 1 part HCl, 1 part HNO_3 and 1 part H_2O.

TEM analysis

TEM of the Armacor M coating was undertaken to obtain more detailed information on microstructure formation. TEM images of the as-sprayed Armacor M coating and associated diffraction patterns are shown in Fig. 4.13.

Fig. 4.13(a) is a bright field TEM micrograph from a plan-view of the Armacor M coating and reveals that the sample was composed of both amorphous and crystalline regions. The SAD pattern in Fig. 4.13(b) was taken from the region marked B and shows a combination of a diffuse ring and elongated spots. The diffuse ring is indicative of an amorphous phase whilst the elongated spots indicate a crystalline phase. The streaking is due to the phase having closely spaced faulted regions. An example of the amorphous phase regions (200-500 nm size) is shown in Fig. 4.13(c) and (e). The associated SAD patterns Figs. 4.13(d) and (f) are taken from the region in Figs. 4.13(c) and (e), respectively. These patterns show more distinct diffuse rings arising from the amorphous phase as well as spots from crystalline material.

DSC analysis of the coating

Differential scanning calorimetry (DSC) was conducted to analyse the thermal stability of the coating. The DSC analysis of the coating during first and second heating runs at 20K/min up to 900°C is shown in Fig. 4.14(a). In the curve from the first heating run, one peak appears and this corresponds to one exothermic reaction, attributable to crystallization of an amorphous phase. The peak temperature of crystallization (T_{p1}) is 624°C. In the curve after the second heating run, the exothermic peak has completely disappeared. This confirms that the first peak was due to the irreversible primary crystallisation of an amorphous phase in the coating sample. However, it was not possible to identify a glass transition temperature from the DSC traces due to the low volume fraction of the amorphous phase.

Fig. 4.14(b) shows typical DSC curves of the as-deposited Armacor M coating obtained during continuous heating at five different heating rates (10 K/min – 50 K/min). It can be clearly seen that each DSC curve exhibits one exothermic peak. It indicates that the crystallization of the amorphous phase in the coating proceeds via a single stage of reaction. The crystallization reaction occurred at temperatures in the range 610-648 °C (peak temperatures) depending on heating rate. The onset of crystallization temperatures (T_x), peak temperatures (T_p), and enthalpies of crystallization (ΔH) for the Armacor M coating at different heating rates (10K/min to 50K/min) are listed in Table 4.4. The onset temperature is taken to be when is first seen a deviation from the baseline.

Table 4.4 The onset of crystallization temperatures (T_x), peak temperatures (T_p), and entralpies of crystallization (ΔH) for the Armacor M coating at different heating rates.

Heating rate	Onset T_x (°C)	T_p (°C)	ΔH (J/g)
10 K/min	553	610	23
20 K/min	569	624	27
30K/min	579	634	27
40K/min	588	638	23
50 K/min	587	648	32

According to Kissinger's method (see chapter 3), the activation energy for reaction can be calculated from the slope of the straight line of the plot as shown in Fig. 4.15 and the activation energy was found to be 280 kJ/mol. The heat of reaction, *(ΔH)* was also determined using DSC, and the values are given in Table 4.4 for each heat rate employed.

4.1.6 Characterisation of heat treated coating

XRD analysis

Fig. 4.16 shows the XRD traces for the as-received powder (AR), as-sprayed coating (AS) and the coatings following heat treatment for 1 hour at 550°C, 750°C and 925°C. It was found that there was no phase change of the coating after heat treatment at temperatures of 550°C as shown in Fig. 4.16(c). Heat treatment of the coating at a temperature of 750°C, just above the exothermic reaction peak, led to a small increase in the intensities of α-Fe peaks and reduced the width of α-phase peaks and the intensities of the boride phase remained almost unchanged as shown in Fig. 4.16(d). Heat treatment at a temperature 925°C, led to a further increase in the intensities of Fe peaks. The presence of the boride phase $(Fe_{1.1}Cr_{0.9})\ B_{0.9}$ (JCPDS file

072-1073) in the XRD traces was clearly identified as shown in Fig. 4.16 from plots (a) to (e).

SEM analysis

Fig. 4.17 shows the microstructure of the coating after post spray heat treatment at 550°C, 750°C and 925°C for 1 hour.

After heat treatment of the coating for 1 hour at temperature 550°C, just below the peak of crystallization, there was no microstructural change of the coating that could be resolved as shown in Fig. 4.17(a). However, Fig. 4.17(b), a higher magnification BSE image of selected area boxed (B) in Fig. 4.17(a) shows a featureless rim around some particles which is probably where the amorphous phase exists. This particle rim probably melted during spraying and was then rapidly cooled on impact.

The microstructural change after heat treatment of the coating at 750°C for 1 hour is shown in Fig. 4.17(c). Fig. 4.17(d) a higher magnification BSE image of selected area boxed (D) in Fig. 4.17(c), fine precipitates within the rim region can be observed (probably crystallisation occurred here).

Furthermore, heating the sample to a temperature of 925°C for 1 hour, larger precipitates within the rim region can be observed as seen in Fig. 4.17(e), a low magnification BSE image of the coating and Fig. 4.17(f) a higher magnification BSE images of selected area boxed (F) in Fig. 4.17(d).

4.1.7 Microhardness

One set of heat treatments was performed for a fixed time of 60 minutes at the following temperatures: 550, 750 and 925°C.

Microhardness data for the as-sprayed coating and following heat treatment at 550°C, 750°C and 925°C for 1 hour are shown in Table 4.5.

Table 4.5 Hardness (GPa) of the as-deposited and samples heat treated for 1 hour

Sample	As-deposited	550°C	750°C	925°C
Hardness / GPa	11.1	10.6	9.3	8.6
Standard deviation	0.9	0.7	0.7	0.6
Standard error	0.3	0.2	0.2	0.2

The results show that as the temperature increased up to 550°C, the hardness of the coating decreased somewhat and gradually decreased to 9.3 GPa at temperature 750°C and after increasing the temperature up to 925°C, the hardness decreased to 8.6 GPa. This indicates that fine scale precipitates due to crystallization did not increase the coating hardness. The fall in hardness is probably due to a number of factors such as loss of solute from a supersaturated matrix phase as well as some coarsening of the boride phase.

4.1.8 Summary (Armacor M)

(1) The present study reports a detailed microstructure investigation of HVOF-thermal sprayed Armacor M powder of composition (in at %) Fe-35.9%Cr-22%B-0.5%C-7.1%Si. The deposits, which are approximately 260 μm thick, have a splat-like microstructure characteristic of thermally sprayed metals.

(2) The predominant phases present in the as-sprayed Armacor M coating, as identified by XRD, are a bcc α-Fe matrix and boride ($Fe_{1.1}Cr_{0.9}B_{0.9}$).

(3) The addition of metalloid elements (e.g. boron) to the alloy increases the ability of the alloy to form the amorphous structure on deposition. However, a high level of chromium (35.9 at%) and boron (22.0 at%) also leads to the formation of primary boride phase during gas atomisation from the melt.

(4) The activation energy for the crystallization reaction was calculated from DSC data using the Kissinger peak shift equation. The activation energy for the peak of reaction corresponds to the energy required for crystallization of amorphous Fe-based phase and/or precipitation of boride phase.

(5) The as-sprayed Armacor M coating shown a high hardness (~11.1 GPa). The hardness of the sample could be due to a number of factors including the presence of a proportion of amorphous/nanocrystalline phase as well as precipitation of a boride ($Fe_{1.1}Cr_{0.9}B_{0.9}$). However, after annealing at temperature 550-925°C, the annealed coating sample exhibits a lower hardness (~ 8.6 GPa) than that of the coating in the as-sprayed condition.

(6) The thermally sprayed Armacor M coatings, containing a proportion of hard borides of $Fe_{1.1}Cr_{0.9}B_{0.9}$ and a mixture of amorphous and/or crystalline material can offer effective coatings with high hardness and potentially wear resistance especially in the as-sprayed condition.

Result: Fe-Cr-B alloy (Armacor M)

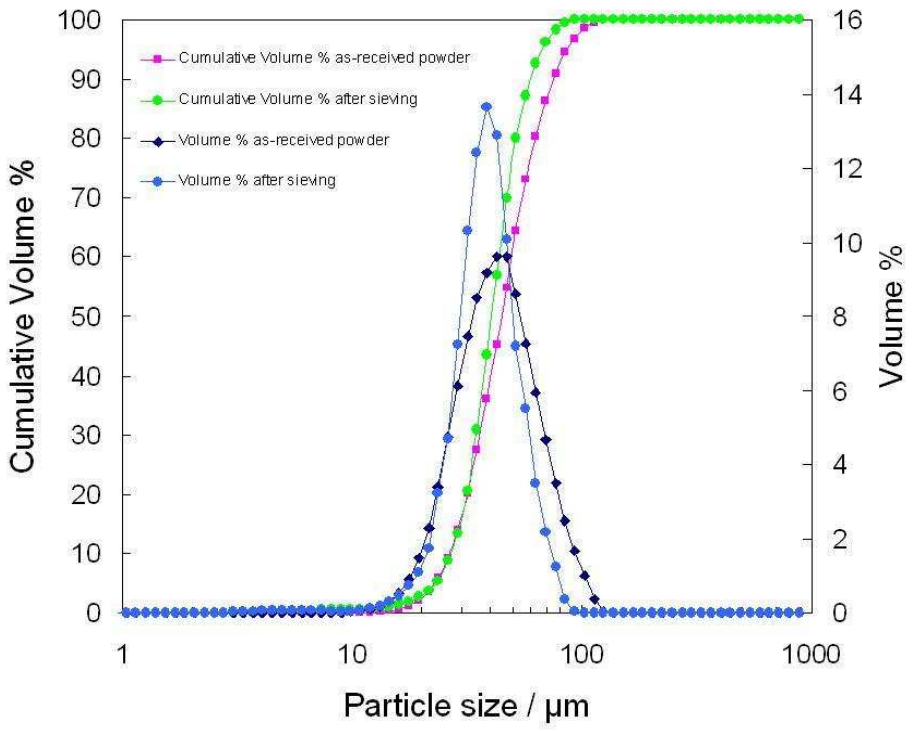

Fig. 4.1 Plot of powder distribution and cumulative vol % versus particle size for Armacor M powder both as-received and after sieving.

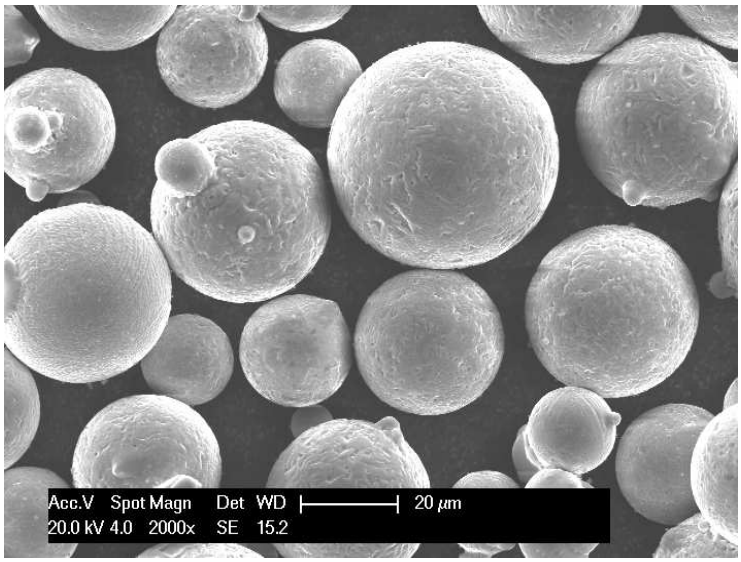

Fig. 4.2 The external morphology of the Armacor M powder after sieving.

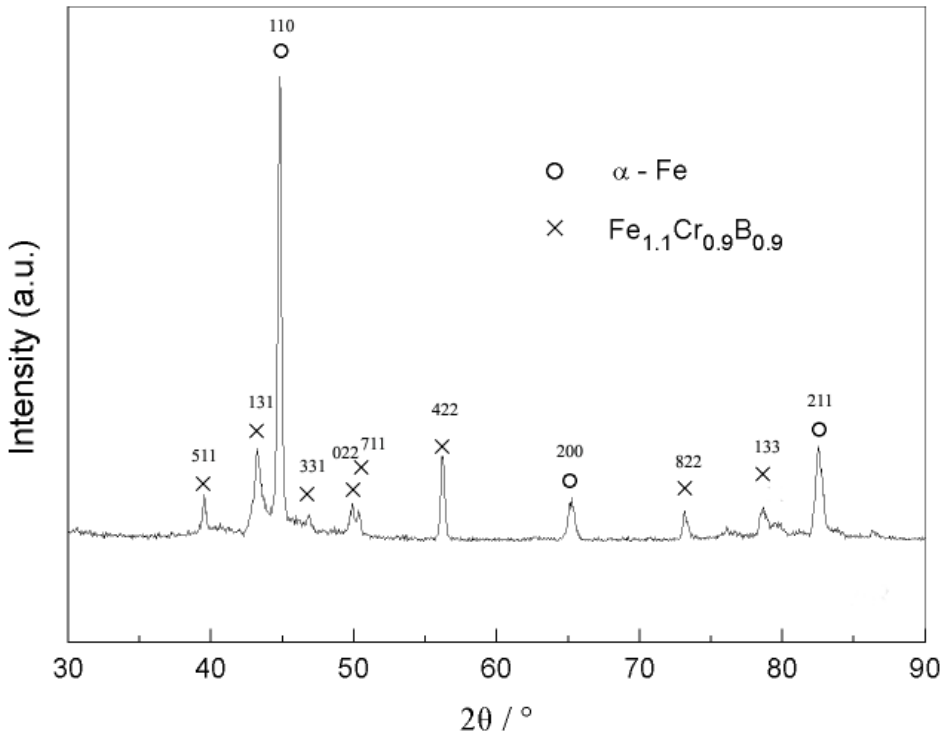

Fig. 4.3(a) XRD pattern of the as-received Armacor M powder.

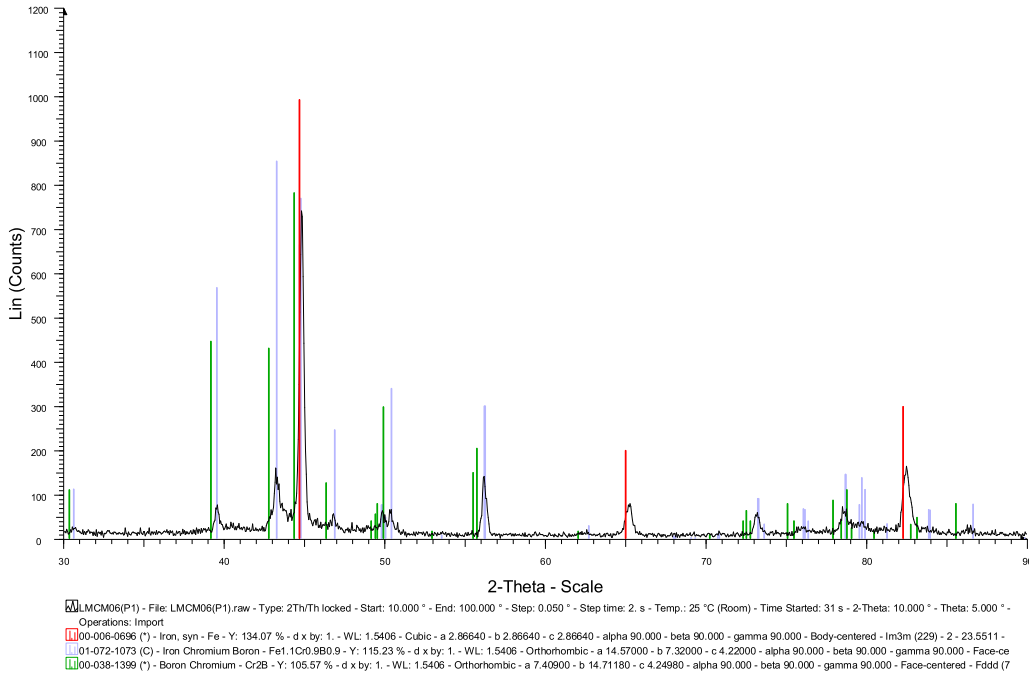

Fig. 4.3(b) Comparison of experimental XRD pattern with JCPDS files for Cr_2B and $Fe_{1.1}Cr_{0.9}B_{0.9}$

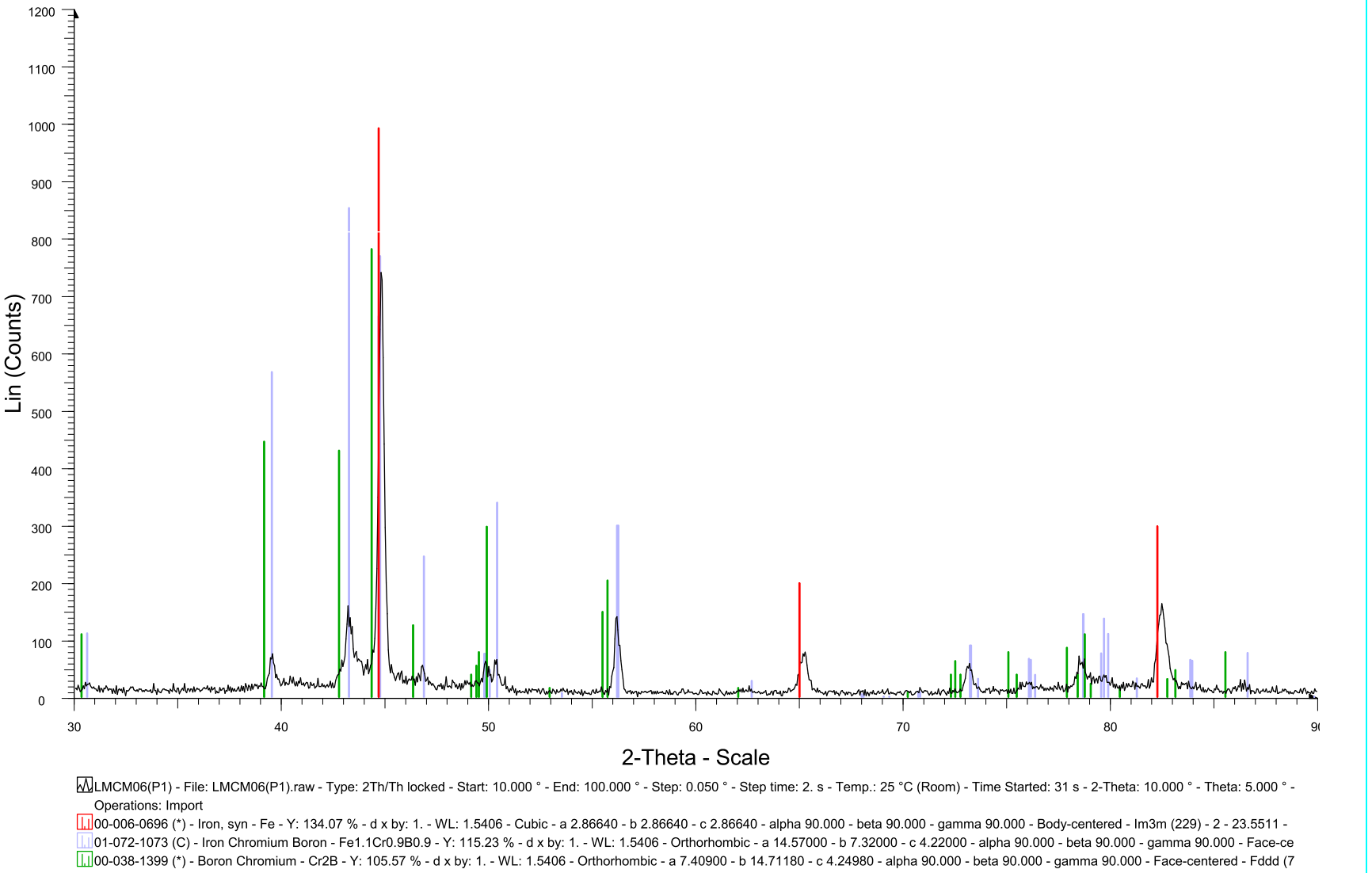

Fig. 4.3(c) Comparison of experimental XRD pattern (2θ = 30–90°) with JCPDS files for Cr_2B and $Fe_{1.1}Cr_{0.9}B_{0.9}$.

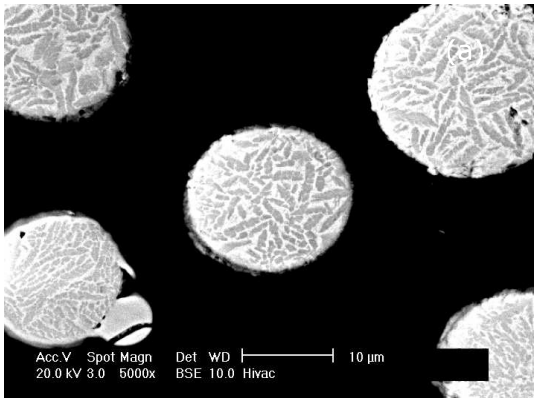

Fig. 4.4(a)

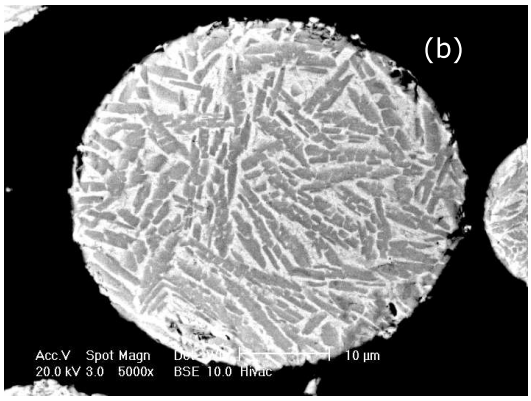

Fig. 4.4(b)

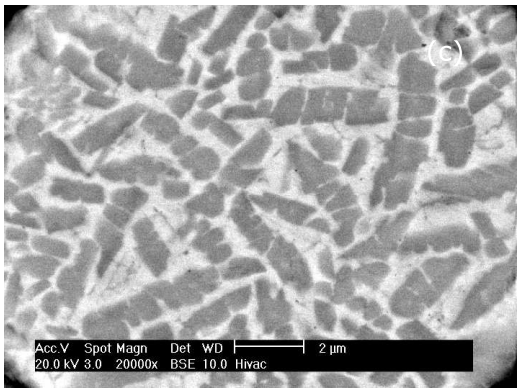

Fig. 4.4(c)

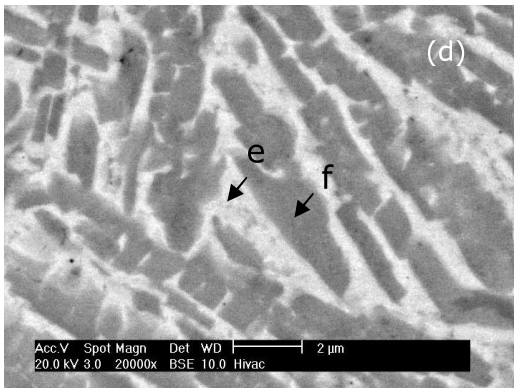

Fig. 4.4(d)

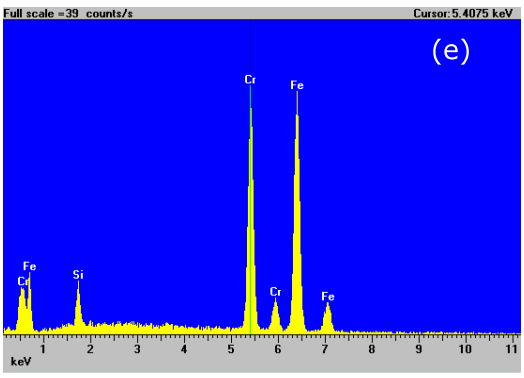

Fig. 4.4(e)

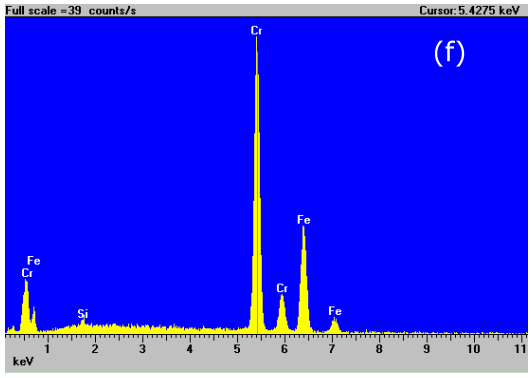

Fig. 4.4(f)

Fig. 4.4 BSE images of the cross-section of a small particle (a) and a large particle (b). (c,d) Higher magnification of regions in images (a) and (b). (e,f) EDX spectra of regions in (d) arrowed e and f, respectively.

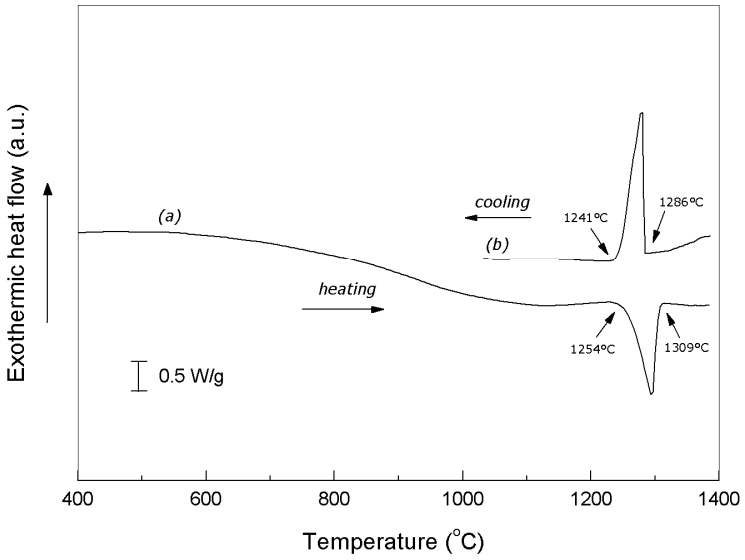

Fig. 4.5 The DSC heating (a) and cooling (b) scans for the as-received Armacor M powder obtained at a scanning rate of 20 K/min

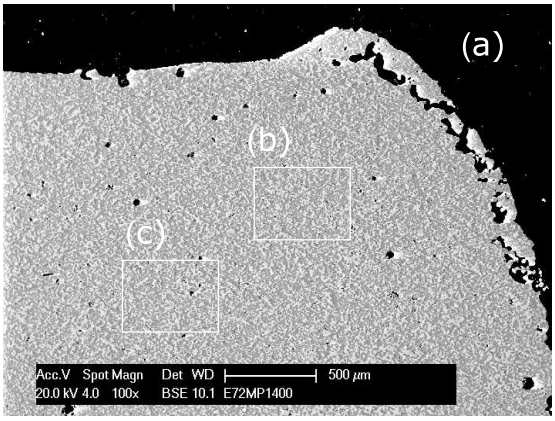

Fig. 4.6(a)

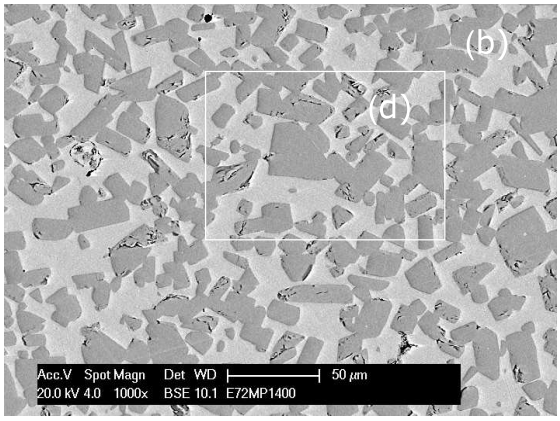

Fig. 4.6(b)

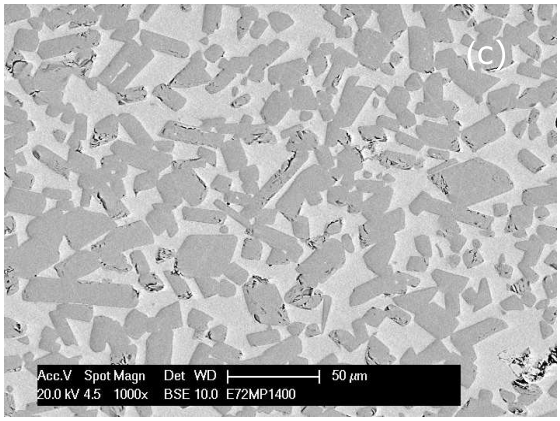

Fig. 4.6(c)

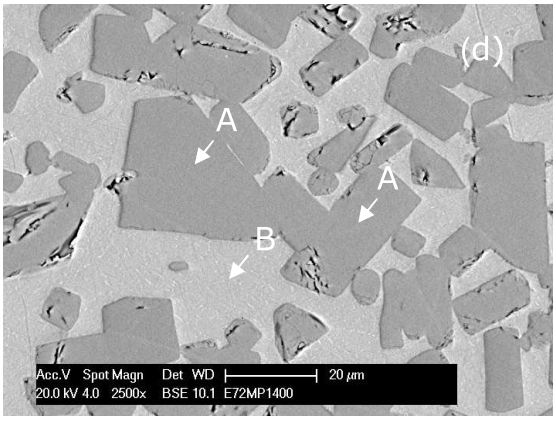

Fig. 4.6(d)

Fig. 4.6 BSE micrographs of the Armacor M powder following slow cooling in the DSC at 20K/min (a) low magnification, and (b-d) show higher magnification images of the boxed areas.

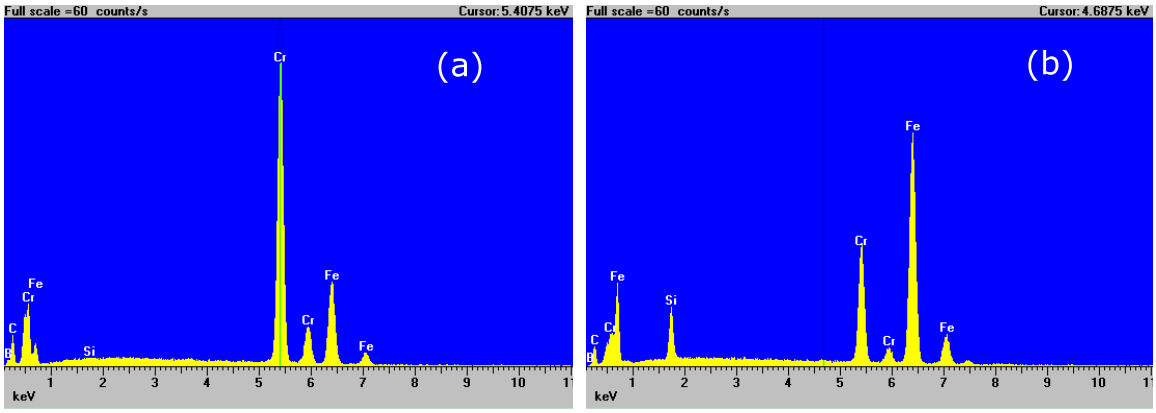

Fig. 4.7(a)-(b) EDX spectra of regions in Fig. 4.6(d) arrowed A and B, respectively.

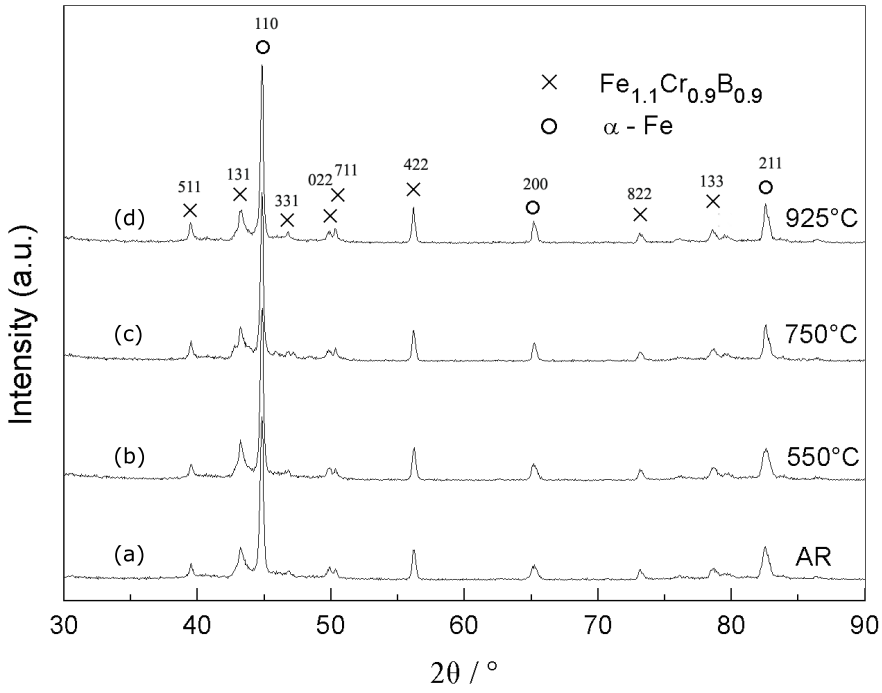

Fig. 4.8 XRD patterns for the heat treated powder at 550°C, 750°C and 925°C for 1 hour.

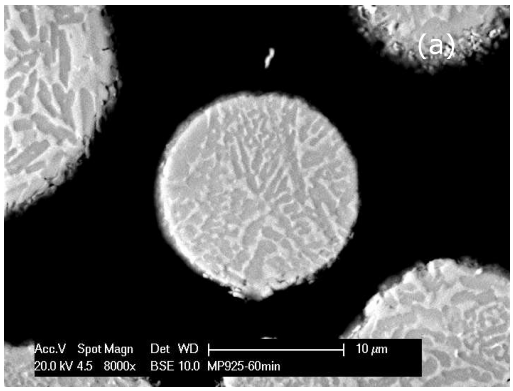

Fig. 4.9(a) Fine particle at 925°C

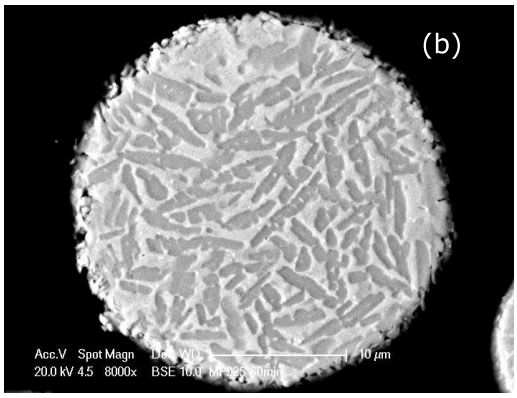

Fig. 4.9(b) Coarse particle at 925°C

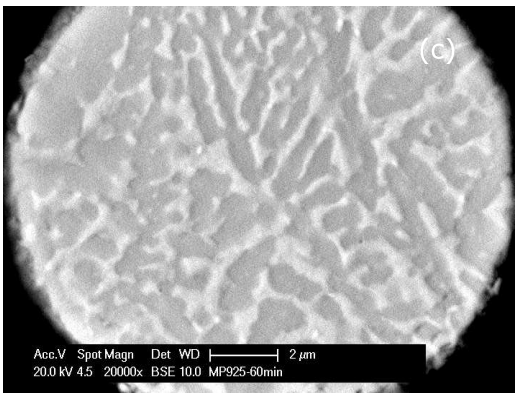

Fig.4.9(c) Fine particle
(high magnification)

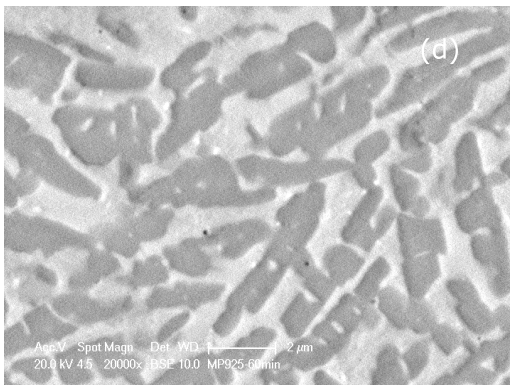

Fig.4.9(d) Coarse particle
(high magnification)

Fig. 4.9 Backscattered electron micrograph of the cross-section of a small particle Fig. 4.9(a) and a large particle Fig. 4.9(b) after heat treatment at 925°C (low magnification) and at high magnification Fig. 4.9(c) and 4.9(d).

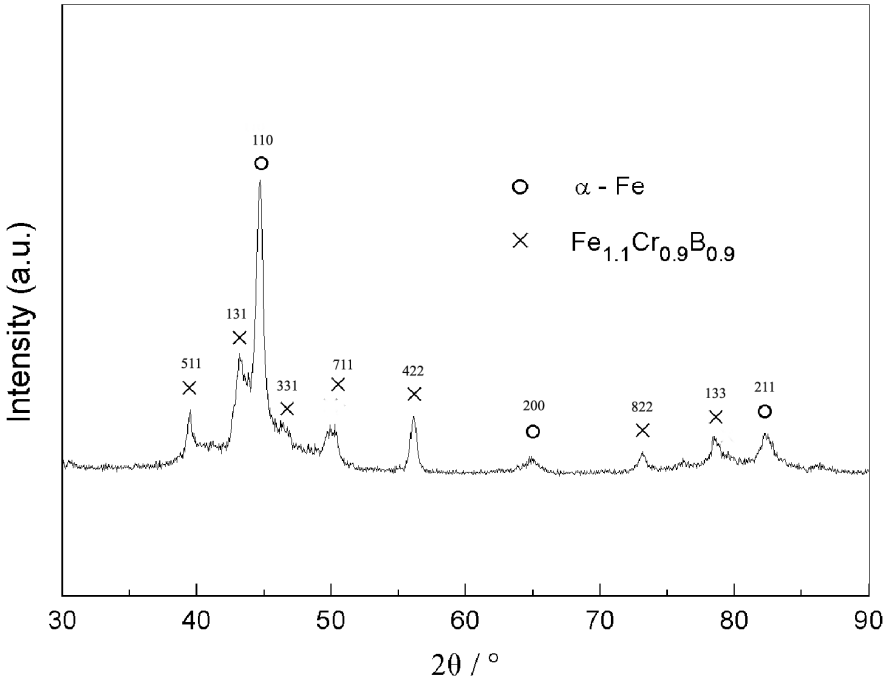

Fig. 4.10(a) XRD pattern of the as-sprayed Armacor M coating.

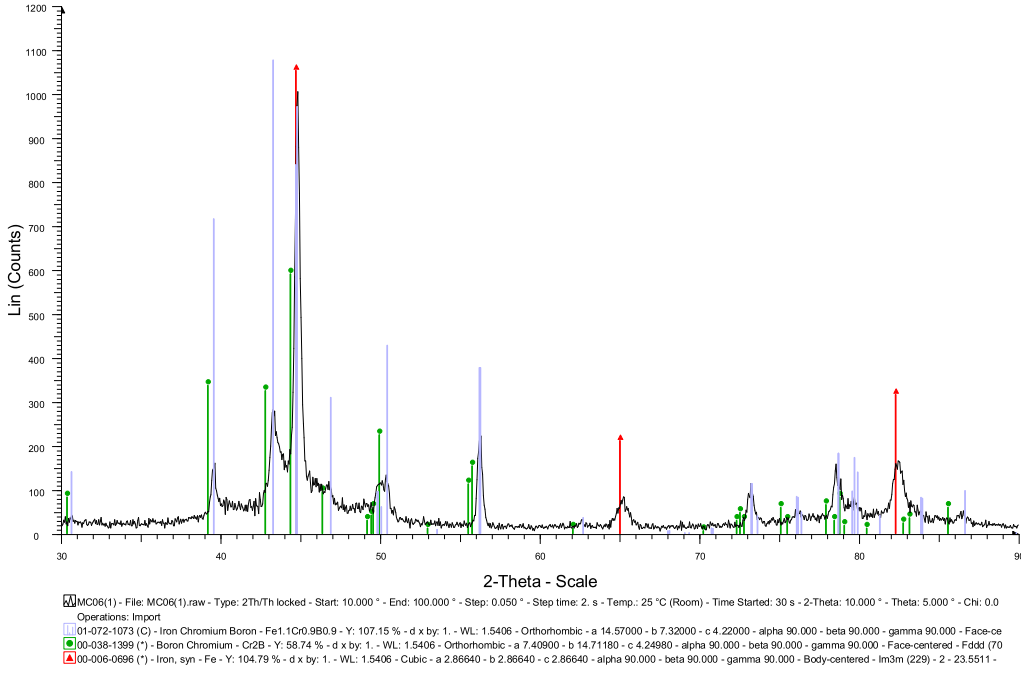

Fig. 4.10(b) Comparison of experimental XRD pattern of the as-sprayed coating with JCPDS files for Cr_2B and $Fe_{1.1}Cr_{0.9}B_{0.9}$.

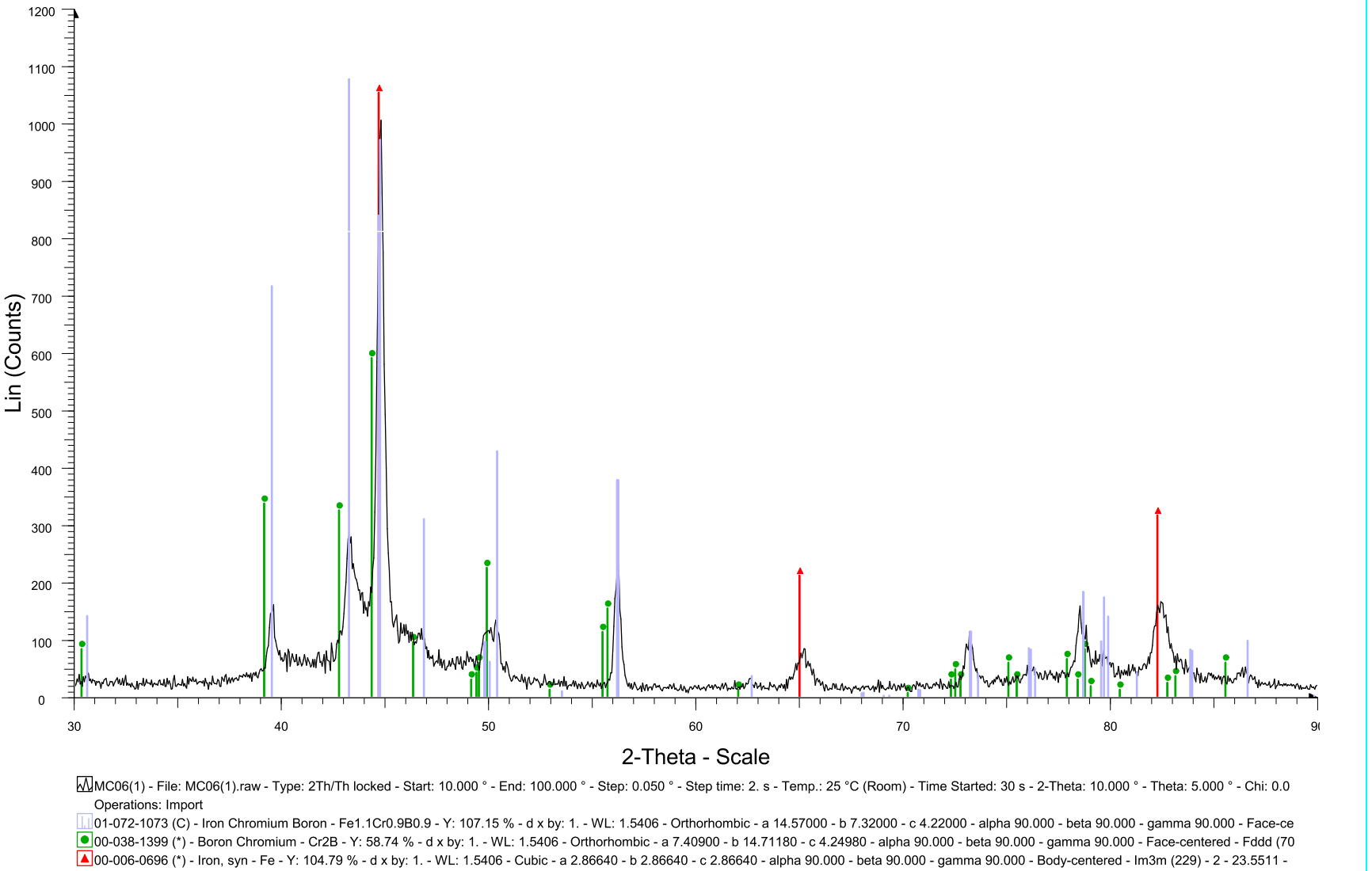

Fig. 4.10(c) Comparison of experimental XRD pattern (2θ = 30–90°) with JCPDS files for Cr_2B and $Fe_{1.1}Cr_{0.9}B_{0.9}$.

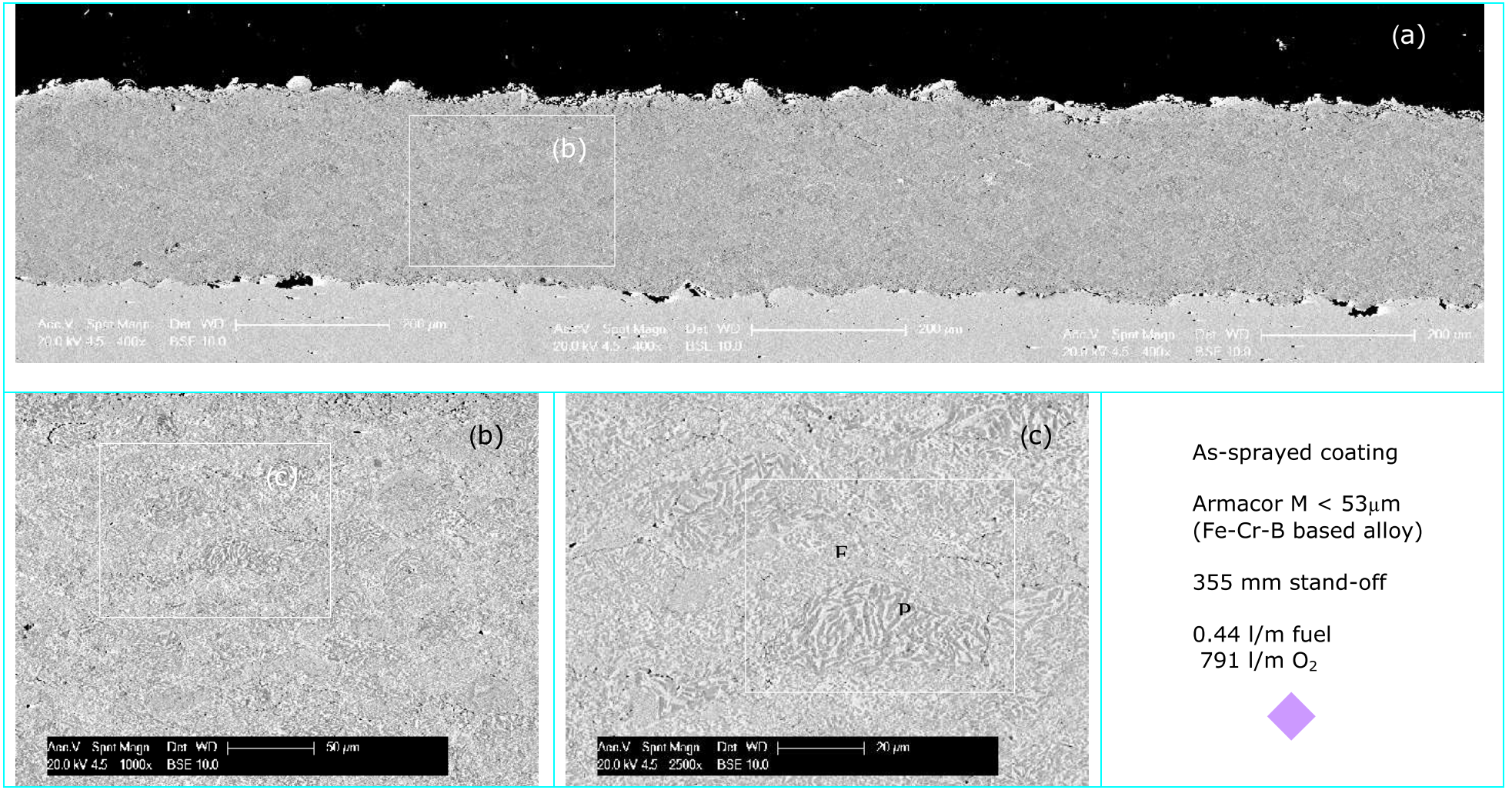

Fig. 4.11 BSE micrographs of cross-sections of a HVOF-sprayed coating: (a) low magnification unetched cross-section. (b),(c) High magnification image of the region b in (a) showing splat-like structure comprising fully melted (F) and partially melted (P) particles.

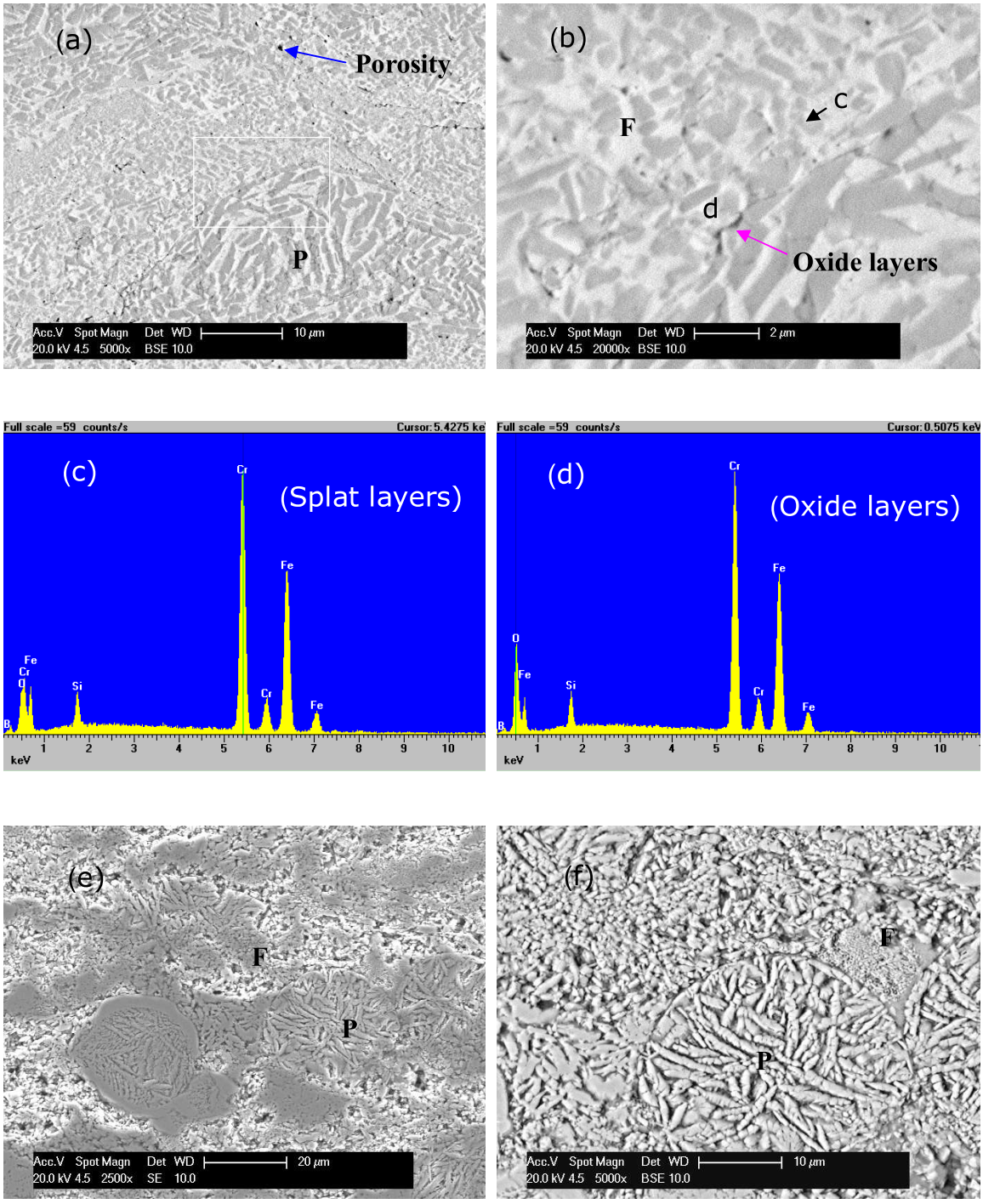

(heat treated at 920°C) (High magnification)

Fig. 4.12 BSE images showing cross-sections of a HVOF-sprayed coating. (a) Higher magnification image of the region P in Fig. 4.11(c) showing boride (dark region), Fe-Cr rich (bright region) and porosity. (b) Region F at higher magnification showing oxide layers. (c,d) EDX spectra of regions in image (b) arrowed c and d, respectively. (e,f) Low and high magnification of the as-sprayed coating following etching.

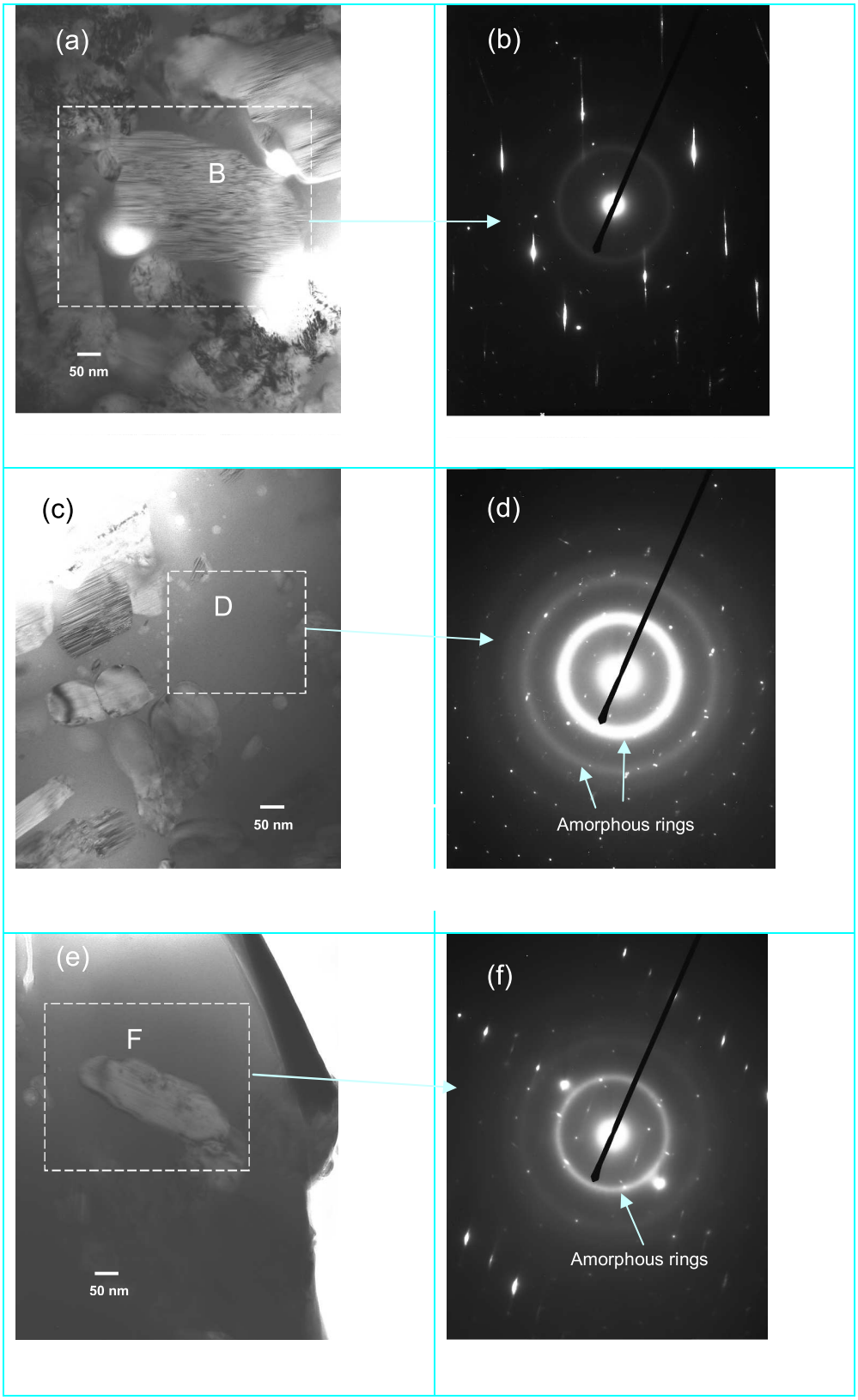

Fig. 4.13 TEM images of the as-sprayed Armacor M coating and associated diffraction patterns (a) Bright field of fully melted region; (b) diffraction pattern of (a). (c,e) Bright field of nanocrystalline region, (d,f) diffraction pattern of (c) and (e).

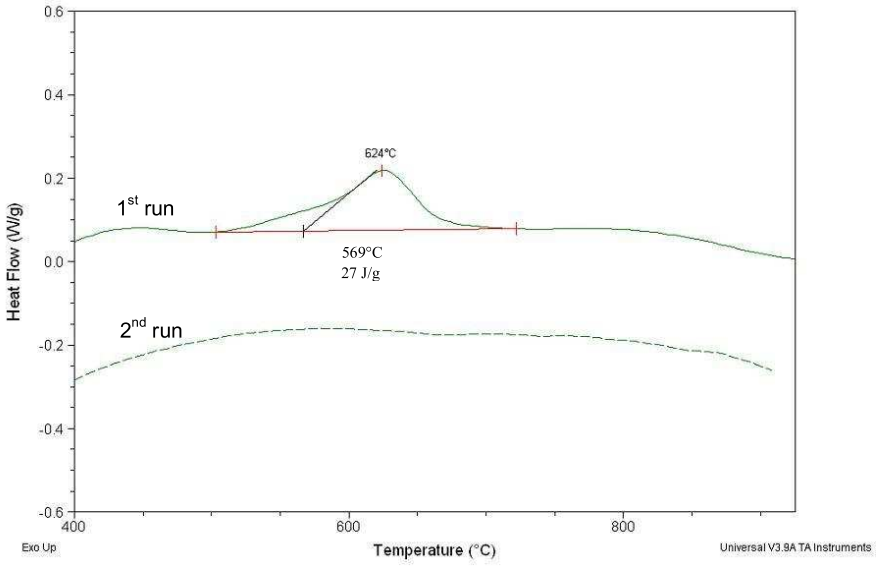

Fig. 4.14(a) DSC analysis of coating, 1st and 2nd heating runs at 20K/min.

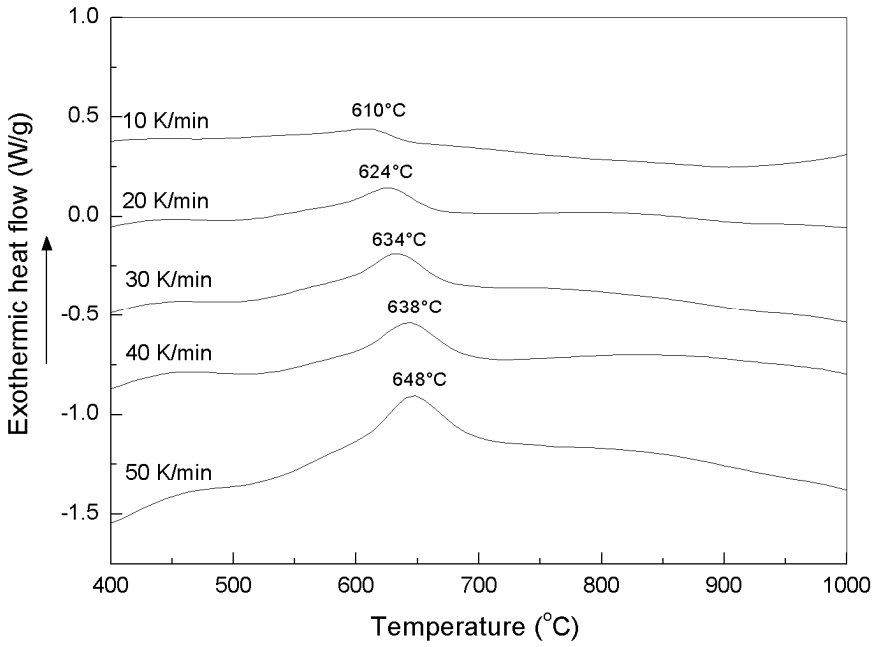

Fig. 4.14(b) DSC analysis of the Armacor M coating at heating rates 10 K/min, 20 K/min, 30 K/min, 40 K/min and 50 K/min

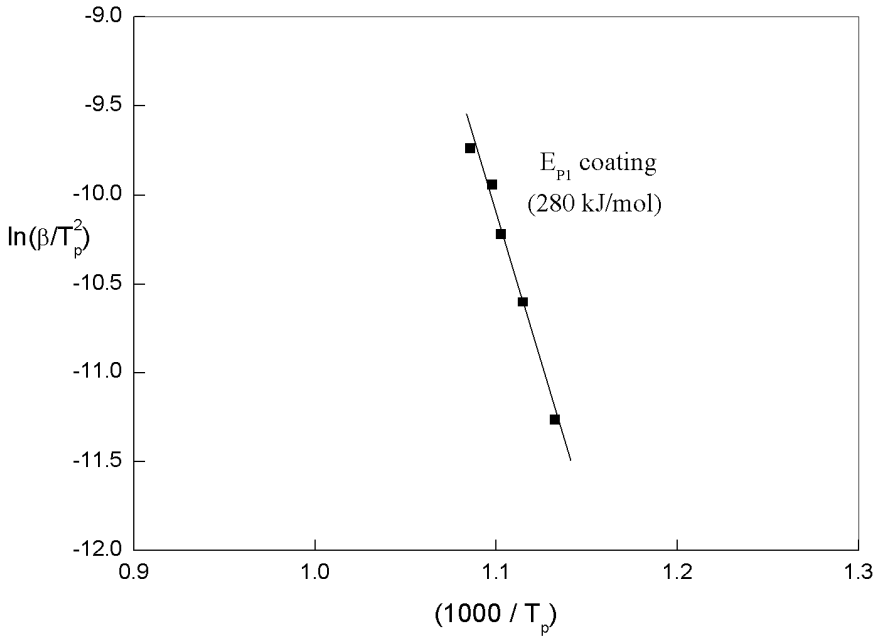

Fig. 4.15 Kissinger's plot of $\ln(\beta/T_p^2)$ versus $1000/T_p$ for peak temperature T_{p1} and T_{p2} of the as-sprayed Armacor M coating.

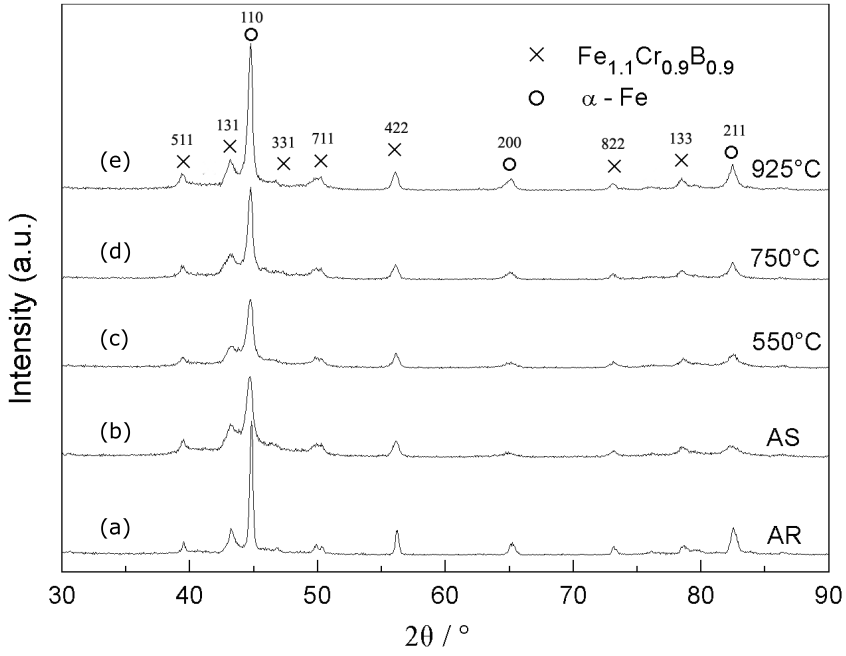

Fig. 4.16 XRD patterns of the as-received powder (AR), as-sprayed coating (AS) and the coatings following heat treatment at 550°C, 750°C and 925°C for 1 hour.

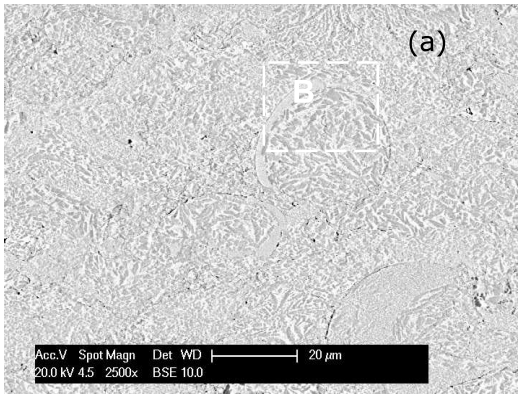

(heat treated at 550°C)

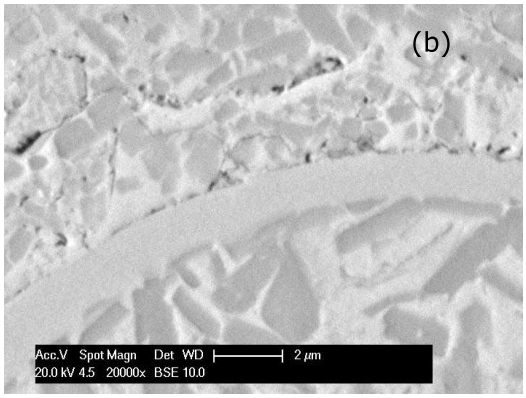

(High magnification)

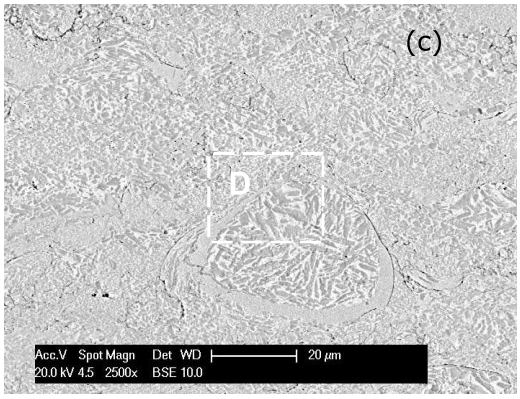

(heat treated at 750°C)

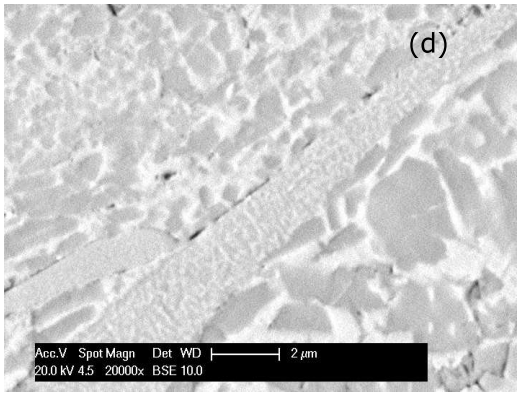

(High magnification)

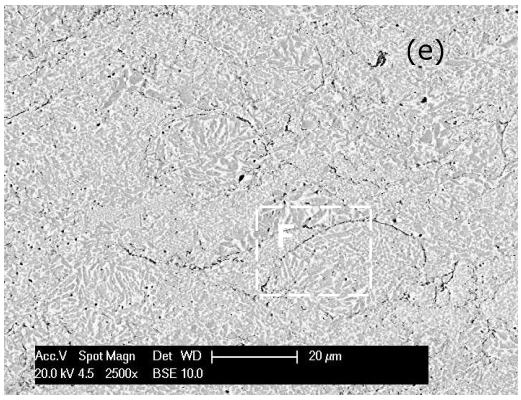

(heat treated at 925°C)

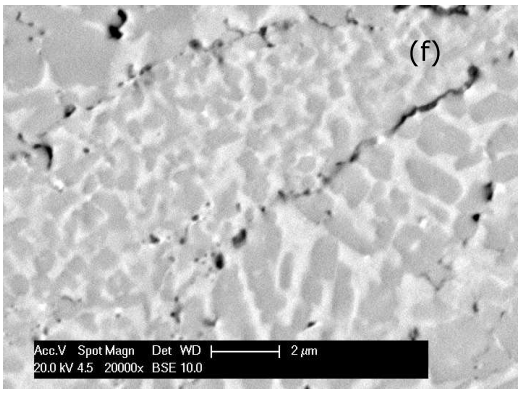

(High magnification)

Fig. 4.17 Backscattered electron micrograph of coating following heat treatment at 550°C, 750°C and 925°C (low and high magnification)

4.2 Armacor C

4.2.1 Powder size and composition

The chemical composition of a commercially available powder, Armacor C, from the Liquidmetal company (Texas, CA, USA), was determined by XRF, ICP and a combustion method and the result is given in Table 4.6. The powder had a nominal size range between 15 and 53 μm. The powder particle size distribution as measured by laser diffractometry, is shown as both cumulative volume percentage and volume percentage in Fig. 4.18. It was found that the volume mean particle diameter was 32.8 μm and there was approximately 10% above the nominal 53 μm upper limit, and 10% below 18 μm with a d_{50} of 30 μm.

Examination in the SEM (Fig. 4.19) showed that powder had a near-spherical morphology and some particles with satellites are also seen to be present. This is consistent with manufacture by the inert gas atomisation process.

Table 4.6 The composition of the Armacor C powder (as determined by XRF, ICP and a combustion method)

Element	Fe	Cr	B	Si	Mo	Ni	Cu	Co	C
wt.%	Bal.	30.4	3.5	3.1	3.6	20.3	2.7	8.7	0.1
atom.%	Bal.	27.9	15.4	5.3	1.8	16.5	2.0	7.1	0.4

4.2.2 Characterisation of as-received powder

XRD analysis

Fig. 4.20(a) shows the XRD traces obtained from the as-received Armacor C powder. The principal peaks are found to be a fcc γ – Fe and the boride phase either $(Cr_{1.65}Fe_{0.35})B_{0.96}$ or $(Fe_{1.1}Cr_{0.9})B_{0.9}$. Figs. 4.20(b) and (c) compare indexing of the

pattern with lines for Cr_2B (JCPDS file # 038-1399), $(Fe_{1.1}Cr_{0.9})B_{0.9}$ (JCPDS file # 072-1073) and $(Cr_{1.65}Fe_{0.35})B_{0.96}$ (JCPDS file # 035-1180). The last two phases give a better fit to peaks at $2\theta = 44.6°$, 49.7°, 56.1°, 78.3°. However, it is very difficult to make a precise identification between $(Fe_{1.1}Cr_{0.9})B_{0.9}$ and $(Cr_{1.65}Fe_{0.35})B_{0.96}$. Thus, the boride phase in the form of M_2 B is most probably the boride phase in the sample where M is either $(Fe_{1.1}Cr_{0.9})B_{0.9}$ or $(Cr_{1.65}Fe_{0.35})B_{0.96}$.

SEM analysis

The powder particle cross-sections were examined using BSE imaging. It was found typically that both small particles, Fig. 4.21(a) and large particles, Fig. 4.21(b) show varying contrast suggesting a multiphase structure. Bright areas indicate a higher mean atomic number and dark contrast needles have lower mean atomic number. A higher magnification BSE image of small particles Fig. 4.21(c) shows clearly a different contrast between two phases and more detail of the dark contrast needles or plates which appears ~ 0.5 μm in size can be observed. At higher magnification the BSE image of large particles Fig. 4.21(d) shows again a different contrast between two phases, but with larger dark contrast needles or plates ~ 1 μm in width as compared to that of small particles. EDX analysis of a bright area and a darker area are shown in Fig. 4.21(e) and Fig. 4.21(f), respectively. It can be seen that the bright area had a higher Fe/Cr ratio, whilst a darker area had a lower Fe/Cr ratio. The peak ratio of Fe to Cr for each phase was calculated from the measured intensities of EDX spot analysis and the values were obtained for comparison. It was found that the Fe/Cr peak ratio for a bright area and a dark area are 0.88 and 0.45, respectively. This suggests that the bright matrix was the metallic fcc phase and the dark needles were the boride phase.

4.2.3 Characterisation of Slow Cooled Solidified Powder

The melting and solidification behaviour of the Armacor C powder was studied by continuous heating and cooling DSC experiments in which the powder was melted, as shown in Fig. 4.22.

The DSC trace (Fig. 4.22) shows a wide endothermic double peak, observed at an onset temperature of 1201°C. These could be due to the melting of γ – Fe and possibly, the dissolution of boride phase. The critical temperatures are listed in Table 4.7.

Table 4.7 The melting temperature T_m and the liquidus temperature T_{liq} obtained from a DSC curve of the Armacor C powder at a scanning rate of 20 K/min.

Heating rate	T_m (°C)	T_{liq} (°C)
20 K/min	1201	1255

During cooling, one major exothermic peak with the 2nd overlapping peak was observed as shown in Fig. 4.22(b). This large peak just below 1226°C was observed on the DSC scan to have a relatively high enthalpy of reaction. These exothermic peaks during cooling of the melt suggest that the Armacor C sample has a slightly off-eutectic composition compared to Armacor M.

The DSC sample was then examined in the SEM at varying magnifications as shown in Fig. 4.23. At low magnification Fig. 4.23(a) – 4.23(b) there are 200 μm size dark needles or plates in a matrix. From Fig. 4.23(c) and (d) the matrix comprises a 2-phase eutectic. At the highest magnification, Fig. 4.23(e) all the phases are visible and are labelled A, B and C. EDX analysis was performed on these phase regions

and EDX spectra are shown in Fig. 4.24. Table 4.8 shows quantitative EDX analysis data for elements present (excluding the low atomic number elements boron and carbon).

Table 4.8 EDX analysis data for the elements present in the different regions in Fig. 4.6(e) (excluding B and C)

	Element (wt%)					
Regions	Fe	Cr	Ni	Mo	Co	Others
(A) dark	20.5	69.9	1.6	4.4	3.4	0.2(Cu,Si)
(B) light grey	36.1	15.6	28.7	1.8	11.8	5.9(Cu,Si)
(C) white	20.3	31.3	10.9	29.8	5.6	2.2(Cu,Si)

The dark regions arrowed (A) correspond to the boride phase, the bright regions arrowed (B) are attributed to γ – (Fe, Ni, Cr, Co) phase and the fine scale phase (white regions) arrowed (C) correspond to γ – Fe (high Cr, Mo) phase. Therefore from the DSC trace, Fig. 4.22, and the SEM/EDX observations the following possible solidification sequence when cooling at 20 K/min is proposed

$$L \xrightarrow{1226C^\circ} L + \text{boride} \xrightarrow{\sim 1210C^\circ} L + \text{boride} + (\gamma - Fe)$$

$$\xrightarrow{1174C^\circ} L + \text{boride} + (\gamma - Fe) + \text{white phase}$$

where boride is M_2B, either $(Fe_{1.1}Cr_{0.9})B_{0.9}$ or $(Cr_{1.65}Fe_{0.35})B_{0.96}$

4.2.4 Characterisation of heat treated powder

XRD analysis

Fig. 4.25 shows the XRD traces for the as-received powder (AR) and samples heat treated for 1 hour at 550°C, 750°C and 925°C. It was found that there is no phase change of the powder after heat treatment at temperatures of 550°C as shown in Fig. 4.25(b).

On further heating of the powder at a temperature of 750°C led to small increase in the intensities of γ – Fe peaks and the intensities of peaks from other phases (the boride phase, $Cr_{1.65}Fe_{0.35}B_{0.96}$) remained almost unchanged as shown in Fig. 4.25(c).

After the powder was heated to a temperature of 925°C, Fig. 4.25(d), the intensities of γ – Fe peaks and the intensities of peaks from other phases (the boride phase, $Cr_{1.65}Fe_{0.35}B_{0.96}$) remained almost unchanged as shown in Fig. 4.25(c).

SEM analysis

The microstructure of the Armacor C powder after heat treatment has been investigated using BSE imaging. After heat treatment of powder at temperature 925°C, there was no detectable microstructural change in both a small particle Fig. 4.26(a) and a larger particle Fig. 4.26(b).

The corresponding XRD trace is Fig. 4.25(d). A higher magnification BSE image of small particles Fig. 4.26(c) shows boride needles or plates with somewhat rounded edges and a similar result can be observed in the higher magnification BSE image of

large particles Fig. 4.26(d), revealing possibly a first sign of dissolution of the dark boride phase in to Fe-matrix phase.

4.2.5 Characterisation of as-sprayed coating

XRD analysis

The gas atomised Armacor C powder was deposited onto mild steel substrates using HVOF thermal spraying. The phases present in the as-sprayed coating were determined by X-ray diffraction. The XRD trace from the top surface of the as-sprayed coating is shown in Fig. 4.27(a). Again, fcc γ – Fe and the boride phase of either $(Fe_{1.1}Cr_{0.9})B_{0.9}$ or $(Cr_{1.65}Fe_{0.35})B_{0.96}$ are the principal peaks shown in the XRD traces. There has been a significant increase in the proportion of the amorphous phase as shown by a broader diffraction halo around $2\theta = 39 – 48°$ as compared with that of the as-received powder. Figs. 4.27(b) and 4.27(c) compare indexing of the pattern of the Armacor C coating with lines for Cr_2B, $(Fe_{1.1}Cr_{0.9})B_{0.9}$ and $(Cr_{1.65}Fe_{0.35})B_{0.96}$. The boride phase could not be conclusively identified the XRD pattern as peaks from the phases $(Fe_{1.1}Cr_{0.9})B_{0.9}$ and $(Cr_{1.65}Fe_{0.35})B_{0.96}$ can all be fitted equally well to the experimental data and thus either $(Fe_{1.1}Cr_{0.9})B_{0.9}$ or $(Cr_{1.65}Fe_{0.35})B_{0.96}$ seems to be possible the boride phase in the sample.

SEM analysis

The HVOF as-sprayed Armacor C coatings were also characterised by SEM using BSE imaging. Fig. 4.28(a) shows a low magnification unetched cross-section of the as-deposited coating. The coating is seen to be around 365 μm thick with an irregular top surface. Generally, the coating has a dense layered structure typical of HVOF thermally sprayed deposits. The rough interface between the coating and mild steel

substrate, resulting from the grit blasting of the latter prior to coating deposition, can be seen. The splats from the spray process have not deformed sufficiently to fill the roughened surface in some regions, possibly suggesting a high viscosity molten material.

At higher magnification, the cross-section of the coating imaged in the BSE mode of the area (b) in Fig. 4.28(a), is shown in Fig. 4.28(b) and (c). The coatings exhibit regions such as P which appear to have structures retained from the powder. Other regions such as F are also visible which apparently formed from melted and resolidified powder and have finer scale borides.

Fig. 4.29(a) shows a BSE image of a typical region P from a cross-section of coating is shown in Fig. 4.28(c). This reveals a near- spherical morphology of unmelted or partially melted particles, labelled P in the coating and some porosity is visible as a very dark contrast region, generally outside the region P. Porosity of the coating producing by this HVOF thermally spray process is relatively low.

Fig. 4.29(b), a higher magnification BSE image of the selected area in Fig. 4.29(a) shows details of the interface area between a fully melted region (F) and partially melted particle (P). The EDX spectra and analysed data of the arrowed regions C and D of image Fig. 4.29(b) are shown in Fig. 4.29(c) and Fig. 4.29(d), respectively. It is indicated that the splat layers, as marked (C) in Fig. 4.29(b) correspond to Fe-rich matrix phase. There is no evidence of oxygen from the thin dark contrast stringers as marked (D) indicating that this is probably a thin extended pore rather than an oxide.

Fig. 4.29(e) is a low magnification BSE image, following etching in a solution of 1 part HCl, 1 part HNO_3 and 1 part H_2O. The coating appears to have a low overall porosity. At high magnification (Fig. 4.29(f)), greater details in the regions of unmelted or partially melted powder particles (labelled P) and the regions (F) arising from solidified splats can be observed. Unmelted or partially melted particles (labelled P) from the original powder etch strongly while the splat regions (F) exhibit a low etching response.

TEM analysis

TEM images of a sample from the as-sprayed Armacor C coating (plan view) is shown in Fig. 4.30. Fig. 4.30(a) is a bright field TEM micrograph and reveals that the sample was composed of mainly crystalline regions. The SAD pattern in Fig. 4.30(b) was taken from the region in Fig. 4.30(a) and shows well defined diffraction spots which indicate the presence of crystalline phase in the coating.

An example of crystalline regions (500-1000 nm size) in what appears to be an amorphous matrix is shown in Figs. 4.30(c) and (e). The associated diffraction patterns Fig. 4.30(d) and (f) taken from the region in Fig. 4.30(c) and (e), respectively show a combination of diffraction spots and diffuse rings.

DSC analysis

Fig. 4.31(a) shows the DSC analysis of the coating during first and second heating runs at 20K/min. In the curve from the first heating run, one peak appears and this corresponds to one exothermic reaction, attributable to crystallization of the amorphous phase. The peak crystallization temperature (T_{p1}) is 654°C. In the curve

after the second heating run, the exothermic peak has completely disappeared. This confirms that the first peak was due to the irreversible primary crystallisation of an amorphous phase in the coating sample.

Fig. 4.31(b) shows typical DSC curves of the as-deposited Armacor C coating obtained during continuous heating at five different heating rates (10 K/min – 50 K/min). It can be clearly seen that each DSC curve exhibits one exothermic peak. It indicates that the crystallization of the amorphous phase in the coating proceeds via a single stage of reaction. The crystallization reaction occurs at temperatures in the range 635-683 °C (peak temperatures) depending on the heating rate. The onset of crystallization temperatures *(T_x)*, peak temperatures *(T_p)*, and enthalpies of crystallization *(ΔH)* for the Armacor M coating at different heating rates (10K/min to 50K/min) are given in Table 4.9. The onset temperature is taken to be when is first seen a deviation from the baseline is first observed.

Table 4.9 The onset of crystallization temperatures (T_x), peak temperatures (T_p), and enthalpies of crystallization (ΔH) for the Armacor C coating at different heating rates where (ΔH) has units of per g of sample.

Heating rate	Onset T_x (°C)	T_p (°C)	ΔH (J/g)
10 K/min	603	635	43
20 K/min	621	654	43
30K/min	629	667	45
40K/min	637	676	46
50 K/min	642	683	44

By using Kissinger's method (see Chapter 3), the activation energies of crystallization for the Armacor C coating can be determined from the slope of the straight line plot of $\ln(\beta/T_p^2)$ as a function of $10^3/ T_p$ as shown in Fig. 4.32. The activation energy, E_a was found to be 225 kJ/mol for the peak of the coating sample. In addition, the heat of reactions, (ΔH) was also determined using DSC, and the values are given in Table 4.9 which are in the range of 43 to 46 J/g where these are measured per g of sample.

4.2.6 Characterisation of heat treated coating

XRD analysis

Fig. 4.33 shows the XRD traces for the as-received powder (AR), as-sprayed coating (AS) and the coatings following heat treatment for 1 hour at 550°C, 750°C and 925°C. It was found that there is no evidence for a phase change in the coating after heat treatment at a temperature of 550°C as shown in Fig. 4.33(c).

Heat treatment of coating at a temperature of 750°C, just above the exothermic reaction peak, led to a small increase in the intensities of Fe peaks and a small increase in the intensity of the peaks from the boride phase as shown in Fig. 4.33(d).

Following heat treatment at temperature 925°C, led to further increase in the intensities of Fe peaks while the peaks from the boride phase $(Fe_{1.1}Cr_{0.9})B_{0.9}$ (JCPDS file # 072-1073) or $(Cr_{1.65}Fe_{0.35})B_{0.96}$ (JCPDS file # 035-1180) remained almost unchanged as shown in Fig. 4.33(e). During this stage, the fcc-Fe phase was the major phase, although intensities of the peaks from the boride phase also increased.

SEM analysis

Fig. 4.34 shows the microstructure of the coating after heat treatment at 550°C, 750°C and 925°C for 1 hour. After heat treatment of the coating for 1 hour at temperature 550°C, just below the first exothermic peak of crystallization, there was no observable microstructural change of the coating that could be resolved in the SEM as shown in Fig. 4.34(a). Fig. 4.34(b), a higher magnification BSE image of selected area boxed (B) in Fig. 4.34(a) shows clearly that the presence of micron sized borides, essentially identical to those observed in the as-sprayed coating.

The microstructural change after heat treatment of the coating at 750°C for 1 hour is shown in Fig. 4.34(c). Fig. 4.34(d) shows a higher magnification BSE image of selected area boxed (D) in Fig. 4.34(c). Fine precipitates (low in contrast) within what was the fully melted and resolidified region can now be observed suggesting crystallisation of an amorphous matrix occurred in this region.

Furthermore, following heating of the sample to a temperature of 925°C for 1 hour, larger precipitates within what was fully melted region of the coating can be observed as seen in Fig. 4.34(e), a low magnification BSE image of the coating and Fig. 4.34(f), a higher magnification BSE image of the selected area boxed (F). Fine scale porosity is also evident in Fig. 4.34(f).

4.2.7 Microhardness

Heat treatments of the as-sprayed Armacor C coatings were performed for a fixed time of 60 minutes at the following temperatures: 550, 750 and 925°C.

Microhardness data for the as-sprayed coating and following heat treatment at 550°C, 750°C and 925°C for 1 hour are shown in Table 4.10.

Table 4.10 Hardness (GPa) of the as-deposited and samples heat treated for 1 hour

Sample	As-deposited	550°C	750°C	925°C
Hardness / GPa	8.5	8.8	7.7	6.0
Standard deviation	0.3	0.5	0.3	0.3
Standard error	0.1	0.2	0.1	0.1

The results show that following heat treatment at 550°C, the hardness of the coating increased somewhat but then decreased to 7.7 GPa at temperature 750°C and after increasing the temperature up to 925°C, the hardness decreased to 6.0 GPa. It is suggested that the drop in the hardness of the coating could be due to microstructural coarsening of the boride phase in the sample as well as the disappearance of amorphous regions and the reduction in supersatulation of the γ-Fe matrix.

4.2.8 Summary (Armacor C)

(1) In this study, a microstructural investigation of HVOF-thermally sprayed Armacor C powder of composition (in at %) Fe-27.9%Cr-15.4%B-0.4%C-5.3%Si-1.8%Mo-16.5%Ni-2.0%Cu-7.1%Co is reported. The deposits, which were approximately 365 μm thick, have a splat-like microstructure characteristic of thermally sprayed alloys with a small fraction of oxide phase.

(2) The predominant phases present in the as-sprayed Armacor C coating, as identified by XRD, are a fcc γ-Fe matrix and a boride of the M_2B type. However, it could be either $(Fe_{1.1}Cr_{0.9})B_{0.9}$ or $(Cr_{1.65}Fe_{0.35})B_{0.96}$.

(3) The formation of the amorphous phase is probably due to the high cooling rates of the splats combined with the alloy composition, relatively high B 15.4 at % which is close to a eutectic composition in the Fe-B binary phase diagram. However, the presence of metalloid elements (e.g. boron) and a high level of chromium 27.9 at% can also lead to a formation of boride precipitates.

(4) The thermal stability of the as-sprayed Armacor C coating means this coating can only be subjected into service below ~ 650°C.

(5) The activation energies for reactions were calculated from DSC data using the Kissinger peak shift equations. The activation energy for the peak of reaction corresponds to the energy required for crystallization of amorphous Fe-based matrix phase and/or precipitation of boride phase.

(6) The as-sprayed Armacor C coating showed a moderate hardness (~8.5 GPa). However, after annealing at temperatures above the peak of crystallization (~ 750°C) the annealed coating sample exhibits lower hardness (~ 6.0 GPa) than in the as-sprayed condition. This is thought to be due to crystallisation of the matrix and/or precipitation and coarsening of the boride (M_2B) phase.

Result: Fe-Cr-B alloy (Armacor C)

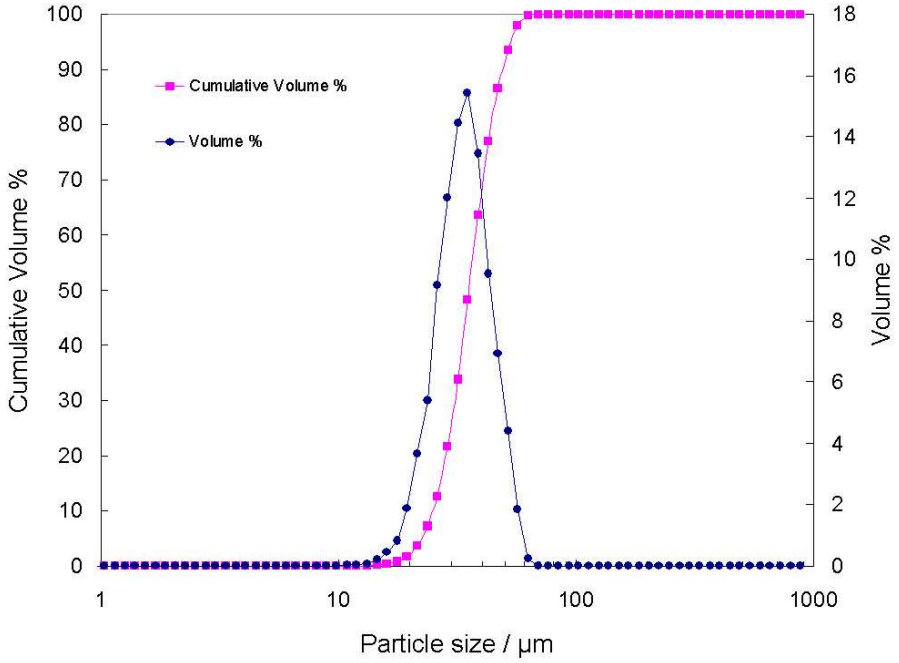

Fig. 4.18 Plot of powder size distribution for the as-received Armacor C powder.

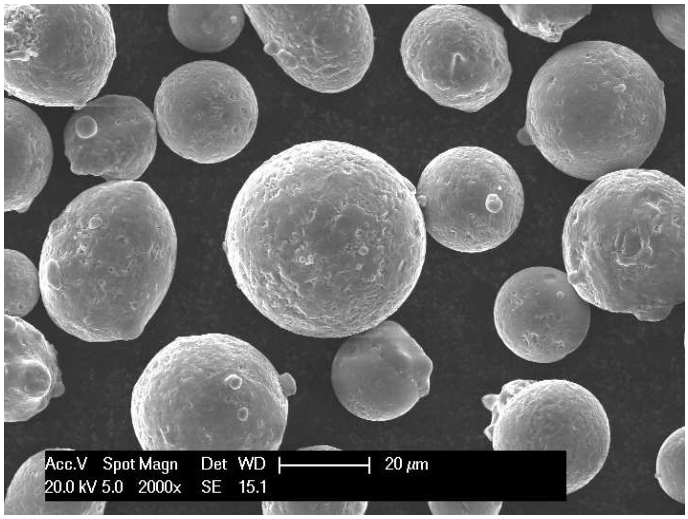

Fig. 4.19 The external morphology of the as-received Armacor C powder.

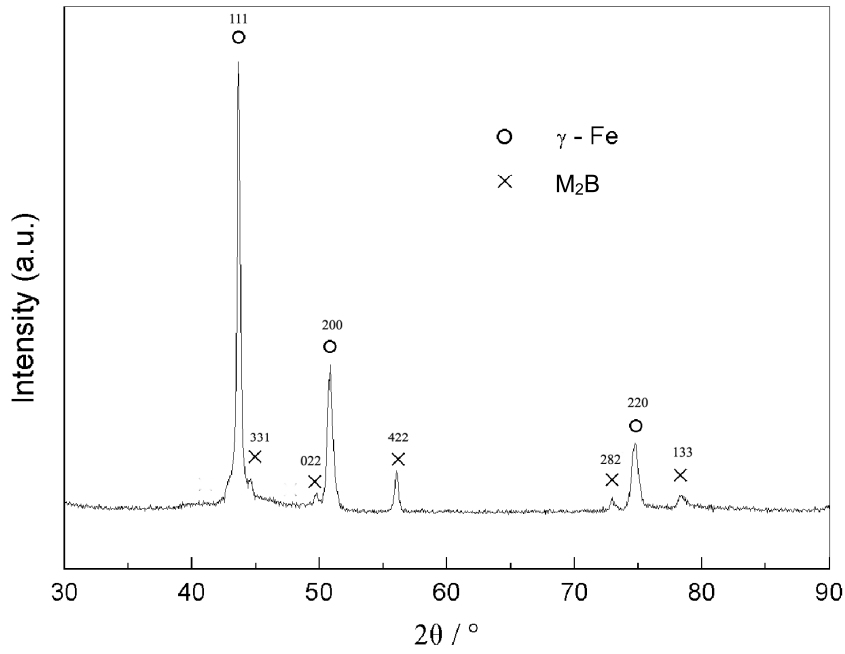

Fig. 4.20(a) XRD pattern of the as-received Armacor C powder.

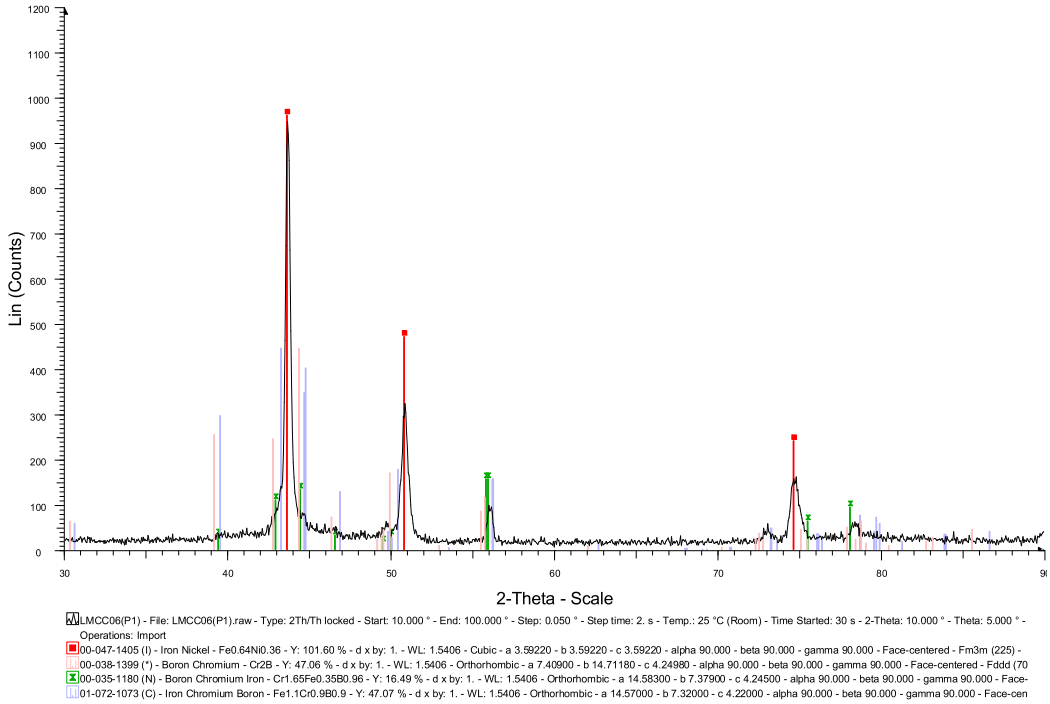

Fig. 4.20(b) Comparison of experimental XRD pattern with JCPDS files for Cr_2B, $Fe_{1.1}Cr_{0.9}B_{0.9}$ and $Cr_{1.65}Fe_{0.35}B_{0.96}$.

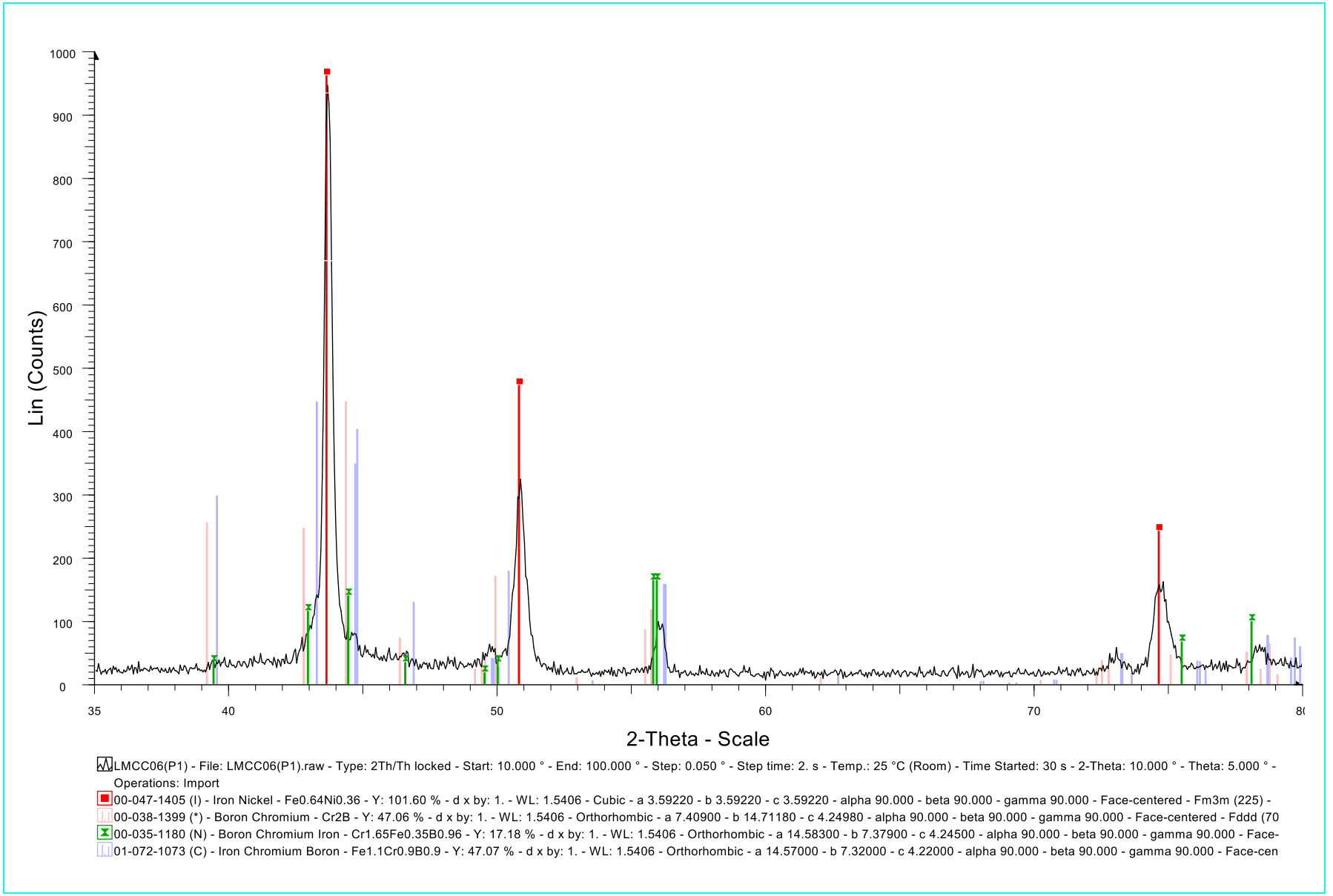

Fig. 4.20(c) Comparison of experimental XRD pattern (2θ = 35–80°) with JCPDS files for Cr_2B, $Fe_{1.1}Cr_{0.9}B_{0.9}$ and $Cr_{1.65}Fe_{0.35}B_{0.96}$.

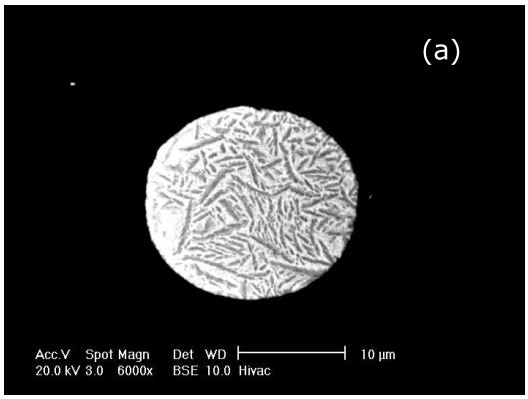

Fig. 4.21(a)

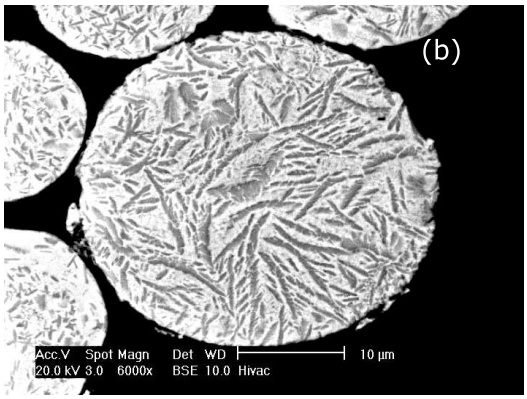

Fig. 4.21(b)

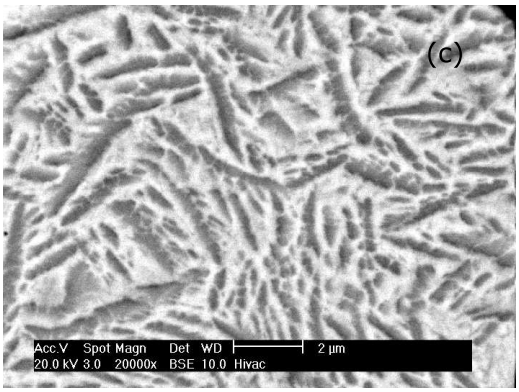

Fig. 4.21(c)

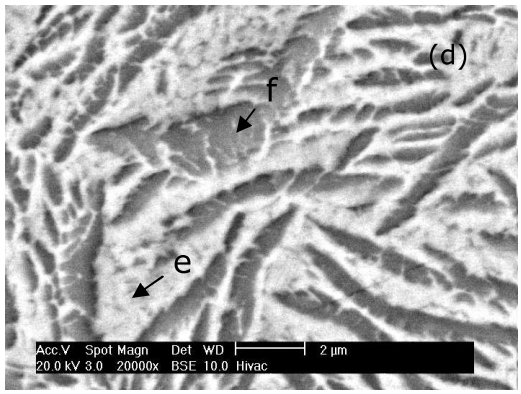

Fig. 4.21(d)

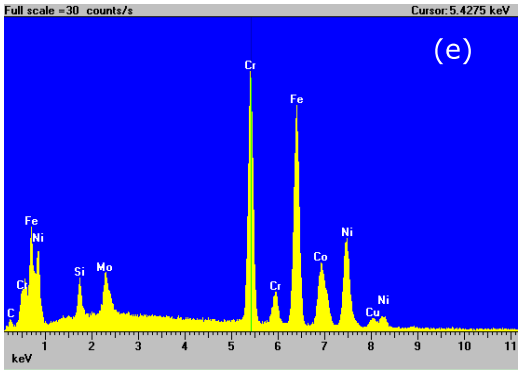

Fig. 4.21(e)

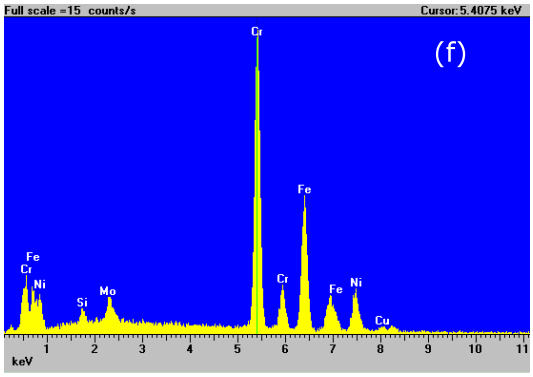

Fig. 4.21(f)

Fig. 4.21 BSE images of the cross-section of a small particle (a) and a large particle (b). (c,d) Higher magnification of regions in images (a) and (b). (e,f) EDX spectra of regions in (d) arrowed e and f, respectively.

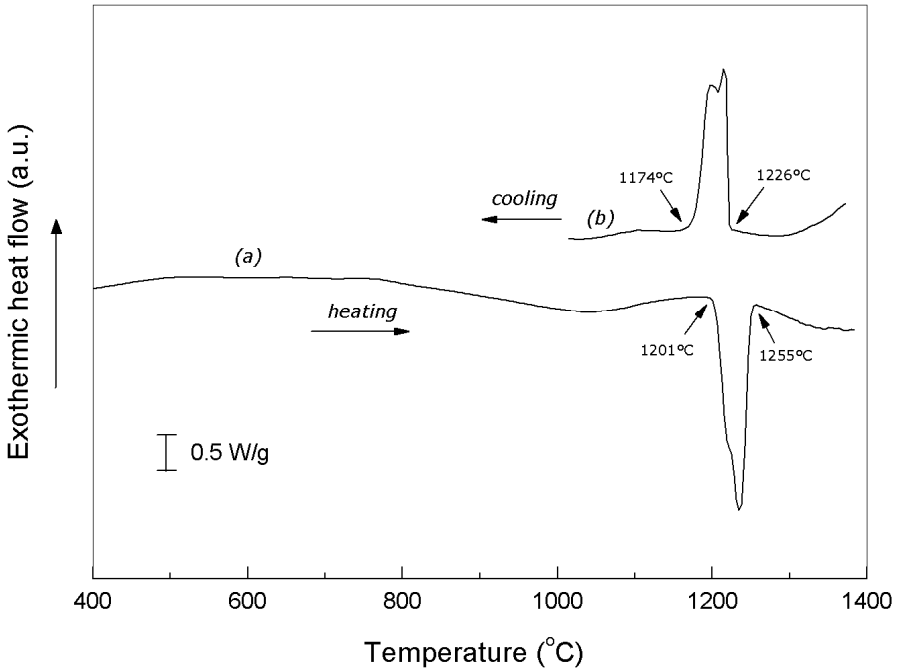

Fig. 4.22 The DSC heating (a) and cooling (b) scans for the as-received Armacor C powder obtained at a scanning rate of 20 K/min

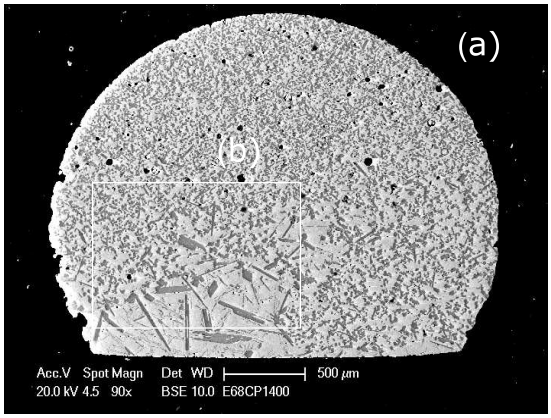

Fig. 4.23(a)

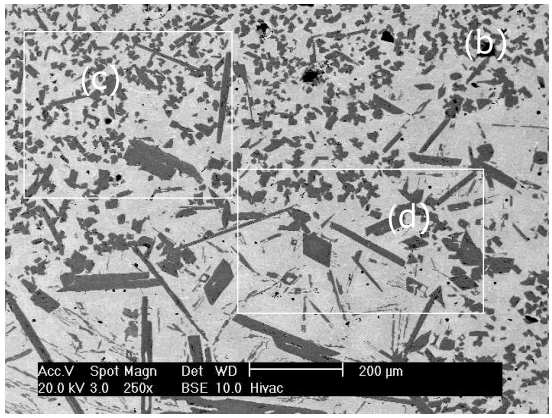

Fig. 4.23(b)

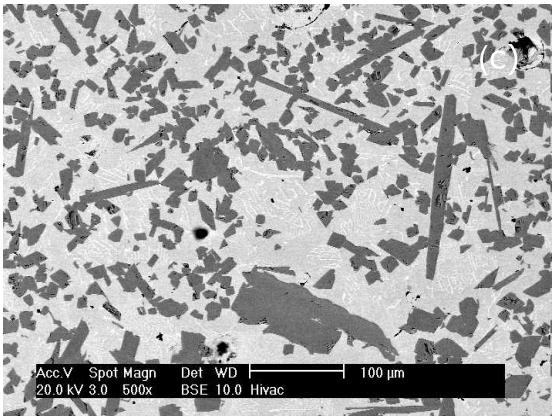

Fig. 4.23(c)

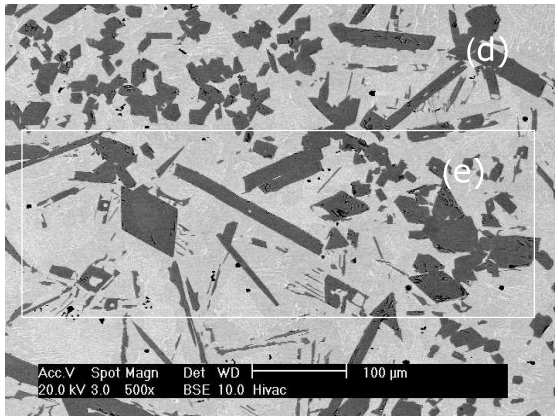

Fig. 4.23(d)

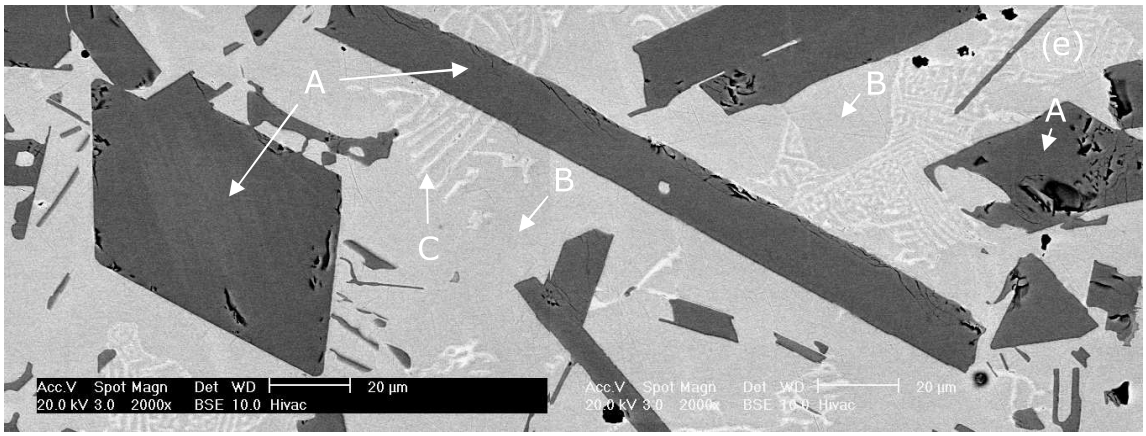

Fig. 4.23(e) at higher magnification of the boxed area (e) in Fig. 4.23(d)

Fig. 4.23 BSE micrographs of the Armacor C powder following slow cooling in the DSC at 20K/min (a) low magnification, and (b-e) show higher magnification images of the boxed areas

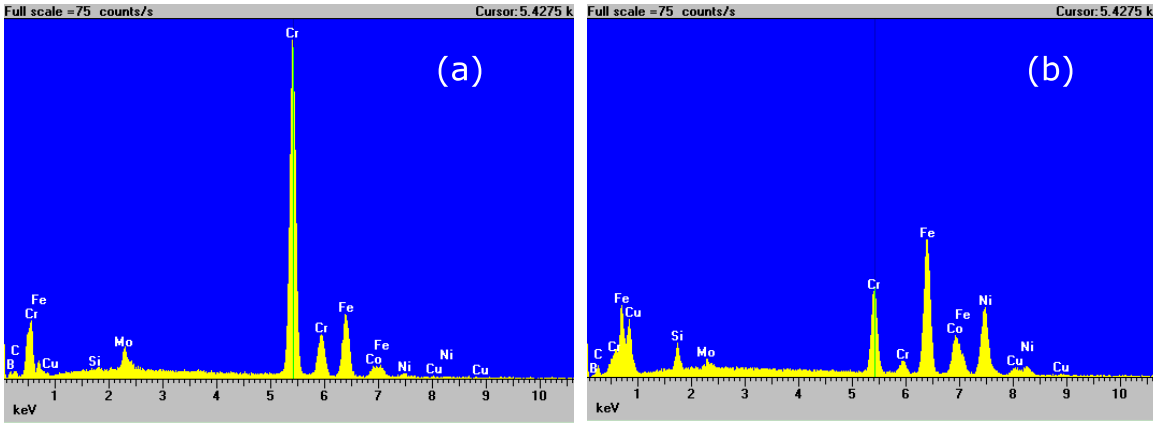

Fig. 4.24(a)-(b) EDX spectra of regions in Fig. 4.23(e) arrowed A-B, respectively.

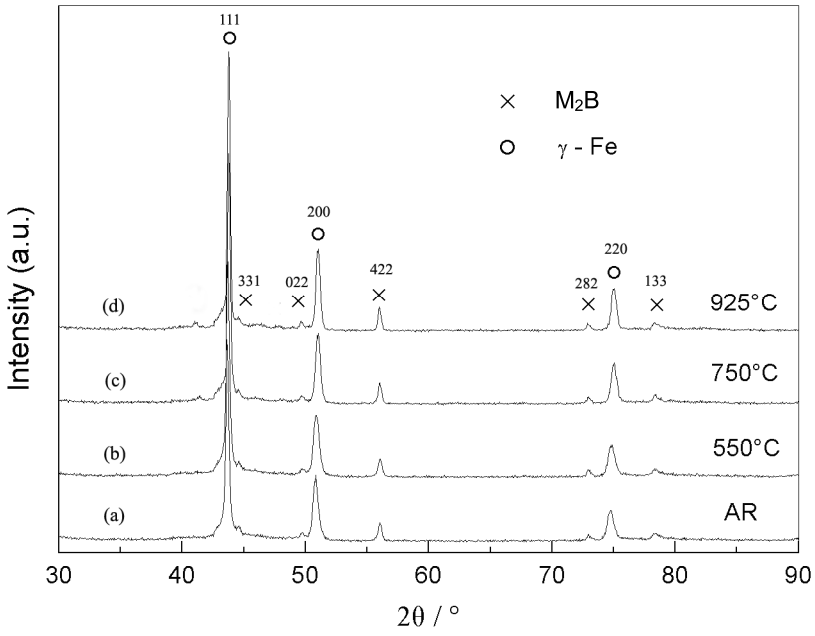

Fig. 4.25 XRD patterns for the heat treated powder at 550°C, 750°C and 925°C for 1 hour.

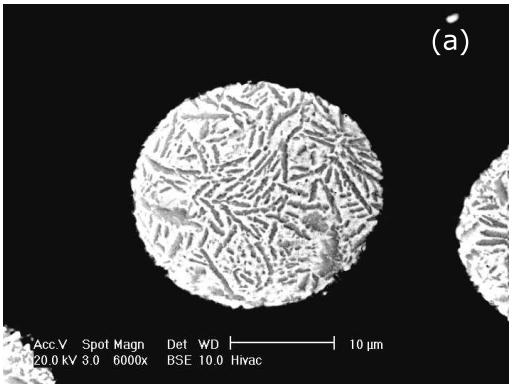

Fig. 4.26(a) Fine particle at 925°C

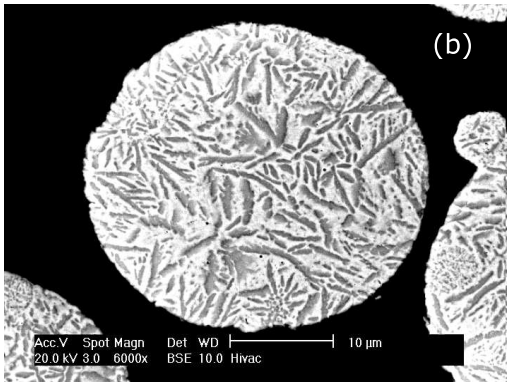

Fig. 4.26(b) Coarse particle at 925°C

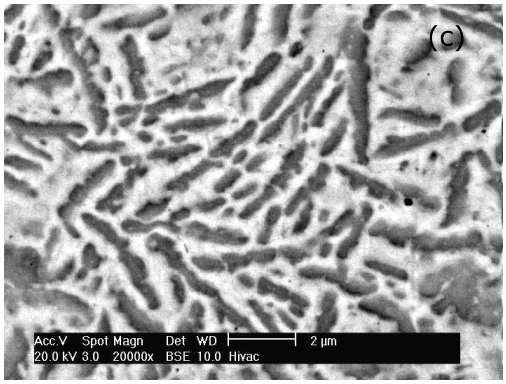

Fig.4.26(c) Fine particle (high magnification)

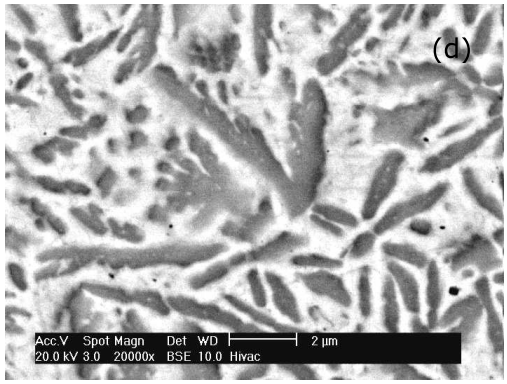

Fig.4.26(d) Coarse particle (high magnification)

Fig. 4.26 Backscattered electron micrograph of the cross-section of a small particle Fig. 4.26(a) and a large particle Fig. 4.26(b) after heat treatment at 925°C (low magnification) and at high magnification Fig. 4.26(c) and 4.26(d).

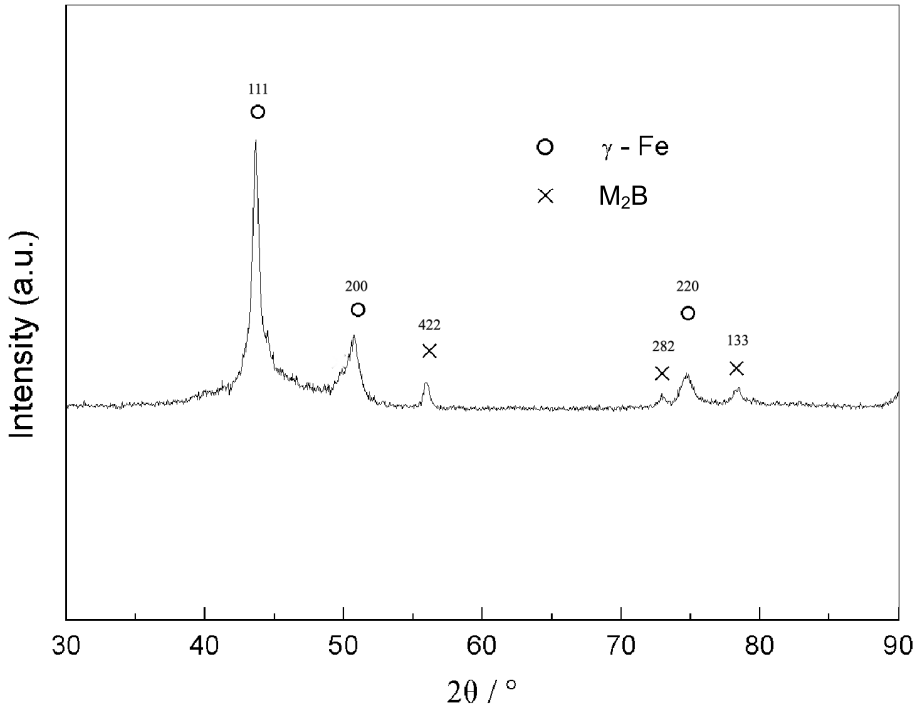

Fig. 4.27(a) XRD pattern of the as-sprayed Armacor C coating.

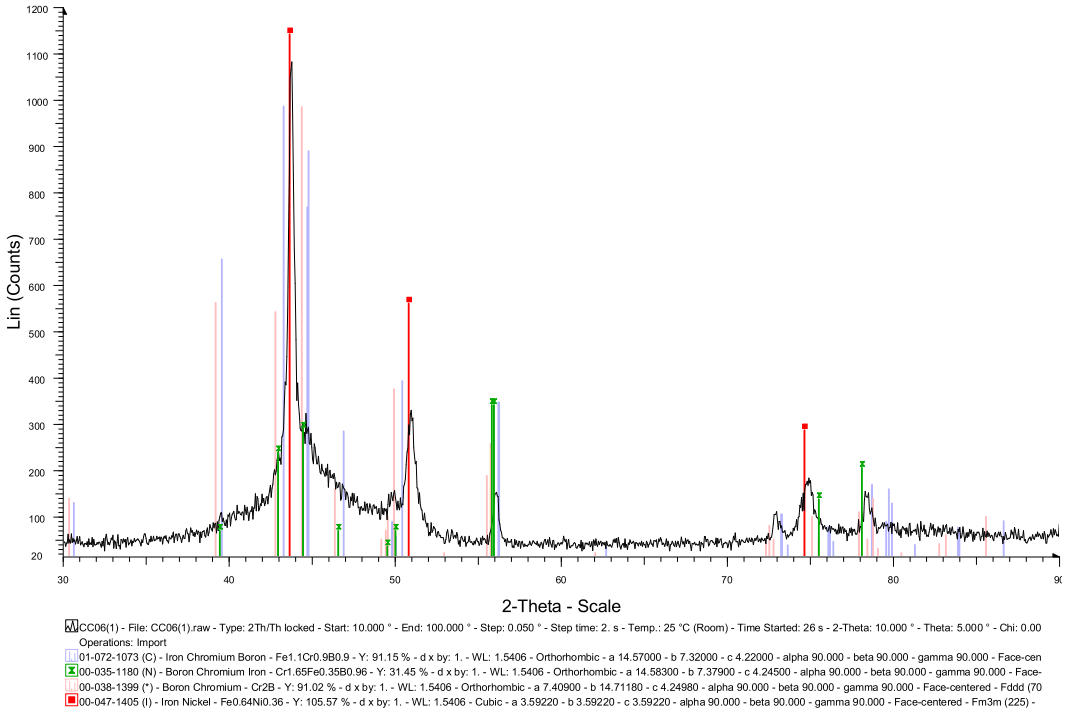

Fig. 4.27(b) Comparison of experimental XRD pattern of the as-sprayed coating with JCPDS files for Cr_2B, $Fe_{1.1}Cr_{0.9}B_{0.9}$ and $Cr_{1.65}Fe_{0.35}B_{0.96}$

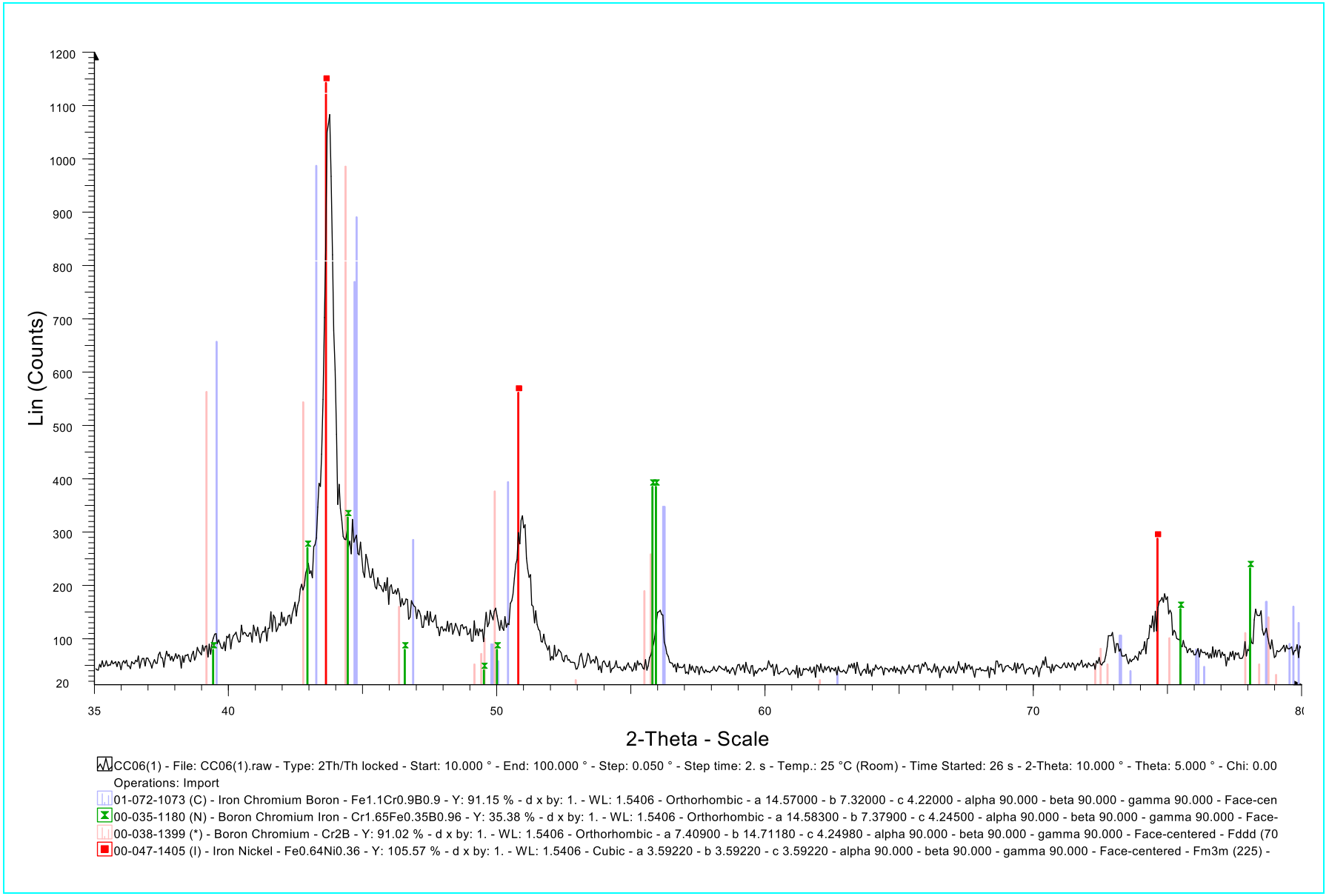

Fig. 4.27(c) Comparison of experimental XRD pattern (2θ = 35–80°) with JCPDS files for Cr_2B, $Fe_{1.1}Cr_{0.9}B_{0.9}$ and $Cr_{1.65}Fe_{0.35}B_{0.96}$.

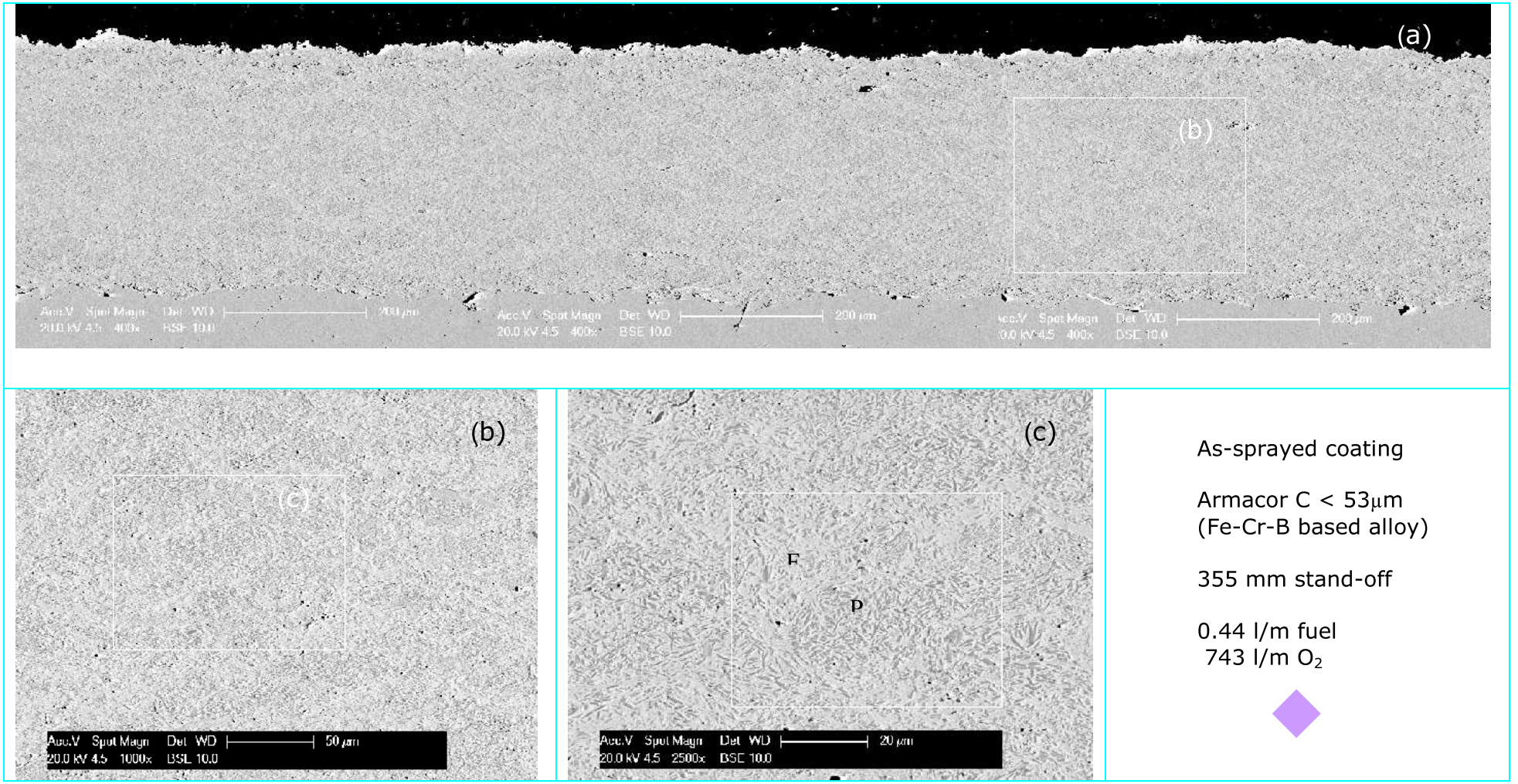

Fig. 4.28 BSE micrographs of cross-sections of a HVOF-sprayed coating: (a) low magnification unetched cross-section. (b),(c) High magnification image of the region b in (a) showing splat-like structure comprising fully melted (F) and partially melted (P) particles.

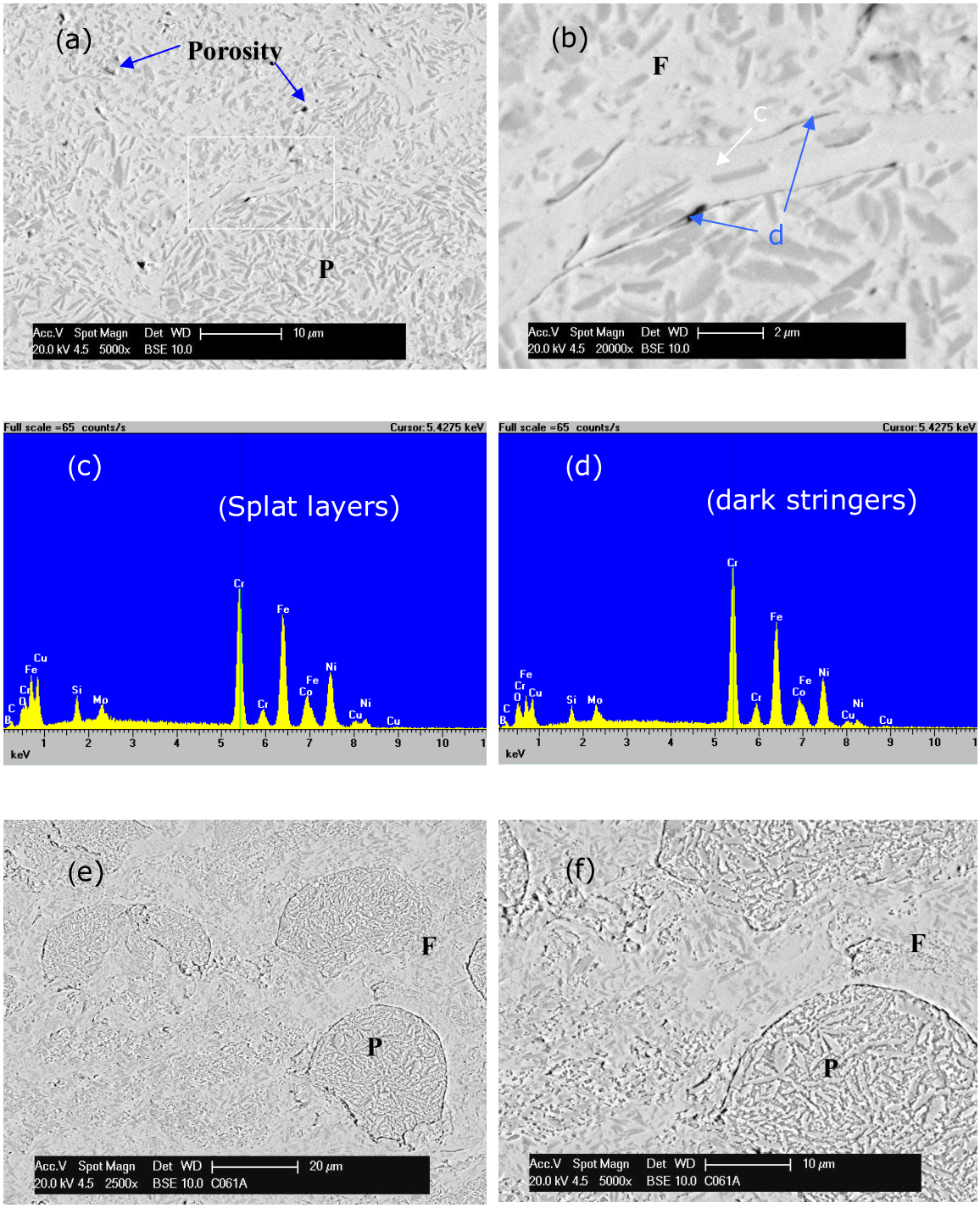

Fig. 4.29 BSE images showing cross-sections of a HVOF-sprayed coating. (a) Higher magnification image of the region P in Fig. 4.28(c) showing boride (dark region), Fe-Cr rich (bright region) and porosity. (b) Region F at higher magnification showing oxide layers. (c,d) EDX spectra of regions in image (b) arrowed c and d, respectively. (e,f) Low and high magnification of the as-sprayed coating following etching.

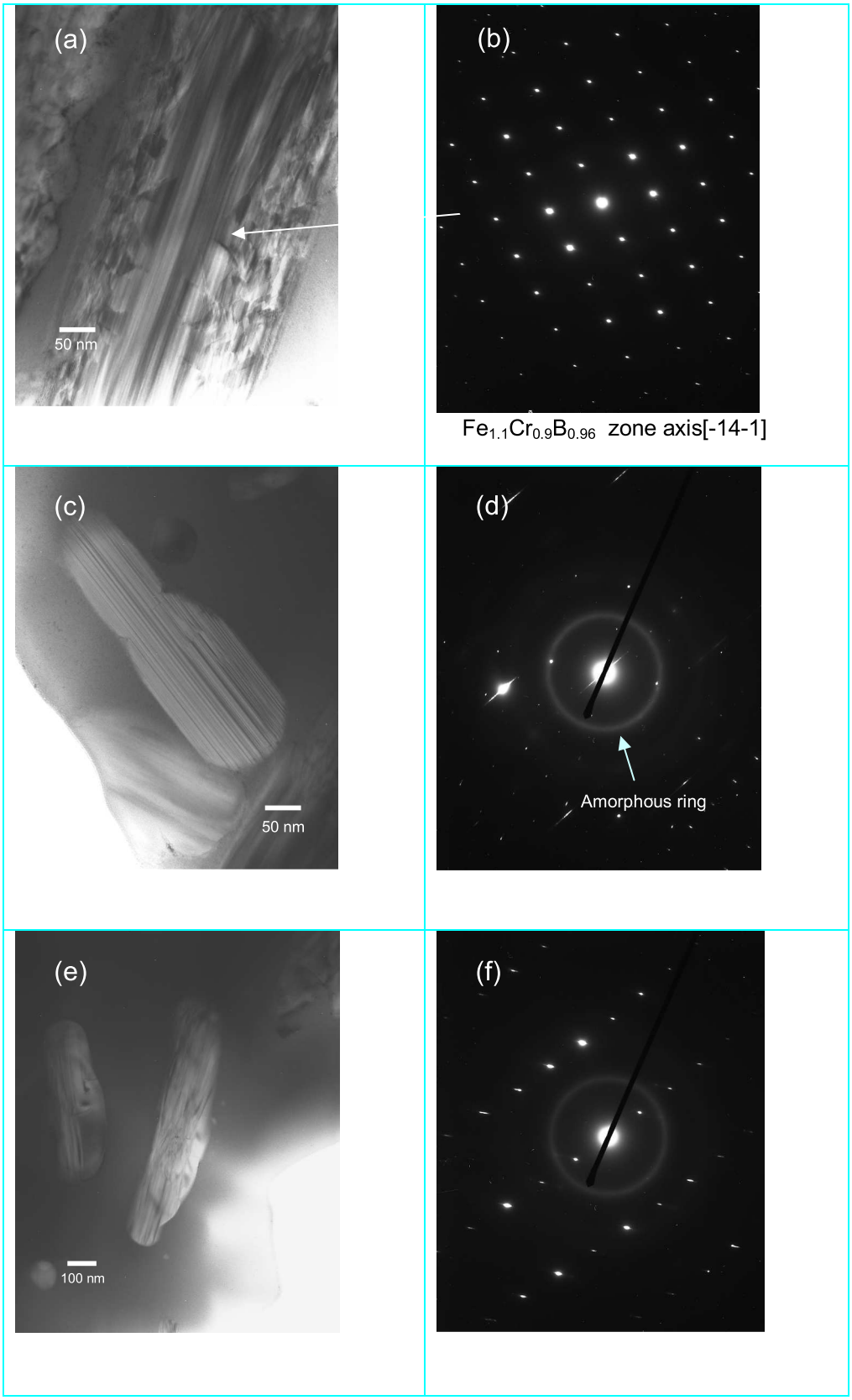

Fig. 4.30 TEM images of the as-sprayed Armacor C coating and associated diffraction patterns (a) Bright field image of partially crystalline region; (b) diffraction pattern of (a). (c,e) Bright field images of amorphous/crystalline region, (d,f) diffraction pattern of (c) and (e).

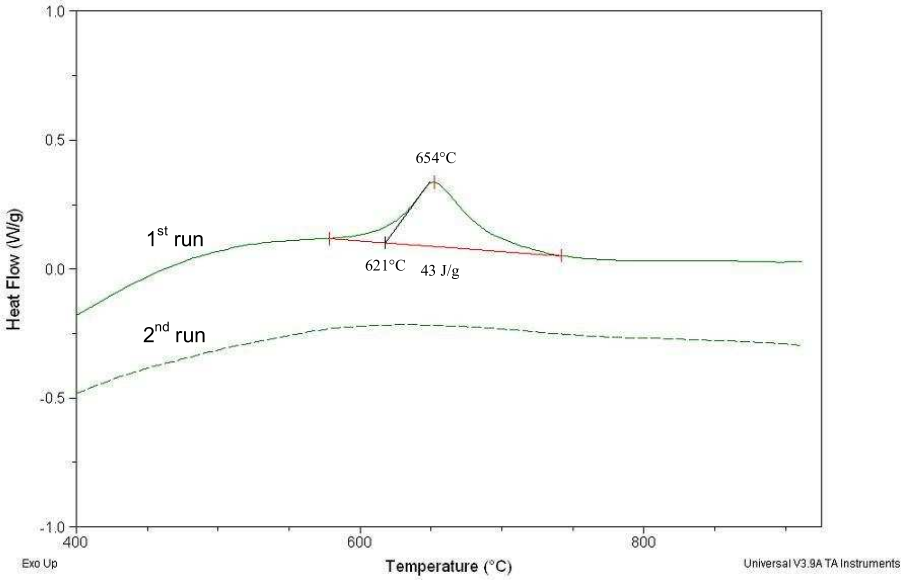

Fig. 4.31(a) DSC analysis of coating, 1st and 2nd heating runs at 20K/min.

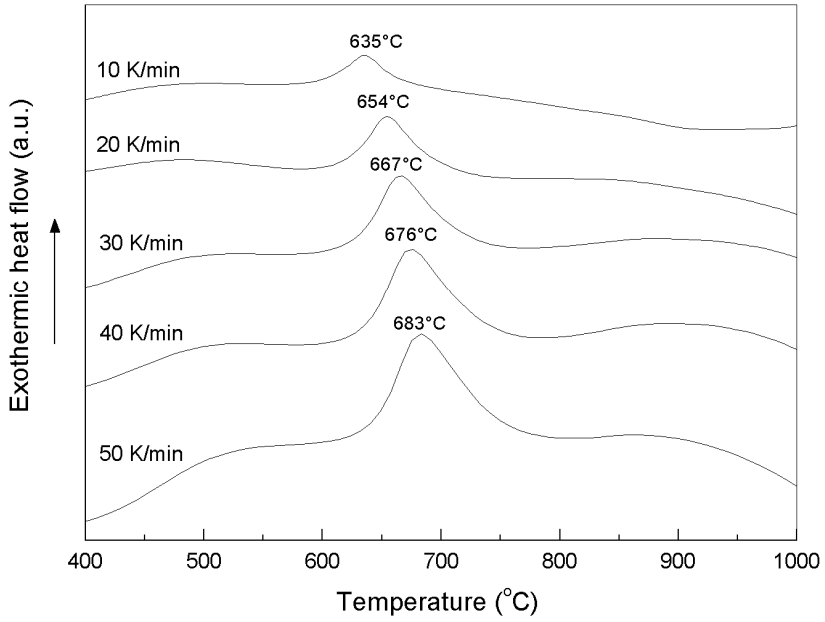

Fig. 4.31(b) DSC analysis of the Armacor C coating at heating rates 10 K/min, 20 K/min, 30 K/min, 40 K/min and 50 K/min

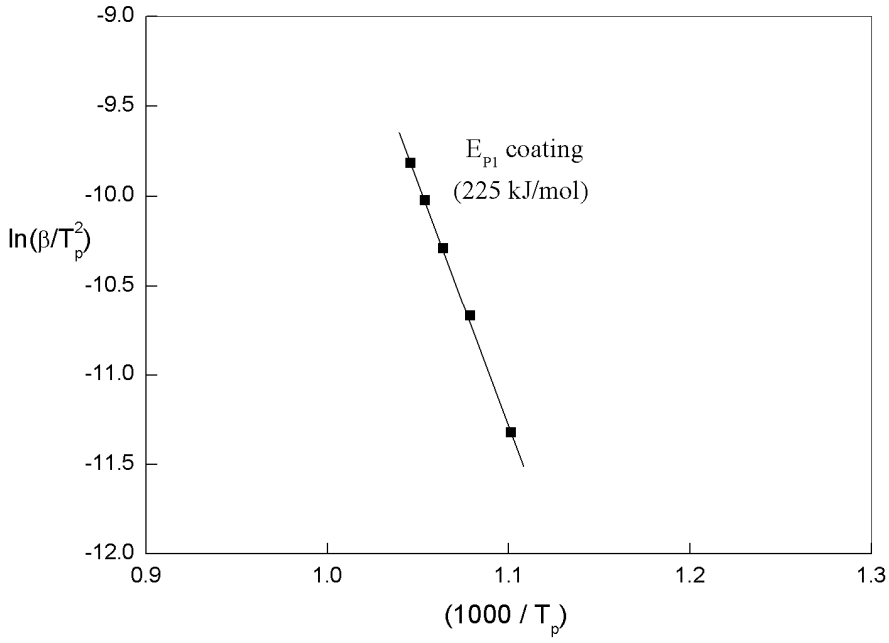

Fig. 4.32 Kissinger's plot of $\ln(\beta/T_p^2)$ versus $1000/T_p$ for peak temperature T_{p1} and T_{p2} of the as-sprayed Armacor C coating.

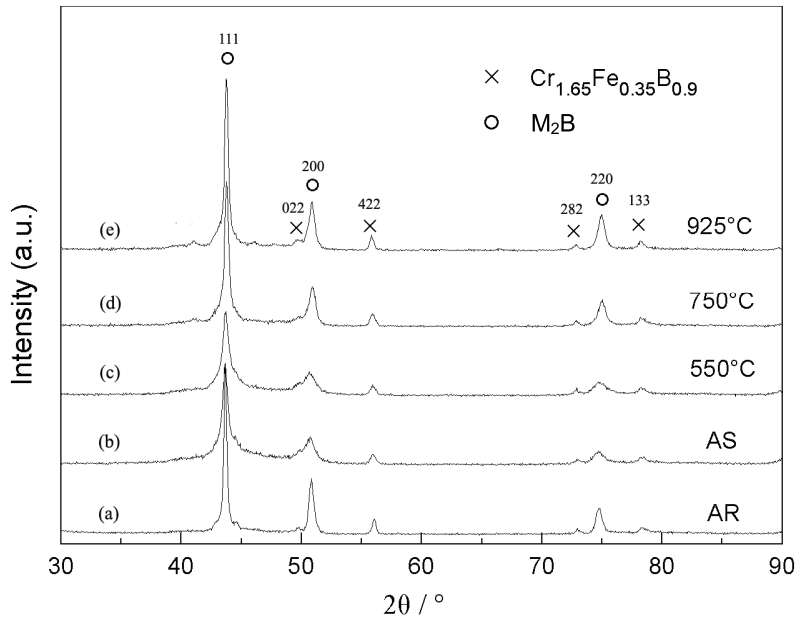

Fig. 4.33 XRD patterns of the as-received powder (AR), as-sprayed coating (AS) and the coatings following heat treatment at 550°C, 750°C and 925°C for 1 hour.

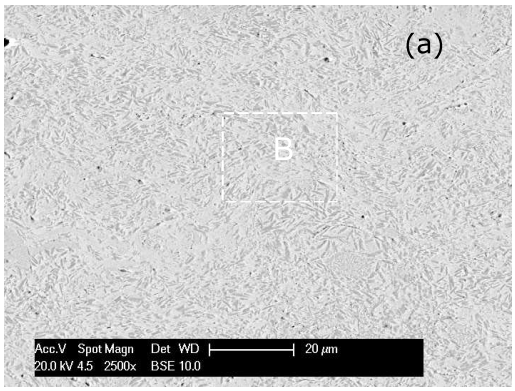

(heat treated at 550°C)

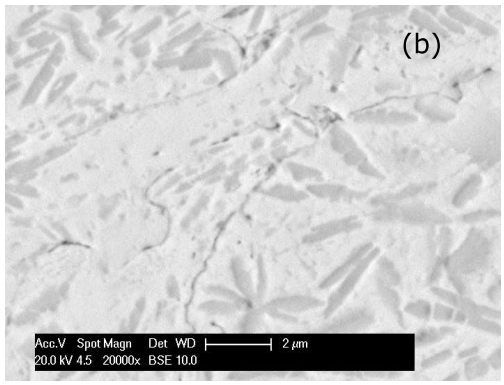

(High magnification)

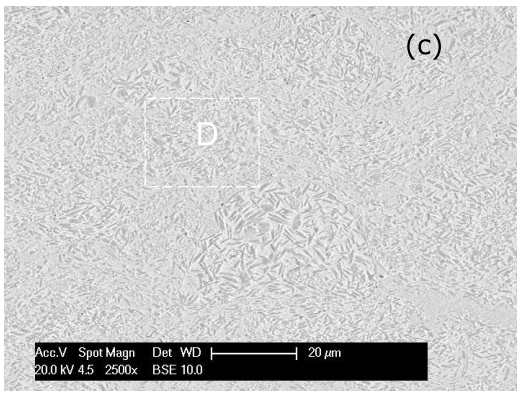

(heat treated at 750°C)

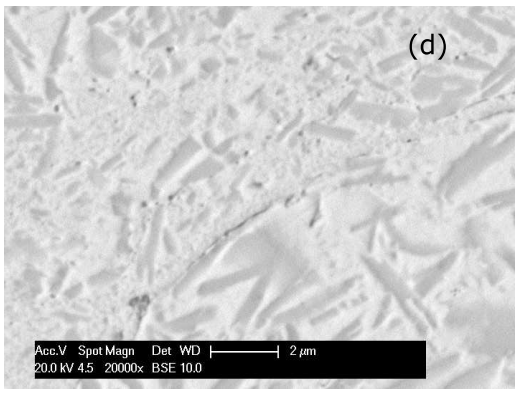

(High magnification)

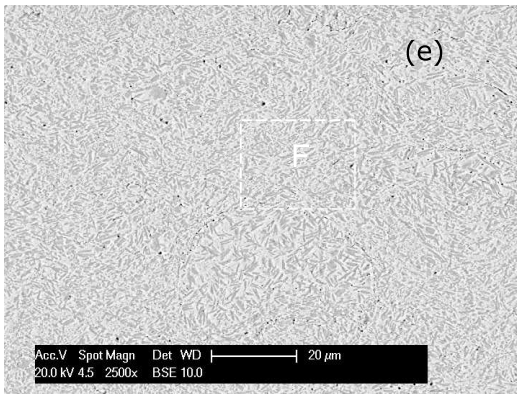

(heat treated at 925°C)

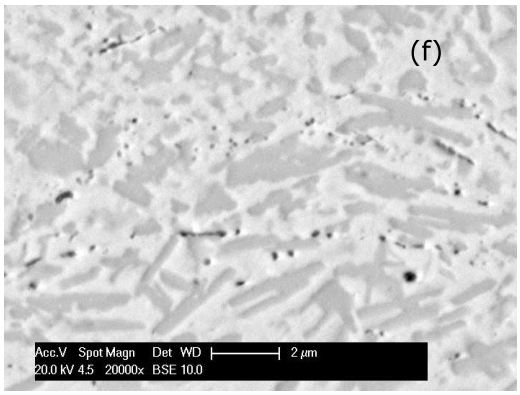

(High magnification)

Fig. 4.34 Backscattered electron micrograph of coating following heat treatment at 550°C, 750°C and 925°C (low and high magnification).

Chapter 5

Results : Microstructure evolution of Fe-Cr-B based alloy powder and coating (Nanosteel SHS7170)

In this chapter, the microstructure of gas atomised SHS7170 powder (based on the Fe-Cr-B system) used as a feedstock for HVOF spraying and as-sprayed coatings are reported. The microstructure of the powders (small particles and large particles) and the coatings were characterised by X-ray diffraction (XRD), scanning electron microscopy (SEM), utilising energy dispersive X-ray spectroscopy (EDS) and transmission electron microscopy (TEM). Differential scanning calorimetry (DSC) was conducted to analyse the thermal stability of the samples which is correlated with the activation energy of the crystallization process. The microhardness of coatings was investigated by mean of Vickers microhardness testing and these are related to their microstructural development.

5. Results: Fe-Cr-B alloy SHS7170

5.1 Powder size and composition

A commercially available powder, SHS7170, from the Nanosteel Company Inc, Providence, Rhode Island, USA, with a chemical composition determined by XRF, ICP and a combustion method is given in Table 5.1. The powder is seen to contain 4 at % C as well as ~19 at% Cr and ~16 at% B with smaller amounts of Si, Mo, Mn and W. It had a nominal size range +15 to 53 μm. The powder particle size distribution, obtained by laser diffractometry, is shown in Fig. 5.1. It is clearly seen that 10% of the powder was above 70 μm, and 10% below 22 μm with a d_{50} of 38 μm. Prior to spraying, the powder was sieved with a 45 μm sieve and after sieving the d_{10}, d_{50} and d_{90} values were 19 μm, 31 μm and 53 μm, respectively. Following sieving the volume mean particle diameter was 30 μm.

Fig. 5.2 presents the SEM image of the SHS7170 feed stock powders following sieving below 45 μm. It can be seen that the majority of the particles produced by gas atomisation are largely spherical with some elongated particles or particles with satellites also being present.

Table 5.1 The composition of the SHS7170 powder (as determined by XRF, ICP and a combustion method)

Element	Fe	Cr	B	Si	Mo	Mn	W	C
wt.%	Bal.	20.3	3.6	1.6	4.8	2.1	6.3	1.0
atom.%	Bal	18.9	16.1	2.8	2.4	1.9	1.7	4.0

5.2 Characterisation of as-received powder

XRD analysis

The XRD traces obtained from the as-received SHS7170 powder are shown in Fig. 5.3. Fig. 5.3(a) shows the presence of a bcc phase with a lattice parameter close to α – Fe (JCPDS file # 006-0696) and the boride phase $(Fe_{1.1}Cr_{0.9})B_{0.9}$ (JCPDS file # 072-1073). In addition, there is a broad diffraction halo peak appearing around 2θ = 42 – 48° indicates a proportion of amorphous structure in the sample. Figs. 5.3(b)-(c) compare indexing of the pattern with lines for Cr_2B (JCPDS file # 038-1399) and $(Fe_{1.1}Cr_{0.9})B_{0.9}$ (JCPDS file # 072-1073). The latter phase gives a better fit to peaks at 2θ = 43.2°, 50.0°, 50.4°, 56.2°, 73.1°, 78.8° and so is most probably the boride phase in the sample.

SEM analysis

Figs. 5.4(a)-(d) show BSE images of powder particle cross-sections and it is clear that the smaller particle, Fig. 5.4(a), has a featureless appearance and was presumably amorphous whereas the larger particle, Fig. 5.4(b), shows a two-phase structure with a large volume fraction of a dark-contrast, needle-like or acicular phase in a lighter contrast matrix.

Fig. 5.4(c), a higher magnification BSE image of small particles, shows clearly a featureless microstructure and a higher magnification image of large particles, Fig. 5.4(d), shows clearly a different contrast between two phases. EDX analyses of a bright area and a darker area are shown in Fig. 5.4(e) and Fig. 5.4(f), respectively. It can be seen that the bright area had a higher Fe/Cr ratio, whilst a darker area had a lower Fe/Cr ratio. Precise compositions of each phase could not be found due to the

spatial resolution of the SEM. The peak ratio of Fe to Cr for each phases were calculated from the measured intensities of EDX spot analysis and the values were obtained for comparison. It was found that the Fe/Cr peak ratio for a bright area is 1.89, whereas the Fe/Cr peak ratio for a darker area is 1.49. It is suggested that the bright matrix was the metallic bcc phase and the dark needles were the boride phase.

DSC analysis

Fig. 5.5(a) shows typical DSC curve of the powder during first and second heating runs at 20K/min. In the curve from the first heating run, two peaks appear and these correspond to two exothermic reactions, with peak temperatures of 640°C and 838°C, respectively. In the curve after the second heating run, no exothermic peak was detected at around 630°C but a small peak was present at around 830°C. It is suggested that the first peak is due to crystallization of an amorphous phase whereas the 2nd peak is from a precipitation reaction.

The DSC traces of the alloy powder obtained at five different heating rates of 10K/min to 50K/min are shown in Fig. 5.5(b). At all heating rates two exothermic peaks can be observed corresponding to the two exothermic reactions during heating the powder up to 1000°C at each different rate. The first (crystallization) reaction occurred at the temperature about 631-659 °C (peak temperatures) and the second exothermic peak occurred at higher temperatures about 821-867 °C. The values of the onset (T_x) and peak temperatures (T_p) recorded along with enthalpies (ΔH) from each peak are given in Table 5.2. The enthalpies were calculated according to the procedure in chapter 3 (method).

Table 5.2 The onset of crystallization temperatures (T_x), peak temperatures (T_p), and enthalpies of transformation (ΔH) of the as-received powder heated at different rates.

Heating rate	Onset T_x (°C)	T_{p1} (1st peak) (°C)	T_{p2} (2nd peak) (°C)	ΔH (1st peak) J/g	ΔH (2nd peak) J/g
10 K/min	623	631	821	20	25
20 K/min	631	640	838	22	26
30K/min	637	647	851	27	25
40K/min	639	655	862	22	24
50 K/min	640	659	867	22	24

Fig. 5.5(c) shows that the peak height ratios for crystallization and precipitation depend on the size range of the powder used in the analysis. Different size ranges were obtained by mechanical sieving. The crystallisation peak was heighest for the 15 to 38 μm range and smallest for +53 μm, thus suggesting that the size range containing smaller particles had a higher proportion of amorphous phase.

Using Kissinger's method (see chapter 3) and the experimental data recorded in Table 5.2, the activation energy for the reactions can be calculated from a straight line fit of a plot of $ln(\beta/T_p^2)$ versus $10^3/T_p$. The activation energies for the reactions were determined to be 375 and 333 kJ/mol for the first and second peaks, respectively as shown in Fig. 5.6.

5.3 Characterisation of heat treated powder

XRD analysis

To further investigate the thermal stability of the alloy powder, samples were annealed for 1 hour at 550°C, 650°C, 750°C and 925°C. Fig. 5.7 shows the XRD traces obtained from these experiments along with the trace from the as-received

powder (AR). It was found that there is no phase change of the powder following heat treatment at a temperature of 550°C as shown in Fig. 5.7(b).

Further heating of the powder to a temperature of 650°C, led to formation of small peaks around the region formerly regarded as the amorphous halo and the intensities of the Fe peaks and the boride phase remained almost unchanged as shown in Fig. 5.7(c).

However, after heating to a temperature of 750°C, the halo intensity decreased, the intensities of Fe peaks increased and the intensities of peaks from other phases (the boride phase, $Fe_{1.1}Cr_{0.9}B_{0.9}$) remained almost unchanged as shown in Fig. 5.7(d), suggesting that the first exothermic reaction was caused by crystallization of the amorphous matrix into α-Fe and $Fe_{1.1}Cr_{0.9}B_{0.9}$.

Additionally, when the powder was heated to a temperature of 925°C, Fig. 5.7(e), the crystallization was completed and the XRD peaks from at least three phases: α – Fe (JCPDS file # 006-0696), the boride phase $(Fe_{1.1}Cr_{0.9})B_{0.9}$ (JCPDS file # 072-1073) and a $M_{23}C_6$ type carbide (JCPDS file # 005-0721) are well defined in the corresponding X-ray diffraction pattern. During this stage, precipitation of the carbide $M_{23}C_6$ phase was the major event, although intensities of the peaks from other phases also increased.

SEM analysis

The microstructure of the SHS7170 powder has therefore been investigated using BSE imaging and EDX analysis. After heat treatment of the powder at a temperature

of 550°C, there was no detectable microstructural change in both a small particle Fig. 5.8(a) and a larger particle Fig. 5.8(b). The corresponding XRD trace is Fig. 5.7(b). Fig. 5.8(c), a higher magnification BSE image of small particles shows no evidence for crystallization in these particles. A higher magnification image of larger particles Fig. 5.8(d) shows two phases present similar to that of the as-received powder particles in Fig. 5.4(d).

BSE images of the cross-sections of small and large powder particles following heat treatment at 750°C for 1 hour are shown in Figs. 5.9(a)-(d). Fig. 5.9(a) is a low magnification BSE image showing crystallization of a small particle derived from the matrix phase, while the large powder particle in Fig. 5.9(b) shows a different contrast between a matrix phase and dark contrast of boride needle. A higher magnification BSE image of a small particle in Fig. 5.9(c) shows more detail of the crystallization products which appear < 1 μm in size and at higher magnification BSE image of a large particle Fig. 5.9(d) reveals a three phase structure made up from the remaining Fe-based matrix, the boride phase and new phase appearing as small white precipitates which could correspond to $M_{23}C_6$.

Furthermore, heating the sample to a temperature of 925°C for 1 hour, similar precipitation was observed but found to be coarser as can be seen in Fig. 5.10(a) and Fig. 5.10(b) which are low magnification BSE images of a small particle and large particles, respectively. It can be seen that significant microstructural coarsening occurred in the small diameter particle, Figs. 5.10(a) and (c), with bright, grey and dark contrast regions visible. In Fig. 5.10(d), the bright phase A has coarsered

compared to Fig. 5.9(d) whereas the dark contrast boride phase appears to have lost its plate/ needle form.

The EDX spectra of the arrowed regions A of image Fig. 5.10(d) are shown in Fig. 5.11. It is indicated that the white region arrowed A probably corresponds to the $M_{23}C_6$ carbide phase because of the high W and Mo levels.

5.4 Characterisation of Slow Cooled Solidified Powder

To help understand the underlying mechanisms of why the current material has a high glass forming ability, the melting and solidification behaviour of the SHS7170 powder was studied by continuous heating, and cooling DSC experiments in which the powder was melted, as shown in Fig. 5.12.

The DSC heating trace shows crystallization onset at 631°C, peak at T_{p1} and precipitation reaction at T_{p2} (exothermic). On further heating, a wide endothermic peak was observed at an onset temperature of 1126 °C, followed by a small peak at the high temperature ~ 1347°C. These could be due to the melting of α – Fe and possibly, at high temperature, the dissolution of carbide and /or boride phases in the melt. The critical temperatures are listed in Table 5.3.

Table 5.3 The onset of crystallization temperature T_x, the crystallization temperatures peak at T_{p1}, precipitation at T_{p2} , the melting temperature T_m , the liquidus temperature T_{liq} obtained from a DSC curve of the SHS7170 powder at a scanning rate of 20 K/min.

Heating rate	Onset T_x (°C)	T_{p1} (1st peak) (°C)	T_{p2} (2nd peak) (°C)	T_m (°C)	T_{liq} (°C)
20 K/min	631	640	838	1126	1347

During cooling, two major exothermic peaks were observed as shown in Fig. 5.12(b), a first small peak arrow indicated an onset temperature at 1334 °C which corresponds to the liquidus temperature on cooling. On further cooling a larger peak was observed on the DSC scan with a relatively high enthalpy of reaction at 1148°C. There is also a secondary peak just below 1148°C. These two exothermic peaks during cooling of the melt suggest that the SHS7170 sample has an off-eutectic composition with a primary phase forming at 1334°C and further solidification reaction at 1148°C.

Fig. 5.13 shows regions the DSC sample at increasing magnification. At low magnification Fig. 5.13(a) – 5.13(b) there are 500 μm size dark needles in a matrix. From Fig. 5.13(c) and (d) the matrix comprises a 2-phase eutectic and bright angular particles. At the highest magnification, Fig. 5.13(e) all the phases are visible and are labelled A, B, C and D. The eutectic comprises B and D. The large needles are C and the small angular particles are A. EDX analysis was performed on these phase regions and EDX spectra are shown in Fig. 5.14. Table 5.4 shows quantitative EDX analysis data for elements present (excluding the low atomic number elements boron and carbon).

Table 5.4 EDX analysis data for the elements present in the different regions in Fig. 3.13(e) (excluding B and C)

	Element (wt%)				
Regions	Fe	Cr	Mo	W	others
(A) white	17.19	22.48	22.62	37.71	
(B) light grey	60.8	25.6	4.6	6.0	3.0 (Mn)
(C) dark	45.1	45.2	2.1	5.4	2.2 (Mn)
(D) dark grey	84.5	7.3	0.7	1.4	6.1 (Si,Mn)

The bright regions arrowed B, of image Fig. 5.13(e) possibly correspond to α – Fe (high Cr) phase and the dark regions arrowed (C) could correspond to the boride phase. The intermediate grey contrast regions arrowed (D) are attributed to α – Fe (low Cr) phase, whilst the white region arrowed (A) are attributed to the carbide $M_{23}C_6$ phase type. Therefore from the DSC trace, Fig. 5.12, and the SEM/EDX observations the following possible solidification sequence when cooling at 20 K/min is proposed

$$L \xrightarrow{1148C^\circ} L + (Fe_{1.1}Cr_{0.9})B_{0.9} \xrightarrow{\sim 1130C^\circ} L + (Fe_{1.1}Cr_{0.9})B_{0.9} + M_{23}C_6$$

$$\xrightarrow{\sim 1120C^\circ} (Fe_{1.1}Cr_{0.9})B_{0.9} + M_{23}C_6 + (\alpha - Fe + \alpha' - Fe)$$

Where the α and α′ form in a eutectic reaction but are of different composition.

5.5 Characterisation of as-sprayed coating

XRD analysis

The phases present in the as-sprayed coating were determined by X-ray diffraction. The XRD trace from the as-sprayed coating, Fig. 5.15(a) shows the presence of a bcc phase with a lattice parameter close to α-Fe (JCPDS file # 006-0696) and the boride phase of $(Fe_{1.1}Cr_{0.9})B_{0.9}$ (JCPDS file # 072-1073). There has been a significant increase in the proportion of the amorphous phase as shown by a broader diffraction halo around $2\theta = 35 - 53°$ as compared with that of the as-received powder. Figs. 5.15(b)-(c) compare indexing of the pattern of the SHS7170 coating with lines for Cr_2B and $Fe_{1.1}Cr_{0.9}B_{0.9}$. The boride phase present in the coating sample could be either Cr_2B or $Fe_{1.1}Cr_{0.9}B_{0.9}$. However, since the powder appears to contain the Fe-Cr boride ($Fe_{1.1}Cr_{0.9}B_{0.9}$) then it is likely that this is also the phase in the coating.

SEM analysis

The HVOF as-sprayed coatings were characterised by SEM using BSE imaging. Fig. 5.16(a), a low magnification unetched cross-section, reveals the microstructure of the as-deposited coating. The coating is seen to be around 340 μm thick with an irregular top surface. The rough interface between the coating and mild steel substrate is due to the grit blasting of the latter prior to coating deposition. The splats from the spray process have not deformed sufficiently to fill the roughened surface in some regions, possibly suggesting a high viscosity molten material.

At higher magnification, the cross-section of the coating imaged in the BSE mode of the area (b) in Fig. 5.16(a), is shown in Fig. 5.16(b) and (c). The coatings exhibited

characteristic lamellar microstructures, with the splat layers parallel to the substrate surface as well as near spherical particles.

A BSE image of a typical region from a cross-section of coating is shown in Fig. 5.17(a). This reveals a near- spherical morphology of partially melted particles, labelled P in the coating, and some porosity is visible as a very dark contrast region, generally outside the region P. Porosity of the coating produced by this HVOF thermal spraying process is relatively low.

Fig. 5.17(b), a higher magnification BSE image of the selected area in Fig. 5.17(a), shows details of the interface between the fully melted region (F) and the partially melted particle (P). The EDX spectra obtained from the arrowed regions C and D of image Fig. 5.17(b) are shown in Fig. 5.17(c) and Fig. 5.17(d), respectively. It is indicated that the splat layers as marked (C) in Fig. 5.17(b) correspond to Fe-rich amorphous matrix phase, whereas, thin dark contrast stringers as marked (D) were enriched in oxygen relative to the matrix phase and correspond to an oxide phase.

Fig. 5.17(e) is a low magnification BSE image, following etching in a solution of 1 part HCl, 1 part HNO_3 and 1 part H_2O. The coating appears to have low overall porosity. At high magnification, greater details in the regions of unmelted or partially melted particles (labelled P) and the featureless regions (F) arising from solidified fully molten splats can be observed, Fig. 5.17(f). Unmelted or partially melted crystalline particles (labelled P) from the original powder etch strongly while the splat regions (F) exhibit a low etching response suggesting an amorphous structure.

TEM analysis

A TEM study of the SHS7170 coating was undertaken to obtain more detailed information on microstructure formation. TEM images of the as-sprayed SHS7170 coating and associated selected area diffraction patterns are shown in Fig. 5.18.

Fig. 5.18(a) is a bright field TEM micrograph from a plan view of the SHS7170 coating and reveals that the sample was composed of both amorphous and crystalline regions. The SAD pattern in Fig. 5.18(b) was taken from the region marked B and shows diffuse rings which are characteristic of an amorphous phase.

More detail of crystalline region marked C is shown in Fig. 5.18(c) and the SAD pattern in Fig. 5.18(d) taken from this region indicates that these grains were the mixture of the boride phase $(Fe_{1.1}Cr_{0.9})B_{0.9}$ (JCPDS file # 072-1073) and α – Fe (JCPDS file # 006-0696) confirming the XRD pattern for the presence of this phase.

An example of the nanocrystalline regions with grains (10-20 nm size) is shown in Fig. 5.18(e). The associated diffraction pattern Fig. 5.18(f) taken from the region in Fig. 5.18(e) indicates that these nanocrystalline grains have a bcc structure with a lattice parameter close to α – Fe (JCPDS file # 006-0696).

DSC analysis

The DSC analysis of the coating during first and second heating runs at 20K/min is shown in Fig. 5.19(a). In the curve from the first heating run, two peaks appear and these correspond to two exothermic reactions, attributable to crystallization of the amorphous phase. However, the traces show that the first peak had a well defined

shoulder to the low temperature side of the peak with an onset at ~ 535°C (the reason for this is at present unclear). The peak temperatures of crystallization and precipitation *(T_{p1}* and *T_{p2})* are 640°C and 778°C, respectively. In the curve after the second heating run, the first exothermic peak completely disappeared and the second peak was much reduced in size. This confirms that the first peak was due to the irreversible primary crystallisation of an amorphous phase in the coating sample whereas the second peak was probably caused by precipitation of boride or carbide phases in the alloy. However, it was not possible to identify a glass transition temperature from the DSC traces.

Fig. 5.19(b) shows typical DSC curves of the as-deposited SHS7170 coating obtained during continuous heating at five different heating rates (10 K/min – 50 K/min). It was found that each DSC curve exhibits two exothermic peaks. It indicates that the crystallization of the amorphous phase in the coating proceeds via a double stage of reactions. The first crystallization reaction occurring at similar temperatures to that found for the powder, about 632-660 °C (peak temperatures) correspond to the crystallization of the amorphous matrix phase. However, the traces show that this first peak had, at all heating rates, a well defined shoulder to the low temperature side of the peak. The second exothermic (higher temperature) peak occurring at about 760-810 °C could be due to the precipitation of one or more additional phases. The onset of crystallization temperatures *(T_x)*, peak temperatures *(T_p)*, and enthalpies of transformation *(ΔH)* for the SHS7170 coating at different heating rates (10K/min to 50K/min) are listed in Table 5.5. The onset temperature is taken to be when is first seen a deviation from the baseline.

Table 5.5 The onset of crystallization temperatures (T_x), peak temperatures (T_p), and enthalpies of transformation (ΔH) for the SHS7170 coating at different heating rates.

Heating rate	Onset T_x (°C)	T_{p1} (1st peak) (°C)	T_{p2} (2nd peak) (°C)	ΔH (1st peak) J/g	ΔH (2nd peak) J/g
10 K/min	535	632	760	50	25
20 K/min	541	640	778	58	16
30K/min	550	646	790	59	14
40K/min	553	653	799	57	9
50 K/min	560	660	810	49	9

Activation energies, E_a for the two reactions in the coating samples were again determined by the Kissinger method and were found to be 385 and 287 kJ/mol for the first and second peaks, respectively as shown in Fig. 5.20. It is noticed that the activation energy of the peak of crystallization for the coating (385 kJ/mol) is larger to that of the peak of crystallization for the powder (375 kJ/mol). In contrast, the activation energy of the second peak for the coating (287 kJ/mol) is much less than that of the second peak for the powder 333 kJ/mol.

The enthalpy of reactions, *(ΔH)* was also determined using DSC, and the values are given in Table 5.5. It can be noticed that the enthalpy of the total reaction (shoulder plus main peak) of the first reaction (49-59 J/g) are more than 2.0 times higher than that of the second reaction (9-25 J/g).

5.6 Characterisation of heat treated coating

XRD analysis

Fig. 5.21 shows the XRD traces for the as-received powder (AR), as-sprayed coating (AS) and the coatings following heat treatment for 1 hour at 550°C, 650°C, 750°C and 925°C. At a temperature of 550°C, the XRD trace Fig. 5.21(c) shows the formation of small peaks at 2θ = 42.8°, around the region formerly the amorphous halo, indicating perhaps the first sign of crystallization. Heat treatment of the coating at a temperature of 650°C, led to small increase in the intensities of Fe peaks and formation of more distinct boride phase peaks. Heat treatment at a temperature 750°C, led to a further increase in the intensities of Fe peaks and the presence of a number of new peaks in the XRD trace was clearly identified. These peaks could be indexed as $M_{23}C_6$ and are additional to peaks from the boride phase.

When the coating was heated to a temperature of 925°C for one hour, the crystallization was completed and the XRD peaks from at least three phases: α-Fe (JCPDS file # 006-0696), the boride phase $(Fe_{1.1}Cr_{0.9})\ B_{0.9}$ (JCPDS file # 072-1073) and $M_{23}C_6$ type carbide (JCPDS file # 005-0721) were well defined on the corresponding x-ray diffraction pattern, Fig. 5.21(f). During this stage, precipitation of the carbide $M_{23}C_6$ phase was the major event, although intensities of the peaks from other crystalline phases also increased.

SEM analysis

Figs. 5.22(a)-(f) show BSE images of cross-sections of the coatings following heat treatment for 1 hour at 550°C, 750°C and 925°C. In Fig. 5.22(a), from the sample annealed at 550°C, there was no microstructural change of the coating that could be

resolved. Fig. 5.22(b), a higher magnification BSE image of selected area boxed (B) in Fig. 5.22(a) shows clearly that the presence of micron sized borides, probably produced during spray deposition.

The microstructural change after heat treatment of the coating at 750°C for 1 hour is shown in Fig. 5.22(c). Fig. 5.22(d) a higher magnification BSE image of the selected area boxed (D) in Fig. 5.22(c) shows a three phase structure made up from a remaining Fe-based matrix (light grey), boride phase (dark grey) and new phase formed of small white particles with could correspond to $M_{23}C_6$.

At the highest heat treatment temperature of 925°C, the white phase appeared to be coarser than that found at 750°C. Fig. 5.22(e) shows a low magnification BSE image of the coating. Fig. 5.22(f) a higher magnification BSE images of a selected area (F) in Fig. 5.22(d). The EDX spectra and analysed data of the arrowed regions A of image Fig. 5.22(f) are shown in Fig. 5.23. It is indicated that the white region arrowed A are attributed to the carbide $M_{23}C_6$ phase type because of the high W and Mo levels.

5.7 Microhardness

One set of heat treatments was performed for a fixed time of 60 minutes at the following temperatures: 550, 650, 750 and 925°C. A second set of heat treatments was performed at only two temperatures, namely 650 and 750°C, with holding times of 60 to 3900 minutes at 650°C and 20 to 120 minutes at 750°C. Microhardness data for the as-sprayed coating and following heat treatment at 550°C, 650°C, 750°C and 925°C for 1 hour are listed in Table 5.6 (using a load of 1.96 N).

Table 5.6 Hardness (GPa) of the as-deposited and samples heat treated for 1 hour

Sample	As-deposited	550°C	650°C	750°C	925°C
Hardness / GPa	9.2	9.1	10.9	11.7	9.2
Standard deviation	0.3	0.4	0.6	0.2	0.5
Standard error	0.1	0.1	0.2	0.1	0.2

The results show that as the temperature increased up to 550°C, the hardness of the coating decreased somewhat and gradually increased to 10.9 GPa at temperature 650°C and reached a maximum at a temperature 750°C. However, after increasing the temperature up to 925°C, the hardness decreased to 9.2 GPa. It is suggested that the drop in the hardness of the coating could be due to microstructural coarsening of the phases formed in the sample.

Following a second set of heat treatments, the temperature of 750°C was firstly selected as the heat treatment temperature for this condition (as the hardness reached a maximum at this temperature for the first set of heat treatments). Microhardness data of the coatings heat treated at 750°C with standard deviation and standard error for the different holding times are shown in Table 5.7.

Table 5.7 Hardness (GPa) of the heat treated samples at temperature 750°C with different holding times

Sample	20 min	40 min	60 min	80 min	100 min	120 min
Hardness / GPa	11.1	11.3	11.7	11.2	10.7	10.4
Standard deviation	0.2	0.3	0.2	0.3	0.2	0.2
Standard error	0.1	0.1	0.1	0.2	0.1	0.1

The effect of the holding times on the hardness of the coating is also summarized in Fig. 5.24. It can be seen that the highest hardness was obtained at a holding time of

60 min. For longer times, the hardness of the coating decreased somewhat. Hardness values of the coatings heat treated at 650°C with standard deviation for the different holding times are listed in Table 5.8.

Table 5.8 Hardness (GPa) of the heat treated samples at temperature 650°C with different holding times

Sample	60 min	600 min	2280 min	3900 min
Hardness / GPa	10.9	11.3	12.4	11.3
Standard deviation	0.6	0.3	0.4	0.5
Standard error	0.2	0.1	0.1	0.2

From Table 5.8, it is observed that with increasing holding times from 60 min to 600 min, the hardness gradually increased from 10.9 GPa to 11.3 GPa and reached a maximum at 2280 min with a value of 12.4 GPa which is the highest hardness of the heat treated coating in this experimental work. However, after this period the hardness decreased somewhat to 11.3 GPa, at a period of 3900 min. Fig. 5.25 shows the dependence of the hardness of the heat treated coating on the holding times at temperature of 650°C and 750°C. It can be seen that the maximum hardness tend to increase when the sample was heat treated at lower temperature such as 650°C in this case.

5.8 Microstructure of coating heat treated at 650°C

The microstructural changes in the coating following heat treatment at a temperature 650°C was also investigated by XRD and SEM. Fig. 5.26 shows XRD patterns of the coatings heat treated at 650°C with different holding times. It was found that there is

no phase change of the coating after heat treatment at temperatures of 650°C for 1 hour as shown in Fig. 5.26(c).

However, after heating at a temperature of 650°C for 10 hours, small peaks are seen around the region formerly the amorphous halo and the intensities of Fe peaks increased as shown in Fig. 5.26(d).

On further heating of the coating at a temperature of 650°C for 38 hours, the intensities of the Fe peaks increased and peaks from the other phases formed in the sample (the boride phase $Fe_{1.1}Cr_{0.9}B_{0.9}$ (JCPDS file # 072-1073) and a $M_{23}C_6$ type carbide (JCPDS file # 005-0721) also gradually increased as shown in Fig. 5.26(e).

Heat treatment of the coating at a temperature of 650°C for 65 hours, led to a further increase in the intensities of α - Fe phase peaks and the peaks from the other phases formed in the sample (the boride phase $Fe_{1.1}Cr_{0.9}B_{0.9}$ and a $M_{23}C_6$ type carbide, as shown in Fig. 5.26(f).

The microstructure of the coating heat treated at 650°C for 1 hour closely resembles the structure of the coating heat treated at 550°C with no detectable change in the microstructure as shown in Fig. 5.27(a) and Fig. 5.27(b), higher magnification BSE image of selected area boxed B.

After heat treatment at 650°C for 10 hours, precipitation of fine particles derived from the amorphous matrix phase occurred as shown in Fig. 5.27(c) and Fig. 5.27(d).

On heating to 650°C for 38 hours, a further increase in a number and fraction of particles as can be seen in Fig. 5.27(e). Extending heat treatment at 650°C to 65 hours produced only a slight further coarsening of precipitated phases formed in the sample as shown in Fig. 5.27(g) and (h).

5.9 Summary (SHS7170)

(1) Gas atomised Fe-18.9 at.%Cr-16.1at.%B-4.0 at.%C-2.8at.%Si-2.4 at.%Mo-1.9 at.%Mn-1.7at.%W powder ($Fe_{52}Cr_{19}Si_3Mo_2W_2Mn_2B_{16}C_4$) contains a mixture of amorphous and crystalline powder particles with crystalline phases α-Fe and $Fe_{1.1}Cr_{0.9}B_{0.9}$. The microstructure of the HVOF sprayed coatings is composed of splat-like regions arising from rapid solidification of fully molten powder and near-spherical/deformed spherical regions which come from partially melted powder and having a microstructure retained from the original powder feedstock material.

(2) The predominant phases present in the as-sprayed SHS7170 coating, as identified by XRD are a bcc α-Fe matrix and boride. TEM reveals that the Fe-matrix is composed of areas of amorphous and crystalline regions with crystalline grain sizes ranging from ~ 200 nm to 20 nm.

(3) DSC analysis of powder and coating samples reveals that, in both of these, devitrification proceeds by a two stage process with pronounced peaks at approximately 640 and 840 °C for the powder and 640 and 780 °C for the coating. The apparent activation energies for reactions were calculated from DSC data using Kissinger peak shift equations. The activation energy for the first peak was found to be higher than the second. The higher activation energy for the first peak of reaction corresponds to the energy required for crystallization of amorphous Fe-based matrix phase whereas the lower activation energy for the second peak of reaction is correspond to the energy required for precipitation of boride and/or carbide $M_{23}C_6$ phases.

(4) The heat treated SHS7170 coating shows a significantly higher hardness than the as-sprayed coatings (~9.0 GPa). After annealing at temperature 650°C and with a holding time of 2280 min the annealed coating sample exhibits the highest hardness (~12.4 GPa) of all the annealed SHS7170 coatings studied in this work. The greater hardness of the sample could be due to a number of factors including the presence of a greater proportion of nanocrystalline precipitated boride or carbide phases.

Result: Fe-Cr-B alloy SHS7170

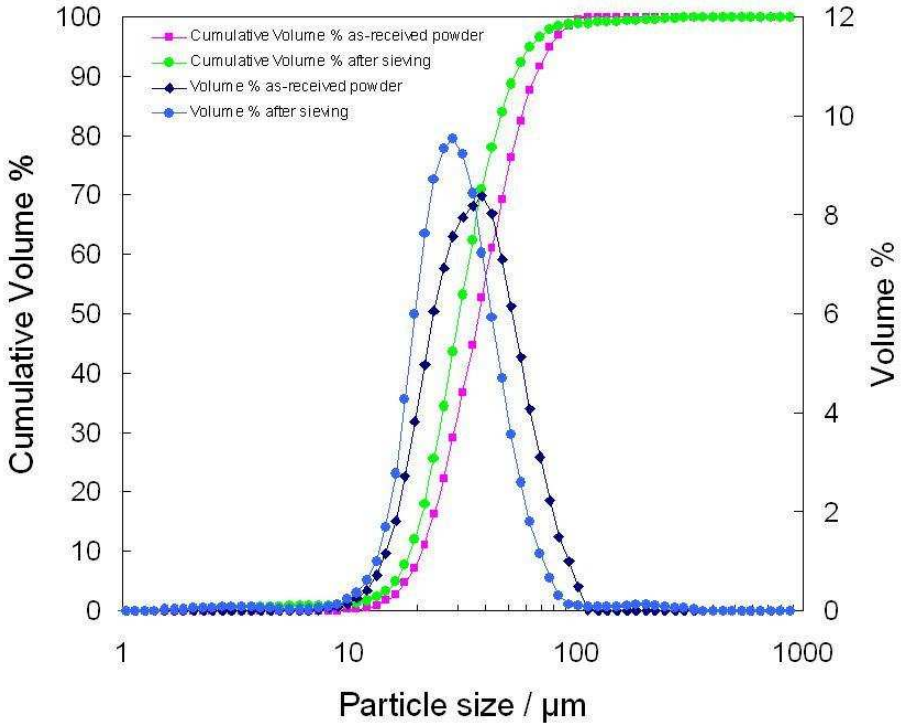

Fig. 5.1 Plot of powder distribution and cumulative vol % versus particle size for SHS7170 powder both as-received and after sieving.

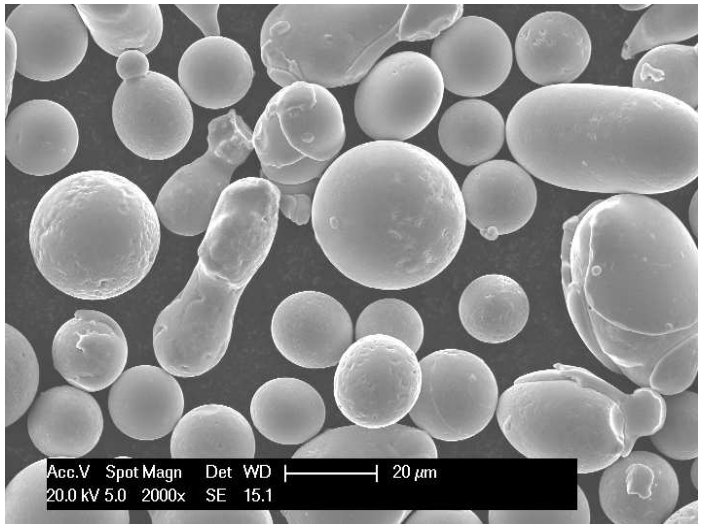

Fig. 5.2 The external morphology of the SHS7170 powder after sieving.

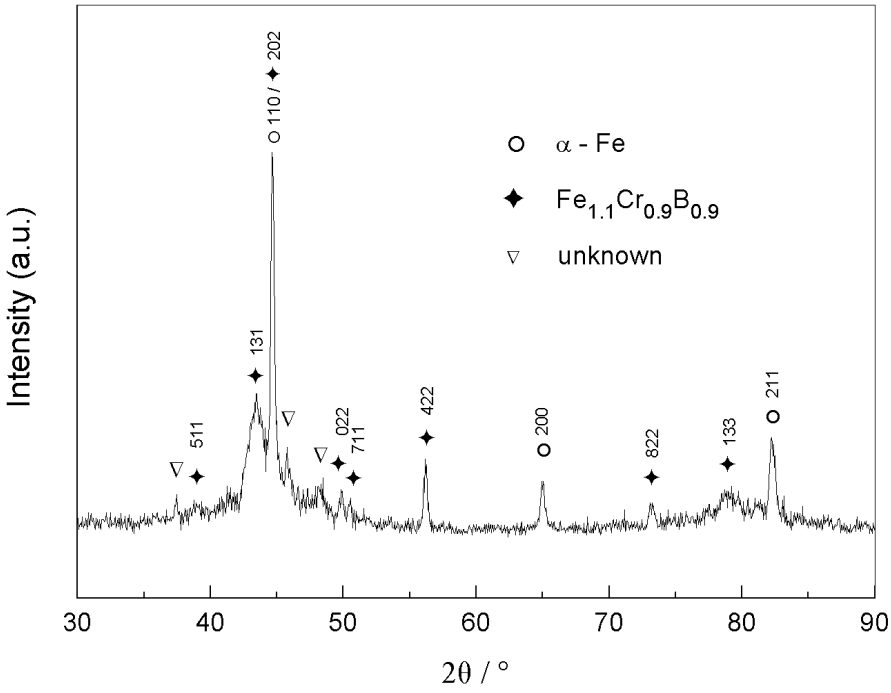

Fig. 5.3(a) XRD pattern of the as-received powder.

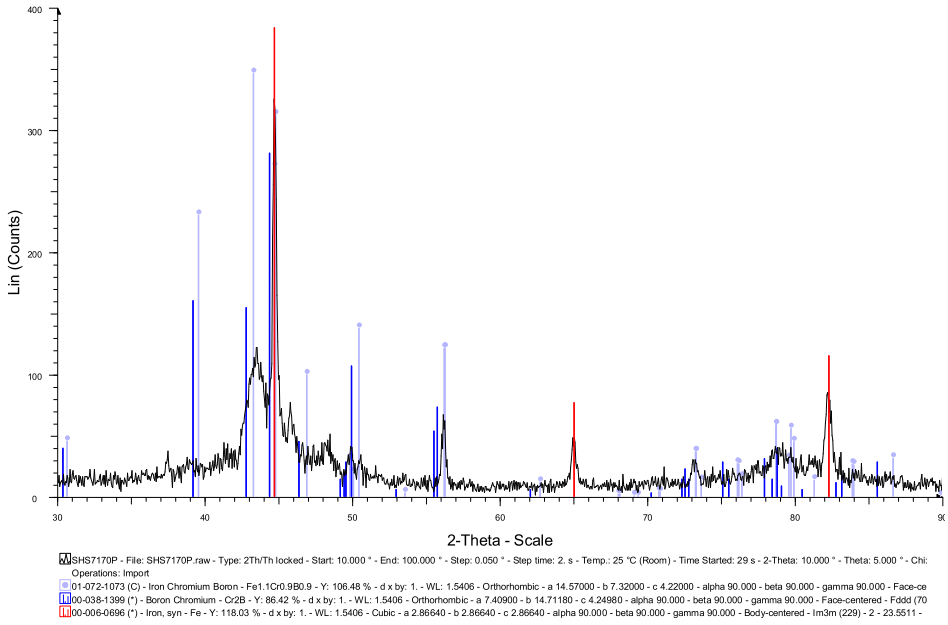

Fig. 5.3(b) Comparison of experimental XRD pattern with JCPDS files for Cr_2B and $Fe_{1.1}Cr_{0.9}B_{0.9}$.

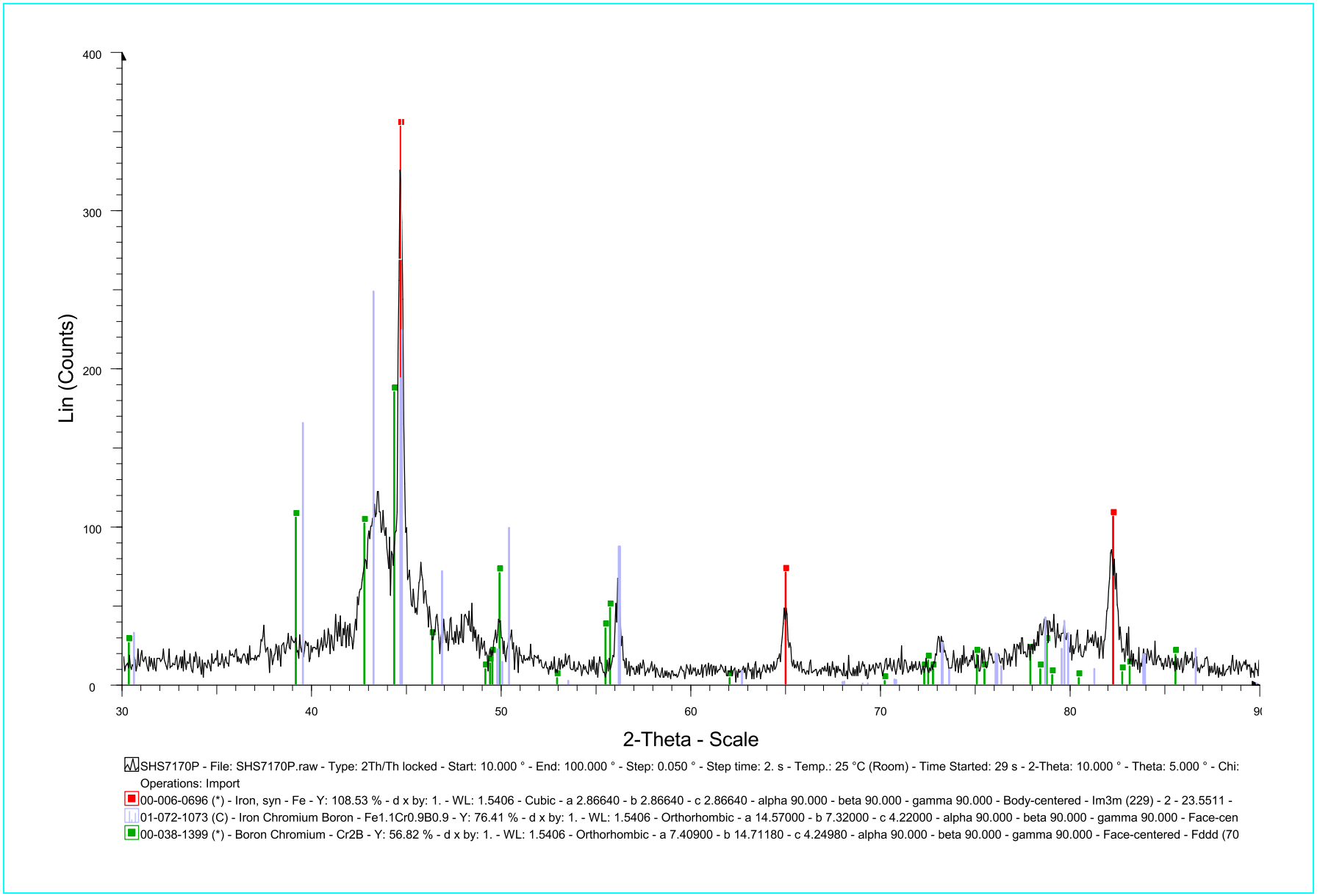

Fig. 5.3(c) Comparison of experimental XRD pattern (2θ = 30–90°) with JCPDS files for Cr_2B and $Fe_{1.1}Cr_{0.9}B_{0.9}$.

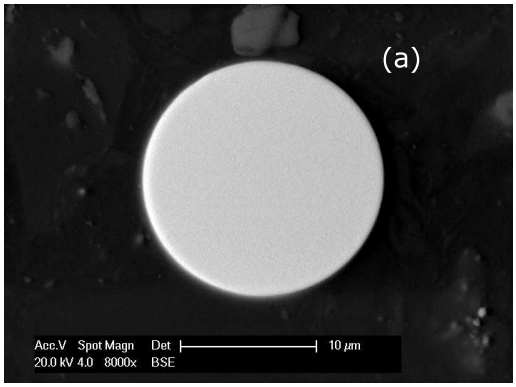

Fig. 5.4(a)

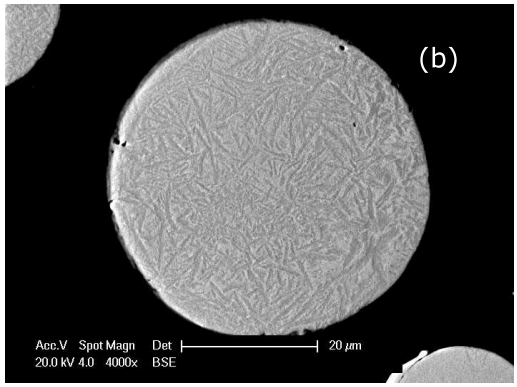

Fig. 5.4(b)

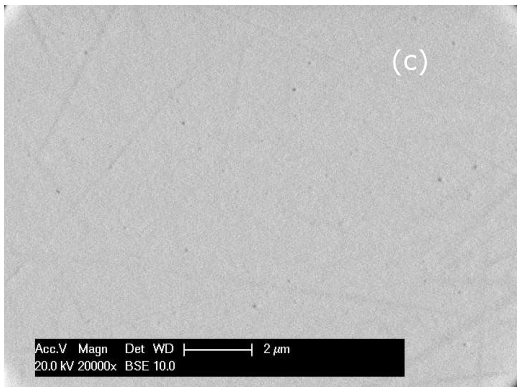

Fig. 5.4(c)

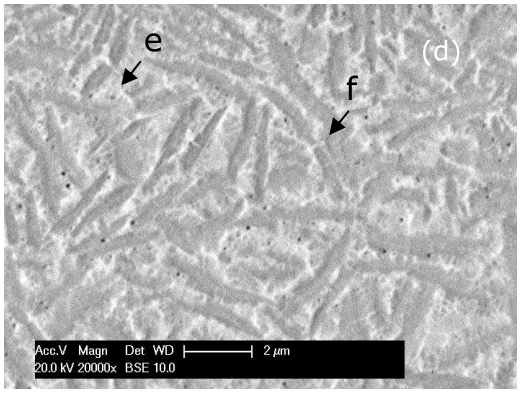

Fig. 5.4(d)

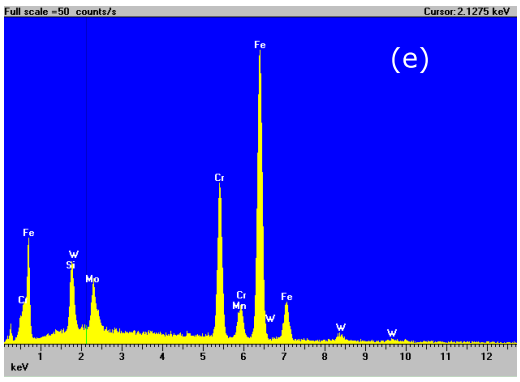

Fig. 5.4(e)

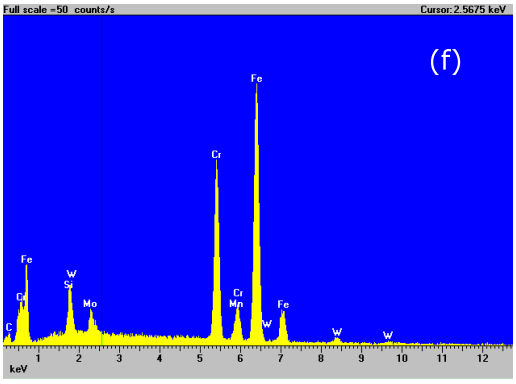

Fig. 5.4(f)

Fig. 5.4 BSE images of the cross-section of a small particle (a) and a large particle (b). (c,d) Higher magnification of regions in images (a) and (b). (e,f) EDX spectra of regions in (d) arrowed e and f, respectively.

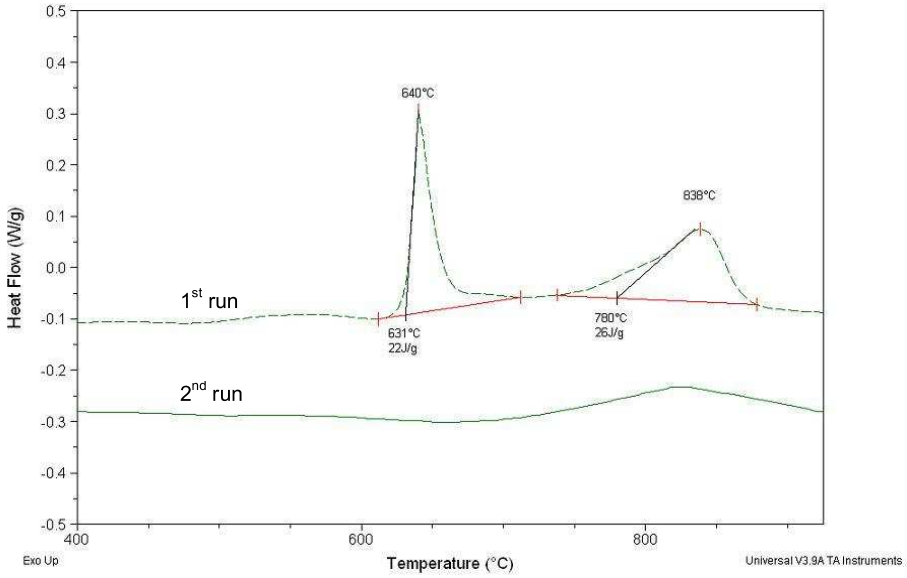

Fig. 5.5(a) DSC analysis of powder, 1st and 2nd heating runs at 20K/min.

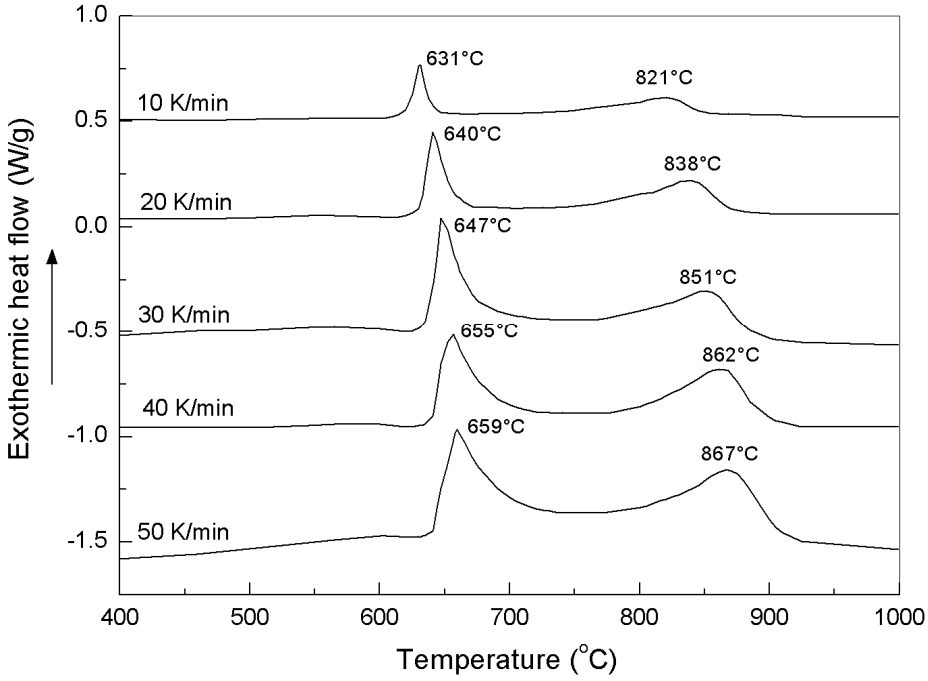

Fig. 5.5(b) DSC analysis of the as-received powder at heating rates 10 K/min, 20 K/min, 30 K/min, 40 K/min and 50 K/min.

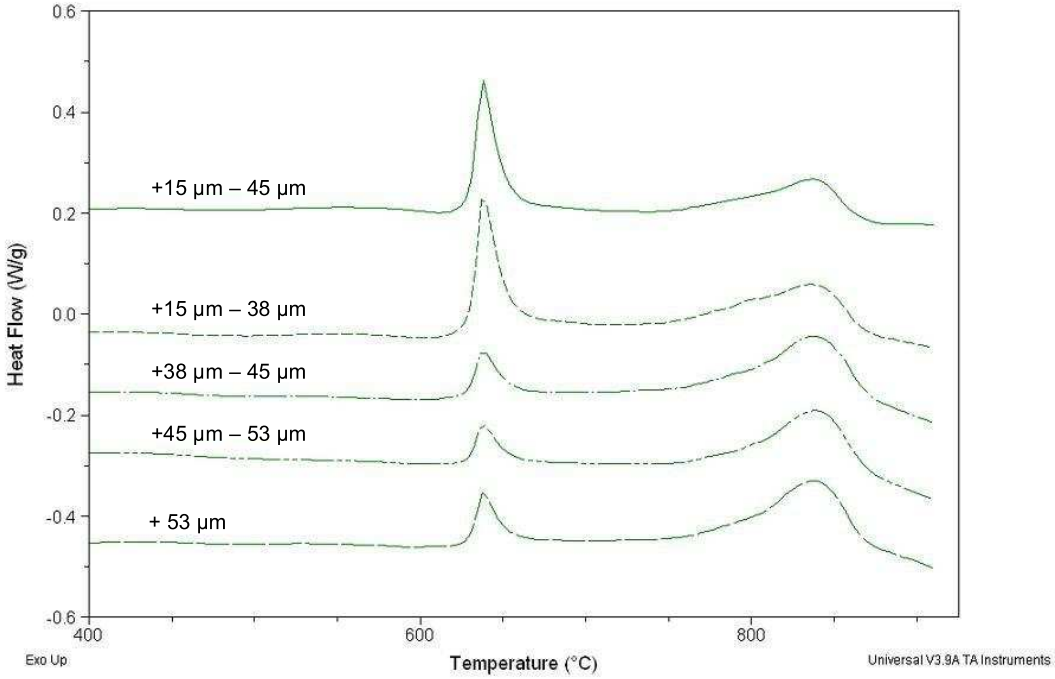

Fig. 5.5(c) DSC analysis of the different size of SHS7170 powder at heating rate 20 K/min.

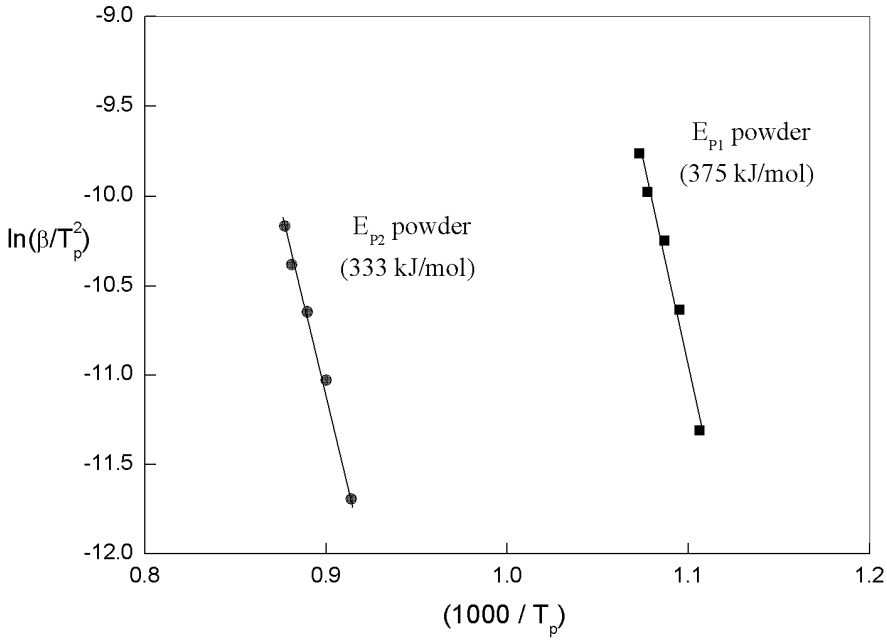

Fig. 5.6 Kissinger's plot of $\ln(\beta/T_p^2)$ versus $1000/T_p$ for peak temperature T_{p1} and T_{p2} of the SHS7170 powder.

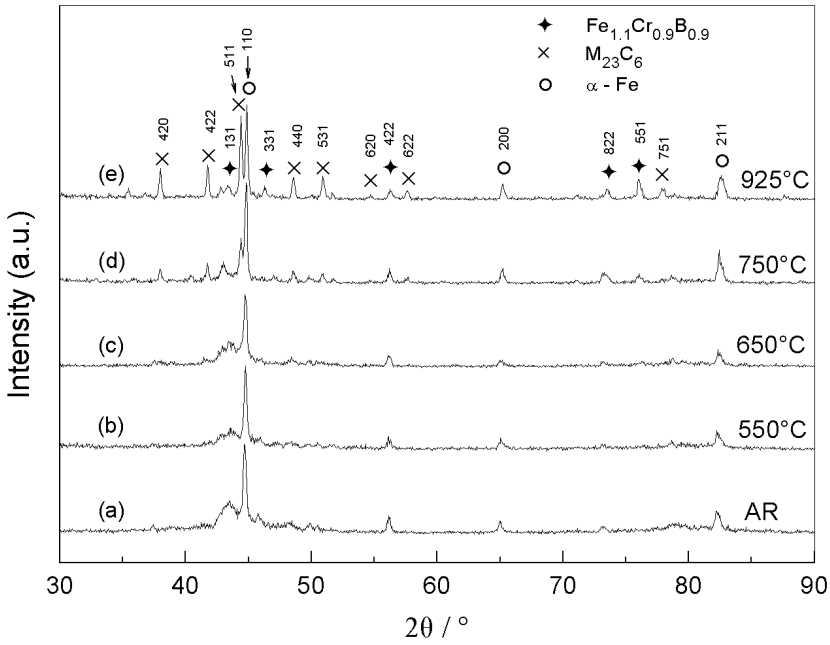

Fig. 5.7 XRD patterns for the heat treated powder at 550°C, 650°C, 750°C and 925°C for 1 hour.

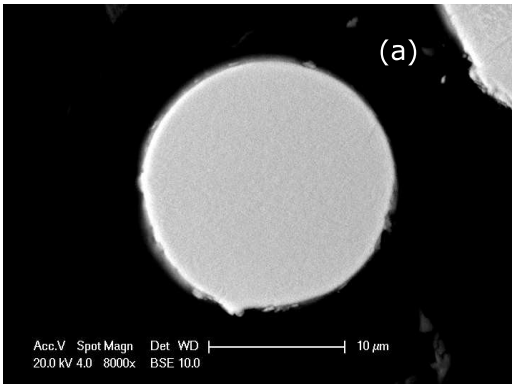

Fig. 5.8(a) Fine particle at 550°C

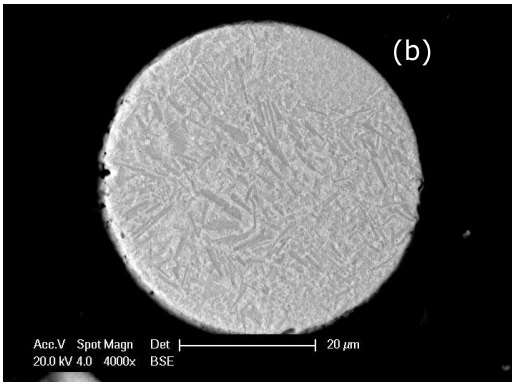

Fig. 5.8(b) Coarse particle at 550°C

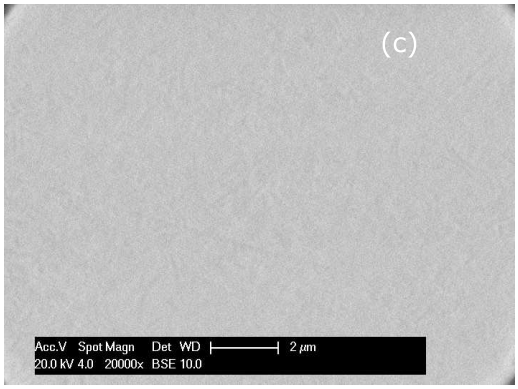

Fig. 5.8(c) Fine particle (high magnification)

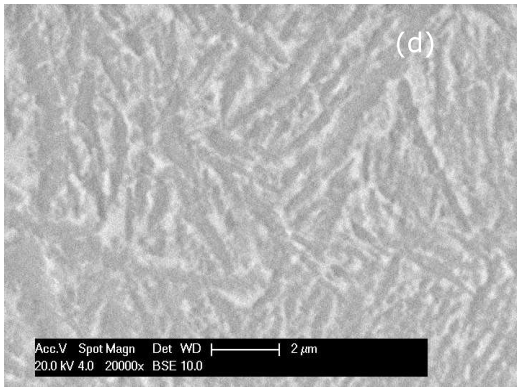

Fig. 5.8(d) Coarse particle (high magnification)

Fig. 5.8 Backscattered electron micrograph of the cross-section of a small particle Fig. 5.8(a) and a large particle Fig. 5.8(b) after heat treatment at 550°C (low magnification) and at high magnification Fig. 5.8(c) and 5.8(d).

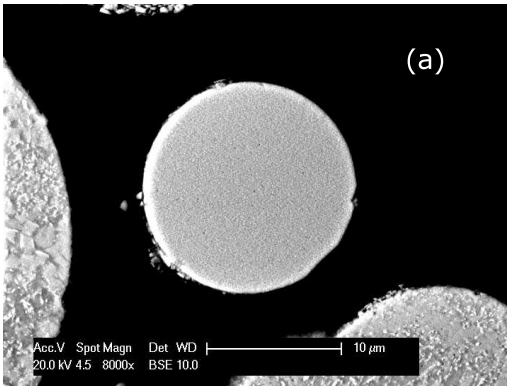

Fig. 5.9(a) Fine particle at 750°C

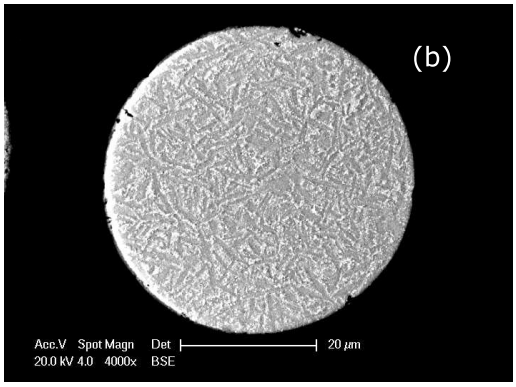

Fig. 5.9(b) Coarse particle at 750°C

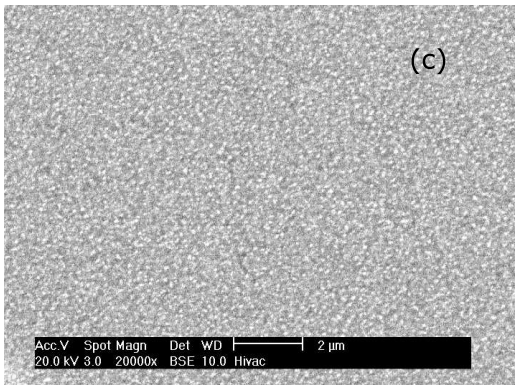

Fig. 5.9(c) Fine particle (high magnification)

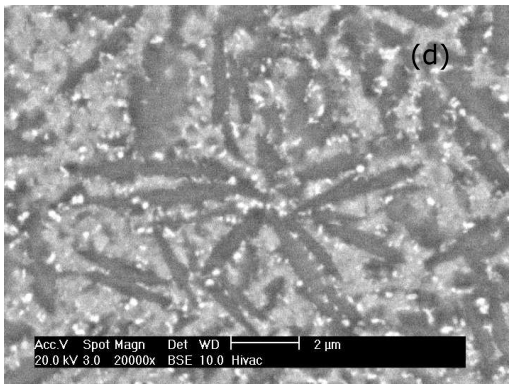

Fig. 5.9(d) Coarse particle (high magnification)

Fig. 5.9 Backscattered electron micrograph of the cross-section of a small particle Fig. 5.9(a) and a large particle Fig. 5.9(b) after heat treatment at 750°C (low magnification) and at high magnification Fig. 5.9(c) and 5.9(d).

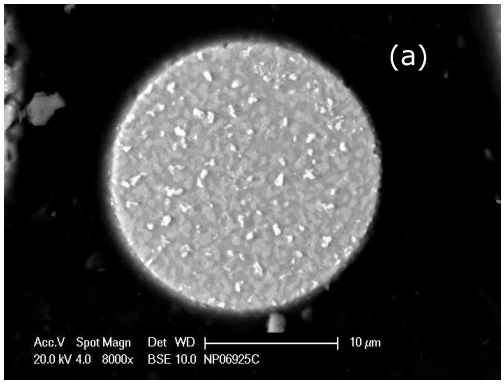

Fig. 5.10(a) Fine particle at 925°C

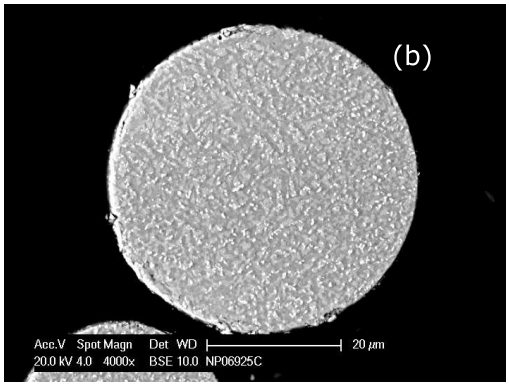

Fig. 5.10(b) Coarse particle at 925°C

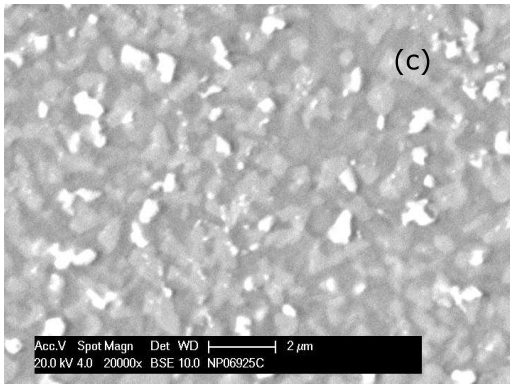

Fig.5.10(c) Fine particle (high magnification)

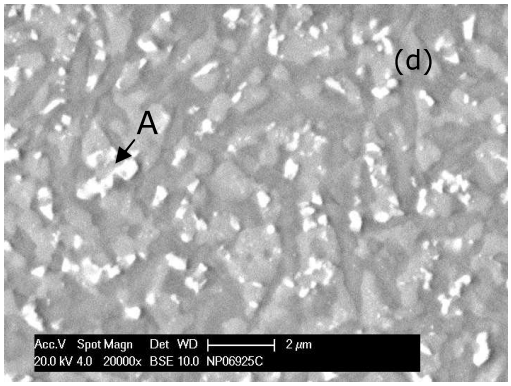

Fig.5.10(d) Coarse particle (high magnification)

Fig. 5.10 Backscattered electron micrograph of the cross-section of a small particle Fig. 5.10(a) and a large particle Fig. 5.10(b) after heat treatment at 925°C (low magnification) and at high magnification Fig. 5.10(c) and 5.10(d).

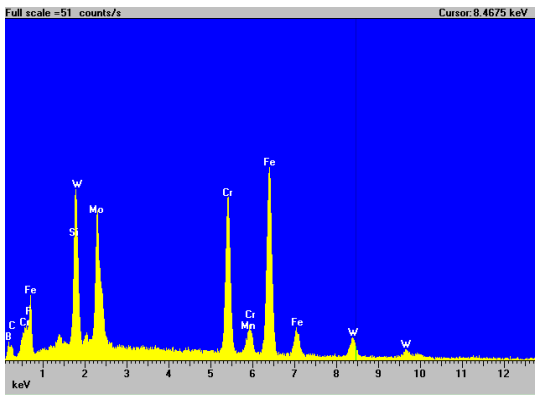

Fig. 5.11 EDX spectra of regions, arrowed A in Fig. 5.10(d)

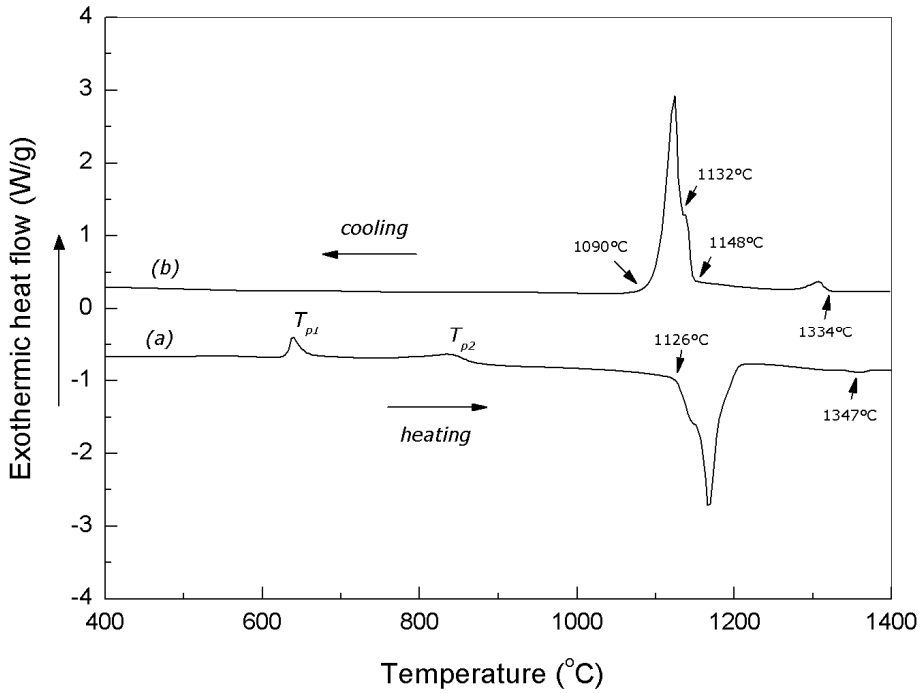

Fig. 5.12 The DSC heating (a) and cooling (b) scans for the as-received SHS7170 powder obtained at a scanning rate of 20 K/min

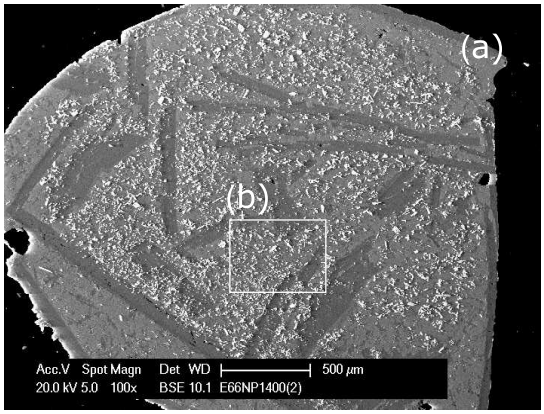

Fig. 5.13(a)

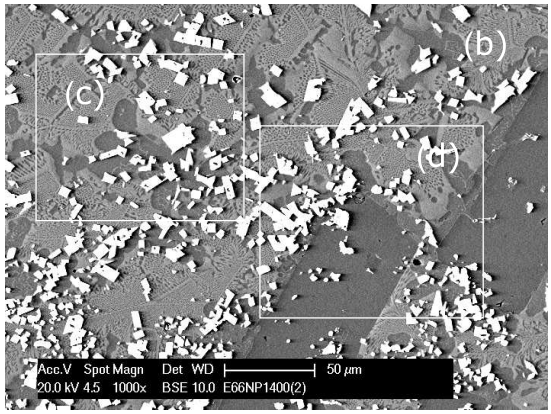

Fig. 5.13(b)

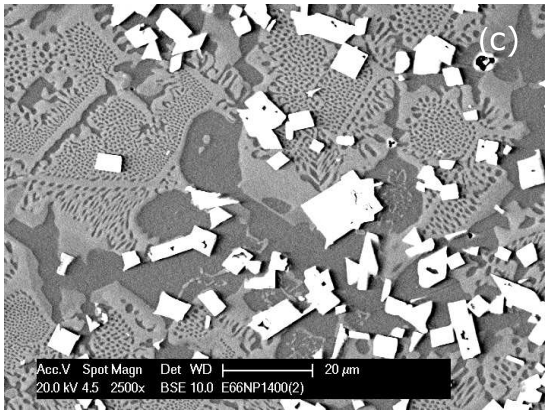

Fig. 5.13(c)

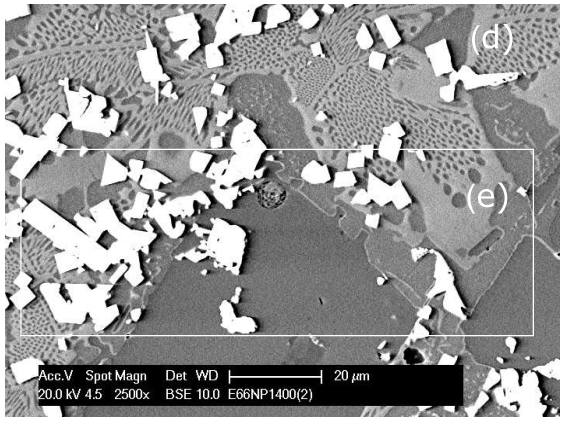

Fig. 5.13(d)

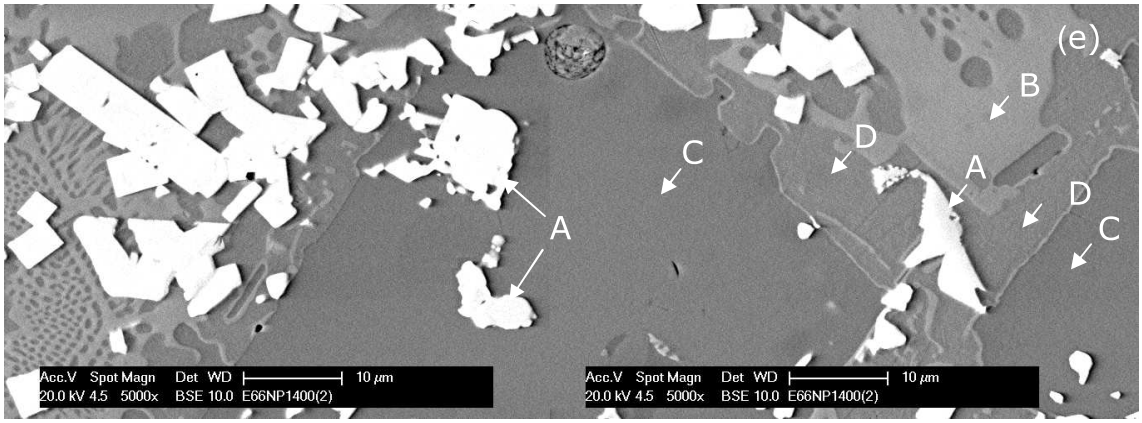

Fig. 5.13(e) at higher magnification of the boxed area (e) in Fig. 5.13(d)

Fig. 5.13 BSE micrographs of the SHS7170 powder following slow cooling in the DSC at 20K/min (a) low magnification, and (b-e) show higher magnification images of the boxed areas

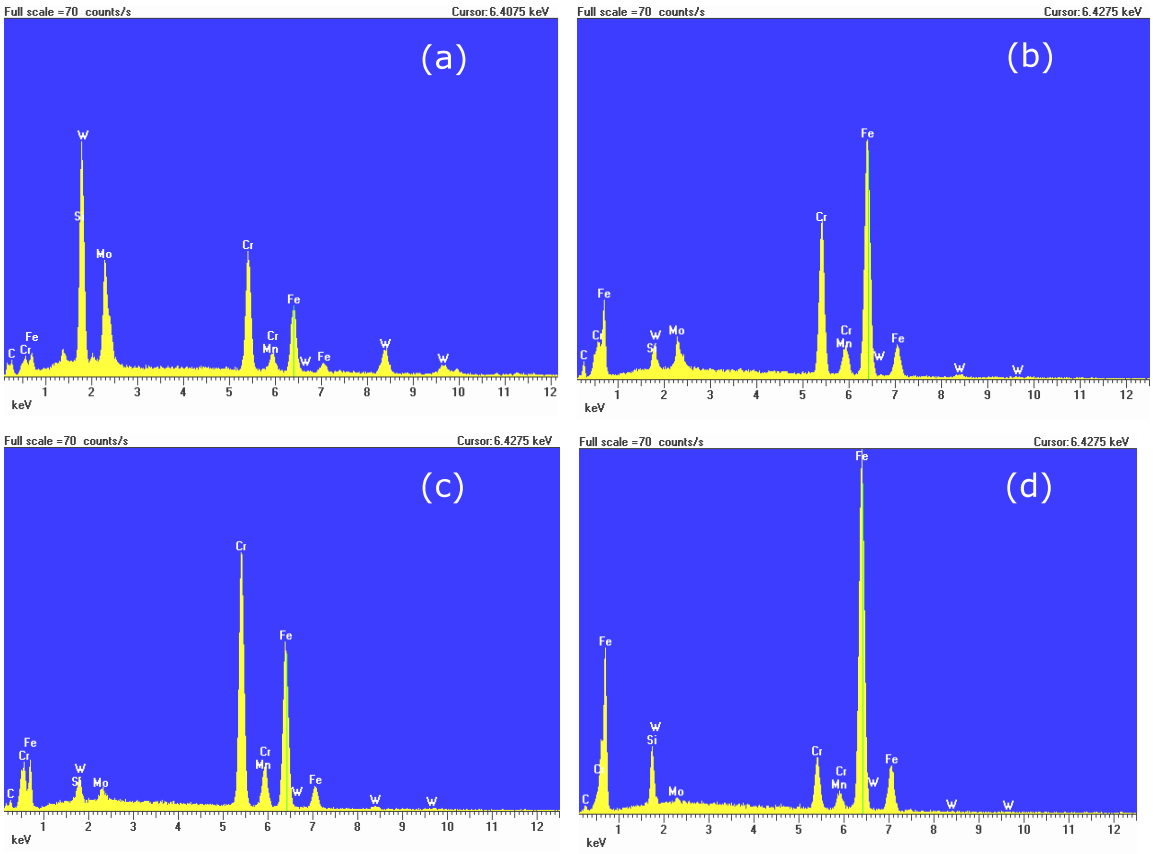

Fig. 5.14(a)-5.14(d) EDX spectra of regions in Fig. 5.13(e) arrowed A-D, respectively.

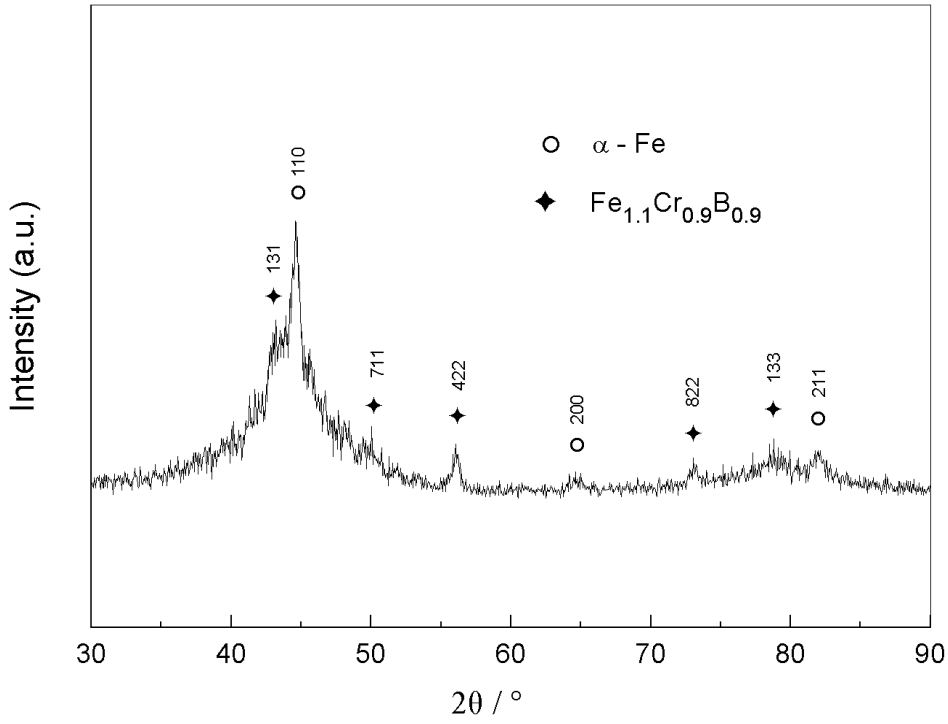

Fig. 5.15(a) XRD pattern of the as-sprayed coating.

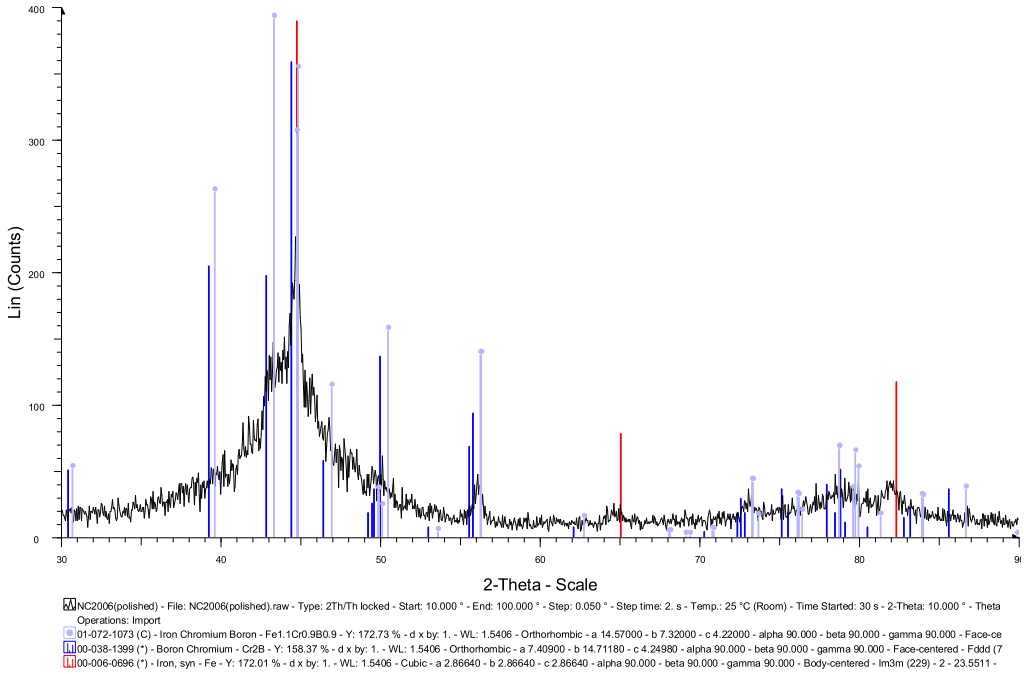

Fig. 5.15(b) Comparison of experimental XRD pattern of the as-sprayed coating with JCPDS files for Cr_2B and $Fe_{1.1}Cr_{0.9}B_{0.9}$

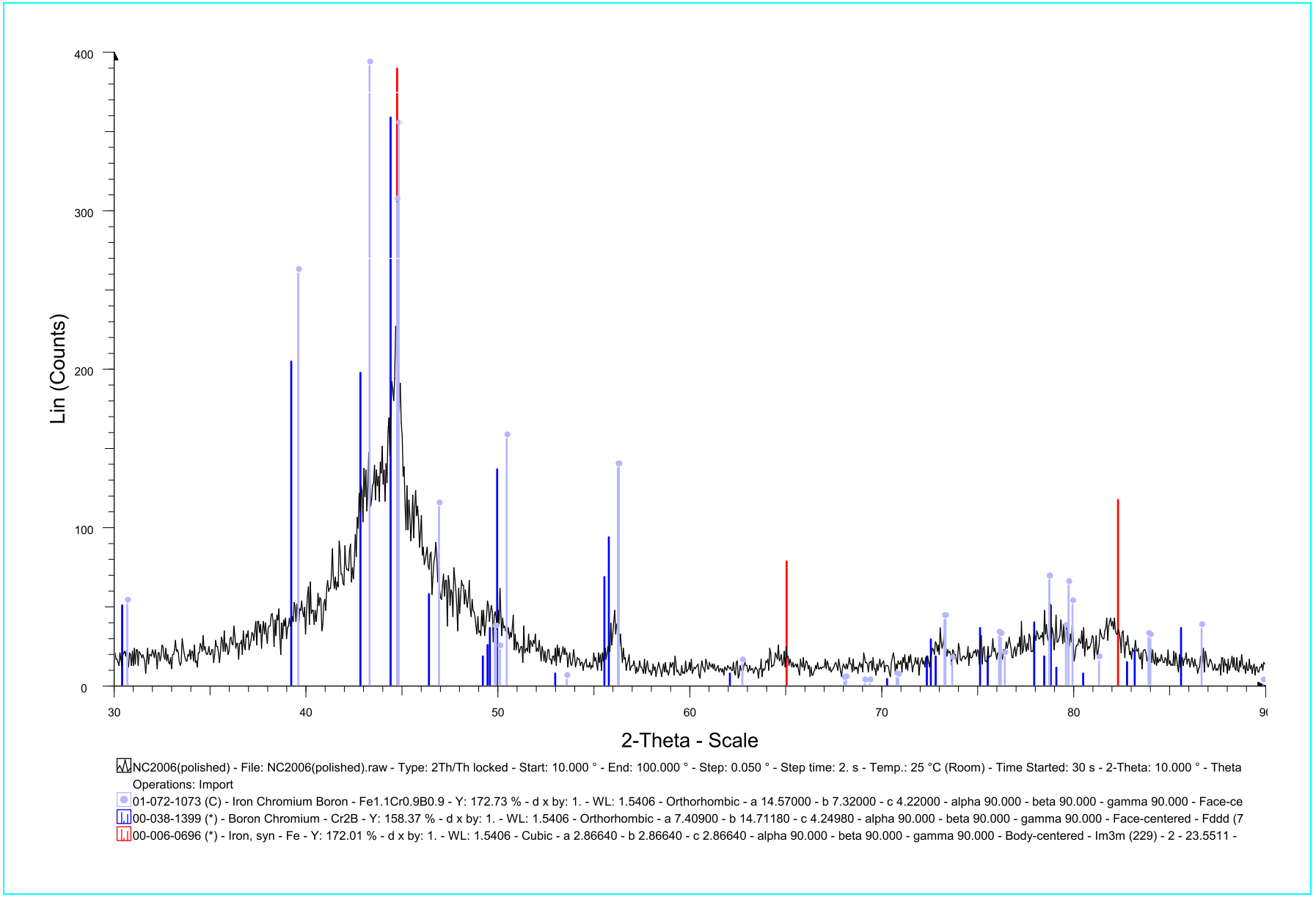

Fig. 5.15(c) Comparison of experimental XRD pattern (2θ = 30–90°) with JCPDS files for Cr_2B and $Fe_{1.1}Cr_{0.9}B_{0.9}$.

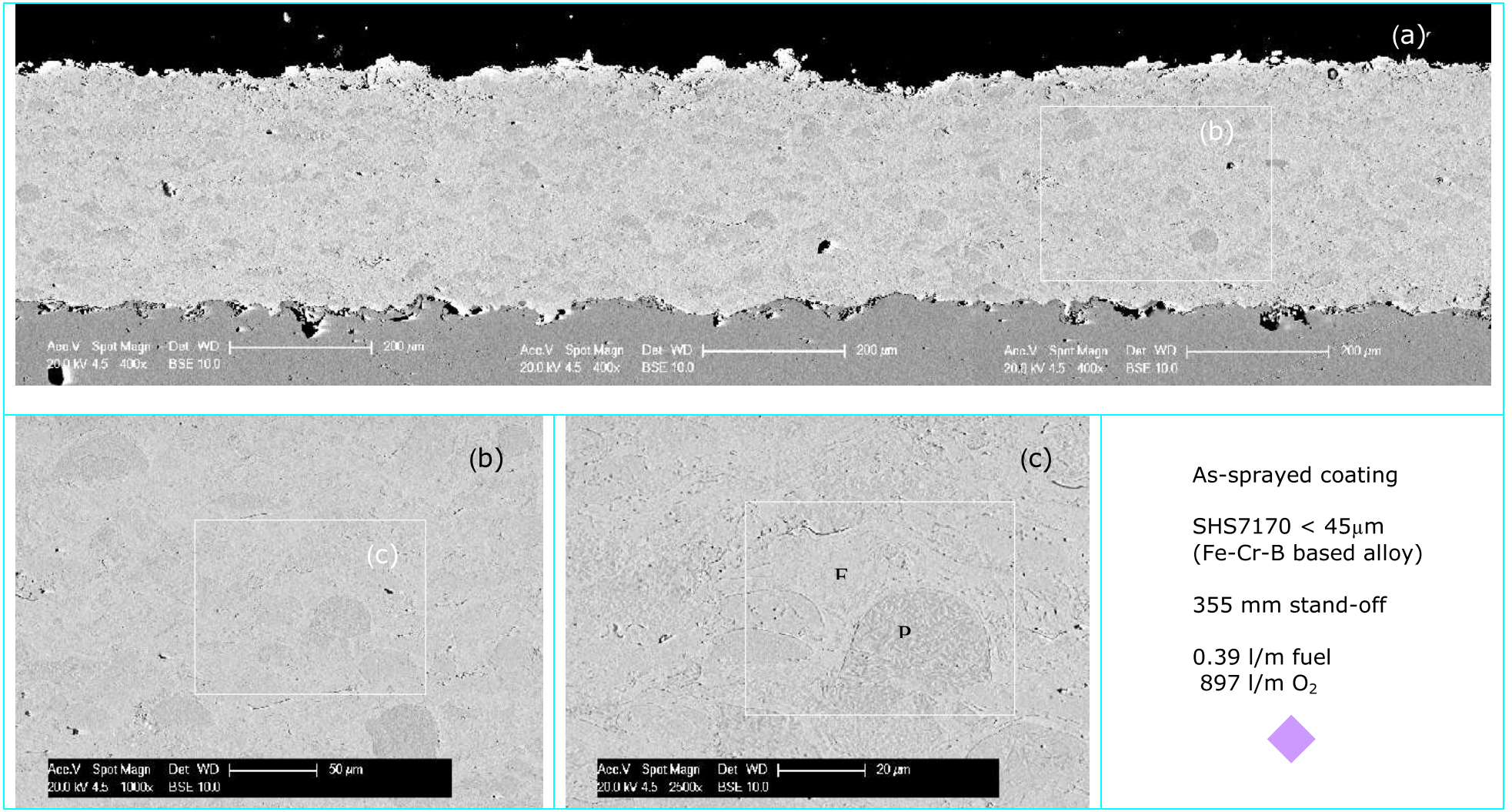

Fig. 5.16 BSE micrographs of cross-sections of a HVOF-sprayed coating: (a) low magnification unetched cross-section. (b),(c) High magnification image of the region b in (a) showing splat-like structure comprising fully melted (F) and partially melted (P) particles.

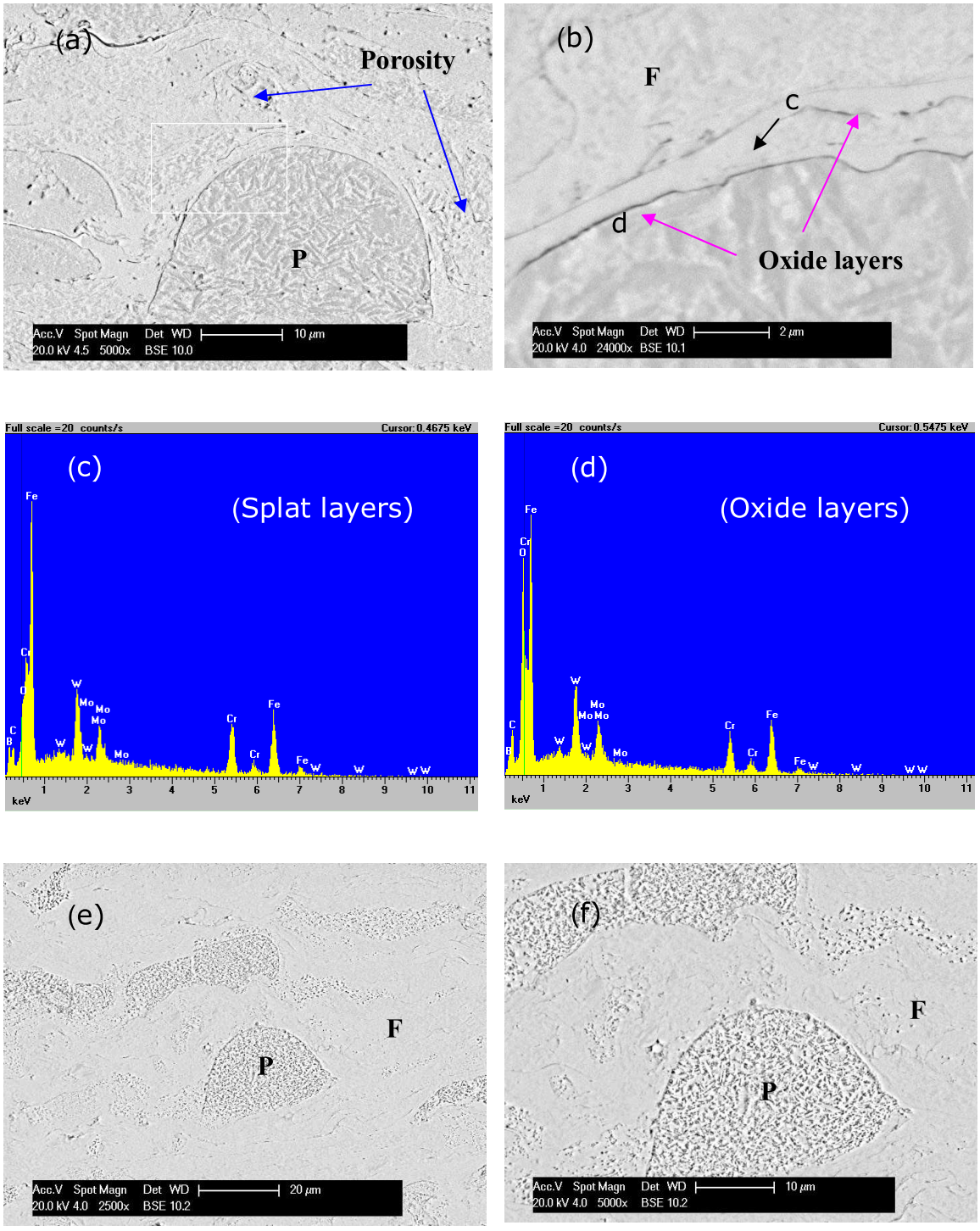

(heat treated at 920°C) (High magnification)

Fig. 5.17 BSE images showing cross-sections of a HVOF-sprayed coating. (a) Higher magnification image of the region P in Fig. 5.16(c) showing boride (dark region), Fe-Cr rich (bright region) and porosity. (b) Region F at higher magnification showing oxide layers. (c,d) EDX spectra of regions in image (b) arrowed c and d, respectively. (e,f) Low and high magnification of the as-sprayed coating following etching.

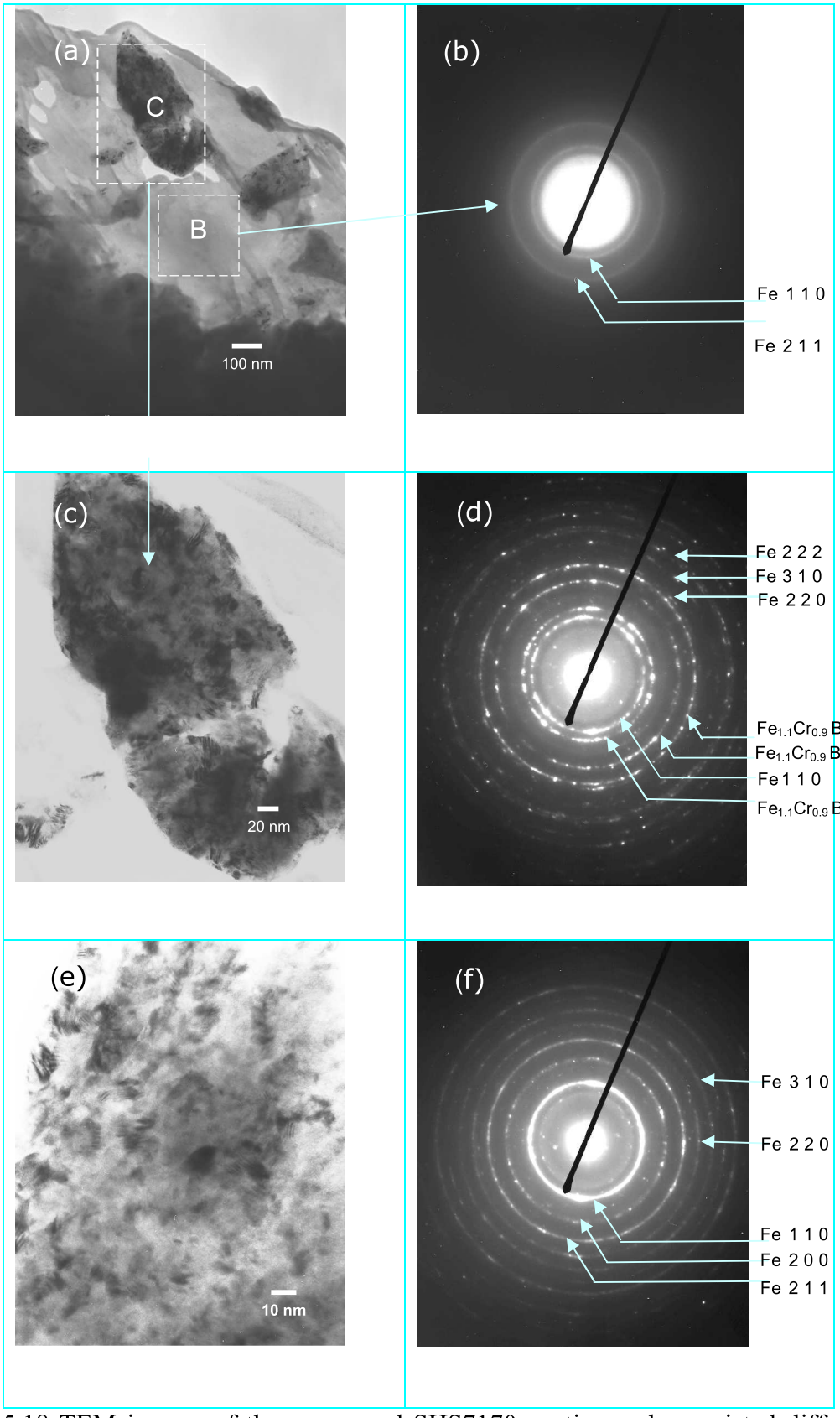

Fig. 5.18 TEM images of the as-sprayed SHS7170 coating and associated diffraction patterns (a) Bright field of fully melted region; (b) diffraction pattern of (a). (c,e) Bright field of nanocrystalline region, (d,f) diffraction pattern of (c) and (e).

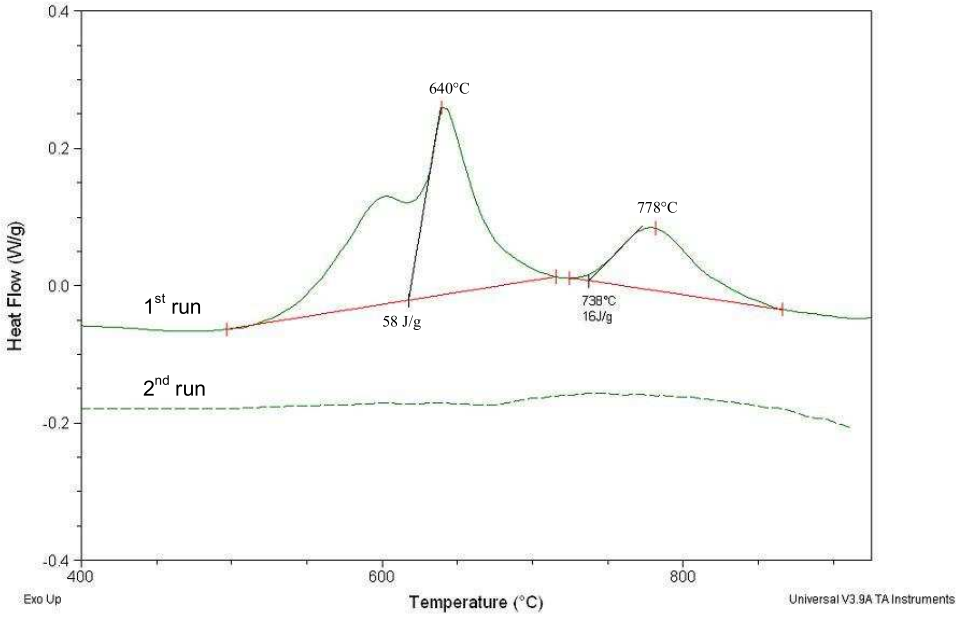

Fig. 5.19(a) DSC analysis of coating, 1st and 2nd heating runs at 20K/min.

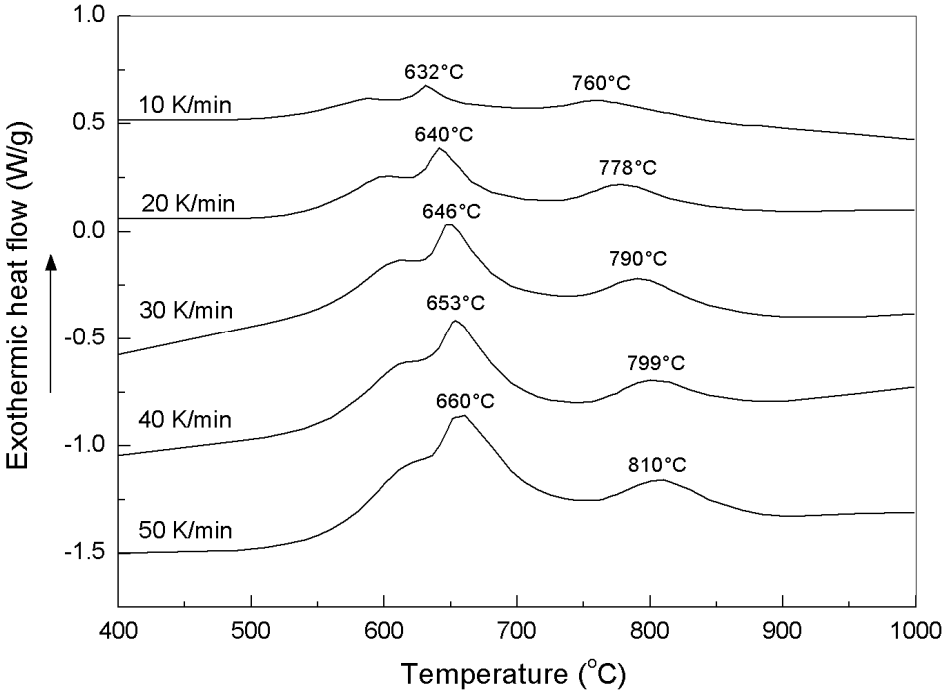

Fig. 5.19(b) DSC analysis of the SHS7170 coating at heating rates 10 K/min, 20 K/min, 30 K/min, 40 K/min and 50 K/min.

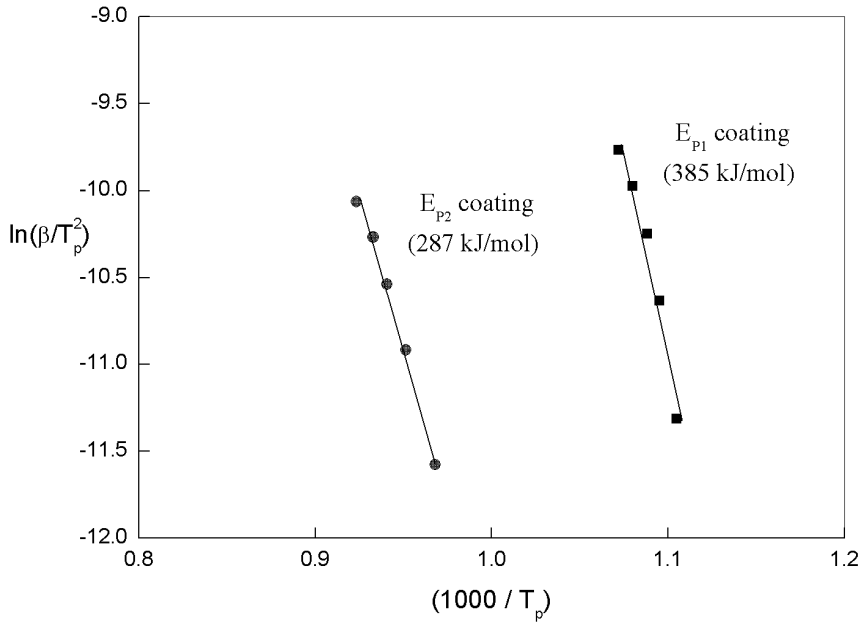

Fig. 5.20 Kissinger's plot of $\ln(\beta/T_p^2)$ versus $1000/T_p$ for peak temperature T_{p1} and T_{p2} of the as-sprayed coating.

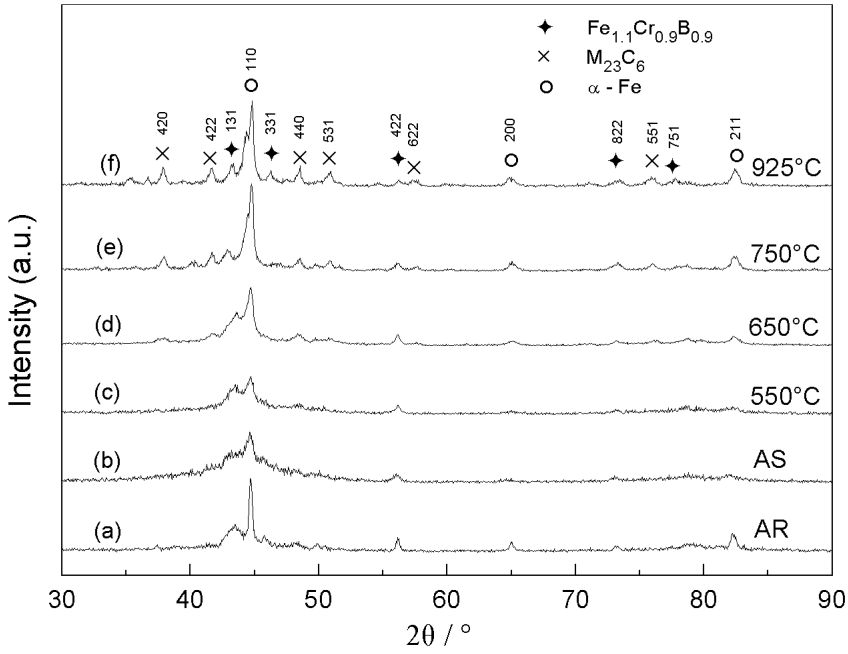

Fig. 5.21 XRD patterns of the as-received powder (AR), as-sprayed coating (AS) and the coatings following heat treatment at 550°C, 650°C, 750°C and 925°C for 1hour.

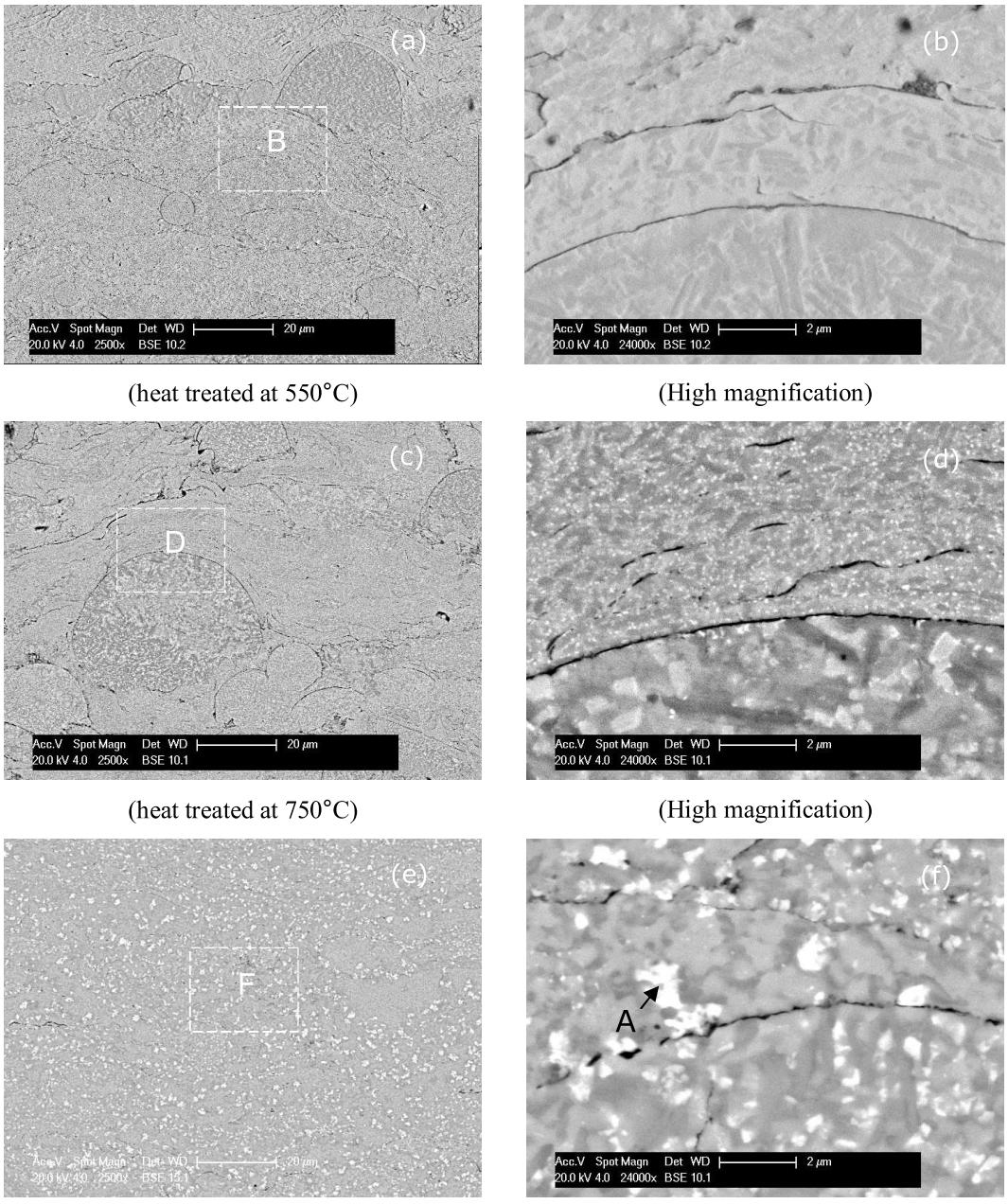

(heat treated at 550°C) (High magnification)

(heat treated at 750°C) (High magnification)

(heat treated at 925°C) (High magnification)

Fig. 5.22 Backscattered electron micrograph of coating following heat treatment at 550°C, 750°C and 925°C (low and high magnification)

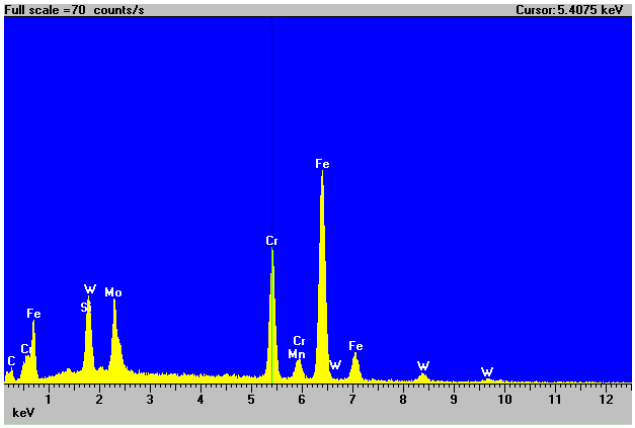

Fig. 5.23 EDX spectra of regions in Fig. 5.22(f) arrowed A

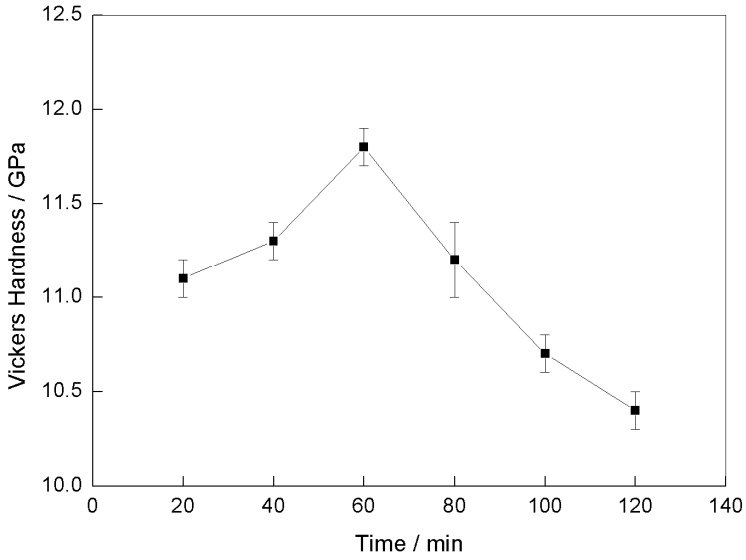

Fig. 5.24 Vickers hardness of the heat treated sample at temperature 750°C vs annealing times.

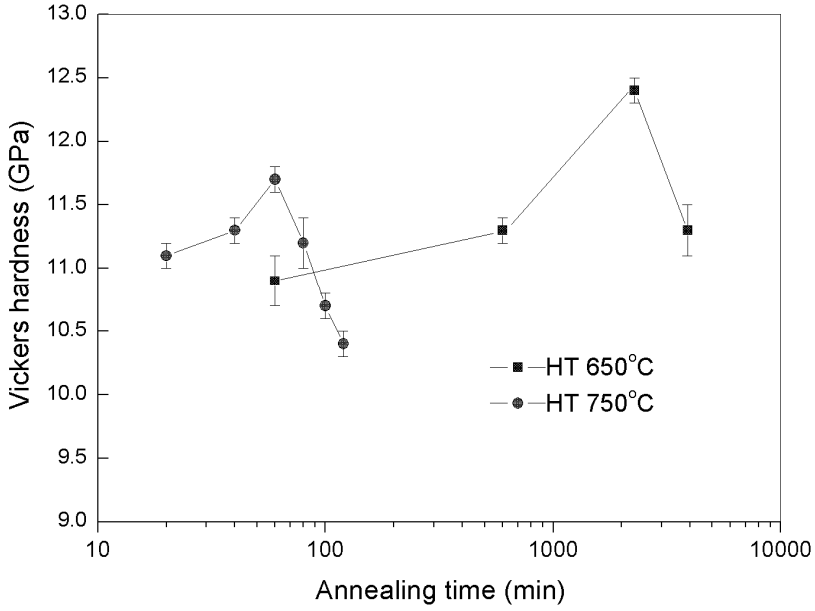

Fig. 5.25 Vickers hardness (GPa) of the samples heat treated at temperature 650°C and 750°C with different holding times.

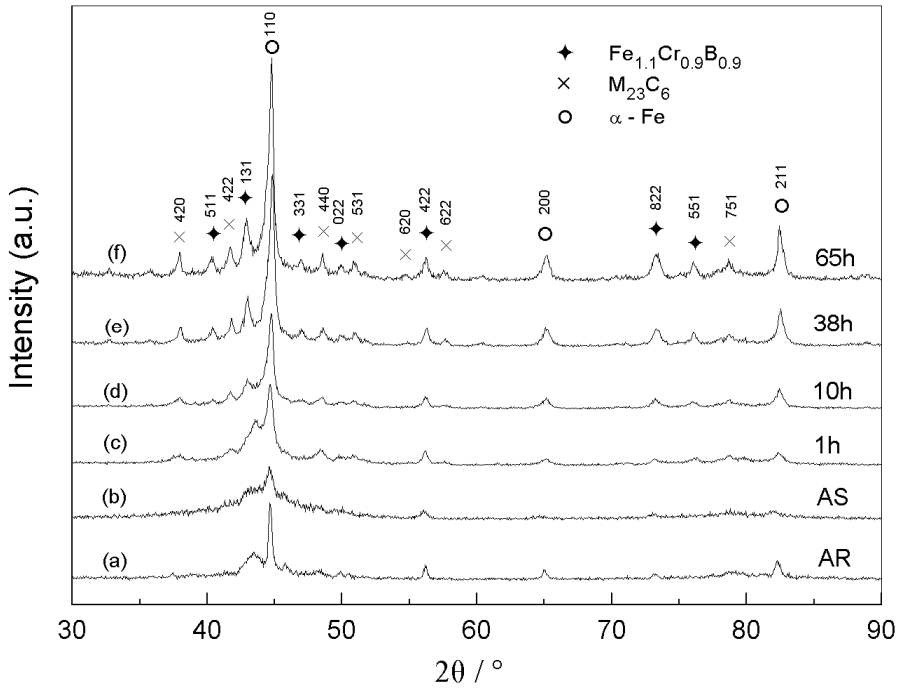

Fig. 5.26 XRD patterns of the as-received powder (AR), as-sprayed coating (AS) and the coatings following heat treatment at 650°C for 1-65 h.

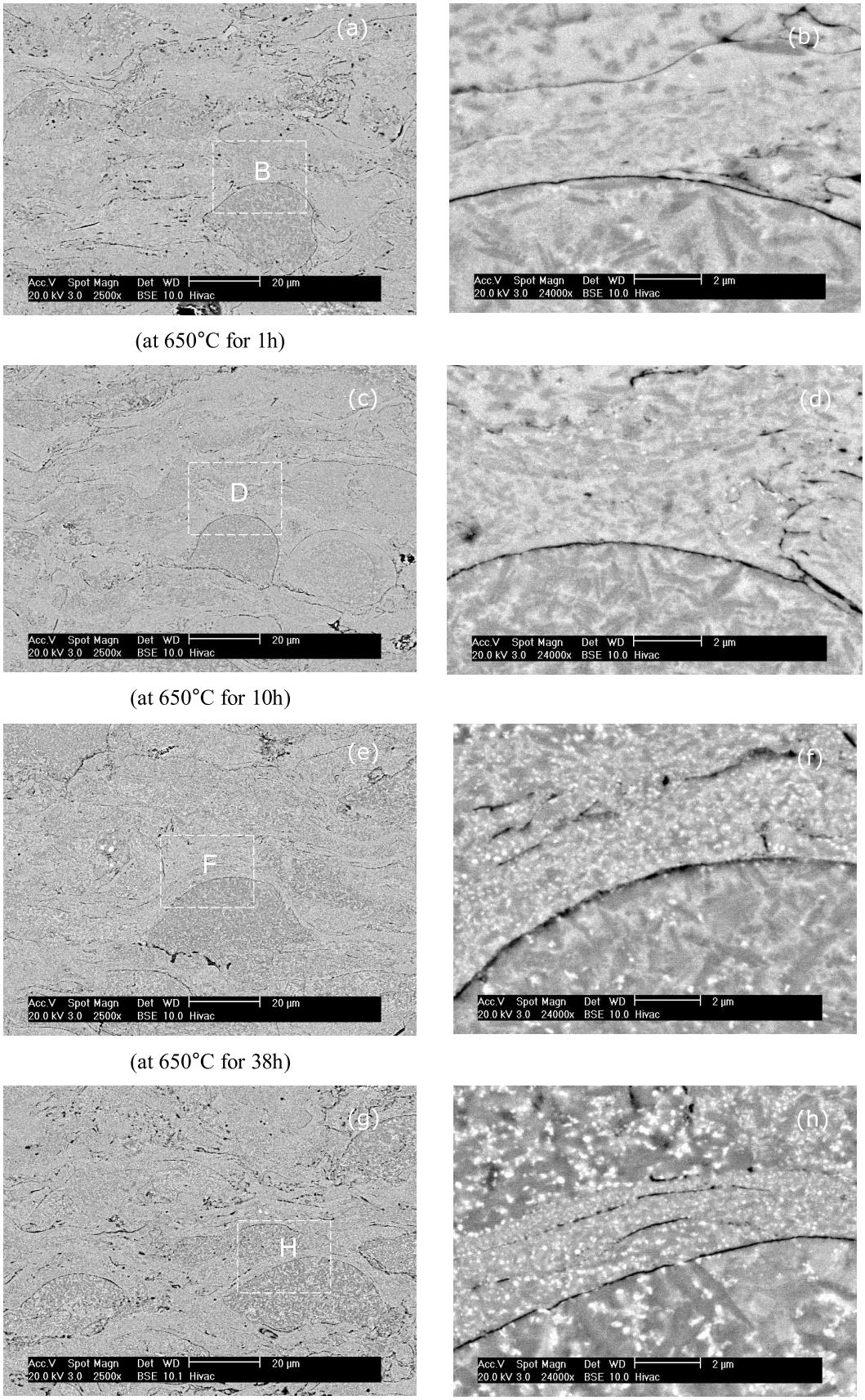

Fig. 5.27 BSE images of the as-sprayed coating and following heat treatment at 650°C for 1h (a and b), 10h (c and d), 38h (e and f) and 65h (g and h).

Chapter 6

Results : Microstructure evolution of Fe-Cr-B-C based alloy powder and coatings (KC1)

In this chapter, the microstructure of a locally designed powder (given the code KC1) based on Fe-Cr-B-C system, used as feedstock for HVOF spraying and as-sprayed coating is reported. The microstructure of the powders (small particles and large particles) and the coatings were characterised by X-ray diffraction (XRD), scanning electron microscopy (SEM), with utilising energy dispersive X-ray spectroscopy (EDS) and transmission electron microscopy (TEM). Differential scanning calorimetry (DSC) was conducted to analyse the thermal stability of the samples which correlated to the activation energy of crystallization process. Mechanical property, such as hardness of the coating was investigated by mean of a Vickers microhardness testing and then will be related to their microstructure development.

6. Results: Fe-Cr-B-C alloy KC1

6.1 Powder size and composition

A specially designed gas atomised powder KC1 was manufactured by Birmingham University, using inert gas atomisation with a chemical composition determined by SEM/EDX for the main elements (excluding B and C) as given in Table 6.1. It had a nominal size range +15 to 63 μm. The actual size distribution was obtained by laser diffractometry and is shown in Fig. 6.1 as both cumulative volume percentage and volume percentage. It can be seen that 10 vol% of the powder was above 65 μm, and 10 vol% below 17 μm with a d_{50} of 31 μm. Fig. 6.2 shows the SEM image of the external morphology of the powder. It is clear that the morphology was largely spherical with some elongated particles or particles with satellites also present. Additionally, a number of fine particles can be obviously observed. It is possible that the unusual size distribution is due to fine particle agglomeration in the Malvern laser diffractrometry instrument.

Table 6.1 The composition of the KC1 powder (as determined by SEM/EDX analysis for Fe, Cr, Mo, Si while B and C are nominal values)

Element	Fe	Cr	Mo	B	C	Si
wt.%	44.2	17.1	32.5	2.1	3.6	0.5
atom.%	40.1	16.7	17.2	10.0	15.0	0.9

6.2 Characterisation of as-received powder

XRD analysis

The phases present in the powder were determined by X-ray diffraction. The XRD trace from the as-received powder in Fig. 6.3(a) shows a broad diffraction halo around $2\theta = 32 – 55°$ and a second halo between 70 and 85°. These are indicative of

an amorphous structure. Furthermore peaks from a crystalline phase could not be detected.

SEM analysis

Figs. 6.4(a)-(d) show BSE images of the cross-section of small and large powder particles at low and high magnifications. It was found typically that all particles show a uniform contrast suggesting a single phase amorphous structure. Fig. 6.4(e), the EDX spectrum from a typical powder particle cross-section, boxed area E in Fig. 6.4(d) shows the presence of Fe, Cr, Mo with small peaks at low energy for B and C.

DSC analysis

The DSC analysis of the powder during first and second heating runs at 20K/min is shown in Fig. 6.5(a). In the curve from the first heating run, two exothermic peaks are observed and these correspond to two exothermic reactions, with a main peak temperature of 698°C and secondary peak at 870°C. It was also possible to detect a glass transition at 616°C. In the thermogram after the second heating run, no exothermic peaks were detected. The main peak corresponds to crystallisation of the metallic glass and the low broad high temperature peak is usually regarded as due to crystal growth or precipitation of another phase.

By means of DSC, the crystallization temperatures of the powder were also measured at five different heating rates of 10K/min to 50K/min. In Fig. 6.5(b) two main exothermic peaks can be observed corresponding to the two exothermic reactions during heating the powder up to 1000°C at each different rate. The first (crystallization) reaction occurred at the temperature about 685-717°C (peak

temperatures). The second exothermic peak occurred at higher temperature about 852-895°C. In Table 6.2, the glass transition temperatures *(T_g)*, onset of crystallization temperatures *(T_x)*, peak temperatures *(T_p)* are recorded along with enthalpies *(ΔH)* from each peak and supercooled liquid region *(ΔT_x)* were also determined. The enthalpies were calculated according to the procedure in chapter 3 (method).

Table 6.2 The glass transition temperatures (T_g), onset of crystallization temperatures (T_x), peak temperatures (T_p), enthalpies of transformation (ΔH) and supercooled liquid region (ΔT_x) of the as-received powder heated at different rates.

Heating rate	T_g (°C)	Onset T_x (°C)	T_{p1} (1st peak) (°C)	T_{p2} (2nd peak) (°C)	ΔH (1st peak) J/g	ΔH (2nd peak) J/g	$\Delta Tx = Tx\text{-}Tg$ (K)
10 K/min	606	677	685	852	105	21	71
20 K/min	616	688	698	870	104	20	72
30K/min	623	693	708	879	100	16	70
40K/min	627	699	712	887	100	16	72
50 K/min	631	702	717	895	99	15	71

By using the Kissinger's method (see Chapter 3), the activation energy of transformation for this alloy powder can be determined by plotting $ln(\beta/T_p^2)$ versus $10^3/T_p$ as shown in Fig. 6.6. The slopes of the straight lines represent the activation energies of the reactions. The activation energies for the reactions were determined to be 377 and 398 kJ/mol for the first and second peaks, respectively.

6.3 Characterisation of heat treated powder

XRD analysis

Fig. 6.7 shows the XRD traces for the as-received powder (AR) and samples heat treated for 1 hour at 550°C, 650°C, 750°C, 850°C and 925°C. It was found that there

is no detectable phase change in the powder after heat treatment at a temperature of 550°C as shown in Fig. 6.7(b).

Heating of the powder at a temperature of 650°C, led to the formation of small peaks around the region formerly the amorphous halo as shown in Fig. 6.7(c).

However, after heating to a temperature of 750°C, the halo intensity decreased, the intensities of α-Fe peaks increased and the formation of the peaks from other phases ($M_{23}(C,B)_6$ and M_6C) can be observed as shown in Fig. 6.7(d), suggesting that the first exothermic reaction was caused by crystallization of α-Fe phase from the amorphous matrix.

Heating of the powder at a temperature of 850°C, Fig. 6.7(e), led to further increase in the intensities of α-Fe peaks and the peaks from the other phases formed in the sample $M_{23}(C,B)_6$ (JCPDS file # 012-0570) and M_6C (JCPDS file # 047-1191) type carbide. In addition, small peaks of M_3B_2 (JCPDS file # 018-0839) type boride at ~ $2\theta = 32.0°$, 59.0° and 75.0° can obviously be observed.

Additionally, when the powder was heated to a temperature of 925°C, Fig. 6.7(f), the crystallization was completed and the XRD peaks from at least four phases: α – Fe (JCPDS file # 085-1410), the borocarbide phase $M_{23}(C,B)_6$ (JCPDS file # 012-0570), the carbide type M_6C (JCPDS file # 047-1191) and M_3B_2 (JCPDS file # 018-0839) type boride were well defined on the corresponding x-ray diffraction pattern.

Fig. 6.8(a) shows XRD patterns for the heat treated powder at 925°C for 1 hour and a comparison of experimental XRD pattern with JCPDS files for α – Fe (JCPDS file # 085-1410), the borocarbide phase $Fe_{23}(C,B)_6$ (JCPDS file # 012-0570), the carbide type Fe_3Mo_3C (JCPDS file # 047-1191) and Mo_2FeB_2 (JCPDS file # 018-0839) type boride are shown in Figs. 6.8(b) and 6.8(c).

SEM analysis

After heat treatment of powder at temperature 550°C, there was no detectable microstructural change in both a small particle Fig. 6.9(a) and a larger particle Fig. 6.9(b). The corresponding XRD trace is Fig. 6.7(b). Fig. 6.9(c), a higher magnification BSE image of small particles and a higher magnification image of larger particles Fig. 6.9(d) show clearly that crystallization did not occur in these particles at least within the resolution of BSE imaging.

Heat treatment of the powder at 750°C, led to microstructural change as seen from the corresponding XRD trace in Fig. 6.7(d). However, BSE imaging could not resolve any of these phases change as shown in Fig. 6.10(a), a low magnification BSE image of a small particle and large powder particles in Fig. 6.10(b) as well as in a higher magnification BSE image of small particles Fig. 6.10(c) and at higher magnification BSE image of large particles Fig. 6.10(d). This could be due to the microstructural change must occur on a scale below the limit of resolution of BSE image i.e. <500 nm.

However, heating the sample to a temperature of 925°C, microstructural change occurs on a scale above the limit of resolution of BSE imaging, therefore phase

change can be observed as shown in Fig. 6.11(a) and Fig. 6.11(b), a low magnification BSE images of a small particle and a large particle, respectively. Fig. 6.11(c) shows a higher magnification BSE image of small particles and at higher magnification BSE image of large particles, Fig. 6.11(d). It can be seen that multiphase structure occurred.

Additionally, heat treatment of the sample was performed at a temperature of 1050°C for 1 hour to aid phase identification, microstructural coarsening can be observed as shown in Fig. 6.12(a) and Fig. 6.12(b), low magnification BSE images of a small particle and a large particle, respectively. Fig. 6.12(c) shows a higher magnification BSE image of small particles and at higher magnification BSE image of large particles, Fig. 6.12(d). It can be clearly seen that at least a four phase structure (bright, light grey, dark grey and dark contrast regions visible) occurred.

6.4 Characterisation of Slow Cooled Solidified Powder

The melting and solidification behaviour of the KC1 powder was studied by continuous heating, and cooling DSC experiments in which the powder was melted, as shown in Fig. 6.13.

DSC trace shows crystallization onset on heating at 688°C, peak at T_{p1} and precipitation reaction at T_{p2} (exothermic). On further heating, a wide endothermic peak was observed at an onset temperature of 1137 °C, followed by a small peak at the high temperature ~ 1359 °C. The critical temperatures are listed in Table 6.3.

Table 6.3 The glass transition temperatures (T_g), onset of crystallization temperature T_x, the crystallization temperatures peak at T_{p1}, precipitation at T_{p2}, the melting temperature T_m , the liquidus temperature T_{liq} obtained from a DSC curve of the KC1 powder at a heating rate of 20 K/min.

Heating rate	T_g (°C)	Onset T_x (°C)	T_{p1} (1st peak) (°C)	T_{p2} (2nd peak) (°C)	T_m (°C)	T_{liq} (°C)
20 K/min	616	688	698	870	1137	1359

During cooling, several exothermic peaks were observed as shown in Fig. 6.13(b), a first small peak arrow indicated an onset temperature at 1255 °C. On further cooling a second peak at 1225°C is seen. There is also a secondary peak just below 1225 °C. Finally, a major peak at ~ 1120 °C is seen. Fig. 6.14 shows regions of the DSC sample at increasing magnification. At low magnification Fig. 6.14(a) shows a multiphase structure and a higher magnification image, Fig. 6.14(b) reveals dark needles with a 50 μm width and white angular particles in a matrix. At the highest magnification, Fig. 6.14(c) the matrix comprises a 2-phase eutectic, bright angular particles and dark needles (all the phases are visible and are labelled A, B, C and D). The eutectic comprises B and D. The large needles are C and the white angular particles are A. EDX analysis was performed on these phase regions and Table 6.4 shows quantitative EDX analysis data for elements present (excluding the low atomic number elements boron and carbon).

Table 6.4 EDX analysis data for the elements present in the different regions in Fig. 6.14(c) (excluding B and C)

	Element (wt %)			
Regions	Fe	Cr	Mo	others
(A) white	15.8	10.3	73.9	-
(B) light grey	62.6	21.8	15.6	Si (0.1)
(C) dark	35.3	43.4	21.3	-
(D) dark grey	90.2	5.1	4.2	Si (0.5)

The light grey regions arrowed B, of image Fig. 6.13(e) probably correspond to α – Fe (high Cr) phase and the dark regions arrowed (C) correspond to the borocarbide phase $M_{23}(C,B)_6$ and the intermediate grey contrast regions arrowed (D) are attributed to α – Fe (low Cr) phase, whilst the white region arrowed (A) are attributed to the molybdenum rich carbide M_6C phase type.

6.5 Characterisation of as-sprayed coating

XRD analysis

The phases present in the as-sprayed coating were determined by X-ray diffraction. The XRD trace from the as-sprayed coating, Fig. 6.15 shows a broad diffraction halo around 2θ = 32 – 55° and a second halo between 70 and 85°. These are indicative of fully amorphous structure. However, peaks from an oxide phase can be detected at 2θ = 30°, 35.7°, 57.2° and 62.8° as shown in Fig. 6.16.

SEM analysis

Fig. 6.17(a) shows a low magnification unetched cross-section of the as-deposited KC1 coating. The coating is seen to be around 360 μm thick with an irregular top surface. At higher magnification, the cross-section of the coating imaged in the BSE

mode of the area (b) in Fig. 6.17(a), is shown in Fig. 6.17(b) and (c). The coatings exhibited layered microstructure typical of thermally sprayed coating (with the splat layers parallel to the substrate surface and also the following: unmelted particles, oxide layers, porosity).

Fig. 6.18(a) shows a BSE image of a typical region P from a cross-section of coating in Fig. 6.17(c). This reveals a near-spherical morphology of a partially melted particle and some porosity is visible as a very dark contrast region, generally outside the region P. Fig. 6.18(b), a higher magnification BSE image of selected area in Fig. 6.18(a) shows details of the interface area between fully melted region (F) and partially melted particle (P). The EDX spectra and analysed data of the arrowed regions C and D of image Fig. 6.18(b) are shown in Fig. 6.18(c) and Fig. 6.18(d), respectively. It is indicated that the splat layers as marked (C) in Fig. 6.18(b) correspond to Fe-Mo rich phase, whereas, thin dark contrast stringers as marked (D) were enriched in oxygen relative to the matrix phase and correspond to an oxide phase.

TEM analysis

TEM images of the as-sprayed KC1 coating and associated diffraction patterns are shown in Fig. 6.19. Figs. 6.19(a) and (c) are a bright field TEM micrograph from a plan-view of the KC1 coating and reveals that this region of the sample was composed of a fully amorphous region. The SAD patterns in Figs. 6.19(b) and (d) were taken from the region marked B and D in Figs. 6.19(a) and (c), respectively, and show diffuse rings which are characteristic of an amorphous phase.

DSC analysis

The DSC analysis of the coating during first and second heating runs at 20K/min is shown in Fig. 6.20(a). In the curve from the first heating run, two peaks appear and these correspond to two exothermic reactions, attributable to crystallization of the amorphous phase. The peaks temperatures *(T_{p1}* and *T_{p2})* are 697°C and 870°C, respectively. In the curve after the second heating run, no exothermic peak was detected. In this coating, the glass transition was also detected at 613°C.

Fig. 6.20(b) shows typical DSC curves of the as-deposited KC1 coating obtained during continuous heating at five different heating rates (10 K/min – 50 K/min). It can be clearly seen that each DSC curve exhibits a main exothermic peak and a broad shallow secondary peak. The first crystallization reaction occurring at the temperature about 683-718 °C (peak temperatures) corresponds to the crystallization of the amorphous matrix phase. The second exothermic peak occurring at about 853-898 °C could be due to the precipitation of one or more additional phases. The glass transition temperatures *(T_g),* onset of crystallization temperatures *(T_x)*, peak temperatures *(T_p)*, enthalpies of transformation *(ΔH)* and supercooled liquid region *(ΔT_x)* for the KC1 coating at different heating rates (10K/min to 50K/min) are listed in Table 6.5. The glass transition and onset temperature is taken to be when is first seen a deviation from the baseline.

Table 6.5 The glass transition temperatures (T_g), onset of crystallization temperatures (T_x), peak temperatures (T_p), enthalpies of transformation (ΔH) and supercooled liquid region (ΔT_x) for the KC1 coating at different heating rates.

Heating rate	T_g (°C)	Onset T_x (°C)	T_{p1} (1st peak) (°C)	T_{p2} (2nd peak) (°C)	ΔH (1st peak) J/g	ΔH (2nd peak) J/g	ΔTx = Tx-Tg (K)
10 K/min	601	674	683	853	101	16	73
20 K/min	613	684	697	870	101	11	71
30K/min	618	689	701	878	97	8	71
40K/min	621	692	711	888	92	8	71
50 K/min	627	696	718	898	98	8	69

Similar to the powder, the activation energies of crystallization for the KC1 coating can be calculated by using Kissinger's method (see chapter 3). Fig. 6.21 shows the plot $\ln(\beta/T_p^2)$ as a function of $10^3/T_p$ and the activation energy, E_a can be determined to be 351 and 382 kJ/mol for the first and second peaks of the coating sample, respectively. It can be noticed from Table 6.5 that the enthalpy of the total reaction (main peak plus shoulder) of the first reaction (92-101 J/g) are more than 5 times higher than the heat of the second reaction (8-16 J/g).

6.6 Characterisation of heat treated coating

XRD analysis

Figs. 6.22(a)-(g) show the XRD traces for the as-received powder (AR), as-sprayed coating (AS) and the coatings following heat treatment for 1 hour at 550°C, 650°C, 750°C, 850°C and 925°C, respectively. In comparison to AR (Fig. 6.22(a)) and AS (Fig. 6.22(b)), it was found that there is no detectable phase change in the coating after heat treatment at a temperature of 550°C as shown in Fig. 6.22(c).

At a temperature of 650°C, the XRD trace Fig. 6.22(d) shows a formation of a small peak at ~ 2θ = 44.0°, around the region formerly the amorphous halo. This corresponds to α-Fe formation. Following heat treatment of the coating at a temperature of 750°C, the presence of a number of new peaks are seen around the region formerly amorphous halo.

Following heat treatment at temperature 850°C, the intensities of α-Fe peaks and the peaks from the other phases formed in the sample (the borocarbide phase $M_{23}(C,B)_6$ (JCPDS file # 012-0570) and M_6C (JCPDS file # 047-1191) type carbide gradually increased. In addition to the formation of small peaks of M_3B_2 (JCPDS file # 018-0839) type boride at ~ 2θ = 32.0°, 59.0° and 75.0° can be observed as shown in Fig. 6.22(f).

After the coating was heated to a temperature of 925°C, the crystallization was completed and the XRD peaks from at least four phases: α – Fe (JCPDS file # 085-1410), the borocarbide phase $M_{23}(C,B)_6$ (JCPDS file # 012-0570), the carbide type M_6C (JCPDS file # 047-1191) and M_3B_2 (JCPDS file # 018-0839) type boride were

well defined on the corresponding x-ray diffraction pattern as shown in Fig. 6.22(g). During this stage, precipitation of the borocarbide type $M_{23}(C,B)_6$, M_6C type carbide and M_3B_2 type boride were the major event, although intensities of the peaks from other phases also increased.

Fig. 6.23(a) shows XRD patterns for the coating following heat treatment at 925°C for 1 hour and a comparison of the experimental XRD pattern with JCPDS files for α – Fe (JCPDS file # 085-1410), $Fe_{23}(C,B)_6$ (JCPDS file # 012-0570), eta-Fe_3Mo_3C (JCPDS file # 047-1191) and Mo_2FeB_2 (JCPDS file # 018-0839) are shown in Figs. 6.23(b) and 6.23(c).

SEM analysis

Fig. 6.24 shows the microstructure of the coating following heat treatment at 550°C, 750°C and 925°C for 1 hour.

After heat treatment of the coating for 1 hour at temperature 550°C, there was no microstructural change of the coating that could be resolved as shown in Fig. 6.24(a). Fig. 6.24(b), a higher magnification BSE image of selected area boxed (B) in Fig. 6.24(a) shows clearly a featureless microstructure.

The microstructure of the coating following heat treatment at 750°C is shown in Fig. 6.24(c). Fig. 6.24(d) is a higher magnification BSE image of the selected area boxed (D) in Fig. 6.24(c). With regard to the corresponding XRD trace as shown in Fig. 6.22(e), indicating that the microstructural change occurred, but could not be resolved by SEM-BSE imaging.

However, microstructural change can be observed after heat treatment of the coating at 925°C. Fig. 6.24(e) shows a low magnification BSE image of the coating and Fig. 6.24(f) a higher magnification BSE images of selected area boxed (F) in Fig. 6.24(e) shows at least three phases structure (size < 0.2 μm). The XRD pattern corresponding to this heat treatment showed the presence of four phases, so not all can be resolved in the SEM.

6.7 Microhardness

One set of heat treatments was performed for a fixed time of 60 minutes at the following temperatures: 550, 650, 750, 850 and 925°C. A second set of heat treatments was performed at only two temperatures, namely 750 and 850°C, with holding times of 60 to 6000 minutes at 750°C and 20 to 100 minutes at 850°C. Microhardness data for the as-sprayed coating following heat treatment at 550°C, 650°C, 750°C, 850°C and 925°C for 1 hour are shown in Table 6.6.

Table 6.6 Hardness (GPa) of the as-deposited and samples heat treated for 1 hour at various temperatures

Sample	As-deposited	550°C	650°C	750°C	850°C	925°C
Hardness / GPa	7.6	8.5	9.8	11.3	12.3	12.0
Standard deviation	1.2	1.2	1.0	1.3	0.7	1.0
Standard error	0.4	0.4	0.3	0.4	0.2	0.3

The results show that as the temperature increased up to 550°C, the hardness of the coating increased somewhat and gradually increased to 11.3 GPa at temperature 750°C and reached a maximum at a temperature 850°C. However, after increasing the temperature up to 925°C, the hardness decreased to 12.0 GPa. This is suggested

that the drop in the hardness of the coating could be due to microstructural coarsening of the phases formed in the sample.

Following a second set of heat treatments, samples were heat treated at 750°C and 850°C for times ranging from 20 minutes to 6000 minutes and the results are shown in Table 6.7 and 6.8.

Table 6.7 Hardness (GPa) of the heat treated samples at temperature 850°C with different holding times

Sample	20 min	40 min	60 min	80 min	100 min
Hardness / GPa	10.3	11.2	12.3	11.6	11.2
Standard deviation	0.4	0.5	0.6	0.7	0.3
Standard error	0.1	0.2	0.2	0.2	0.1

Table 6.8 Hardness (GPa) of the heat treated samples at temperature 750°C with different holding times

Sample	60 min	600 min	2280 min	3240 min	6000 min
Hardness / GPa	11.2	11.3	11.6	13.2	12.0
Standard deviation	0.6	0.9	0.9	0.6	0.9
Standard error	0.2	0.3	0.3	0.2	0.3

From Table 6.8, it is observed that with increasing holding times from 60 min to 600 min, the hardness gradually increased from 11.2 GPa to 11.3 GPa and reached a maximum at 3240 min with a value of 13.2 GPa which is the highest hardness of the heat treated coating in this experimental work. However, after this period the hardness decreased somewhat to 12.0 GPa, at a period of 6000 min. Fig. 6.26 shows the dependence of the hardness of the heat treated coating on the holding times at temperature of 750°C and 850°C. It can be seen that the maximum hardness tends to

increase when the sample was heat treated at lower temperature such as 750°C in this case.

6.8 Microstructure of coating heat treated at 750°C

The microstructural changes in the coating following heat treatment at a temperature 750°C with different holding times was also investigated by XRD and SEM. Fig. 6.27 shows XRD patterns of the coatings heat treated at 750°C with different holding times. After heating at a temperature of 750°C for 1 hour, small peaks are seen around the region formerly the amorphous halo as shown in Fig. 6.27(b), probably due to α-Fe formation.

Heat treatment of the coating at a temperature of 750°C for 10 hours, led to a gradual increase in the intensities of Fe peaks and the peaks from the other phases formed in the sample (the borocarbide phase $M_{23}(C,B)_6$ (JCPDS file # 012-0570), M_6C (JCPDS file # 047-1191) type carbide and M_3B_2 (JCPDS file # 018-0839) type boride as shown in Fig. 6.27(c).

Further heating of the coating at a temperature of 750°C for 38, 54 and 100 hours, led to a further increase in the intensities of Fe peaks and the peaks from the other phases formed in the sample (the borocarbide phase $M_{23}(C,B)_6$ (JCPDS file # 012-0570), M_6C (JCPDS file # 047-1191) type carbide and M_3B_2 (JCPDS file # 018-0839) type boride as shown in Fig. 6.27(e). Fig. 6.28 shows XRD patterns for the coating following heat treatment at 750°C for 100 hours.

Heat treatment of the KC1 coating at 750°C for 1 hour, led to phase change as can be seen from the corresponding XRD trace shown in Fig. 6.27(b). However, the microstructure of the coating could not be resolved by SEM-BSE imaging mode as shown in Fig. 6.29(a) and Fig. 6.29(b), higher magnification BSE image of selected area boxed B.

However, microstructural change could be resolved by BSE imaging after heat treatment at 750°C for 38 hours. Precipitation of fine particles derived from the amorphous matrix phase occurred as shown in Fig. 6.29(c) and (d). Heating at 750°C for 54 hours and 100 hours increased the size of the crystalline phase rendering them visible by BSE imaging in the SEM (Fig. 6.29(f) and (h)).

6.9 Summary (KC1)

(1) The present study reports a detailed microstructure investigation of HVOF-thermal sprayed KC1 powder of composition (in at %) Fe-16.7%Cr-10%B-15%C-0.9%Si-17.2%Mo. The deposits, which are approximately 360 μm thick, have a splat-like microstructure characteristic of thermally sprayed metals.

(2) The as-sprayed KC1 coating obtained, as identified by XRD, is composed of a fully amorphous structure with some oxide formation. TEM result also reveals that the Fe-matrix is mainly composed of a fully amorphous region.

(3) The formation of the amorphous phase is probably due to the high cooling rates of the splats combined with the alloy composition, relatively high B(10 at.%), C(15 at.%) and Mo levels.

(4) The addition of metalloid elements (e.g. boron and carbon) to the alloy increases the ability of the alloy to form the amorphous structure on deposition. The presence of boron and carbon also increases the crystallization temperature of the alloy thus reducing the proportion of material crystallizing due to heating of the coating by subsequent impinging splats.

(5) The thermal stability of the as sprayed KC1 coating is higher than those of the as-sprayed Fe-Cr-B based alloy coatings (Branagan et al., 2002), representing more resistance to crystallization of the as-sprayed coating and this coating can be subjected into service up to about 750°C.

(6) The apparent activation energies for reactions were calculated from DSC data using various peak shift equations. The activation energy for the second peak was found to be higher than the first peak. The activation energy for the first peak of reaction is correspond to the energy required for crystallization of amorphous Fe-based matrix phase, whereas the activation energy for the second peak of reaction is correspond to the energy required for precipitation of borocarbide $M_{23}(C,B)_6$, carbide M_6C phases and boride Mo_2FeB_2.

(7) The heat treated KC1 coating shown a significantly higher hardness than in the as-sprayed condition. After annealing at temperature 750°C and holding time for 3240 min the annealed coating sample exhibits the highest hardness (~13.2 GPa) of all these annealed Fe-Cr-B based alloy coatings, studied in this test. The greater hardness of the sample could be due to a number of factors including the presence of a greater proportion of amorphous/nanocrystalline phase as well as precipitation of a borocarbide $M_{23}(C,B)_6$, carbide M_6C and boride Mo_2FeB_2.

Result: Fe-Cr-B alloy KC1

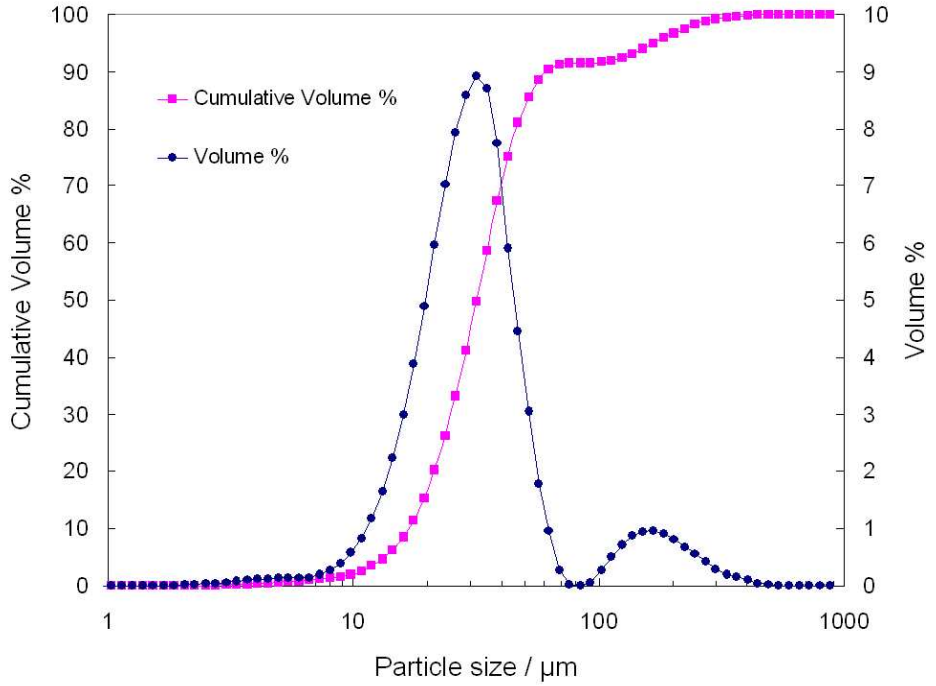

Fig. 6.1 Plot of cumulative vol % versus particle size of the as-received KC1 powder.

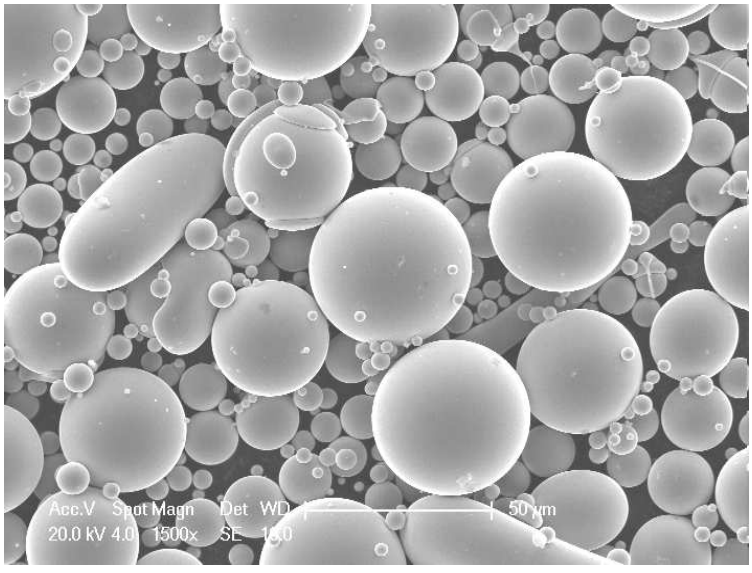

Fig. 6.2 The external morphology of the as-received KC1 powder.

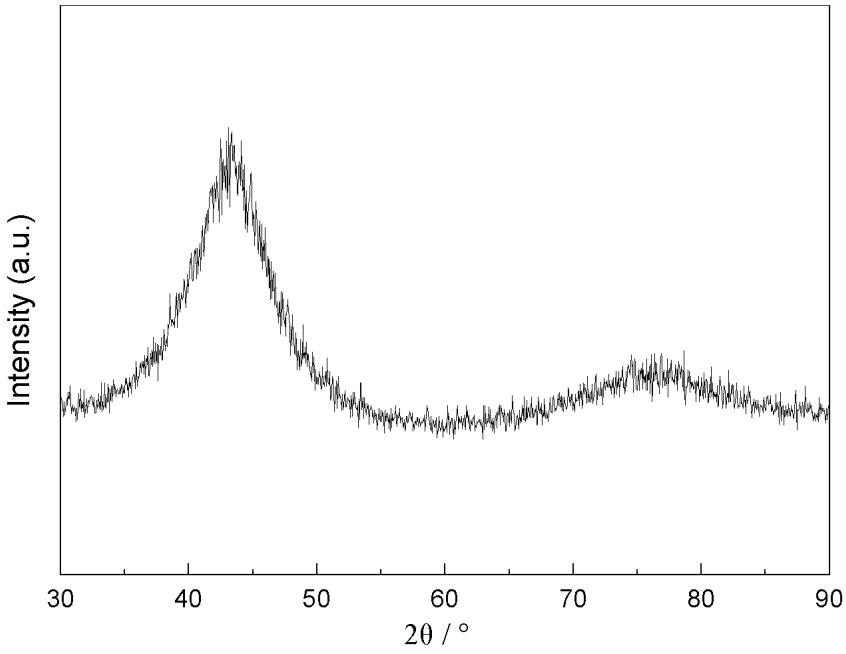

Fig. 6.3 XRD pattern of the as-received powder.

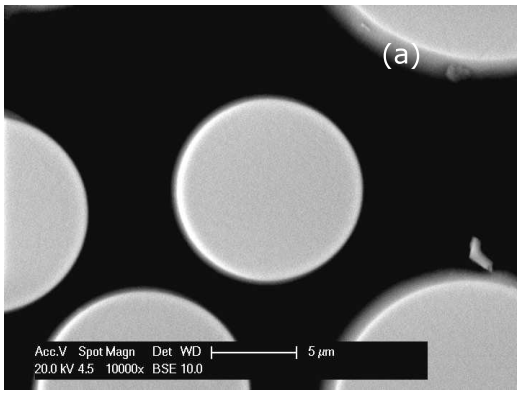

Fig. 6.4(a)

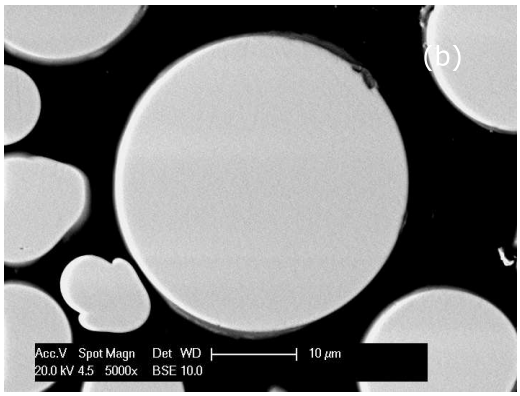

Fig. 6.4(b)

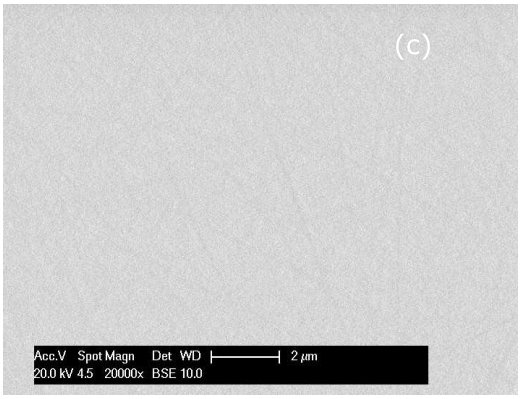

Fig. 6.4(c)

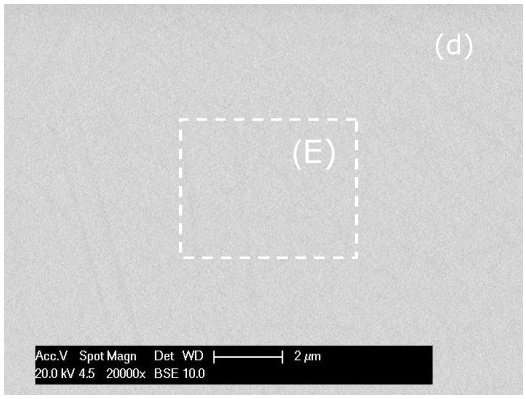

Fig. 6.4(d)

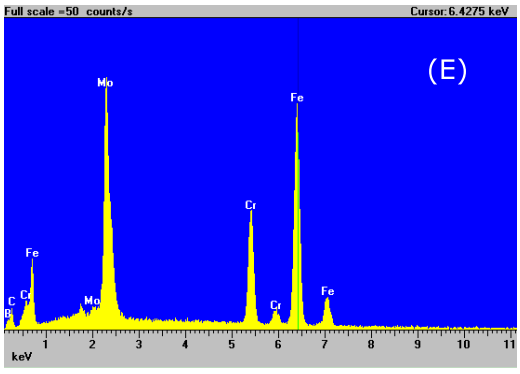

Fig. 6.4(e)

Fig. 6.4 BSE images of the cross-section of a small particle (a) and a large particle (b). (c,d) Higher magnification of regions in images (a) and (b). (e) is EDX spectrum of the boxed area E in (d).

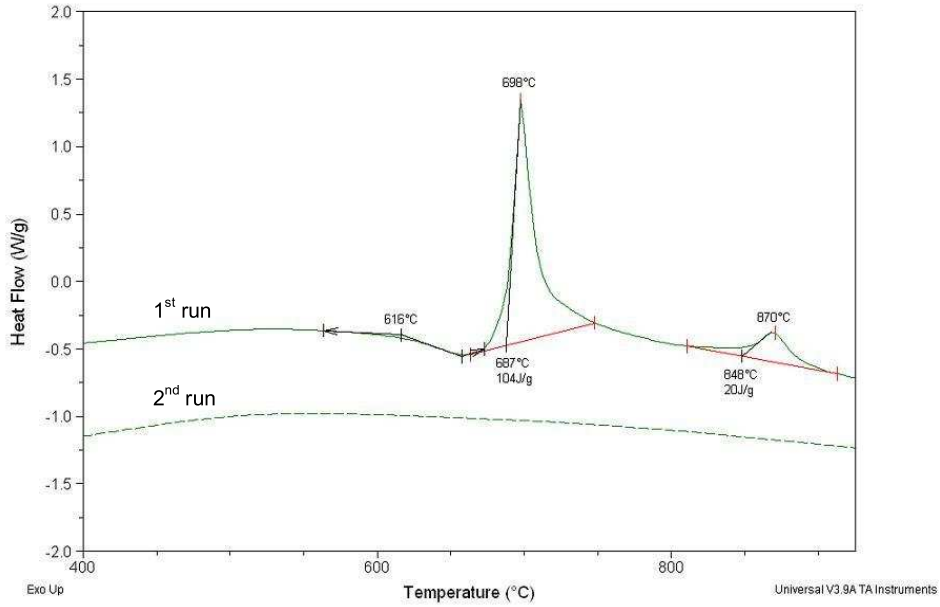

Fig. 6.5(a) DSC analysis of powder, 1st and 2nd heating runs at 20K/min.

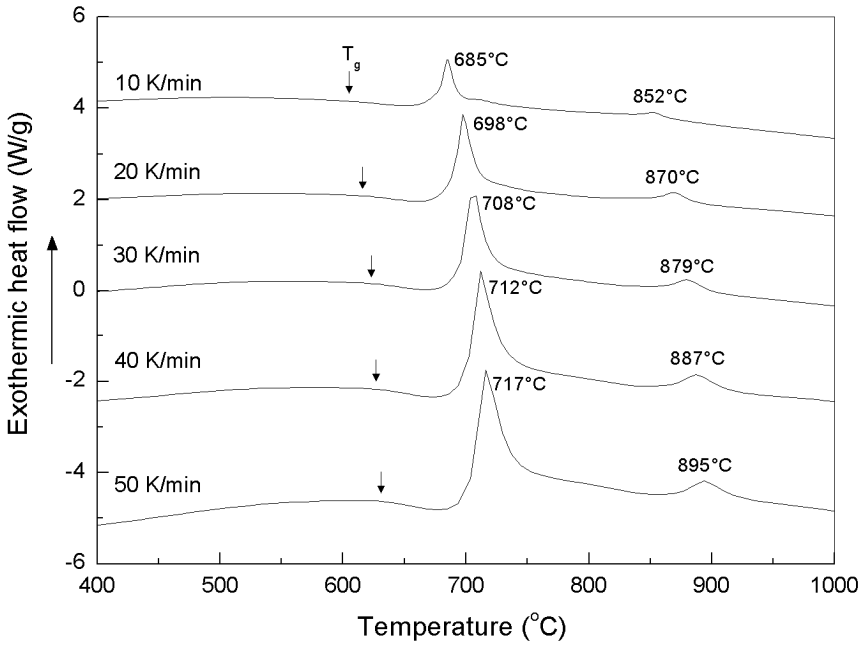

Fig. 6.5(b) DSC analysis of the as-received powder at heating rates 10 K/min, 20 K/min, 30 K/min, 40 K/min and 50 K/min

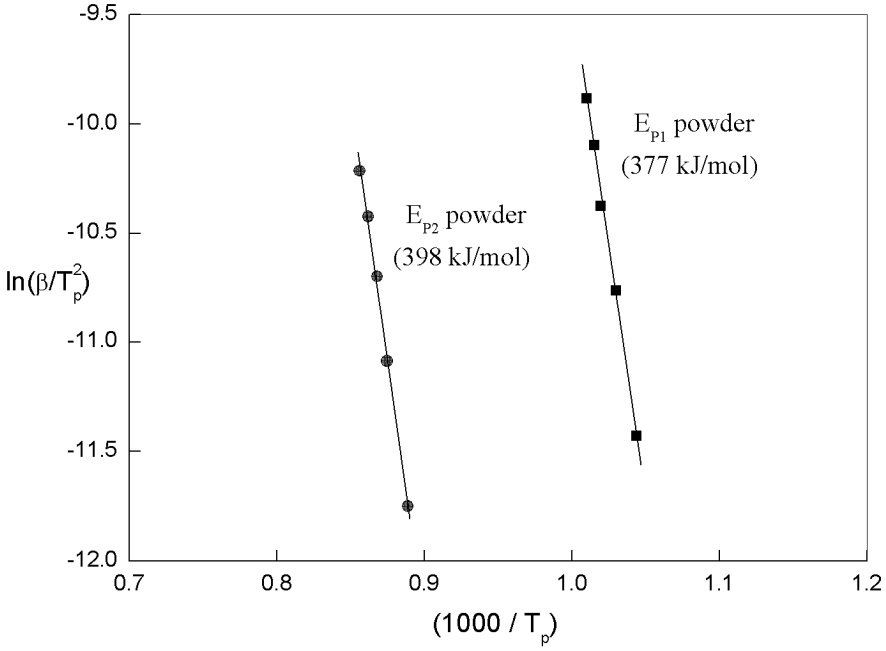

Fig. 6.6 Kissinger's plot of $\ln(\beta/T_p^2)$ versus $1000/T_p$ for peak temperature T_{p1} and T_{p2} of the KC1 powder.

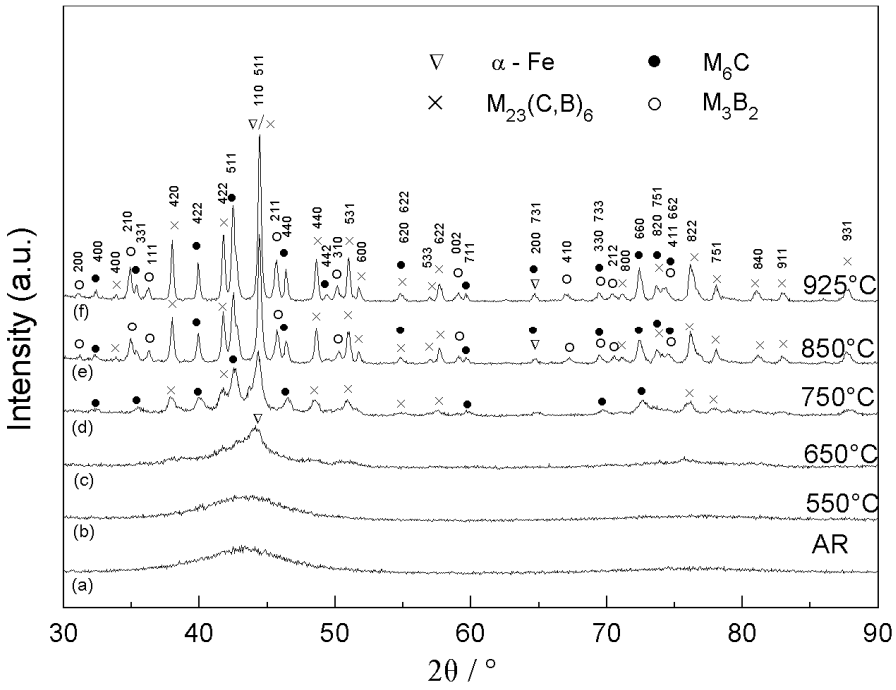

Fig. 6.7 XRD patterns for the heat treated powder at 550°C, 650°C, 750°C, 850°C and 925°C for 1 hour.

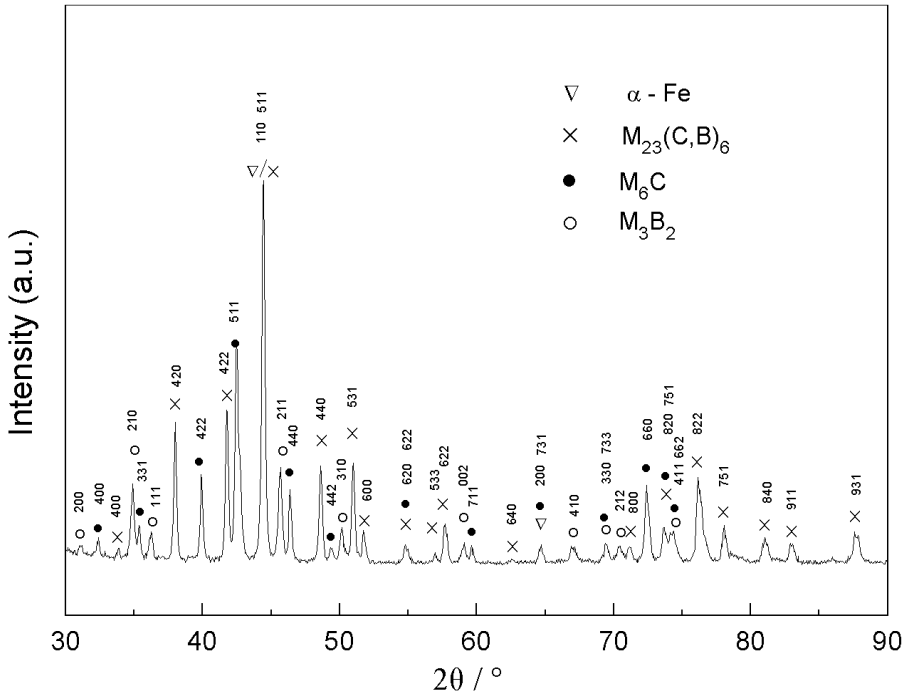

Fig. 6.8(a) XRD patterns for the heat treated powder at 925°C for 1 hour.

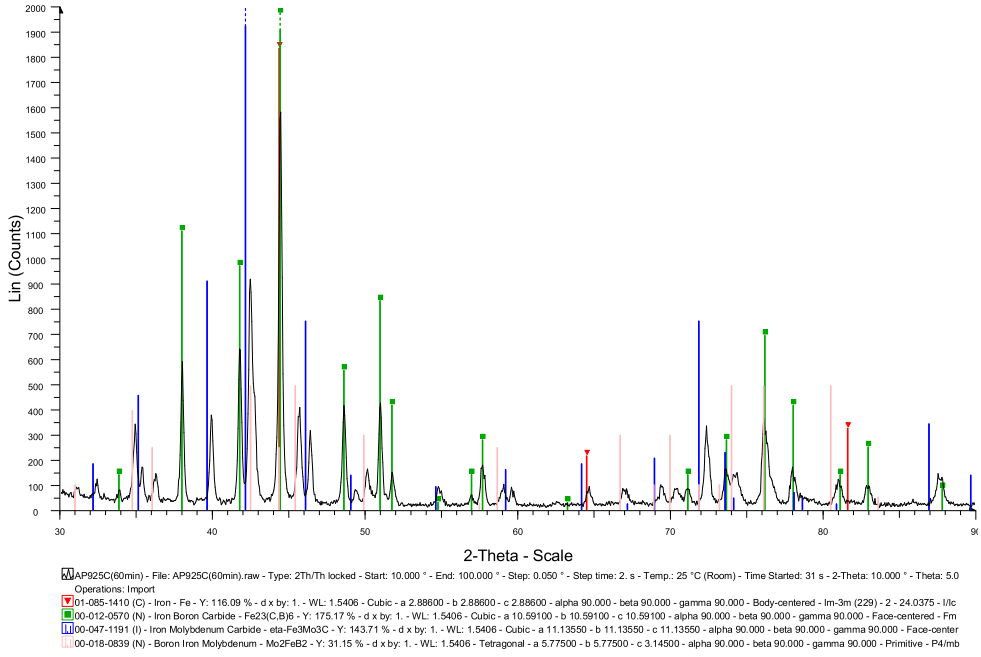

Fig. 6.8(b) Comparison of experimental XRD pattern (2θ = 30–90°) with JCPDS files for α-Fe, $Fe_{23}(C,B)_6$, eta-Fe_3Mo_3C and Mo_2FeB_2

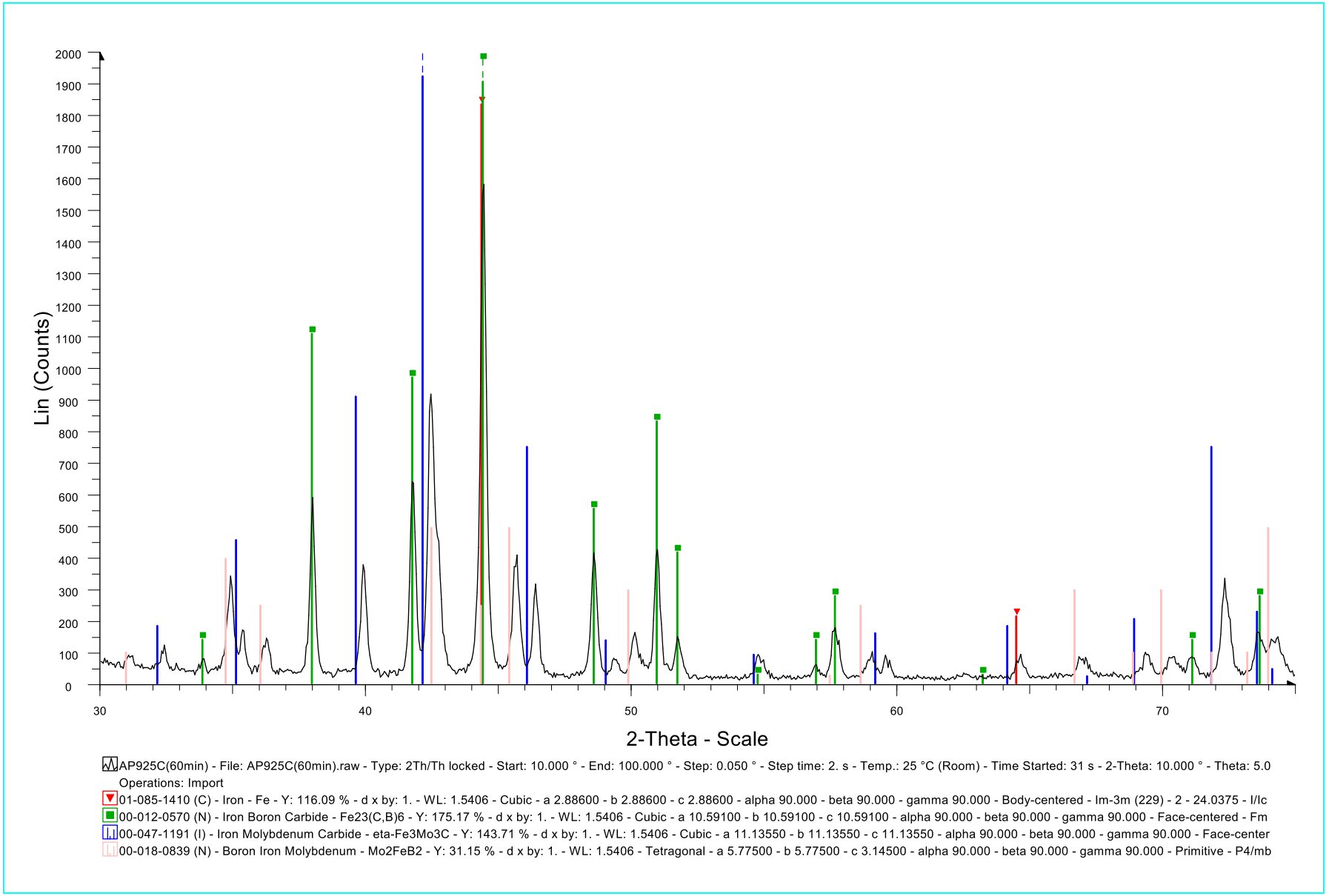

Fig. 6.8(c) Comparison of experimental XRD pattern (2θ = 30–75°) with JCPDS files for α-Fe, $Fe_{23}(C,B)_6$, eta-Fe_3Mo_3C and Mo_2FeB_2

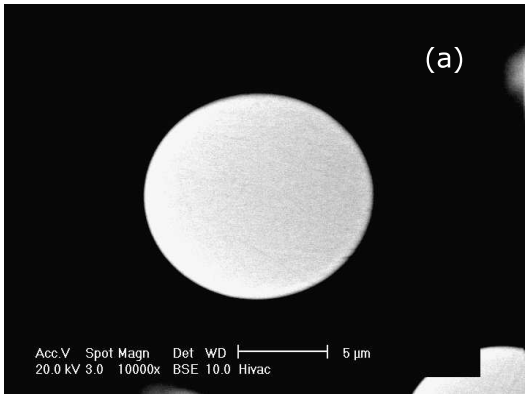

Fig. 6.9(a) Fine particle at 550°C

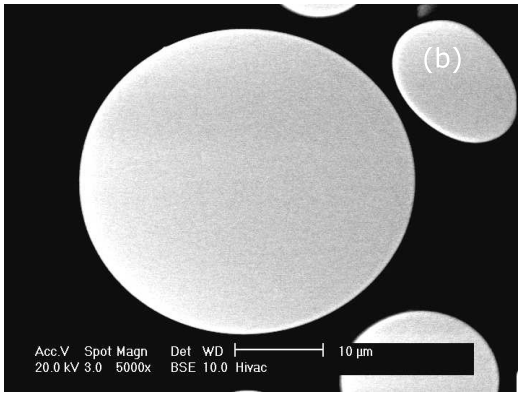

Fig. 6.9(b) Coarse particle at 550°C

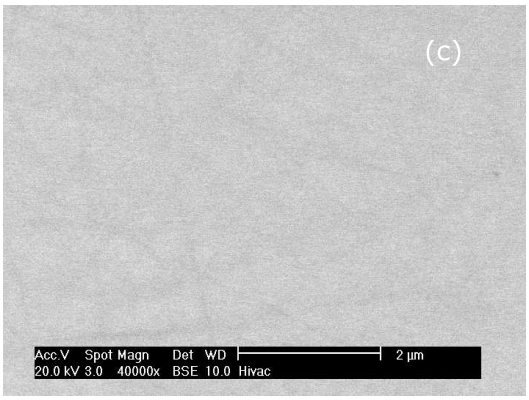

Fig. 6.9(c) Fine particle (high magnification)

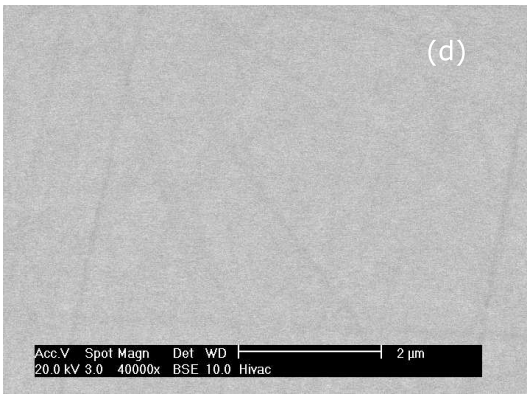

Fig. 6.9(d) Coarse particle (high magnification)

Fig. 6.9 Backscattered electron micrograph of the cross-section of a small particle Fig. 6.9(a) and a large particle Fig. 6.9 (b) after heat treatment at 550°C (low magnification) and at high magnification Fig. 6.9(c) and 6.9(d).

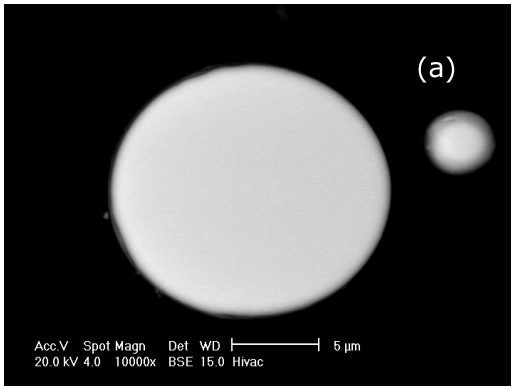

Fig. 6.10(a) Fine particle at 750°C

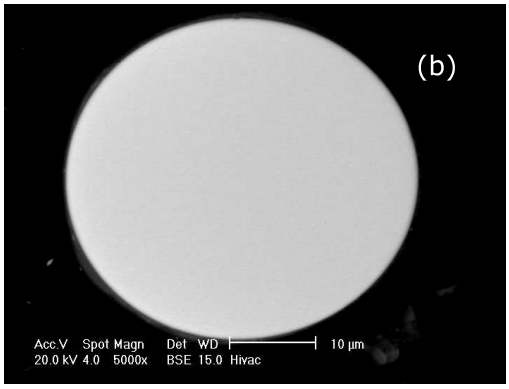

Fig. 6.10(b) Coarse particle at 750°C

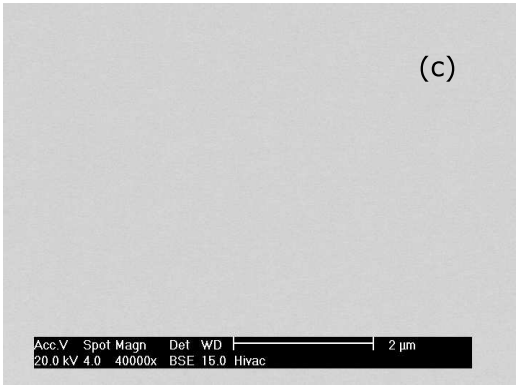

Fig.6.10(c) Fine particle (high magnification)

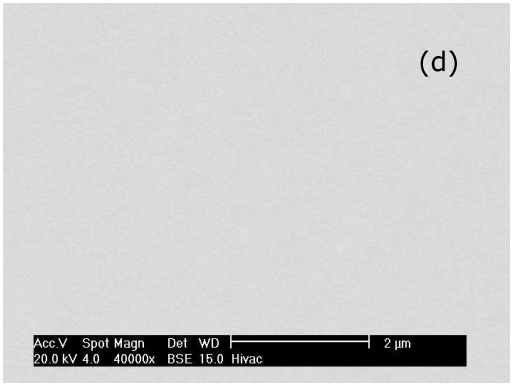

Fig.6.10(d) Coarse particle(high magnification)

Fig. 6.10 Backscattered electron micrograph of the cross-section of a small particle Fig. 6.10(a) and a large particle Fig. 6.10(b) after heat treatment at 750°C (low magnification) and at high magnification Fig. 6.10(c) and 6.10(d).

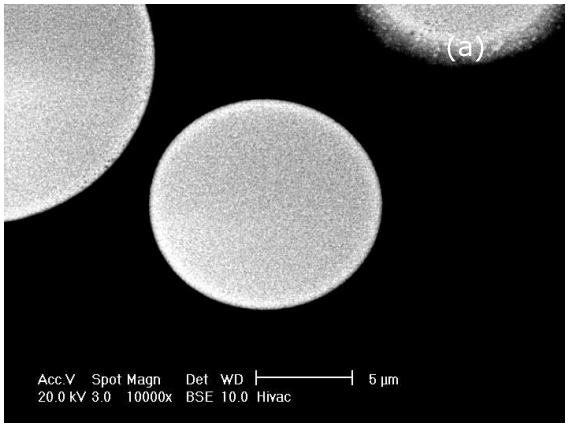

Fig. 6.11(a) Fine particle at 925°C

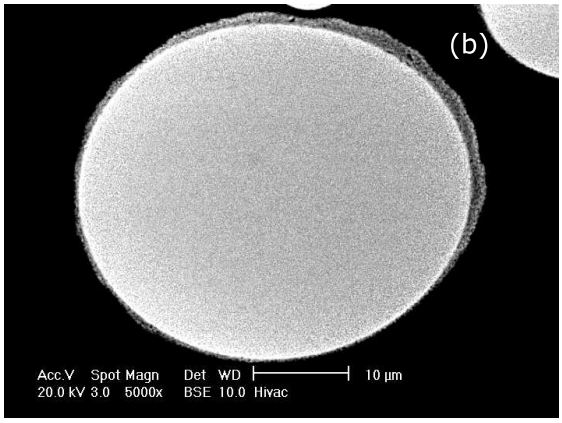

Fig. 6.11(b) Coarse particle at 925°C

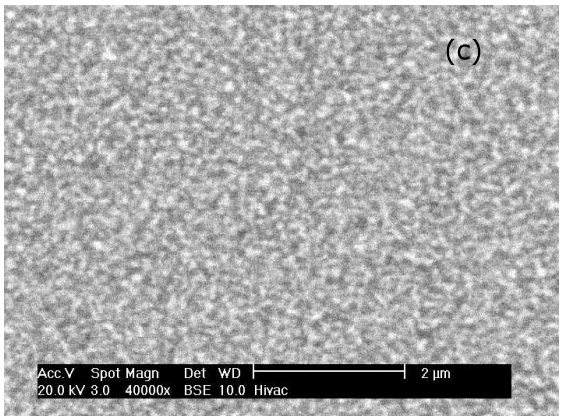

Fig.6.11(c) Fine particle(high magnification)

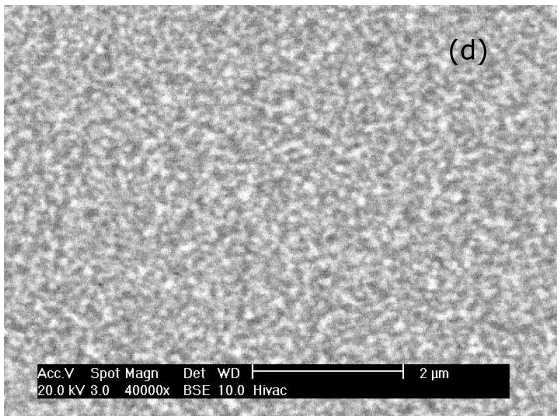

Fig.6.11(d) Coarse particle(high magnification)

Fig. 6.11 Backscattered electron micrograph of the cross-section of a small particle Fig. 6.11(a) and a large particle Fig. 6.11(b) after heat treatment at 925°C (low magnification) and at high magnification Fig. 6.11(c) and 6.11(d).

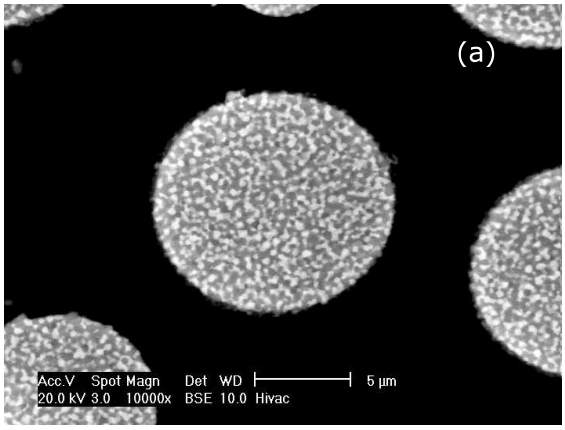

Fig. 6.12(a) Fine particle at 1050°C

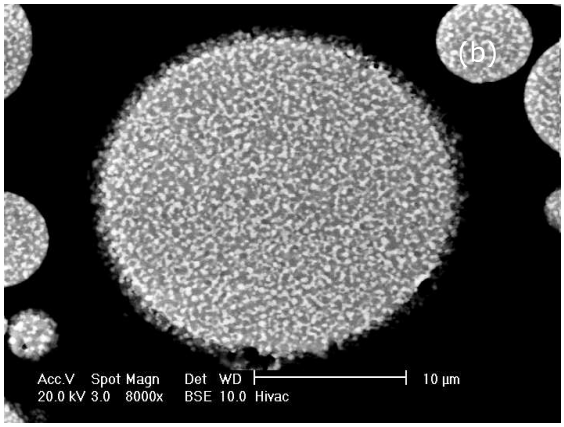

Fig. 6.12(b) Coarse particle at 1050°C

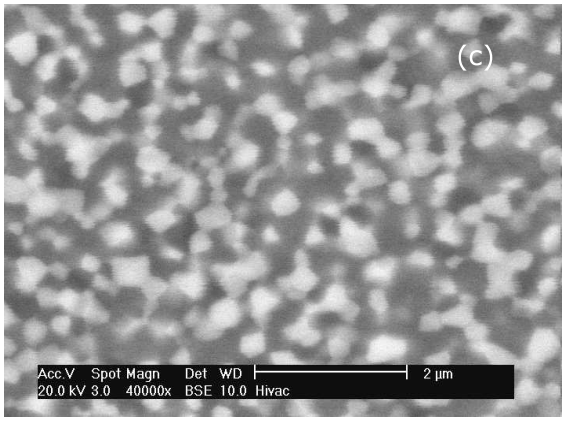

Fig.6.12(c) Fine particle(high magnification)

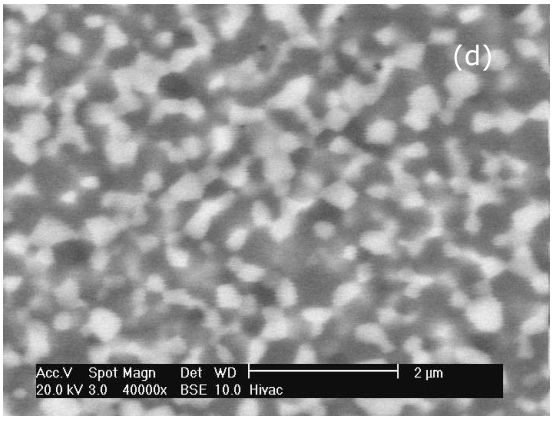

Fig.6.12(d) Coarse particle(high magnification)

Fig. 6.12 Backscattered electron micrograph of the cross-section of a small particle Fig. 6.12(a) and a large particle Fig. 6.12(b) after heat treatment at 1050°C (low magnification) and at high magnification Fig. 6.12(c) and 6.12(d).

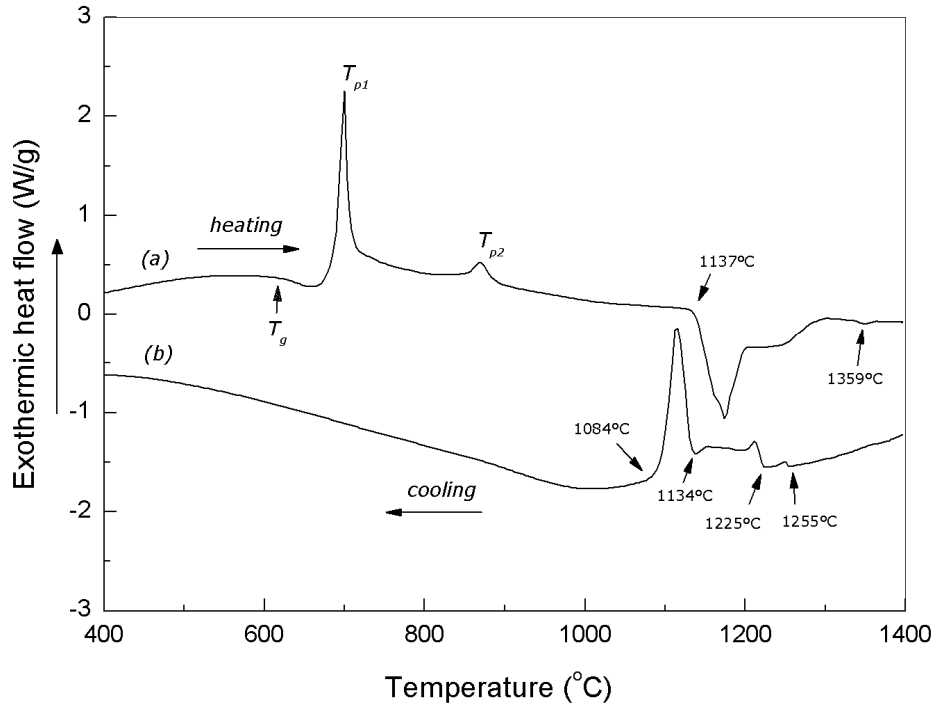

Fig. 6.13 The DSC heating (a) and cooling (b) scans for the as-received KC1 powder obtained at a scanning rate of 20 K/min.

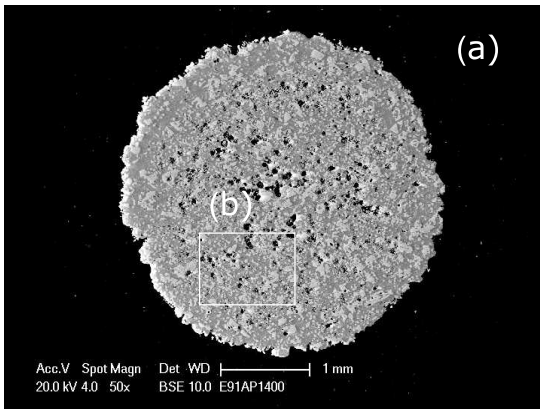

Fig. 6.14(a)

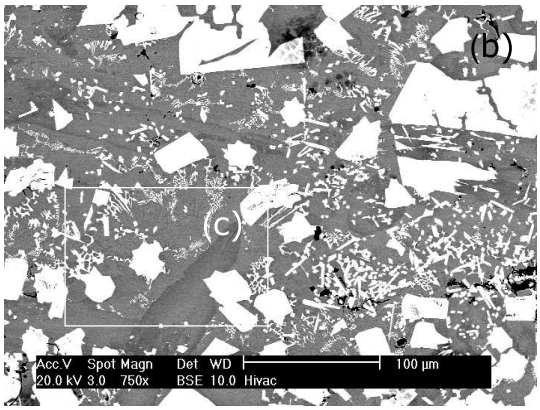

Fig. 6.14(b)

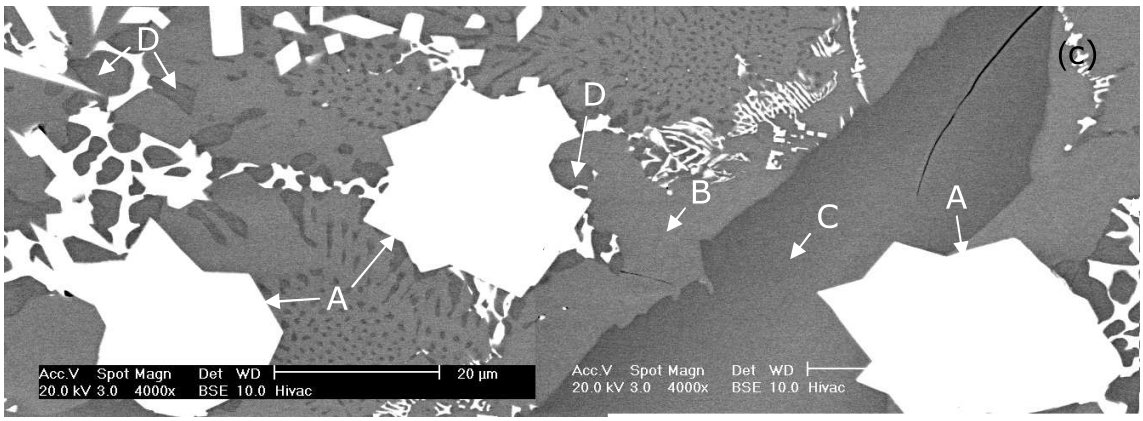

Fig. 6.14(c) at higher magnification of the boxed area (c) in Fig. 6.14(b)

Fig. 6.14 BSE micrographs of the KC1 powder following slow cooling in the DSC at 20K/min (a) low magnification, and (b-c) show higher magnification images of the boxed areas.

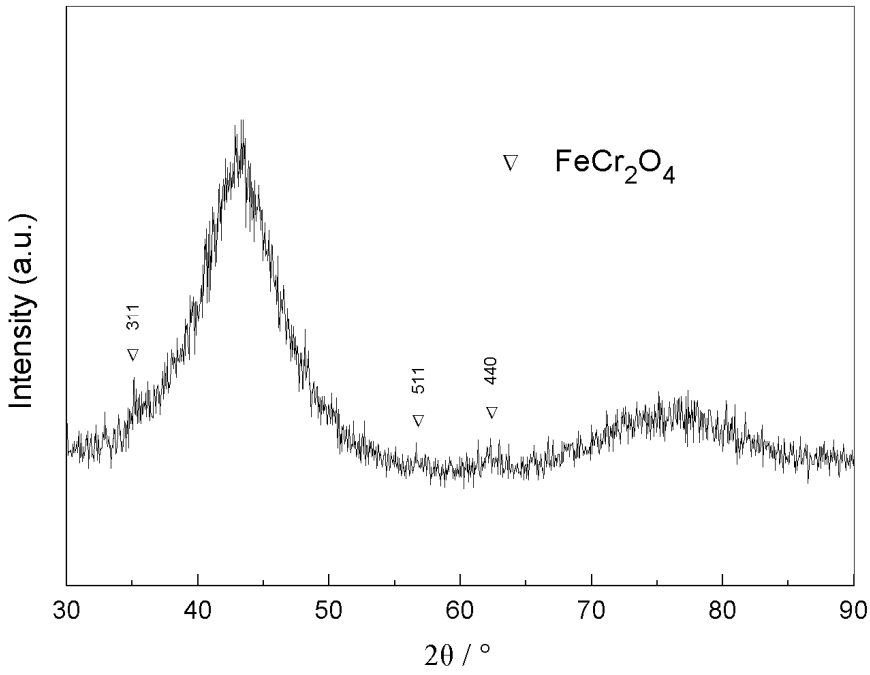

Fig. 6.15 XRD pattern of the as-sprayed coating.

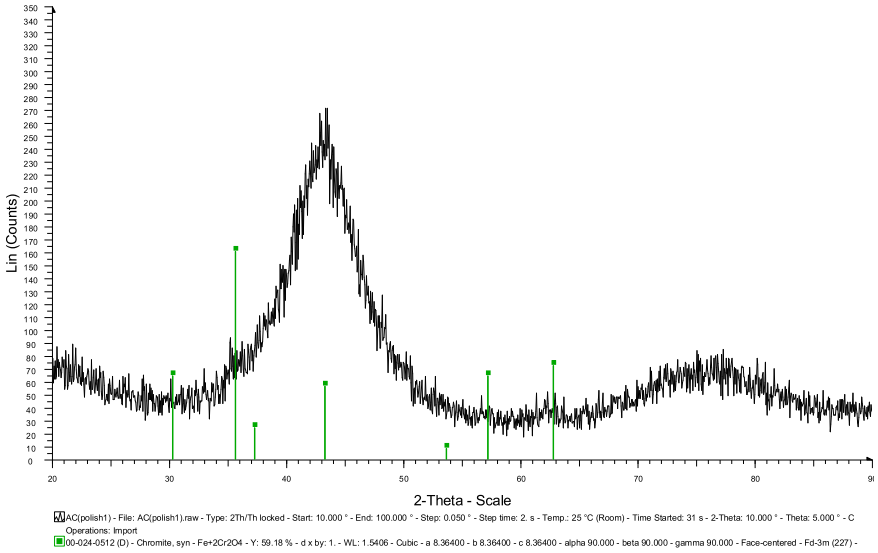

Fig. 6.16 Comparison of experimental XRD pattern (2θ = 20–90°) with JCPDS file for oxide $FeCr_2O_4$.

.

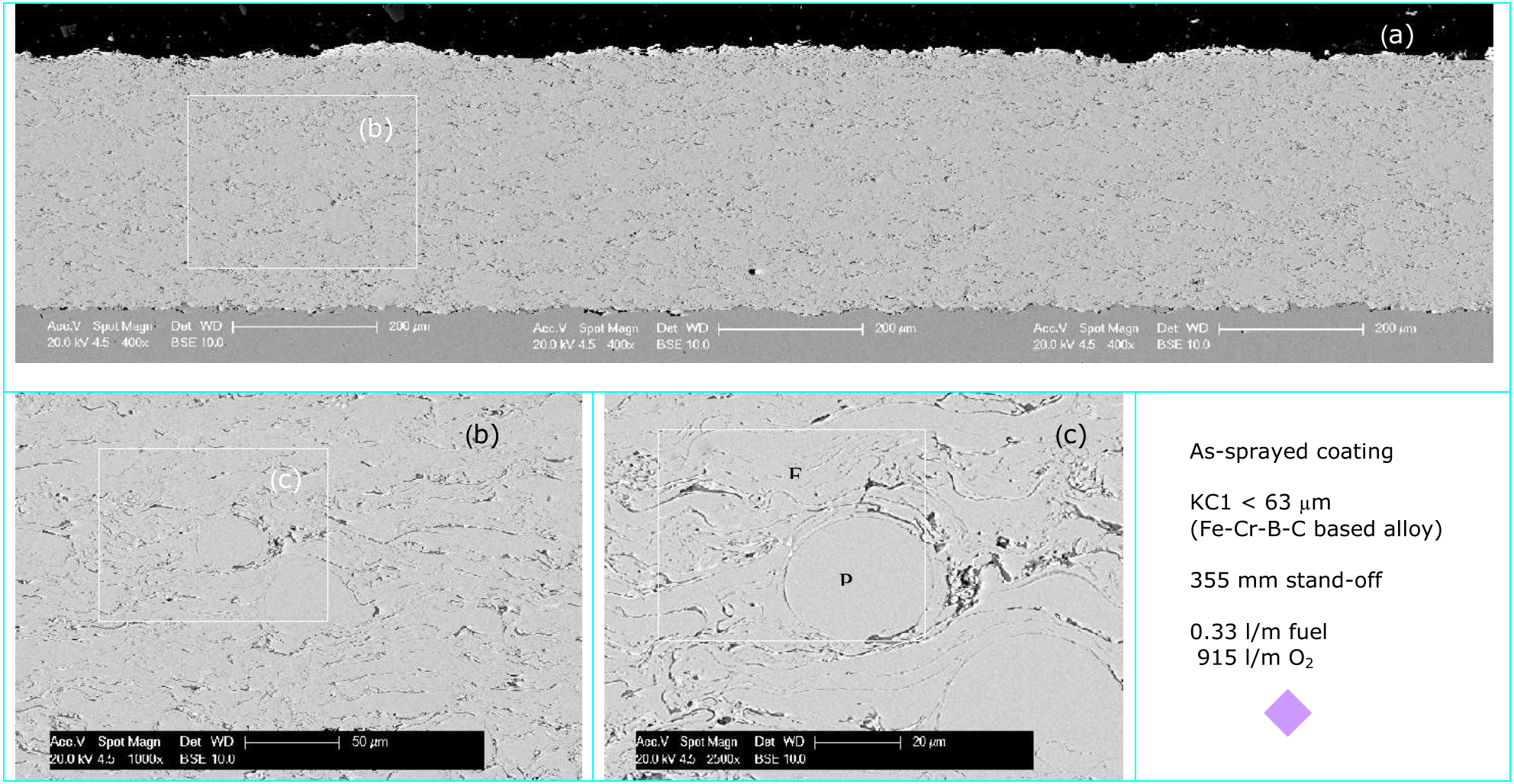

Fig. 6.17 BSE micrographs of cross-sections of a HVOF-sprayed coating: (a) low magnification unetched cross-section. (b),(c) High magnification image of the region b in (a) showing splat-like structure comprising fully melted (F) and partially melted (P) particles.

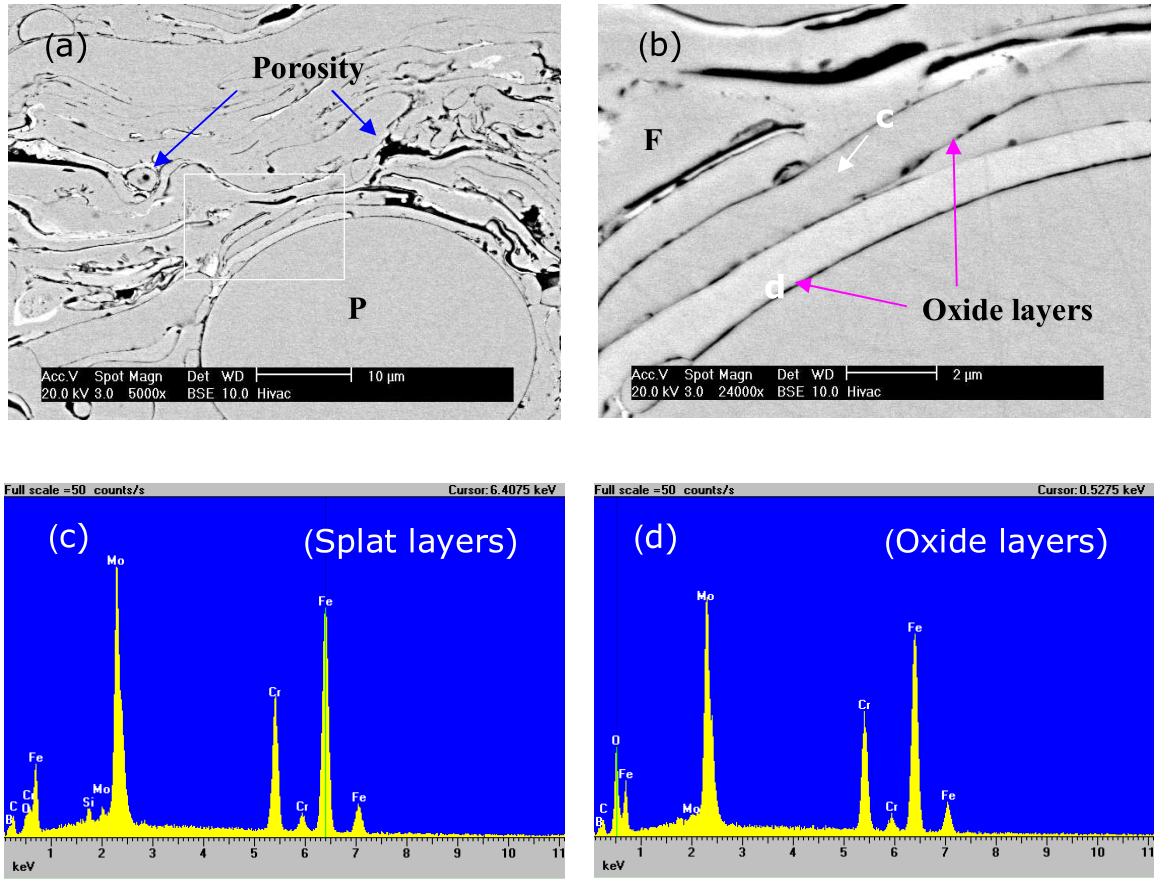

Fig. 6.18 BSE images showing cross-sections of a HVOF-sprayed coating. (a) Higher magnification image of the region P in Fig. 6.17(c) showing unmelted particle, splat layers and porosity. (b) Region F at higher magnification showing oxide layers. (c,d) EDX spectra of regions in image (b) arrowed c and d, respectively.

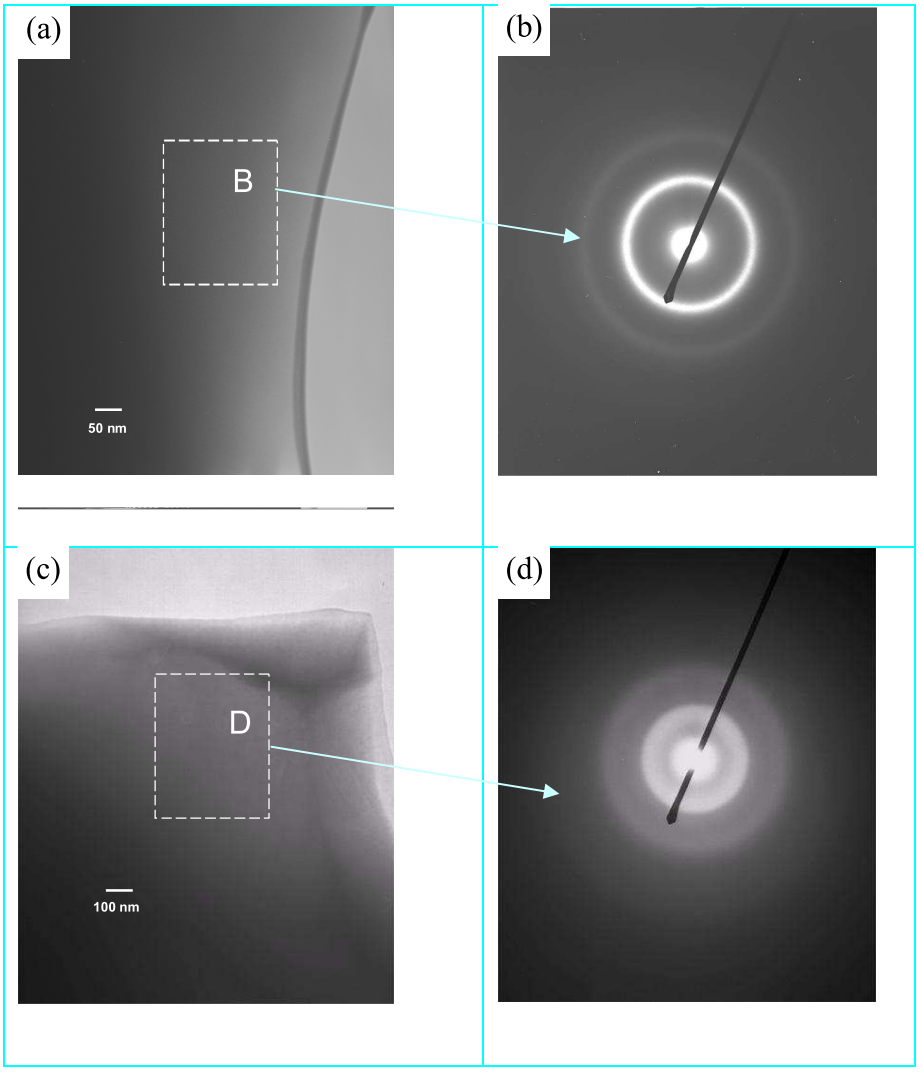

Fig. 6.19 TEM images of the as-sprayed KC1 coating and associated diffraction patterns: (a) Bright field of fully melted region; (b) diffraction pattern of area B in (a). (c) Bright field of some region around (a) and (d) diffraction pattern of the boxed area D in (c).

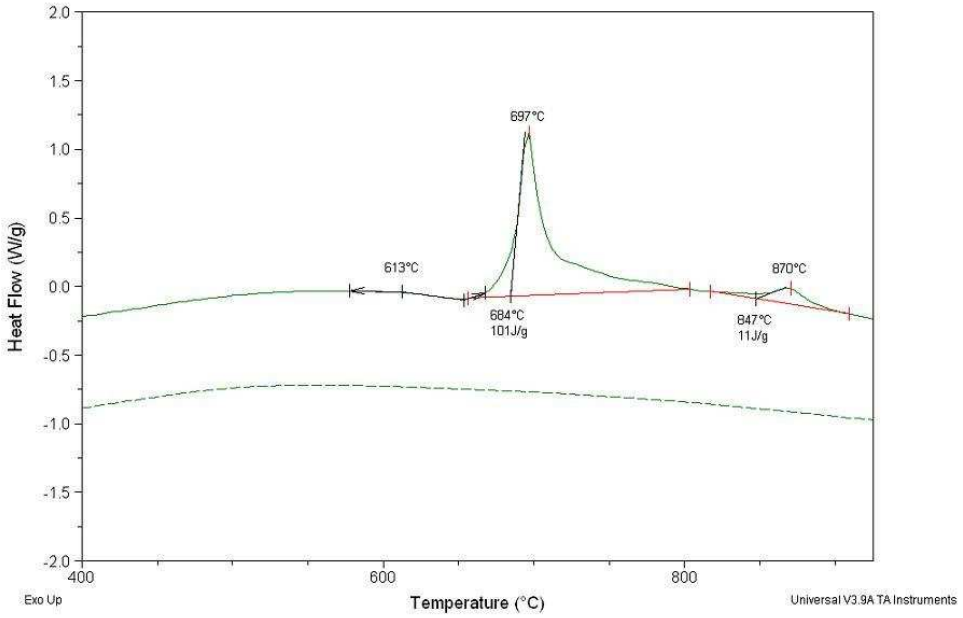

Fig. 6.20(a) DSC analysis of coating, 1st and 2nd heating runs at 20K/min.

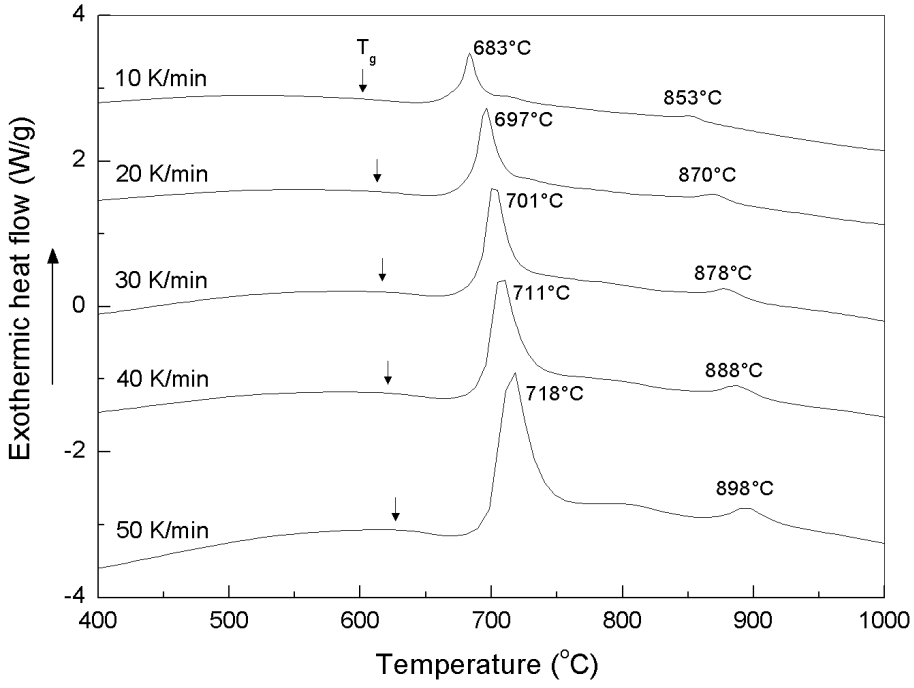

Fig. 6.20(b) DSC analysis of the KC1 coating at heating rates 10 K/min, 20 K/min, 30 K/min, 40 K/min and 50 K/min.

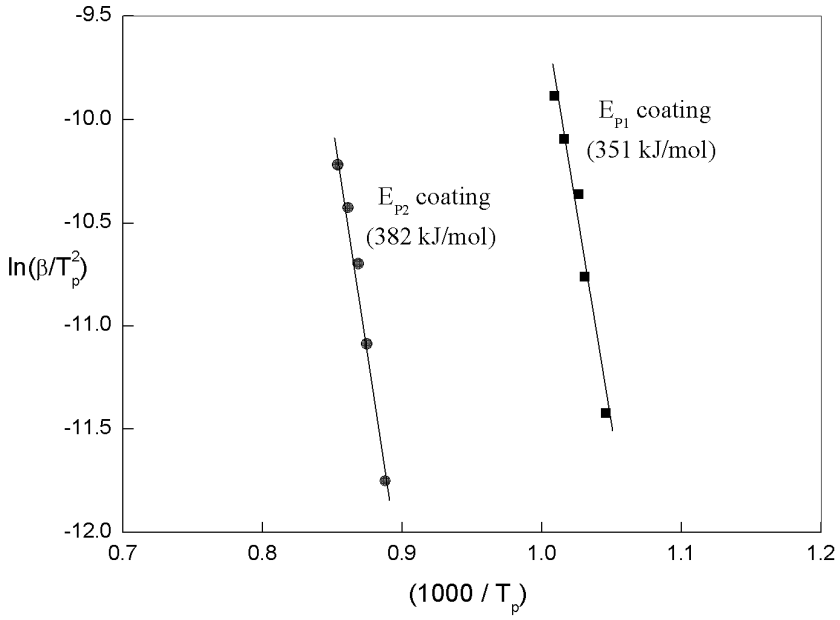

Fig. 6.21 Kissinger's plot of $\ln(\beta/T_p^2)$ versus $1000/T_p$ for peak temperature T_{p1} and T_{p2} of the as-sprayed coating.

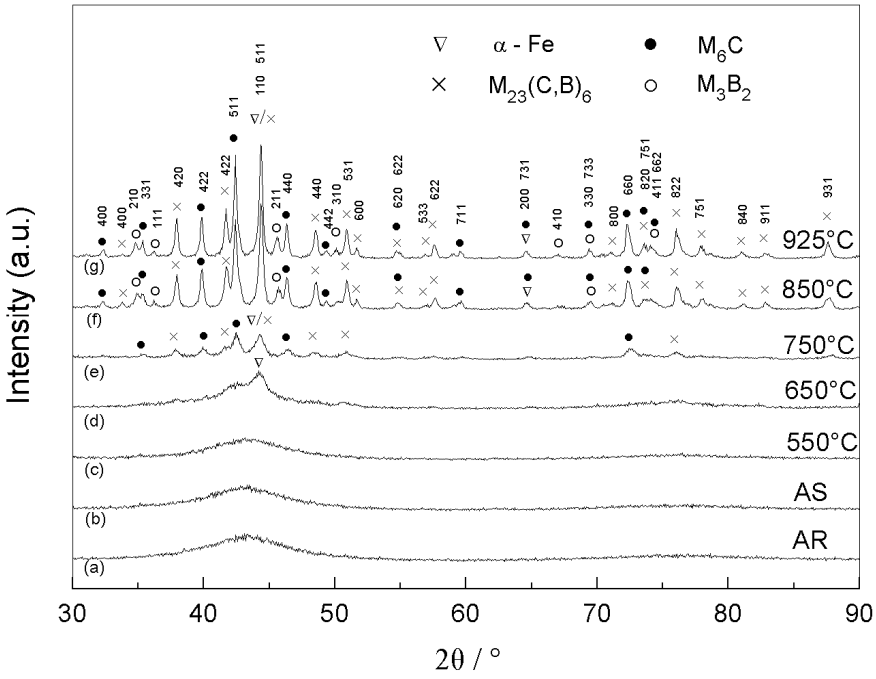

Fig. 6.22 XRD patterns of the as-received powder (AR), as-sprayed coating (AS) and the coatings following heat treatment at 550°C, 650°C, 750°C, 850°C and 925°C for 1 hour.

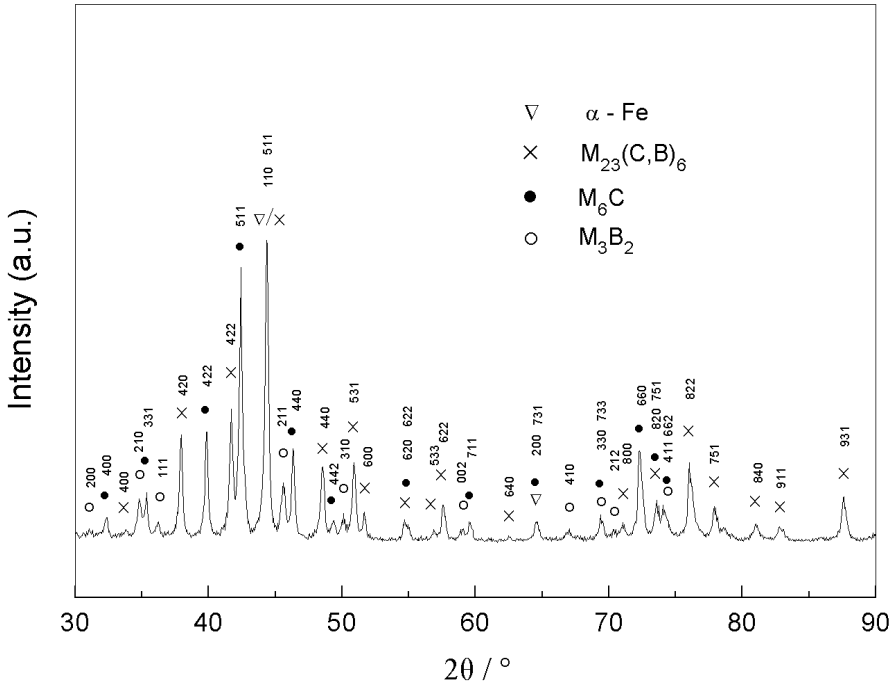

Fig. 6.23(a) XRD patterns for the coating following heat treatment at 925°C for 1 hour.

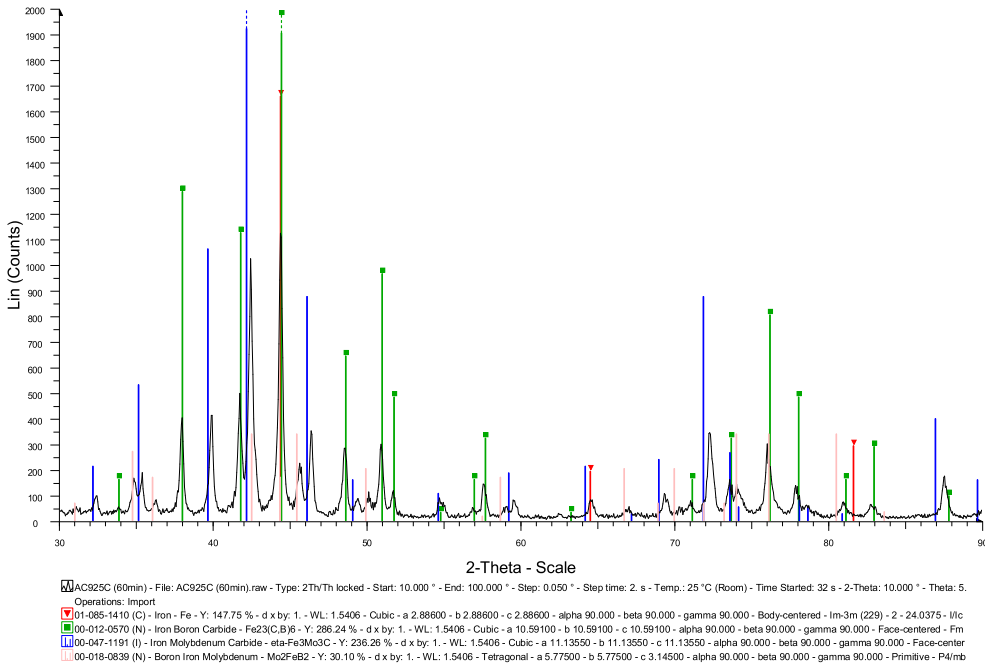

Fig. 6.23(b) Comparison of experimental XRD pattern (2θ = 30–90°) with JCPDS files for α-Fe, $Fe_{23}(C,B)_6$, eta-Fe_3Mo_3C and Mo_2FeB_2

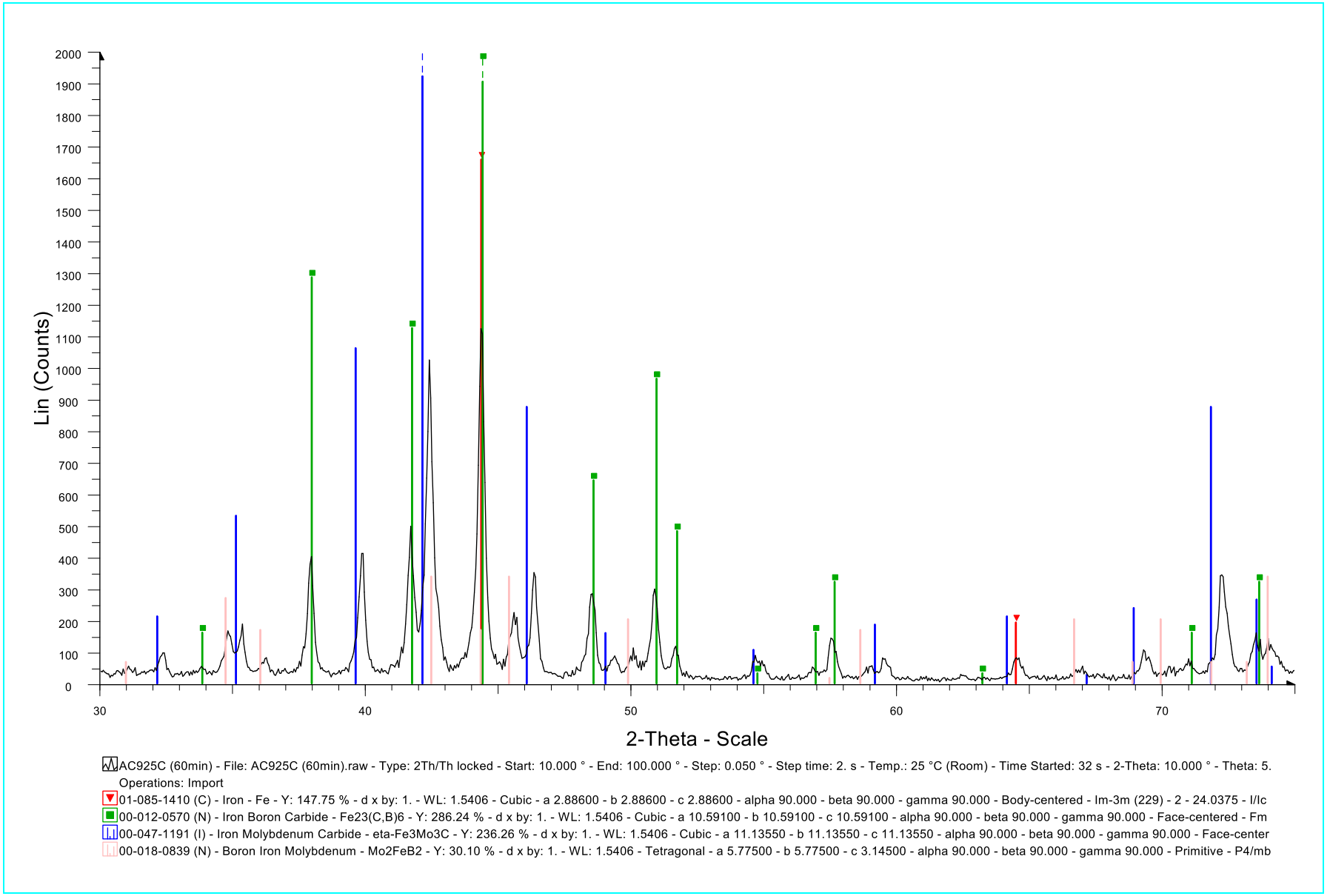

Fig. 6.23(c) Comparison of experimental XRD pattern (2θ = 30–75°) with JCPDS files for α-Fe, $Fe_{23}(C,B)_6$, eta-Fe_3Mo_3C and Mo_2FeB_2

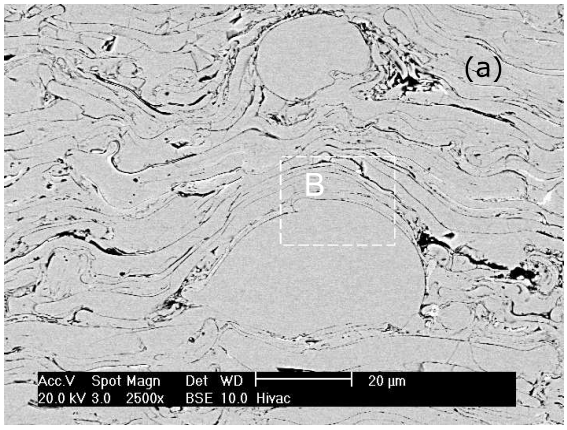

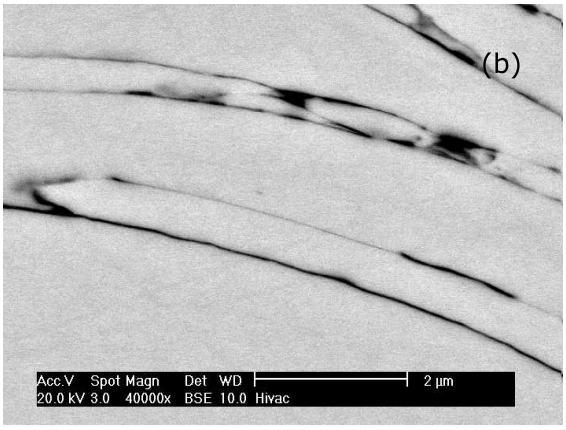

(heat treated at 550°C) (High magnification)

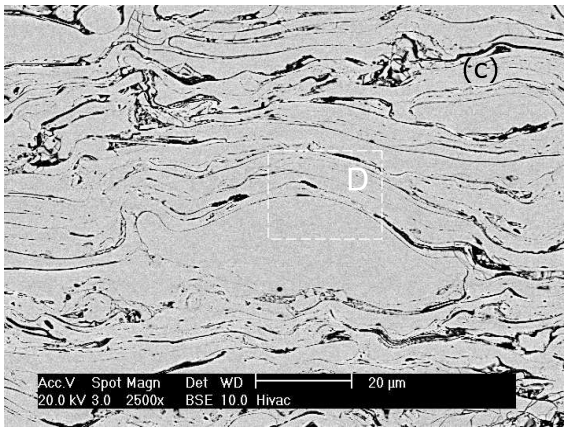

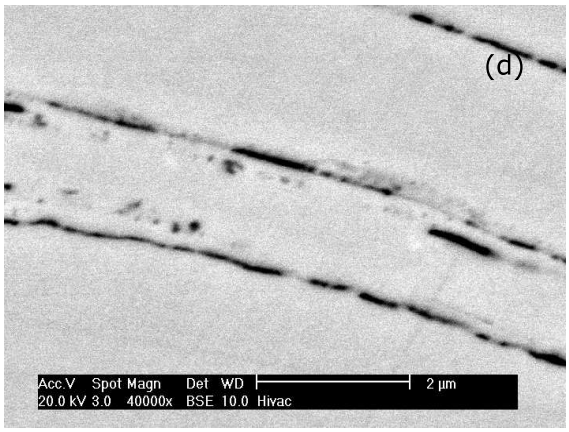

(heat treated at 750°C) (High magnification)

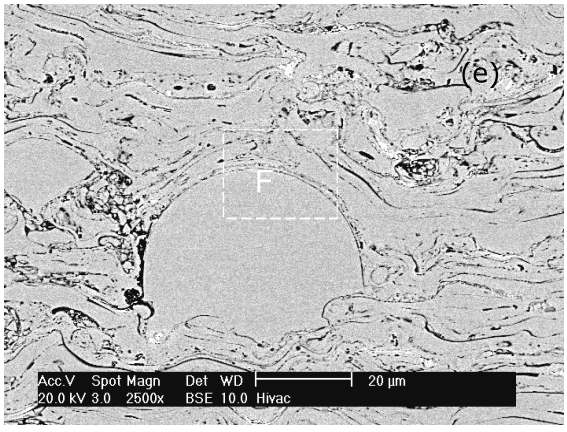

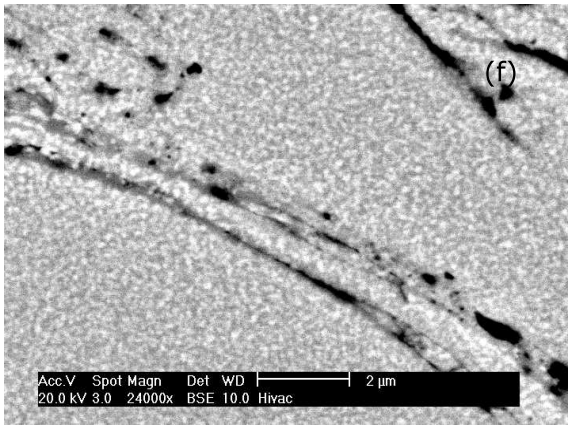

(heat treated at 925°C) (High magnification)

Fig. 6.24 Backscattered electron micrograph of coating following heat treatment at 550°C, 750°C and 925°C (low and high magnification)

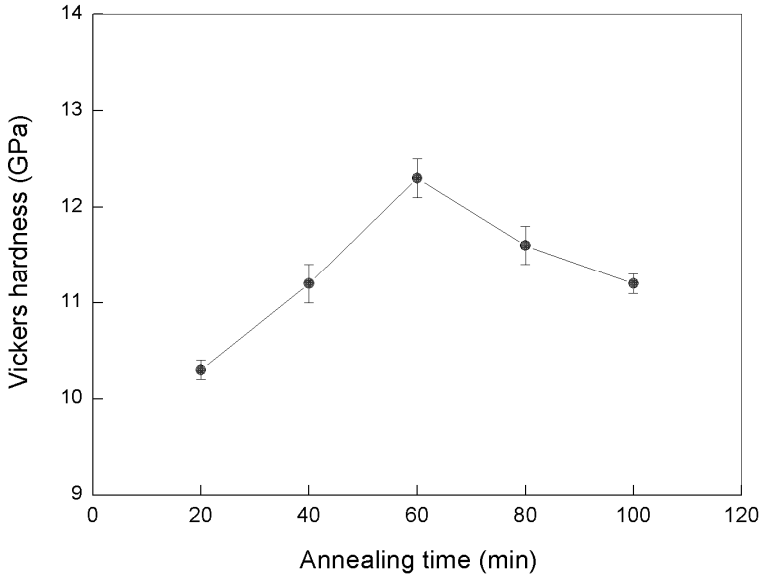

Fig. 6.25 Vickers hardness of the heat treated sample at temperature 850°C vs. annealing times

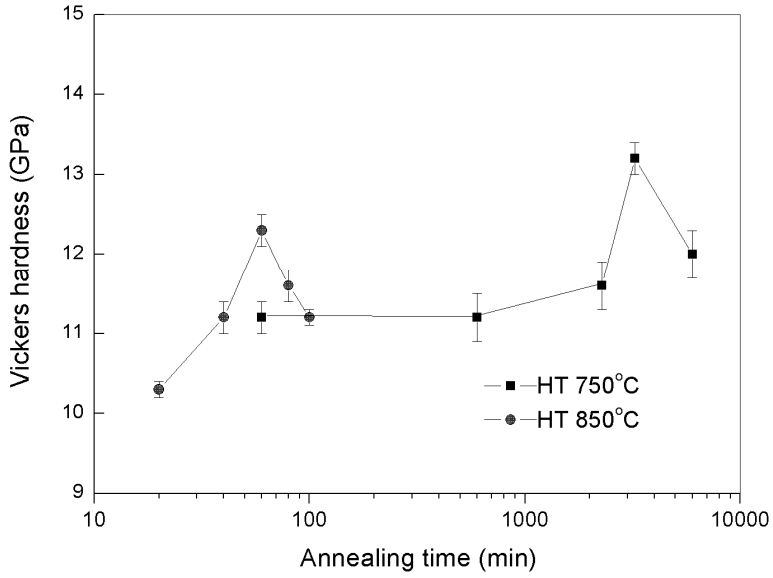

Fig. 6.26 Vickers hardness (GPa) of the samples heat treated at temperature 750°C and 850°C with different holding times

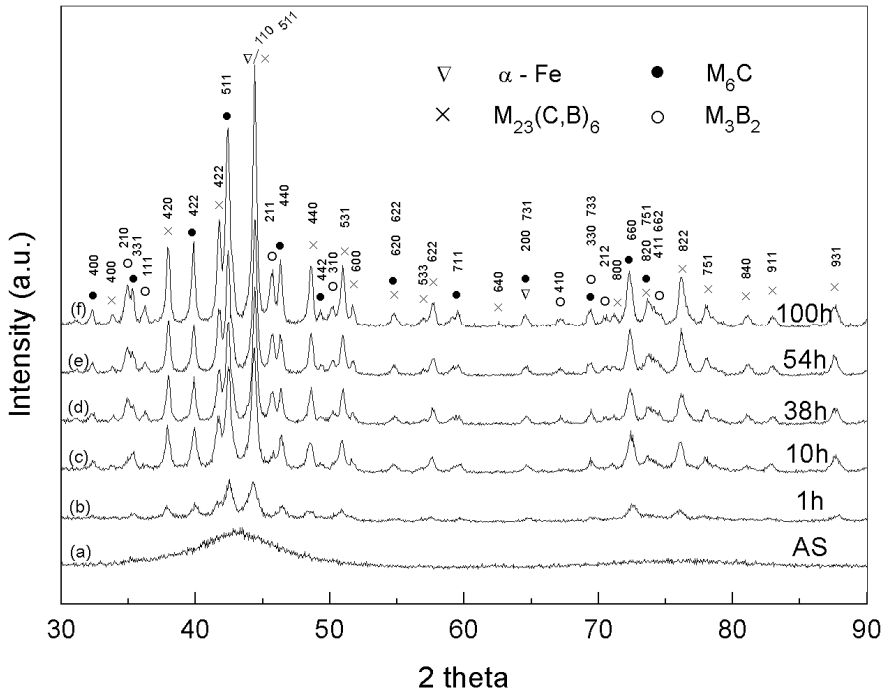

Fig. 6.27 XRD patterns of the as-sprayed coating (AS) and the coatings following heat treatment at 750°C for 1-100 h (ie. 60, 600, 2280 etc. minutes).

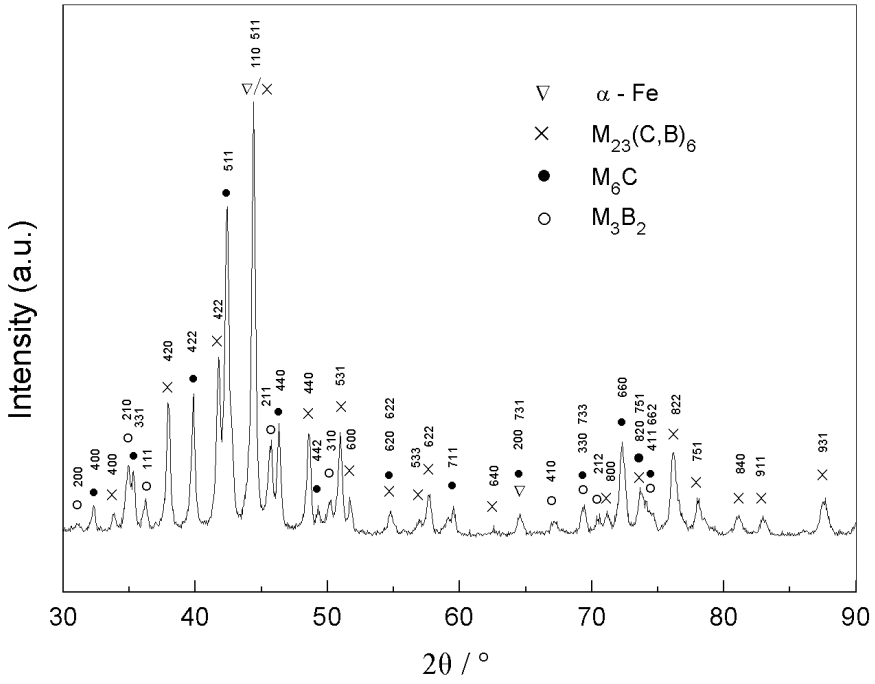

Fig. 6.28 XRD patterns for the coating following heat treatment at 750°C for 100 hour.

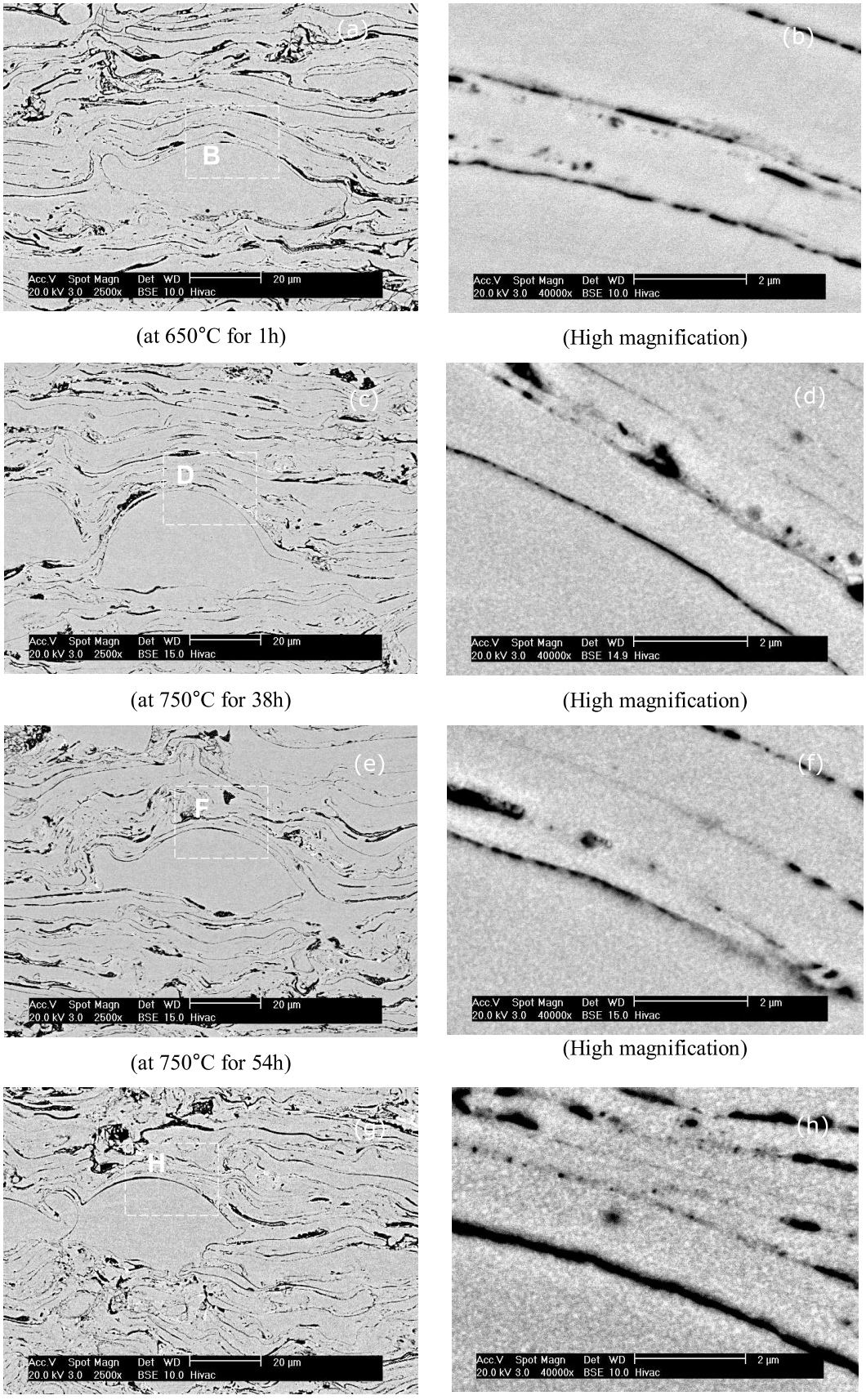

(at 650°C for 1h) (High magnification)

(at 750°C for 38h) (High magnification)

(at 750°C for 54h) (High magnification)

(at 750°C for 100h) (High magnification)

Fig. 6.29 BSE images of the as-sprayed coating and following heat treatment at 750°C for 1h (a and b), 38h (c and d), 54h (e and f) and 100h (g and h).

Chapter 7

Wear of HVOF sprayed Fe-Cr-B based alloy coatings

This chapter describes the ball-on-disc (BOD) sliding wear test results of the as-sprayed Fe-Cr-B based alloy coatings when tested against spherical ceramic (alumina and zirconia) and metal (steel 440C) counterfaces. The tests were performed in dry sliding wear mode. The coatings were examined in two sets of experiments. In the first set the coatings were tested against three different counterface types (alumina, zirconia and steel 440C) at speed of 0.3 m/s for 1000 m under different loads (ranging from 5.8 N to 70 N). The results are reported in terms of coefficient of friction and the average wear rate (calculated by dividing the total volume loss by the total sliding distance) as a function of the applied load. The second set of tests was performed using only an alumina counterface at a load of 23.3 N and at a range of sliding distances. The load of 23.3 N was chosen in order to minimize the degree of damage to the alumina ball, since the debris generated can act as an agressive third body in the test. In addition to the Fe-Cr-B coatings, the sliding wear behaviour of two reference materials (namely mild steel and a thermally sprayed WC-Co-Cr coating) was examined. The mild steel surface was used as a reference material for sliding wear testing at a low load of 23.3 N and the as-sprayed WC-Co-Cr coating was used as a reference material for sliding wear testing at loads of 23.3 N and 70 N. The micrographs of the worn surfaces of both the coatings and the counterfaces are also presented, and the wear mechanisms related to the coating microstructures.

Results

7.1 Coating mechanical properties

The results of hardness and fracture toughness for each coating are presented in Table 7.1. In the present study, the fracture toughness of coatings was determined by an indentation method using a load of 9.8 N and at least 30 indentations from each coating were examined. The indentations on coatings were made along the centreline of the cross-section. Under certain conditions, the material may crack upon indentation, with cracks evaluating from the corner of the Vickers indenter. The equation for indentation fracture toughness given by Evans and Wilshaw was used to calculate the fracture toughness (K_c) of the coatings (Lotfi et al., 2003),

$$K_c = 0.079 \left(\frac{P}{a^{3/2}}\right) \log \left(\frac{4.5a}{c}\right)$$

where P is the applied indentation load (N), the indentation half diagonal (m), and c is the crack length from the centre of the indent (m).

In the case of thermally sprayed coatings, it has been shown that cracking takes place preferentially parallel to the coating-substrate interface. It was found that not all indentations gave rise to cracks parallel to the coating-substrate interface. However, when cracking did occur, c/a values always fell within the range $0.6 \leq c/a < 4.5$ for which the Evans and Wilshaw equation is valid. No cracking was observed following indentation at this load for measurement of fracture toughness for WC-Co-Cr.

Table 7.1 Results of hardness and fracture toughness of the coatings

Coating	Boride phase (%)	Microhardness (GPa)	Fracture toughness (MPa $m^{1/2}$)
Armacor C	37.8	8.50	3.1
Armacor M	64.5	12.09	3.8
SHS7170	35.2	9.38	4.1
WC-Co-Cr	67.2 (carbide)	12.17	N/A

7.2 Friction coefficients

Tables 7.2-7.4 present the average friction coefficient of the sliding samples at steady-state for each test condition for the three counterface types.

The plot of the average coefficient of friction of the sliding samples as a function of applied load during sliding wear testing against alumina ball are shown in Fig. 7.1(a). The coefficient of friction associated with the SHS7170 was almost independent of load, having a value of ~ 0.7, consistently higher than that of the other two materials. The coefficient of friction associated with the Armacor C coating decreased from 0.56, at a load of 5.8 N to 0.47 at a load of 11.7 N and then remained stable with further increase of load. The coefficient of friction of the Armacor M coating slid against alumina ball was 0.43 at the lowest load and then gradually increased with increase of the load, reaching a steady value of ~ 0.58 at a load of 46.6 N.

The plot of the coefficient of friction of the coatings as a function of applied load during sliding wear testing against a zirconia ball are shown in Fig. 7.1(b). The behaviour here is very different to that observed when sliding against alumina. The Armacor C, the Armacor M and the SHS7170 coatings all show low values of coefficient of friction for applied loads below 11.7 N ($\mu \sim 0.2$) which then increase

significantly, with the value associated with the higher loads for SHS7170 being ~ 0.6 and that associated with the other two coatings being ~ 0.45. These values are slightly lower then those observed for sliding against the alumina balls.

The plot of the coefficient of friction of the coatings as a function of applied load during sliding wear testing against a steel 440C ball are shown in Fig. 7.1(c). The Armacor C and the Armacor M coatings show a similar trend, with values of coefficient of friction of ~ 0.2 at the lowest load, which then rise to ~ 0.5 at the higher loads. The coefficient of friction of the SHS7170 again exhibits a low value of ~ 0.2 at the lowest load, which rises to ~ 0.7 as the load is increased.

7.3 Wear rates

Dry sliding wear tests were performed on the as-sprayed HVOF deposited coatings. It was found that under loads of 5.8 N to 23.3 N, the wear rates of the coatings during sliding wear tests against ceramic balls (alumina and zirconia) increased approximately linearly with the load. Volumetric wear rates for each coating are presented in Table 7.2-7.4, being derived from the measured four traces of the cross-section areas from the wear track. These data are presented graphically in Fig. 7.2.

At the low load of 5.8 N to 23.3 N, when the coatings were slid against alumina balls, the SHS7170 coating shows the lowest volumetric wear rate whilst the Armacor C coating exhibits the highest wear rate as shown in Fig. 7.2(a). As the load is increased, Armacor M continues to exhibit a lower wear rate than Armacor C, but that of SHS7170 increases in comparison to these two to become the largest of the three of a load of 70 N.

The wear rates of the coatings when slid against a zirconia ball are shown in Fig. 7.2(b). All the coatings exhibit an approximately linear increase in wear rate with applied load, with the Armacor C sample exhibiting the highest rates of wear at all loads, and the Armacor M and SHS7170 samples exhibiting very similar behaviour. The wear rate of Armacor C increases linearly with load, but it has a significant offset from the origin (i.e. its extrapolated wear rate at zero load is a significant positive value). As such, the ratio of the wear rate of Armacor C to the other materials is high at the lowest loads, and decreases with increasing load.

The wear rate of the SHS7170 coating tested against steel 440C balls exhibits similar behaviour to that of the Armacor M coating tested at all loads as seen in Fig. 7.2(c). Under the loads of 5.8 N to 46.6 N, the wear rate of the Armacor C coating tested against steel 440C balls exhibits lower values than that of the SHS7170 coatings. At a high load of 70 N, the Armacor C coating exhibits a higher wear rate compared to that of the SHS7170 and the Armacor M coatings tested against the steel 440C balls at the same load.

Table 7.2 Sliding wear data for the coatings tested against alumina ball

Specimen	BOD conditions		Friction coefficient	Wear track depth (μm)	Wear track width (mm)	Disc wear rate ($x10^{-15}m^3m^{-1}$)	Ball wear rate ($x10^{-15}m^3m^{-1}$)
	Load (N)	Distance (m)					
Armacor C	5.8	1000	0.56	6.25	0.574	215	0.8
	11.7	1000	0.47	8.50	0.645	334	3.4
	23.3	1000	0.45	10.00	0.967	544	4.0
	46.6	1000	0.47	15.00	1.2	930	18.8
	70.0	1000	0.47	18.50	1.5	1083	33.0
Armcaor M	5.8	1000	0.43	4.50	0.481	127	1.6
	11.7	1000	0.47	8.50	0.766	238	4.6
	23.3	1000	0.49	8.50	1.19	431	25.0
	46.6	1000	0.60	7.00	1.1	595	17.2
	70.0	1000	0.57	13.00	0.88	720	2.9
SHS7170	5.8	1000	0.66	3.00	0.5	75	2.2
	11.7	1000	0.73	3.50	1.1	156	17.9
	23.3	1000	0.69	4.00	1.97	313	130.0
	46.6	1000	0.73	11.50	1.91	623	143.0
	70.0	1000	0.70	12.00	2.62	1229	549.0

Table 7.3 Sliding wear data for the coatings tested against zirconia ball

Specimen	BOD conditions		Friction coefficient	Wear track depth (μm)	Wear track width (mm)	Disc wear rate ($x10^{-15}m^3m^{-1}$)	Ball wear rate ($x10^{-15}m^3m^{-1}$)
	Load (N)	Distance (m)					
Armacor C	5.8	1000	0.23	5.50	0.9	244	4
	11.7	1000	0.16	8.50	0.95	331	6
	23.3	1000	0.29	7.30	1.17	487	18
	46.6	1000	0.44	10.50	1.5	799	45
	70.0	1000	0.41	12.00	1.8	1098	112
Armcaor M	5.8	1000	0.21	3.50	0.8	124	6
	11.7	1000	0.14	4.75	0.95	173	5
	23.3	1000	0.30	5.00	0.98	335	10
	46.6	1000	0.48	15.00	1.35	519	22
	70.0	1000	0.45	20.50	1.7	730	84
SHS7170	5.8	1000	0.22	3.50	0.8	100	13
	11.7	1000	0.19	4.00	1.4	122	64
	23.3	1000	0.56	5.50	1.63	284	178
	46.6	1000	0.62	6.50	2.6	598	516
	70.0	1000	0.55	10.00	2.18	853	696

Table 7.4 Sliding wear data of the coatings tested against 440C ball

Specimen	BOD conditions		Friction coefficient	Wear track depth (μm)	Wear track width (mm)	Disc wear rate ($x10^{-15}m^3m^{-1}$)	Ball wear rate ($x10^{-15}m^3m^{-1}$)
	Load (N)	Distance (m)					
Armacor C	5.8	1000	0.27	1.50	1.54	37	70
	11.7	1000	0.46	3.00	1.27	112	167
	23.3	1000	0.58	3.50	2.04	160	287
	46.6	1000	0.52	5.50	1.73	203	304
	70.0	1000	0.45	11.00	2.08	528	490
Armcaor M	5.8	1000	0.25	1.00	1.2	36	72
	11.7	1000	0.47	2.25	1.3	84	140
	23.3	1000	0.41	6.00	1.56	272	123
	46.6	1000	0.58	6.00	2.1	393	260
	70.0	1000	0.49	5.75	2.26	379	255
SHS7170	5.8	1000	0.23	12.00	1.22	66	47
	11.7	1000	0.37	12.00	1.63	177	99
	23.3	1000	0.57	5.50	1.98	257	225
	46.6	1000	0.77	6.50	1.9	367	205
	70.0	1000	0.70	10.00	1.78	345	259

As well as measuring the wear of the coatings of interest, the wear rates of the balls slid against the coatings were also measured. The results for the wear rate of alumina balls slid against the three coating types are shown in Table 7.2 and plotted in Fig. 7.3(a). It can be seen that the wear rate of alumina balls slid against the Armacor C and the Armacor M coatings was similar to that of the alumina balls slid against the SHS7170 coating at a low load of 5.8 and 11.7 N, exhibiting a very small value in each case. However, at a higher load of 23.3, 46.6 and 70 N, the wear rate of alumina balls slid against the SHS7170 coating was an order of magnitude (or more) higher than that of those slid against the Armacor C and the Armacor M coatings.

The results for the wear rate of zirconia balls slid against the three coating types are shown in Table 7.3 and plotted in Fig. 7.3(b). It can be seen that the wear rate of zirconia balls slid against the Armacor C coating was, at all loads, similar to that of

the zirconia balls slid against the Armacor M coating. However, the wear rate of zirconia balls slid against the SHS7170 coating was considerably higher than that of the zirconia balls slid against the Armacor C and the Armacor M coatings at all loads.

The wear rate of steel 440C balls slid against three coating types are shown in Table 8.4 and plotted in Fig. 7.3(c). It can be seen that the wear rate of steel 440C balls slid against the Armacor C coating was, at loads of 5.8, 11.7, 23.3 and 46.6 N, similar to that of the steel 440C balls slid against the Armacor M coating and the SHS7170 coating at the same loads. However, the wear rate of steel 440C balls slid against the Armacor C coating was considerably higher than that of the steel 440C balls slid against the Armacor M and the SHS7170 coatings at a high load of 70 N.

By comparing Figs. 7.3(a), 7.3(b) and 7.3(c), it is notable that the wear rates of the alumina and zirconia balls slid against Armacor M and Armacor C are significantly lower across the range of applied loads than for the 440C ball slid against the same two materials. In contrast, the wear of the alumina and zirconia balls against SHS7170 is generally higher than it is for the 440C steel ball slid against the same material.

7.4 Observations of wear scars

The topology (3D-Profile) of the coatings following sliding wear testing against alumina, zirconia and steel 440C counterfaces was investigated in order to provide more understanding of the evolution of material loss. The depth and width of these

wear tracks were measured and these are presented in table 7.2-7.4 along with the coefficient of friction and wear rate of the coatings as a function of applied load.

Additionally, the microstructural examination of the worn surface by SEM was also used to further identify the wear mechanism of the coatings and the results will be shown in the following sections.

7.4.1 Microstructural observation of the worn surface of the as-sprayed coatings slid against an alumina ball

To understand the wear behaviour, the worn surface was examined by SEM. The SEM plan view and cross-sectional view images of the worn surfaces of the coatings following sliding wear with an alumina ball under a load of 23.3 N and 70 N along with the topology (3D-Profile) of the coatings are shown in Fig.7.4- Fig.7.6.

Fig. 7.4(a) shows the topology of the Armacor C coating following sliding wear test against alumina ball under a load of 23.3 N, revealing that the worn surfaces exhibits a deep groove (with a depth of ~ 10 μm). In Fig. 7.4(b) and (c) (SEM plan view images of the worn surfaces of the Armacor C coating) a relatively smooth surface can be seen with some signs of coating delamination. Fig. 7.4(d) (an SEM cross-sectional view images of the worn surface of the Armacor C coating) shows some cracking near the surface. However, under a load of 70 N, the topology of the worn surface is wider and deeper as shown in Fig. 7.4(e) (with a depth of ~ 18.5 μm) and Fig. 7.4(f)-(g) (the SEM plan view images of the worn surface of the Armacor C coating) show significant pitting and delamination. Fig. 7.4(h) (the SEM cross-sectional view images of the worn surface of the Armacor C coating) shows

significant subsurface disruption with cracks running along splat boundaries resulting in coating removal.

Similar wear behaviour to that observed for the Armacor C coating can be observed for the Armacor M coating (Fig. 7.5). In Fig. 7.5(a) (the topology of the Armacor M coating following a sliding wear test against an alumina ball at a load of 23.3 N) shows wear to a depth of 8.5 μm. The SEM plan view images of the surface are shown Fig. 7.5(b) and (c), showing a relatively flat surface with small scale pitting and delamination. Fig. 7.5(d) (the SEM cross-sectional view image) shows some cracking and fragmentation near the surface. At the highest load of 70 N, the topology of the wear track of the Armacor M coating (Fig. 7.5(e)) is narrower but deeper than that observed at a load of 23.3 N. The SEM plan view image of the worn surfaces of the coating (Fig. 7.5(f)) reveals a wear track of approximately 0.88 mm in width, with more cracking along splat boundaries as shown in Fig. 7.5(g). Fig. 7.5(h), the BSE-SEM cross-sectional view image of the worn surfaces again confirms that the coating exhibits more significant subsurface disruption with coarse subsurface cracking running along splat boundaries.

Substantially different wear behaviour can be observed for the SHS7170 coating following sliding wear testing against an alumina ball as shown in Fig. 7.6. Fig. 7.6(a) shows the topology of the wear track of the SHS7170 coating following sliding at a load of 23.3 N which exhibits a relatively rough surface with some grooves being observed. The wear track is shallow but wide compared to the comparative tracks in Armacor C and Armacor M (Figs. 7.4(a) and 7.5(a)).

The SEM plan view images of the worn surfaces are shown in Fig. 7.6(b)-(c). The SHS7170 coating exhibits a relatively rough morphology, with oxide layers on the worn surface being easily distinguishable, indicating that mild adhesive wear is occurring. However, the evidence of pitting and delamination can also be observed as shown in Fig. 7.6(c). Fig. 7.6(d) shows the cross-sections of these wear scars. There is no clear evidence for subsurface cracking.

At the higher load of 70 N, the topology of the wear track (Fig. 7.6(e)) exhibits a wider and deeper scar compared to that of the coating tested against the alumina ball at a load of 23.3 N (Fig. 7.4(a)). The worn surface shows extensive damage in the form of delamination and oxide-based transfer layers (Fig. 7.6(f) and (g)). Examination of the cross-sectional image of the wear track by BSE-SEM, Fig. 7.6(h) shows evidence of intersplat delamination. However, the damage is apparently less extensive than that of the Armacor C coating in Fig. 7.4(h) and the Armacor M coating in Fig. 7.5(h) at the same load. It can also be seen in Fig. 7.6(h) that alumina wear debris (from the ball) has been incorporated into the oxide-based transfer layer.

7.4.2 Microstructural observation of the worn surface of the as-sprayed coatings slid against a zirconia ball

Coating wear scars for all three coating types resulting from sliding wear with the zirconia ball under a load 23.3 N are shown in Fig. 7.7. Topology of the Armacor C, Armacor M and SHS7170 coatings following sliding wear test against zirconia ball are shown in Fig. 7.5(a), (b) and (c), respectively. The worn surface of the Armacor C coating exhibits a deep groove with similar to that of the Armacor M coating. In

contrast, the wear track on the SHS7170 coating is wider but shallower than that of those two coatings.

Fig. 7.7(d)-(f) shows the cross-sections of these wear scars. In the Armacor C and Armacor M coatings, Fig. 7.7(d) and (e), coarse subsurface cracking is observed which appears to propagate along splat boundaries. However, there is a little evidence for such subsurface cracking for the SHS7170 coating as shown in Fig. 7.7(f). Again, the depressions on the surface can be seen to have been filled with an oxide-based debris.

7.4.3 Microstructural observation of the worn surface of the as-sprayed coatings slid against a steel 440C ball

The topology (3D-Profile), SEM plan view and cross-sectional view images of the worn surfaces of the coatings following sliding wear with steel 440C ball under a load of 23.3 N and 70 N are shown in Figs.7.8- Fig.7.10.

Fig. 7.8(a) shows the topology of the Armacor C coating following sliding wear testing against a 440C ball under a load of 23.3 N which exhibits wear grooves on the worn surface. Figs. 7.8(b) and (c) (the SEM plan view images of the worn surfaces of the Armacor C coating) show a relatively smooth surface with larger patches of oxide-based transferred material. Fig. 7.8(d) (the SEM cross-sectional view image) shows little evidence of subsurface cracking and oxide-based transfer layers on the top of the worn surface can be observed (as the dark region).

However, under a load of 70 N, the topology of the wear track (Fig. 7.8(e)) exhibits a wider and deeper groove compared to that of the groove in the coating tested against the 440C ball at a load of 23.3 N. Figs. 7.8(f) and (g) (the SEM plan view images) exhibit a relatively smooth morphology with scratch marks on the worn surface as well as pitting and delamination. The SEM cross-sectional view image of the worn surface of the Armacor C coating shows the oxide layers on the worn surface (the dark regions) and more evidence of subsurface disruption (Fig. 7.8(h)).

The topology of the wear track of the Armacor M coating following sliding wear testing against a 440C ball at a load of 23.3 N reveals deep grooves of the contact edges on the surface as shown in Fig. 7.9(a). The SEM plan view images of the worn surface of the Armacor M coating (Figs. 7.9(b) and (c)) exhibit a relatively flat surface with small scale pitting and delamination. Fig. 7.9(d) (the SEM cross-sectional view image of the worn surface of the Armacor M coating) shows some cracking and pitting near the surface. It appears that some pits have been filled with wear debris.

At the highest load of 70 N, the topology of the wear track of the Armacor M coating (Fig. 7.9(e)) is wider but shallower than that of the scar in the Armacor M coating tested against the 440C ball at a load of 23.3 N (Fig. 7.9(a)). The SEM plan view of the worn surface of the Armacor M coating following sliding against a 440C ball under a load of 70 N are shown in Fig.7.9(f) and (g). Fig. 7.9(g) shows that the coating exhibits a relatively smooth morphology with scratch marks and larger patches of transferred material on the worn surface. Fig. 7.9(h), the BSE-SEM cross-sectional view image of the worn surface again confirms that the coating exhibits

more significant subsurface disruption with coarse subsurface cracking running along splat boundaries.

The topology and the SEM plan view images of the worn surfaces of the SHS7170 coating resulting from sliding wear with 440C ball under loads of 23.3 N and 70 N are shown in Fig. 7.10. Following sliding at 23.3 N, the SHS7170 coating exhibits a relatively rough morphology and the evidence of pitting and delamination can be observed as shown in Fig. 7.10(b). Fig. 7.10(c) (the SEM cross-sectional view image of the worn surface of the SHS7170 coating) shows significant subsurface cracking.

In contrast, at a higher load of 70 N, the worn surface of the SHS7170 coating (Fig. 7.10d) is smoother compared with that of the SHS7170 coating tested against 440C ball under a load of 23.3 N as shown in Fig. 7.10(a). Fig. 7.10(e) (the SEM plan view image of the worn surface) shows a relatively smooth surface and oxide layers on the worn surface are easily distinguishable, indicating that preferential adhesive wear is occurring. Examination of the cross-sectional image of the wear track by BSE-SEM, Fig. 7.10(f) shows little evidence of sub-surface cracking as compared to that of the Armacor M coating in Fig. 7.9(h) at the same load. Again, an oxide is observed in the cross-section (Fig. 7.10f).

7.4.4 Microstructural observation of the worn surface of the as-sprayed WC-Co-Cr coating slid against an alumina ball and a steel 440C ball at a high load of 70 N

The worn surfaces of the WC-Co-Cr coating following sliding wear with an alumina ball under a load of 70 N reveals a wear track of approximately 1.1 mm in width,

Fig. 7.11(a). A large number of pits and delamination on the sample surfaces can be observed as shown in Fig. 7.11(b). Fig. 7.11(c), a plan view at higher magnification shows some material loss from the wear track and cracking of the surface.

Fig. 7.11(d) is the SEM plan view image of the worn surface of the WC-Co-Cr coating tested against steel 440C ball under a load of 70 N, showing the wear track which is about 1.7 mm in width. Plan view images at higher magnification Figs. 7.11(e) and 7.11(f), indicates that the worn surface exhibits a significantly higher degree of delamination and transferred layer formation as compared to that of the worn surfaces of the WC-Co-Cr coating tested against alumina ball under a load of 70 N, Fig. 7.11(b).

7.4.5 Microstructural observation of the worn surface of alumina ball slid against three coating types

Fig. 7.12 shows the SEM images of the wear scar on alumina balls following sliding against the Armacor C coating at a load of 23.3 N. A low magnification, SE-SEM image of the wear scar of alumina ball (Fig. 7.12(a)) shows that the wear scar was typically about 0.7 mm in diameter and Fig. 7.12(b) (a BSE-SEM image of the same region as wear scar of imaged in Fig. 7.12(a)) shows a little evidence of material from the Armacor C having been adhered to the worn surface. A higher magnification SE-SEM image, Fig. 7.12(c) of the selected area C in Fig. 7.12(a) shows a relatively rough surface and some material adherence to the worn surface. A corresponding BSE-SEM image (Fig. 7.12(d)) shows the contrast of the material adhered to the worn surface. Bright areas indicate a higher mean atomic number and dark contrast areas have lower mean atomic number. Fig. 7.12(e), a higher

magnification SE image of the adhered material, shows clearly a smooth surface with some cracking. EDX analysis of the adhered region A in Fig. 7.12(e) is shown in Fig. 7.12(f) and confirms that this layer consists of the coating material (Armacor C) adhered to the counterface. There is also a strong oxygen peak, which is associated with the adhered material having been oxidised in the transfer process. If this oxygen had been associated with EDX signal from the underlying alumina ball, then a signal for aluminium would have been present too which is not the case.

Fig. 7.13 shows the SEM images of the wear scar on alumina ball following sliding against the Armacor M coating at a load of 23.3 N. A low magnification, SE-SEM image of the wear scar of alumina ball (Fig. 7.13(a)) shows that the wear scar was typically about 1.25 mm in diameter which is larger than that of the wear scar following sliding against the Armacor C coating (Fig. 7.12(a)). Fig. 7.13(b) the corresponding BSE-SEM image shows evidence of a small amount of coating material transferred to the worn surface. A higher magnification SE-SEM image (Fig. 7.13(c)) shows a relatively rough ball surface and the corresponding BSE-SEM image (Fig. 7.13(d)) reveals some small patches of coating materials transferred to the worn surface (the bright areas). Fig. 7.13(e), a higher magnification SE-SEM image of the selected area in Fig. 7.13(c) shows clearly a fracture surface of the wear scar with the adhered material. EDX analysis (Fig. 7.13(f)) of the selected area labelled ‘A’ in Fig. 7.13(e) shows a high peak of aluminium and oxygen and low intensities of Fe, Cr and Si indicating evidence of the material transferred to the worn surface of the counterface is very thin, allowing EDX signal from the alumina ball below the surface to be detected.

Fig. 7.14 shows the SEM images of the wear scar on alumina ball following sliding against the SHS7170 coating at a load of 23.3 N. A low magnification, SE-SEM image of the wear scar of alumina ball, Fig. 7.14(a) shows that the wear scar was typically about 2.0 mm in diameter which is larger than those of the wear scars of the alumina ball tested against the Armacor C and the Armacor M coatings (Fig. 7.12(a) and 7.13(a), respectively). Fig. 7.14(b), the corresponding BSE-SEM image of Fig. 7.14(a) shows more evidence of material having been transferred to the worn surface (as the bright area). A higher magnification SE-SEM image, Fig. 7.14(c) of the selected area C from Fig. 7.14(a) shows a relatively rough surface and large patches of transferred material. The corresponding BSE-SEM image, Fig. 7.14(d) shows the different contrast of the adhered material. A higher magnification BSE image of the transferred layer shows a relatively smooth surface (Fig. 7.14(e)). This material can be shown to contain high levels of Fe, Cr by EDX analysis in Fig. 7.14(f), indicating that this transferred material is predominantly from the SHS7170 coating. Again, there is a reasonably high aluminium content in the transfer film. It is not clear as to whether this is fractured alumina debris in the transfer film or whether the transfer film is thin.

Wear scars of the counterfaces tested against the three coating types at the highest load of 70 N are shown in Fig. 7.15. Fig. 7.15(a) and (b), show the SEM images of the wear scar on the alumina ball following sliding against the Armacor C coating. The wear scar reveals the evidence of a large patch of adhered material with relatively smooth surface, whereas the wear scar on the alumina ball slid against the Armacor M (Fig. 7.15(c) and (d)) exhibit a relatively rough surface with little evidence of large scale transferred material. Fig. 7.15(e) shows that the wear scar of

the alumina ball slid against the SHS7170 coating was typically about 2.6 mm in diameter which was larger than those following sliding against the Armacor C and the Armacor M coatings (Fig. 7.15(a) and (c), respectively). However, the wear scar following sliding against the SHS7170 coating (Fig. 7.15(e) and (f)) exhibits patches of transferred material from the coating. However, these patches of transferred material are not as extensive as those observed following sliding against Armacor C (Fig. 7.15(a)).

7.4.6 Microstructural observation of the worn surface of zirconia ball slid against three coating types at a load of 23.3 N

Fig. 7.16 shows the SEM images of the wear scars on the zirconia balls following sliding against the Armacor C coating at a load of 23.3 N. A low magnification, SE-SEM image of the wear scar of zirconia ball, Fig. 7.16(a) shows that the wear scar was typically about 1.1 mm in diameter and Fig. 7.16(b), the corresponding BSE-SEM image, shows a transferred layer with a higher contrast. The contrast difference is exaggerated due to the higher backscattering coefficient of zirconia compared to that of alumina due to its higher average atomic number. A higher magnification SE-SEM image, Fig. 7.16(c) of the selected area C in Fig. 7.16(a) shows a transfer layer on the worn surface. Fig. 7.16(d) a higher magnification SE-SEM image of a transfer layer in Fig. 7.16(c) shows a relatively smooth morphology with evidence of ploughing and cracking in the layer. EDX analysis of selected area labelled ‘A’ in Fig. 7.16(d) shows a high peak of Fe, Cr and Ni, indicating that this transferred material from the Armacor C coating. The high oxygen peak is partly associated with zirconia itself (either as fragmented debris or from the bulk) and may also be associated with oxides of the elements from the Armacor C.

Fig. 7.17 shows the SEM images of the wear scar of zirconia ball following against the Armacor M coating at a load of 23.3 N. A low magnification, SE-SEM image of the wear scar of zirconia ball, Fig. 7.17(a) shows that the wear scar was typically about 0.9 mm in diameter which is smaller than that following against the Armacor C coating. Fig. 7.17(b), the corresponding BSE-SEM image shows some evidence of coating material having been transferred to the worn surface (indicated by the low contrast region). A higher magnification SE-SEM image, Fig. 7.17(c) and BSE-SEM image (Fig. 7.17(d)) show a relatively rough surface with a transfer layer on the surface. Fig. 7.17(e), a higher magnification SE-SEM image of the transfer layer shows the agglomerated nature of the layer. EDX analysis of selected area labelled 'A' in Fig. 7.17(e) shows peaks of Fe, Cr and Si, indicating that this is in part transferred material from the Armacor M coating.

Fig. 7.18 shows the SEM images of the wear scar of zirconia ball following sliding against the SHS7170 coating at a load of 23.3 N. A low magnification, SE-SEM image of the wear scar of zirconia ball, Fig. 7.18(a) shows that the wear scar was typically about 2.0 mm in diameter which is considerably larger than those of the corresponding wear scars following sliding against the Armacor C and the Armacor M coatings (Fig. 7.16(a) and 7.17(a), respectively). Fig. 7.18(b), the corresponding BSE-SEM image of Fig. 7.18(a) shows evidence of a significant amount of material transferred on the worn surface (as the dark area). A higher magnification SE-SEM image, Fig. 7.18(c) and BSE-SEM image (Fig. 7.18(d)) of the wear scar from the selected area (c) in Fig. 7.18(a) show a relatively rough surface with significant amounts of debris adhered to the worn surface.

Fig. 7.18(e) and (f) show SE-SEM and BSE-SEM images, respectively of a transfer layer in Fig. 7.18(c). BSE image of transferred layer, Fig. 7.18(f) indicates that the transfer layers had lower mean atomic number and exhibits darker contrast compared to that of the counterface (brighter region). A relatively rough surface with some crack can be observed as shown in Fig. 7.18(f). The transfer layers (the dark area with labelled 'A') observed in Fig. 7.18(f) can be shown to contain higher levels of Fe and Cr by EDX analysis as shown in Fig. 7.18(g), whereas the bright area labelled 'B' shows peaks of Zr and O with a small evidence of Fe and Cr as shown in Fig. 7.18(h). It is therefore indicated that this transferred material from the SHS7170 coating.

Fig. 7.19 shows SEM images of wear scars of the zirconia counterface tested against three coating types at the load of 70 N. Fig. 7.19(a) and (b), show the SEM images of the wear scar on the zirconia ball when slid against the Armacor C coating. The wear scar was about 1.8 mm in diameter and at higher magnification image, Fig. 7.19(b) the wear scar exhibits evidence of a small amount of transferred material. In contrast, the wear scar on the zirconia ball tested against the Armacor M coating (Fig. 7.19(c) and 7.19(d)) was about 1.7 mm in diameter and shows large patches of transferred material on the worn surface. Fig. 7.19(e) shows a low magnification SEM image of the wear scar of zirconia ball slid against the SHS7170 coating. The wear scar was typically about 2.8 mm in diameter which was much larger than those of the wear scars following sliding against the Armacor C and the Armacor M coatings (Fig. 7.19(a) and 7.19(c), respectively). The larger patches of transferred material can be clearly observed on the worn surface of the zirconia ball slid against the SHS7170 coating as shown in Fig. 7.19(f).

7.4.7 Microstructural observation of the worn surface of steel 440C ball slid against three coating types

Wear scars of the 440C steel counterface following sliding against three coating types at the highest load of 70 N were shown in Fig. 7.20. Fig. 7.20(a), a low magnification SEM image of the wear scar following sliding against the Armacor C coating shows the wear scar was typically about 2.5 mm in diameter. At higher magnification image, Fig. 7.20(b), the wear scar is seen to be smooth surface with some scratch marks and a small amount of wear debris adhered to the surface. The wear scar of the steel 440C ball tested against the Armacor M coating was about 2.2 mm in diameter as shown in Fig. 7.20(c). Again, at higher magnification, Fig. 7.20(d) the wear scar can be seen to be smooth with only small amounts of adhered wear debris. Fig. 7.20(e), the SEM image of the 440C steel ball following sliding against the SHS7170 coating shows similar behaviour with a wear scar of about 2.2 mm in diameter. At higher magnification, Fig. 7.20(f) again shows a smooth wear scar with a small amount of wear debris adhered. Higher magnification SE-SEM images and BSE-SEM images of the adhered wear debris following sliding of the Armacor C, Armacor M and SHS7170 coatings against 440C steel balls are shown in Figs. 7.20(g)-(l).

7.5 The influence of sliding distance

Wear volumes of the coatings were measured under an applied load of 23.3 N with an alumina ball as a function of sliding distance. The plot of the coating wear volume with sliding distance is shown in Fig. 7.21 and the plot of the ball wear volume is presented in Fig. 7.22.

It can be seen that the wear volume of the four coatings increased linearly with sliding distance, *S*. However, it can be seen that the balls wear quickly initially and then wear less rapidly (Fig. 7.22). This is due to the initially high contact pressures which are reduced as the ball worn. Volumetric wear rates for each coating and alumina ball are presented in Table 7.5.

Topology (3D-profile) of the Armacor C, the Armacor M, the SHS7170 and the WC-Co-Cr coatings following sliding wear test against alumina ball at load 23.3 N for sliding distance 10,000 m. are shown in Fig. 7.23(a)-(d), respectively.

The volumetric wear rates of the coatings were analysed from profilometry and are shown in Table 7.5. It is notable that the SHS7170 coating shows a wear rate only 33% of that of the Armacor C coating and about 50% of that of the Armacor M coating. However, the SHS7170 coating exhibits volumetric wear rate ~ 58 times higher than that of the thermally sprayed WC-Co-Cr coating.

Table 7.5 Results of the steady state wear rate of the coatings and alumina ball at a load of 23.3 N and sliding distance of 10,000 m

Coating	Sliding distance (m)	Disc wear rate ($x10^{-15}$ m^3m^{-1})	Specific wear rate (disc) ($x10^{-15}$ $m^3N^{-1}m^{-1}$)	Ball wear rate ($x10^{-15}$ m^3m^{-1})
Armacor C	10,000	533.69	22.905	0.56
Armacor M	10,000	354.71	15.223	0.33
SHS7170	10,000	174.55	7.489	6.78
WC-Co-Cr	10,000	2.54	0.107	0.89
Substrate	1,000	14332	615.107	N/A

Mild steel surface following sliding against alumina ball was done only for 1,000 m due to the high wear damage on the surface over the range of experimental parameters investigated.

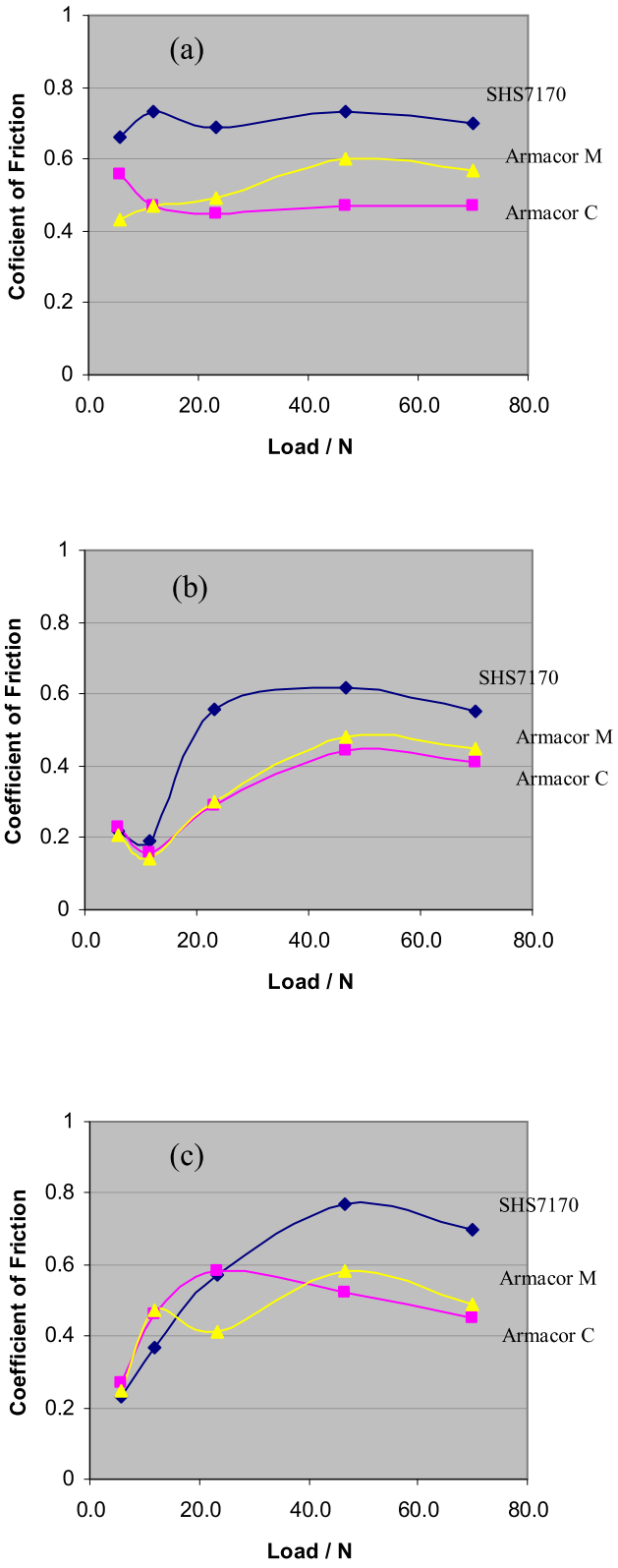

Fig.7.1 Variation of friction coefficient of the coatings as a function of applied load during sliding wear testing against (a) alumina ball, (b) zirconia ball and (c) 440C ball with load.

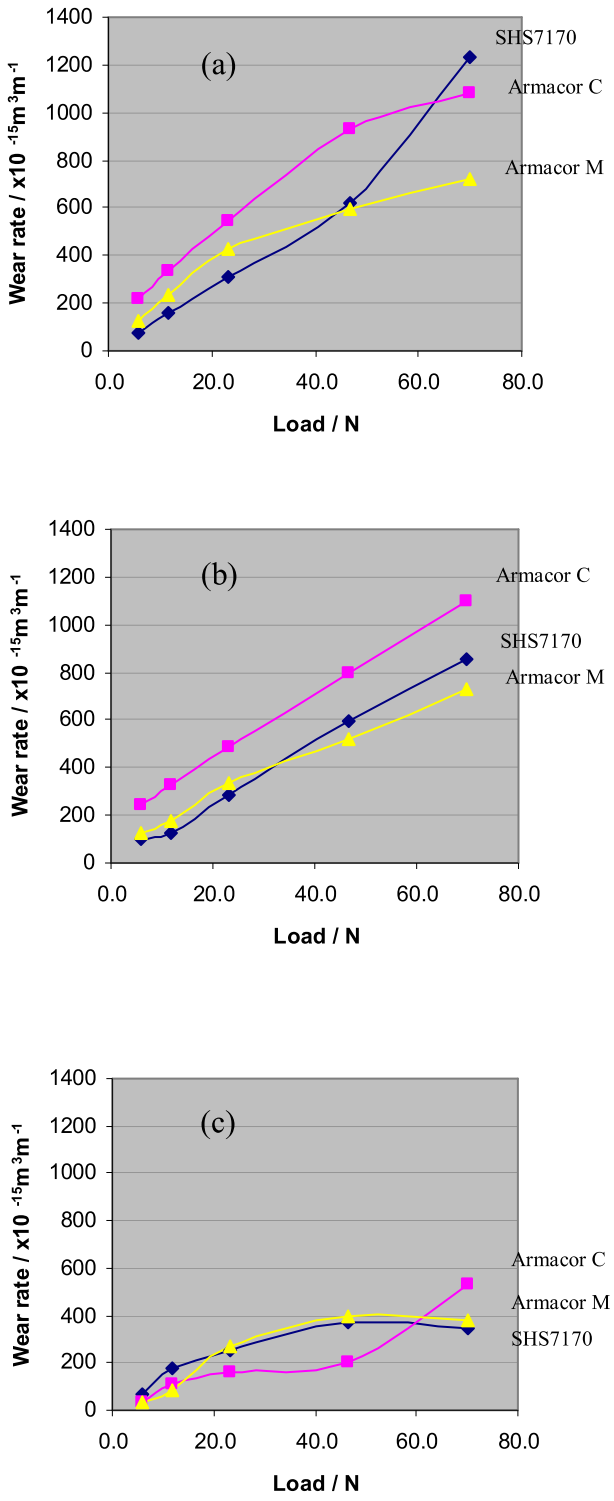

Fig. 7.2 Variation of wear rate of the coatings vs. (a) alumina ball, (b) zirconia ball and (c) 440C ball with load for the sliding distance 1,000 m

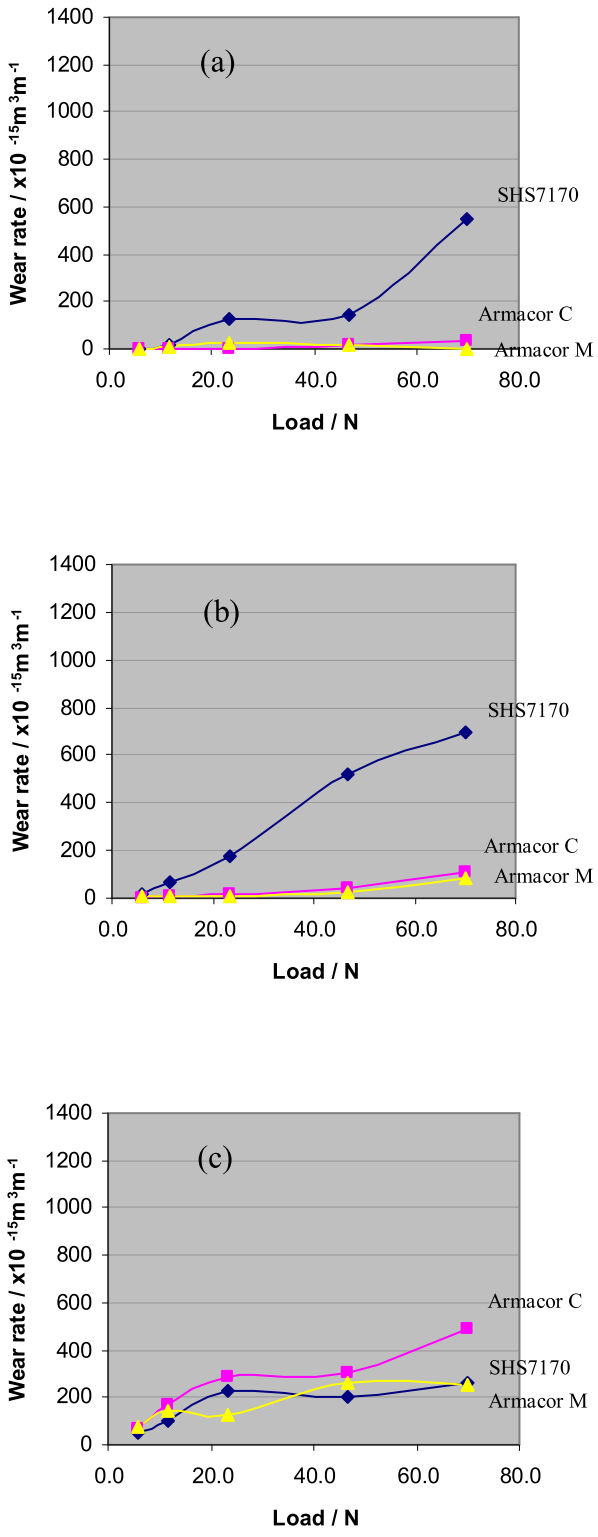

Fig. 7.3 Variation of wear rate of the balls vs. (a) alumina ball, (b) zirconia ball and (c) 440C ball with load for the sliding distance of 1,000 m

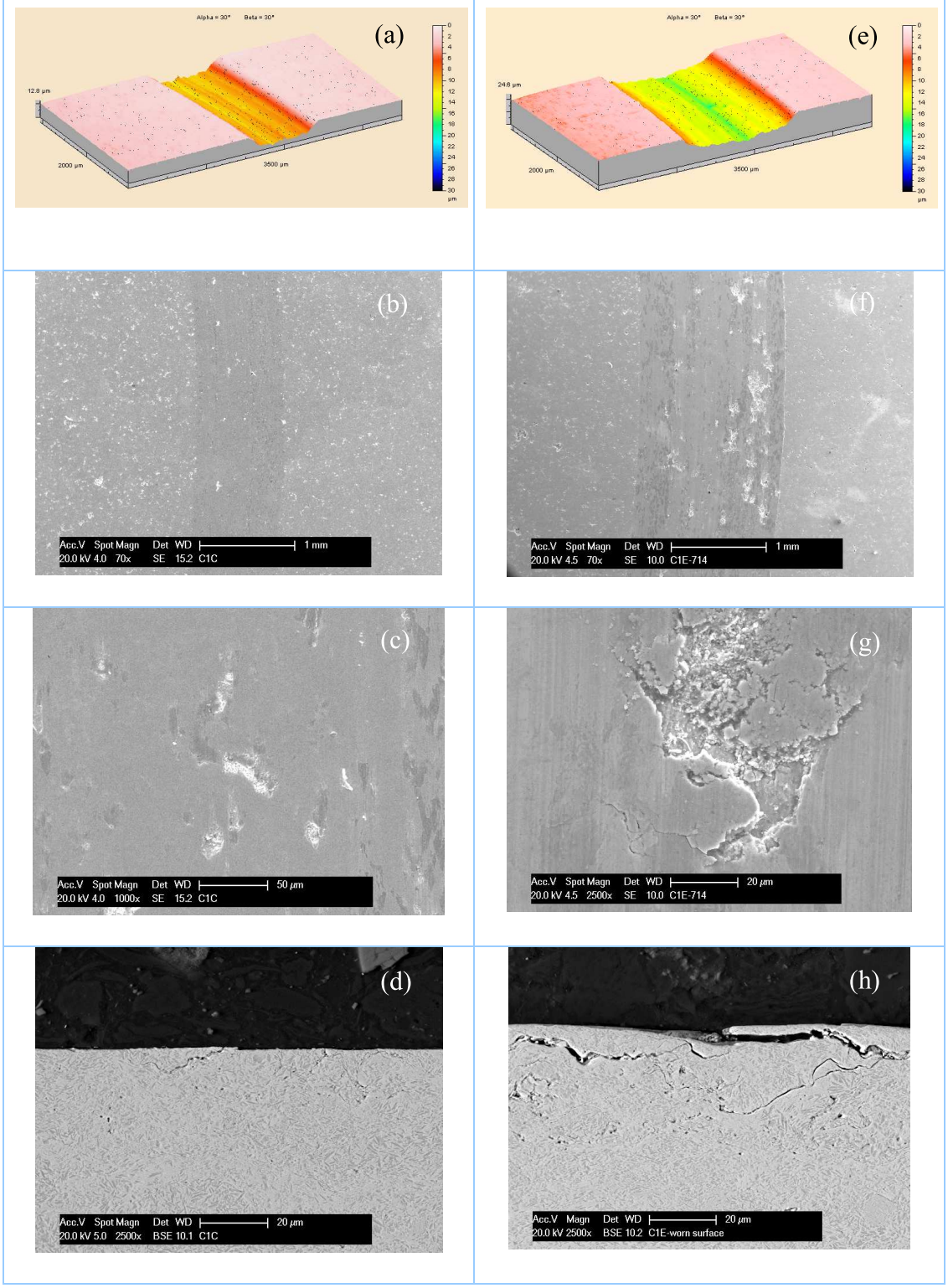

Fig. 7.4 Topology, SEM plan view and cross-sectional view images of the worn surfaces of the Armacor C coatings following sliding wear with alumina ball under a load of 23.3 N (a-d) and load of 70 N (e-h).

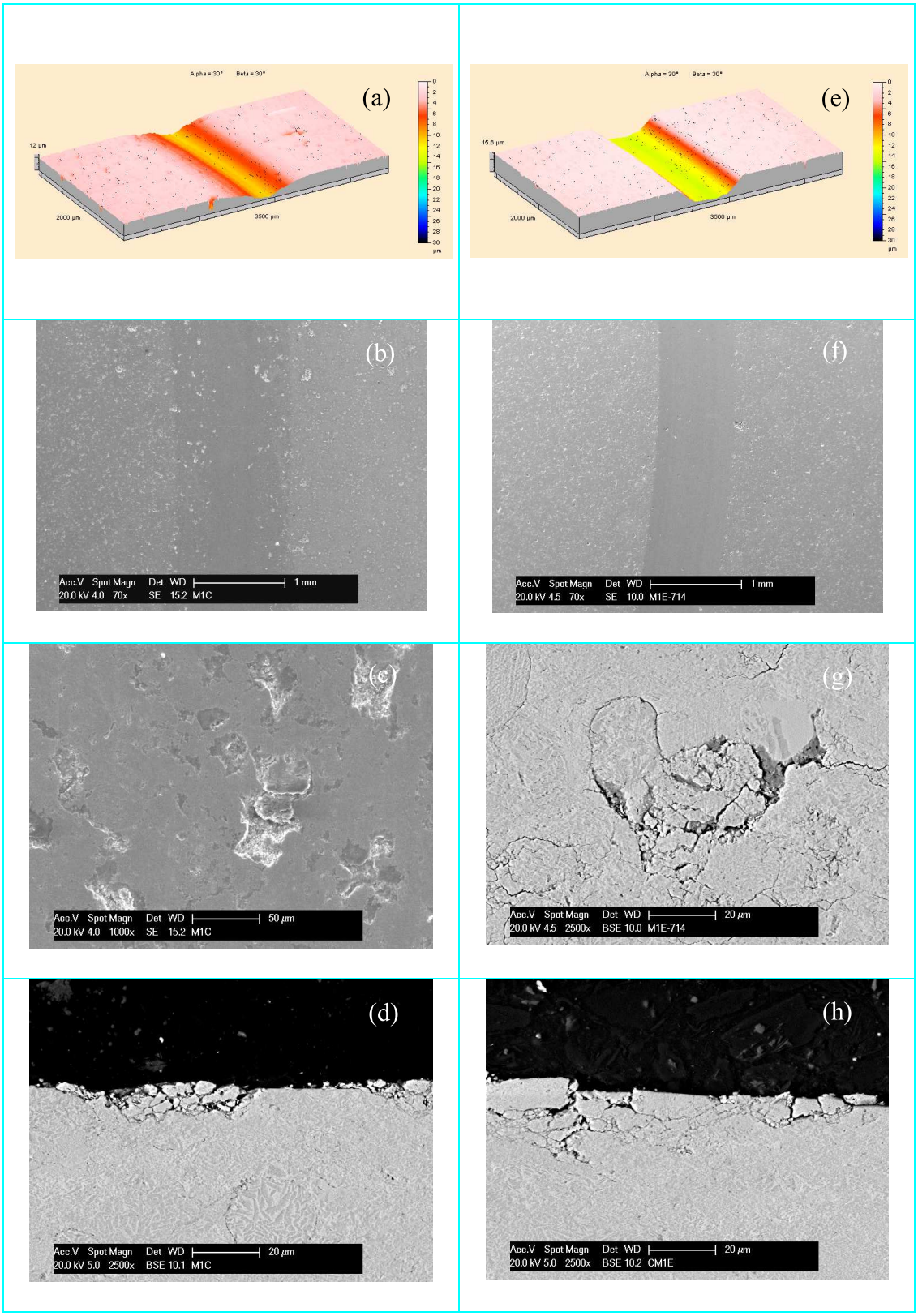

Fig. 7.5 Topology, SEM plan view and cross-sectional view images of the worn surfaces of the Armacor M coatings following sliding wear with alumina ball under a load of 23.3 N (a-d) and load of 70 N (e-h).

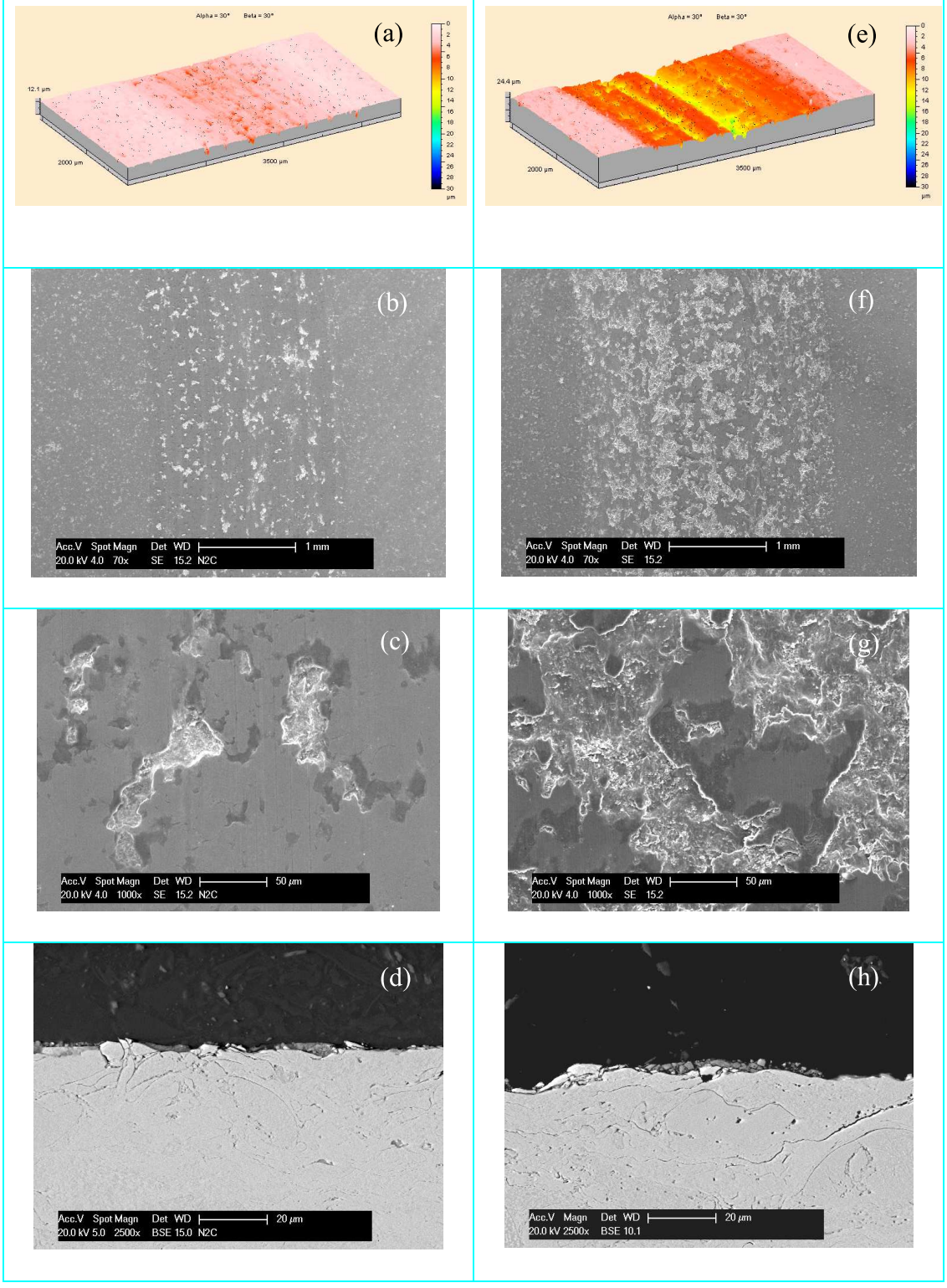

Fig. 7.6 Topology, SEM plan view and cross-sectional view images of the worn surfaces of the SHS7170 coatings following sliding wear with alumina ball under a load of 23.3 N (a-d) and load of 70 N (e-h).

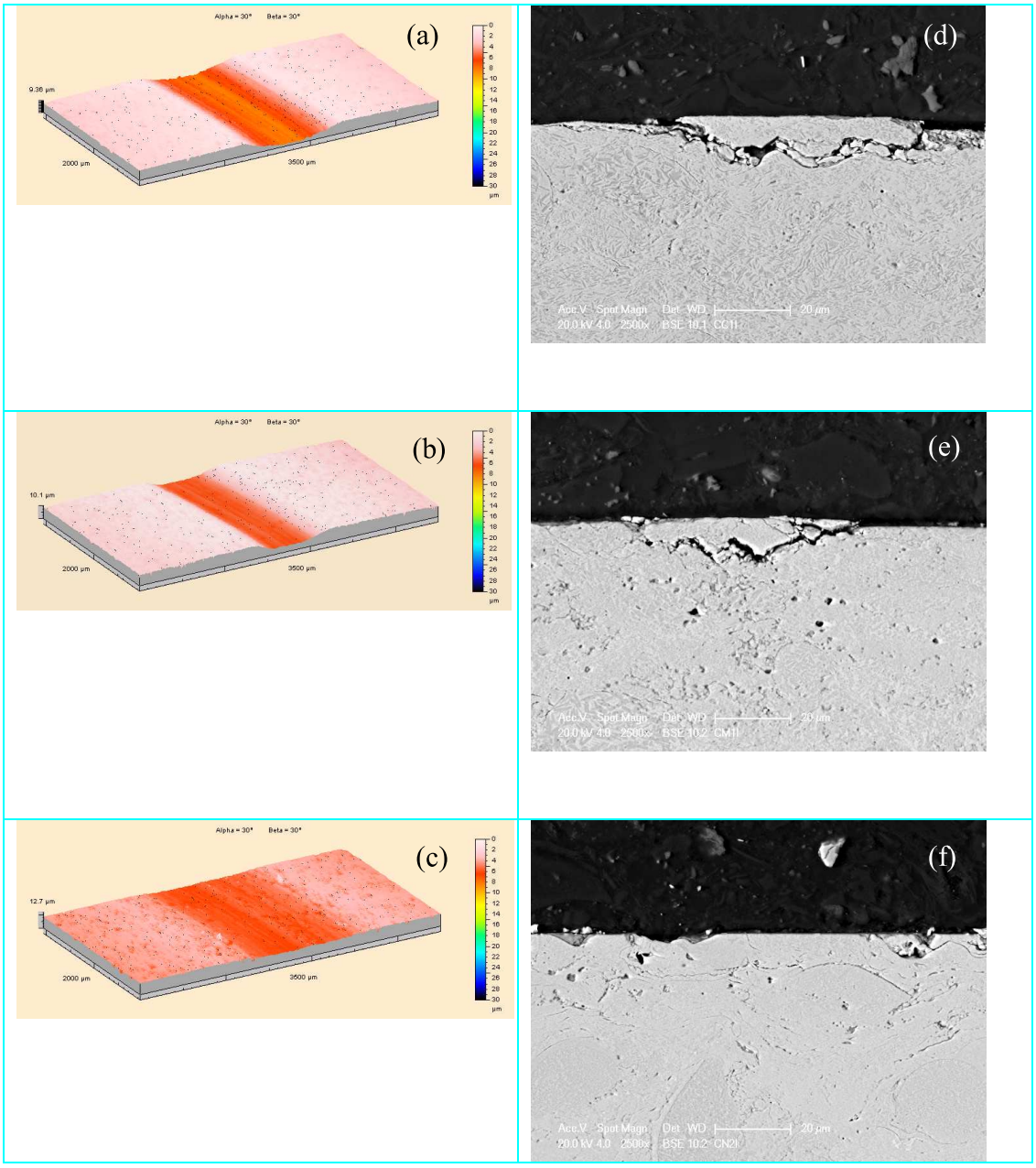

Fig. 7.7 Topology (a-c) and (d-f) SEM cross-sectional view images of the worn surfaces of the Armacor C, Armacor M and SHS7170 coatings following sliding wear with zirconia ball under a load of 23.3 N.

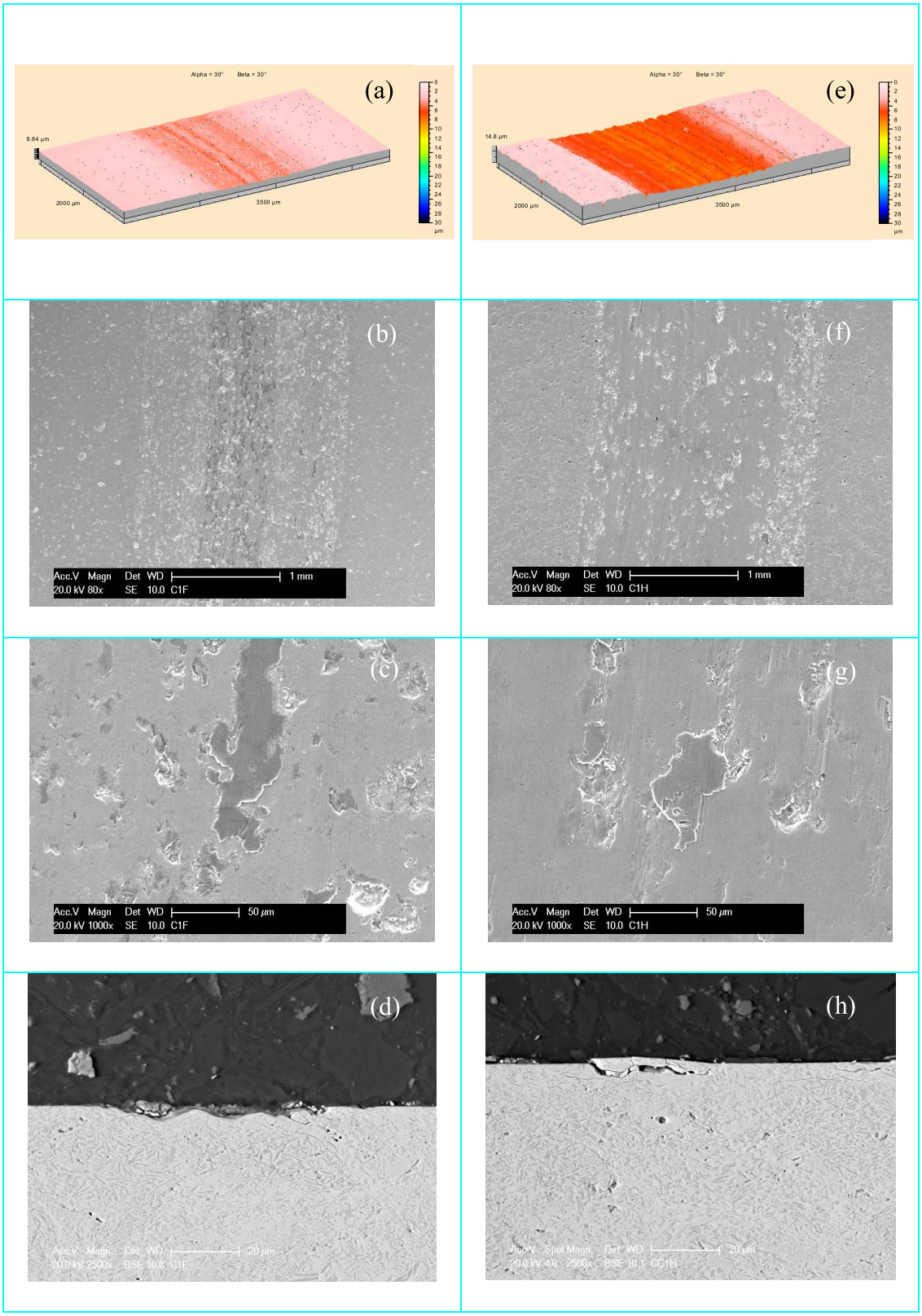

Fig. 7.8 Topology, SEM plan view and cross-sectional view images of the worn surfaces of the Armacor C coatings following sliding wear with 440C ball under a load of 23.3 N (a-d) and load of 70 N (e-h).

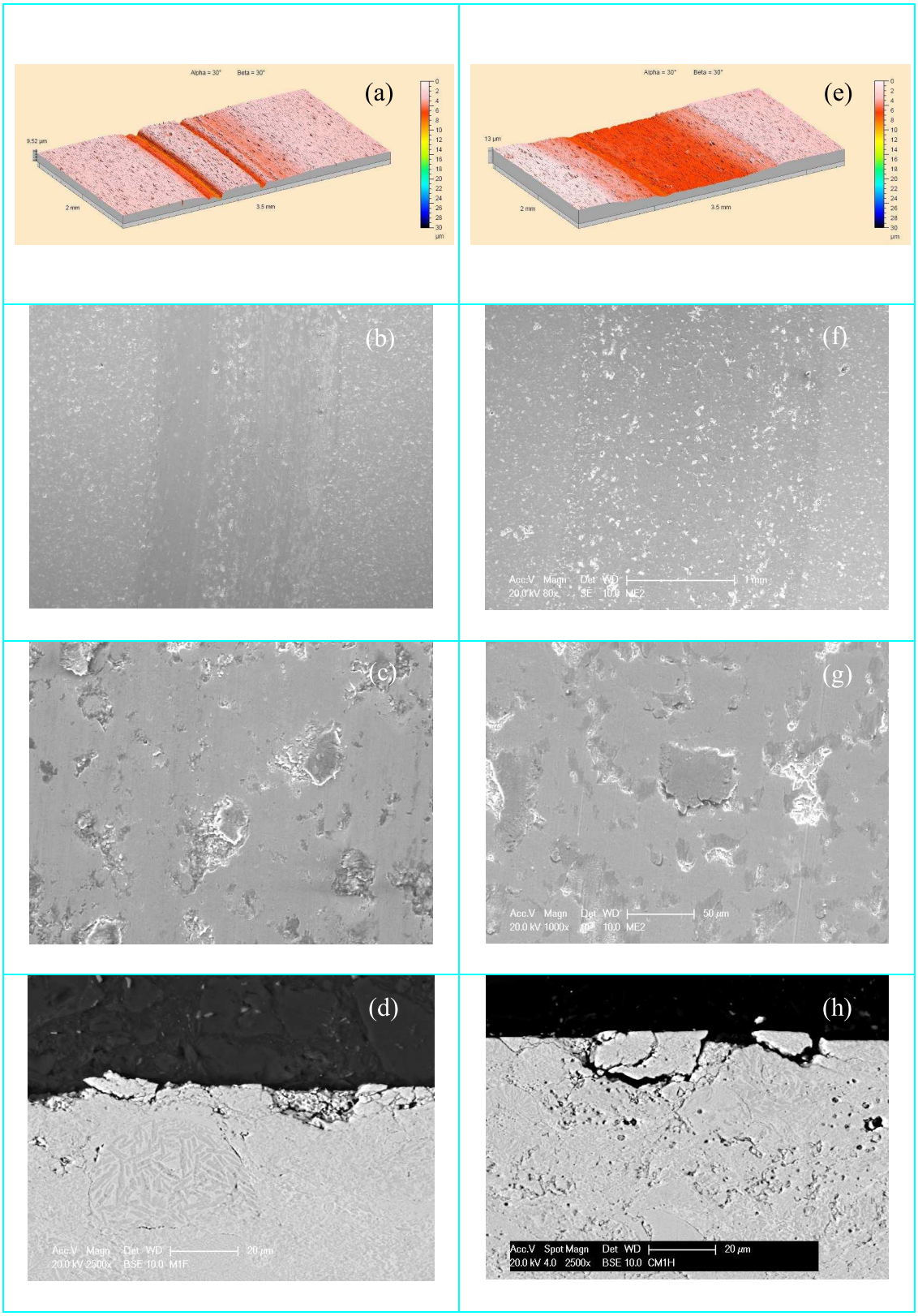

Fig. 7.9 Topology, SEM plan view and cross-sectional view images of the worn surfaces of the Armacor M coatings following sliding wear with 440C ball under a load of 23.3 N (a-d) and load of 70 N (e-h).

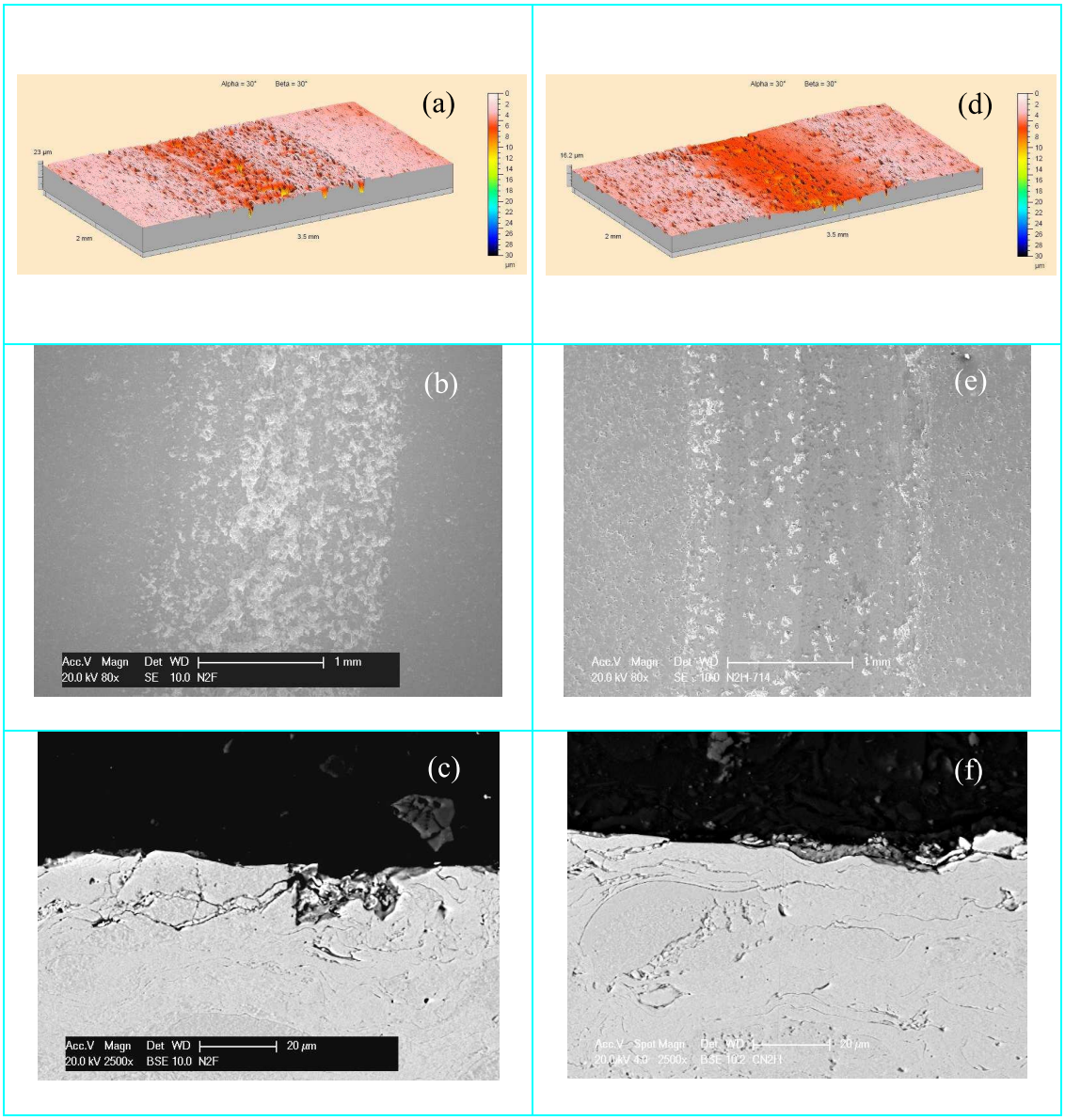

Fig. 7.10 Topology, SEM plan view and cross-sectional view images of the worn surfaces of the SHS7170 coatings following sliding wear with 440C ball under a load of 23.3 N (a-c) and load of 70 N (d-f).

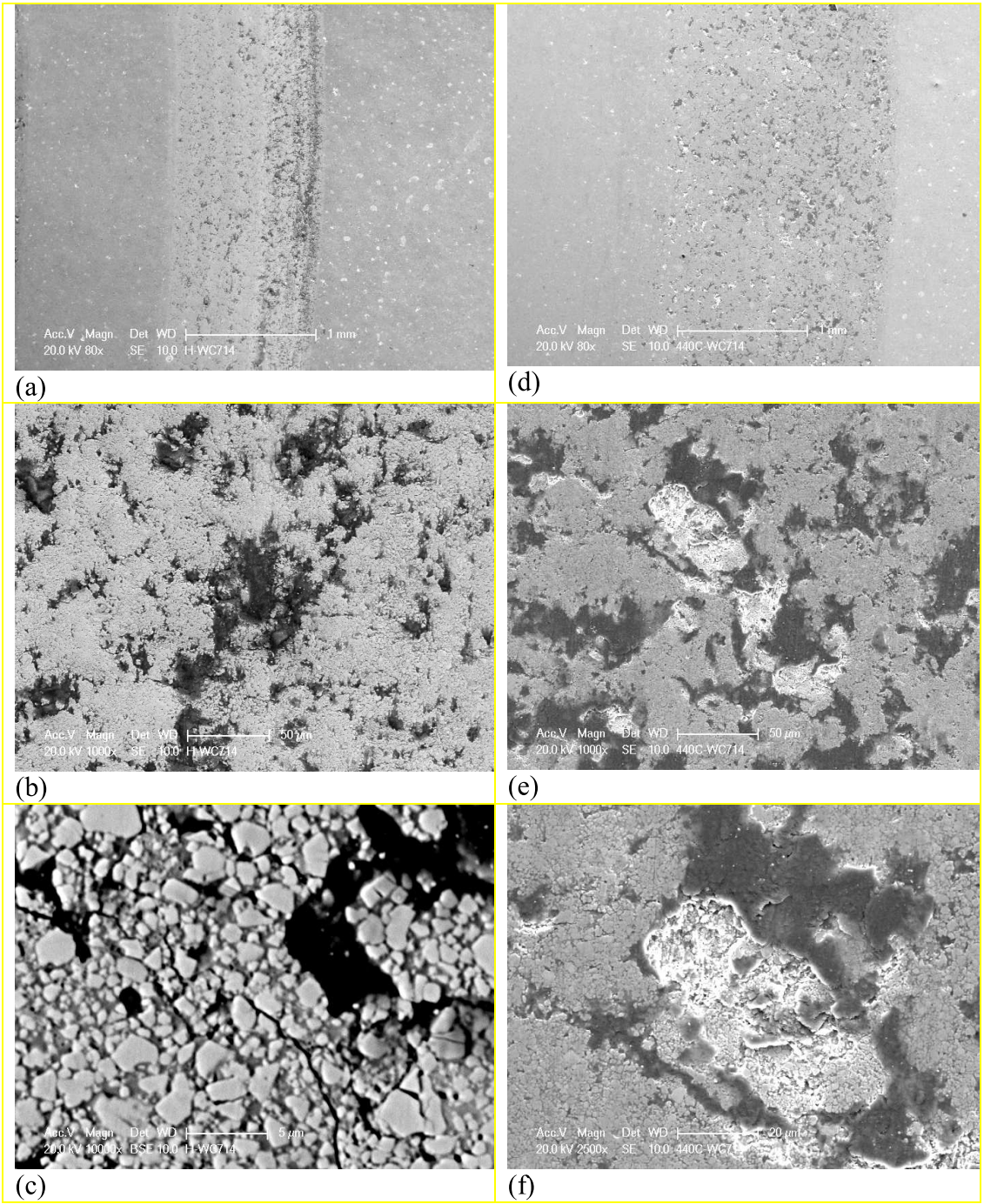

Fig. 7.11 SEM plan view images of the worn surfaces of the WC-Co-Cr coating following sliding wear with alumina ball (a-c) and 440C ball (d-f) under a load of 70 N (sliding distance 1,000m).

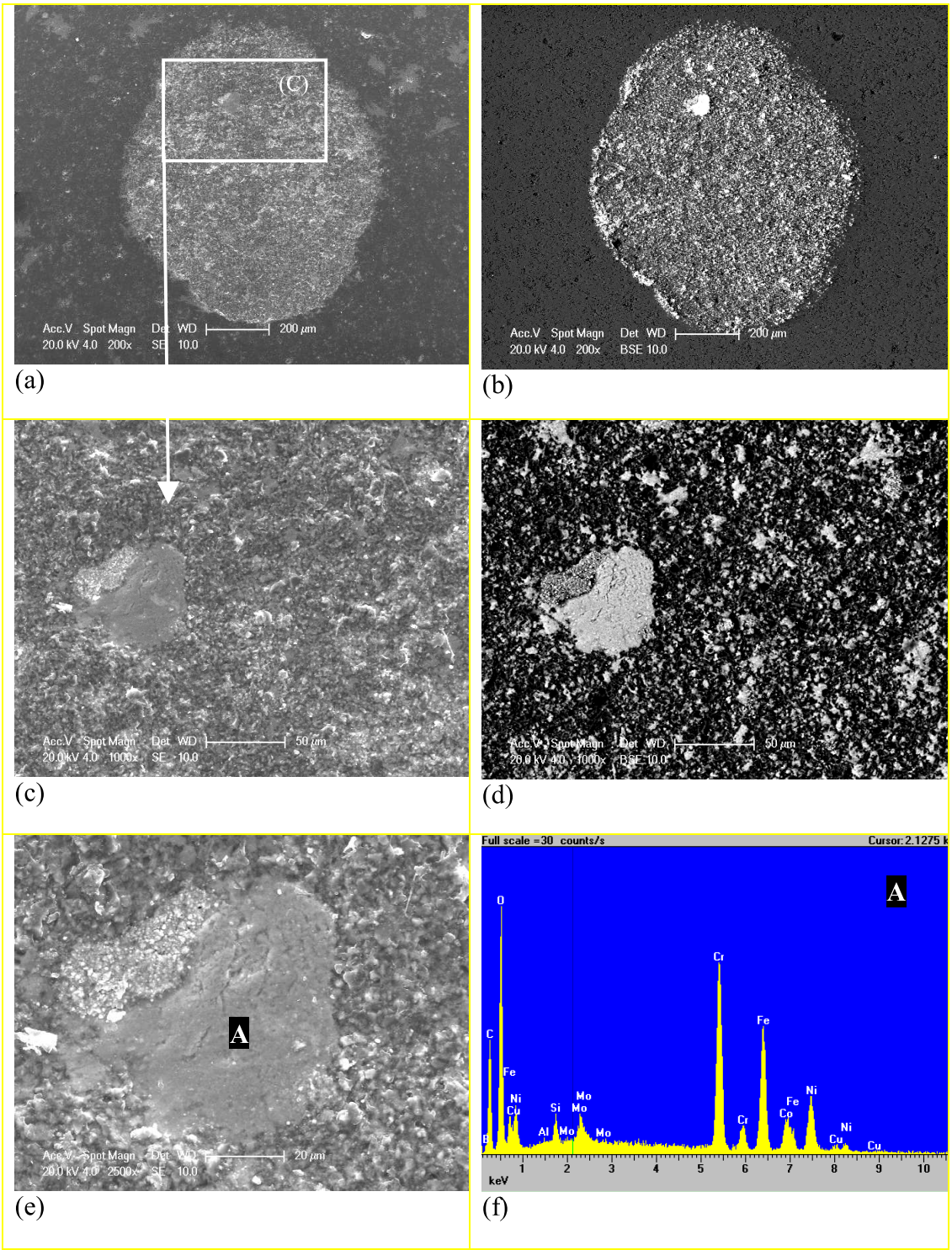

Fig. 7.12 SEM images of a wear scar of alumina ball (a-e) following sliding wear test against the Armacor C coating at a load of 23.3 N and (f) EDX analysis at position A of the adhered material in Fig. 8.12(e). (b) and (d) are the corresponding BSE images of the SE images (a) and (c).

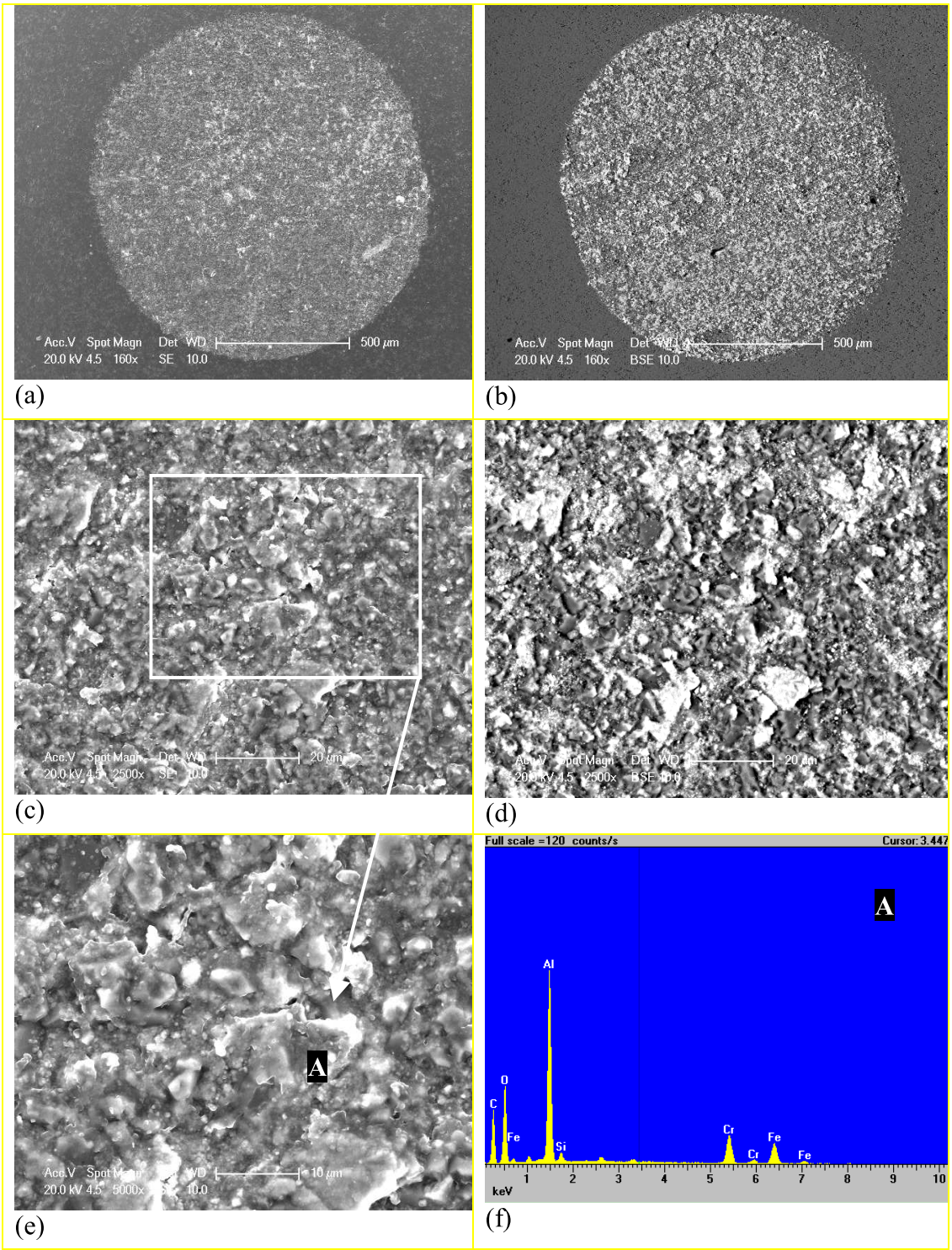

Fig. 7.13 SEM images of a wear scar of alumina ball (a-e) following sliding wear test against the Armacor M coating at a load of 23.3 N and (f) EDX analysis at position A in Fig. 8.13(e). (b) and (d) are the corresponding BSE images of the SE images (a) and (c).

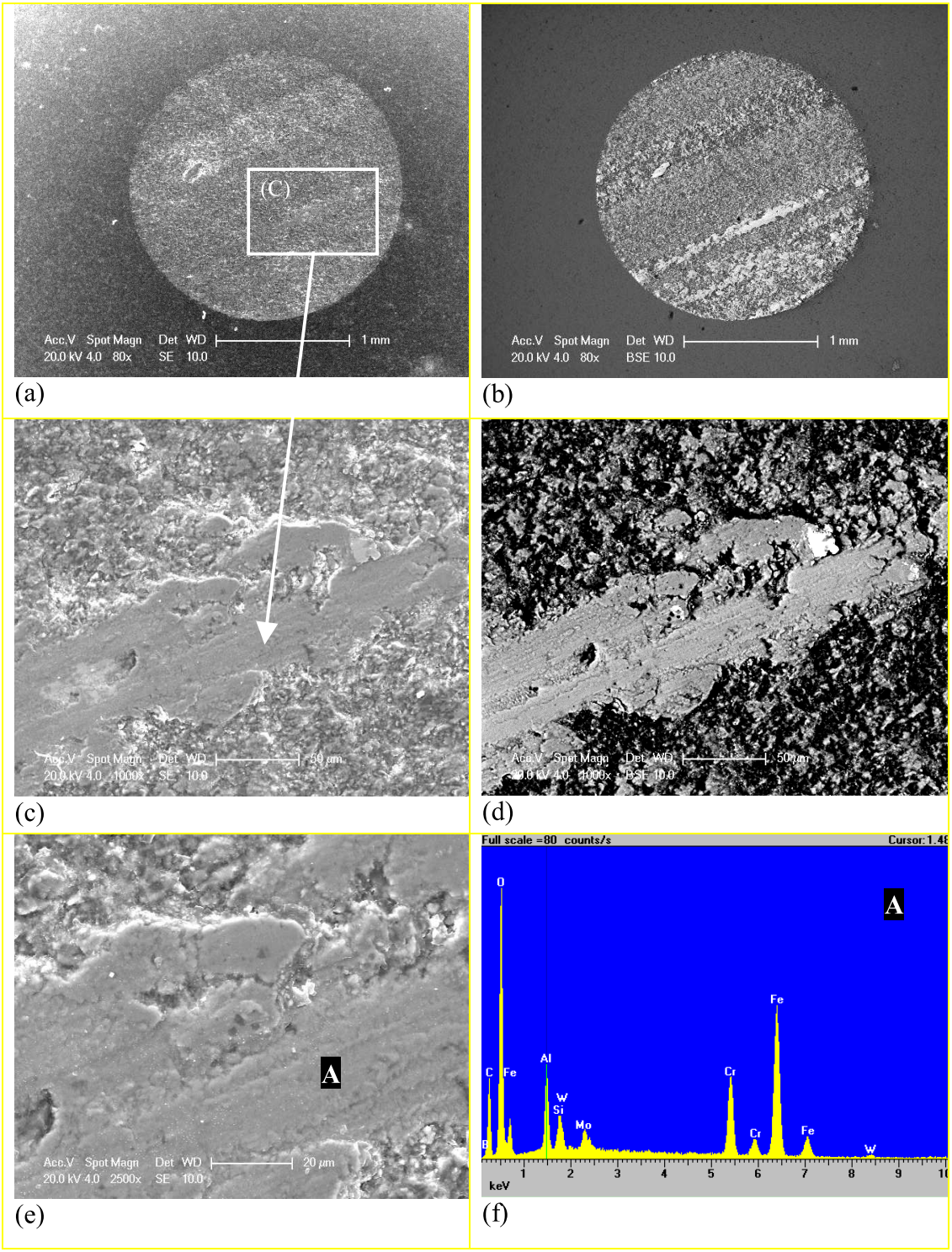

Fig. 7.14 SEM images of a wear scar of alumina ball (a-e) following sliding wear test against the SHS7170 coating at a load of 23.3 N and (f) EDX analysis at position A in Fig. 7.14(e). (b) and (d) are the corresponding BSE images of the SE images (a) and (c).

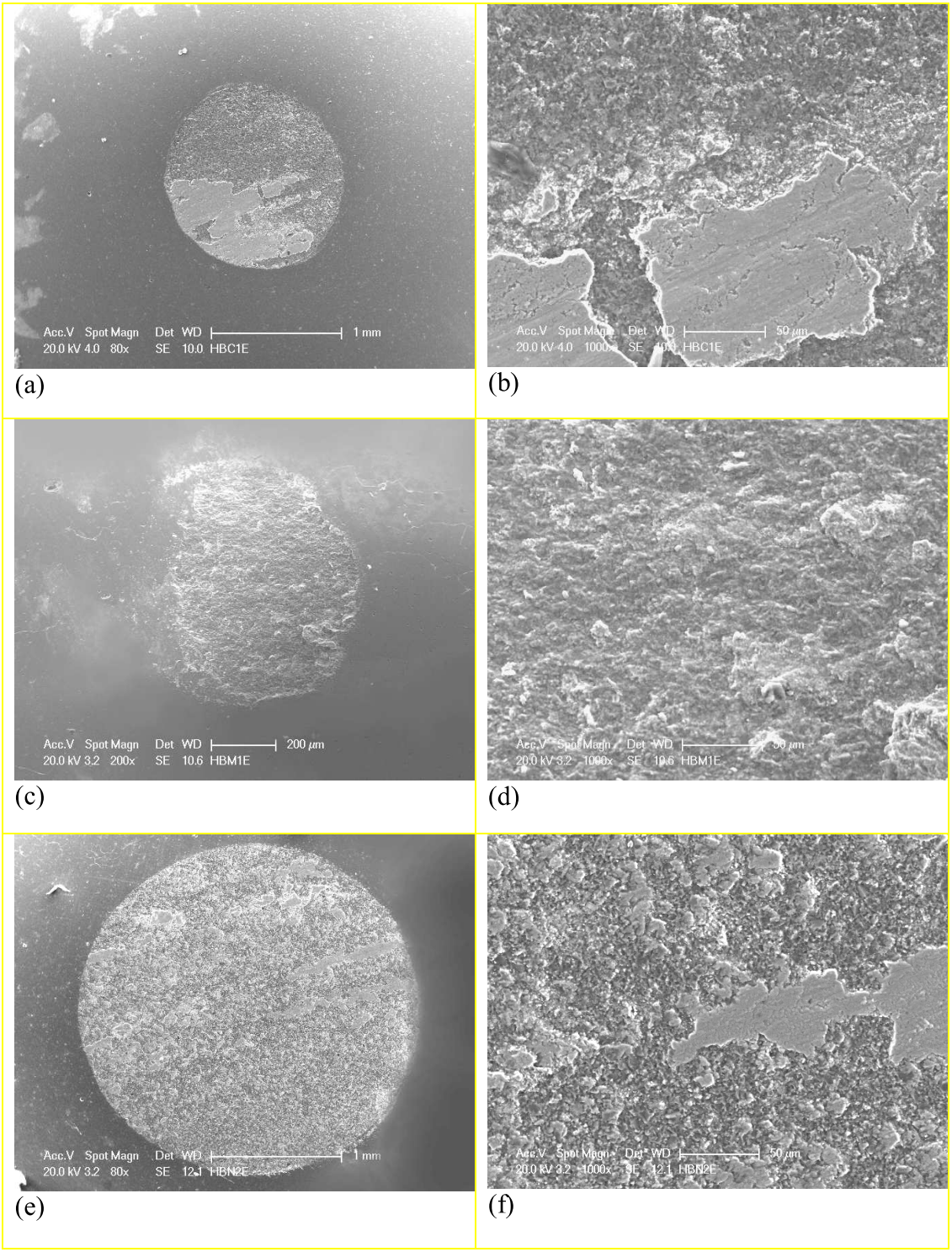

Fig. 7.15 SE-SEM images of worn surfaces of alumina ball slid against (a-b) the Armacor C coating, (c-d) the Armacor M coating and (e-f) the SHS7170 coating under a load of 70 N at low magnification (Fig. 7.15(a)80x, (c)200x and (d)80x) and higher magnification.

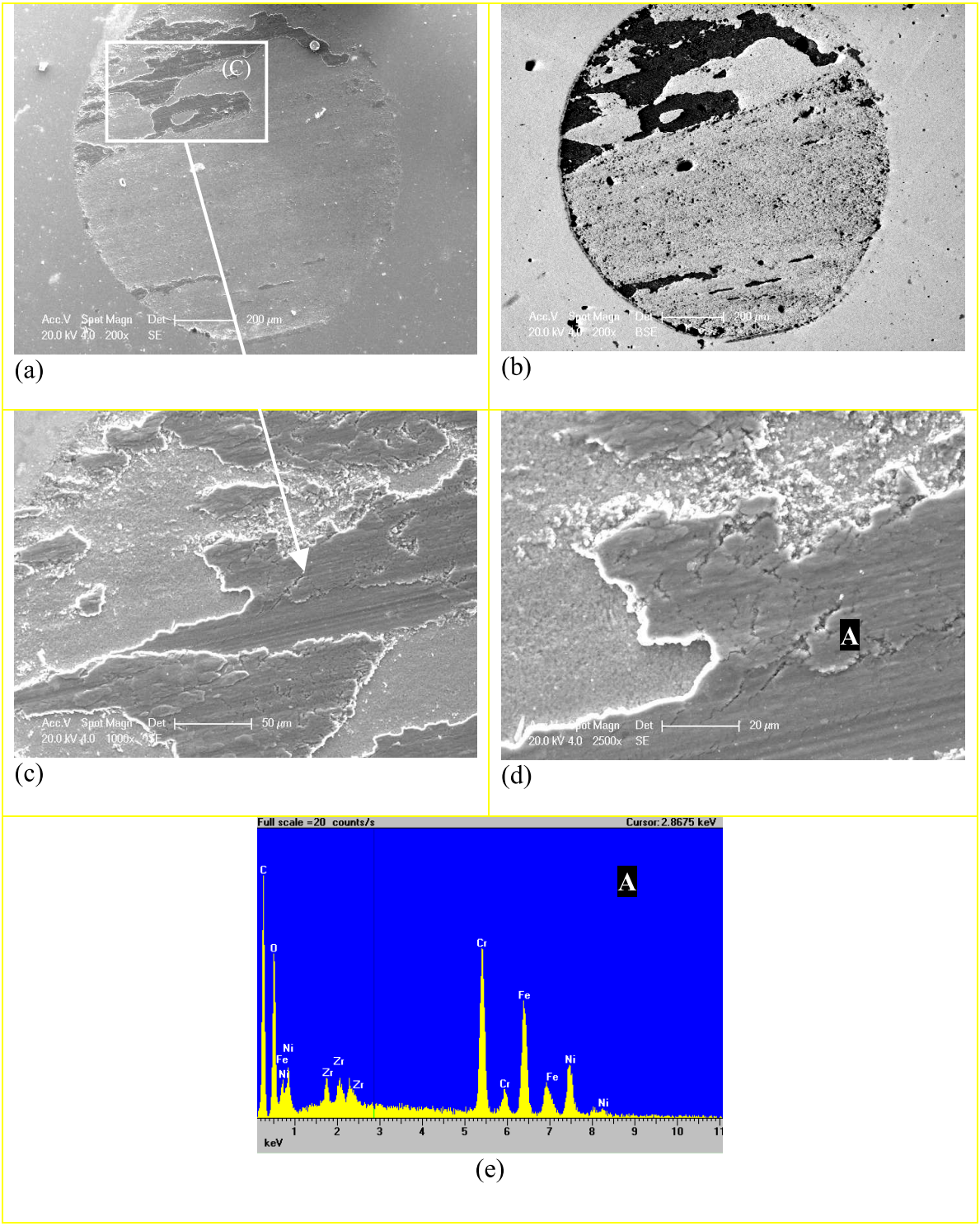

Fig. 7.16 SEM images of a wear scar of zirconia ball (a-d) following sliding wear test against the Armacor C coating at a load of 23.3 N and (e) EDX analysis at position A in Fig. 7.16(d). (b) is the corresponding BSE images of the SE images (a).

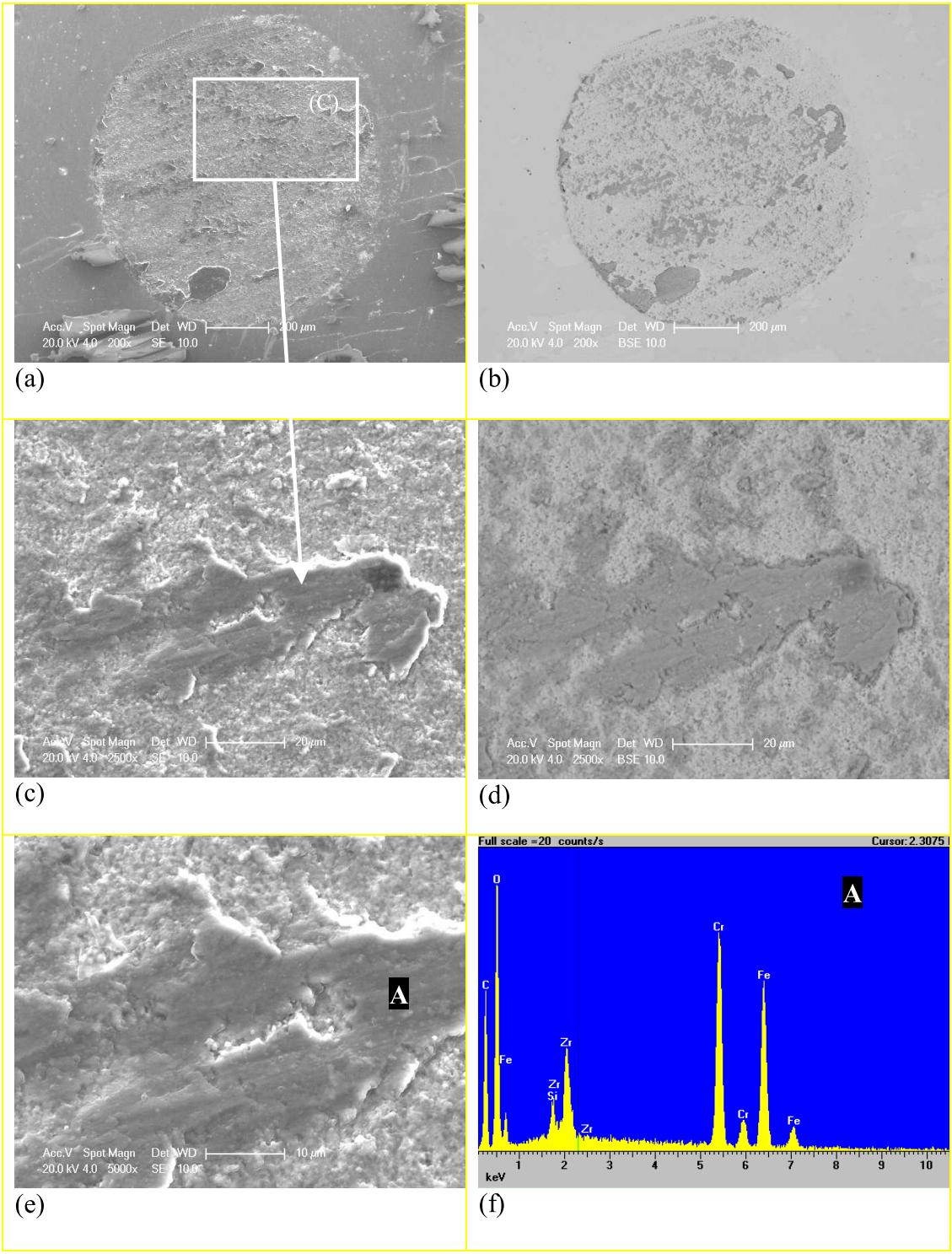

Fig. 7.17 SEM images of a wear scar of zirconia ball (a-e) following sliding wear test against the Armacor M coating at a load of 23.3 N and (f) EDX analysis at position A in Fig. 7.17(e). (b) and (d) are the corresponding BSE images of the SE images (a) and (c).

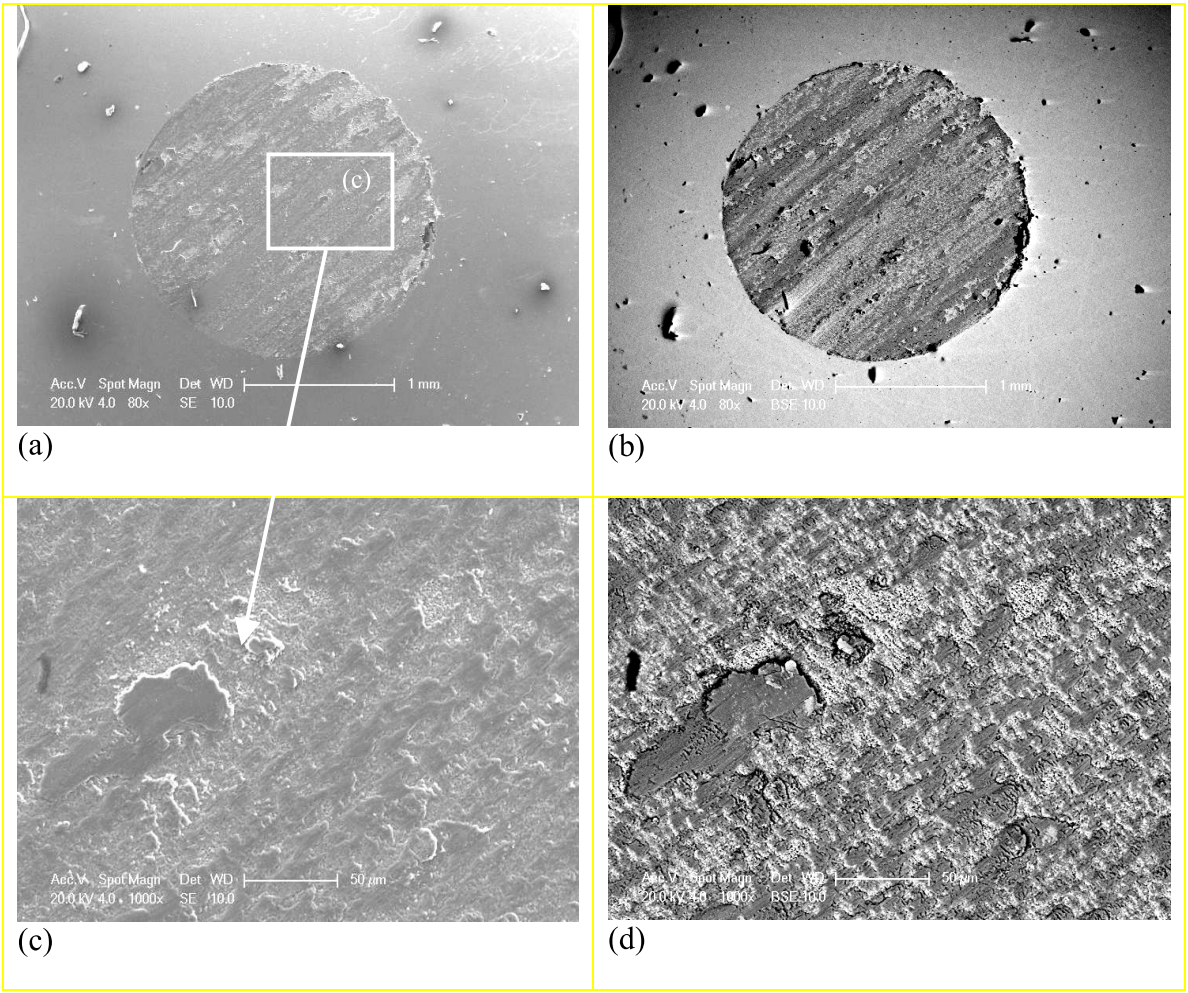

Fig. 7.18 SEM images of a wear scar of zirconia ball (a-d) following sliding wear test against the SHS7170 coating at a load of 23.3 N (b) and (d) are the corresponding BSE images of the SE images (a) and (c).

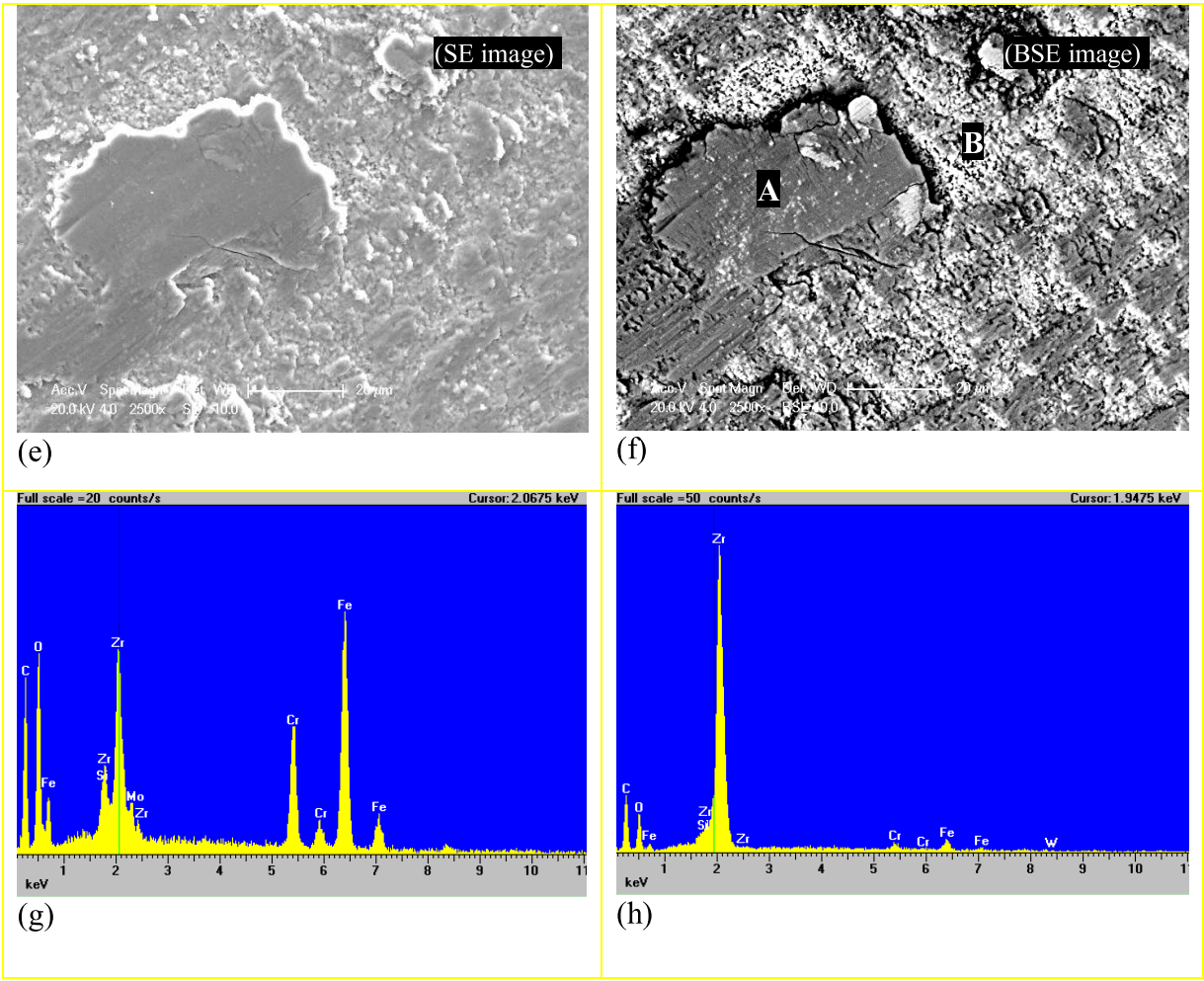

Fig. 7.18 (cont.) A higher magnification SE-SEM images (e) and BSE-SEM image (f) of a wear scar in (c) and (g)-(h) showing EDX analysis at position A and B in Fig. 7.18(f).

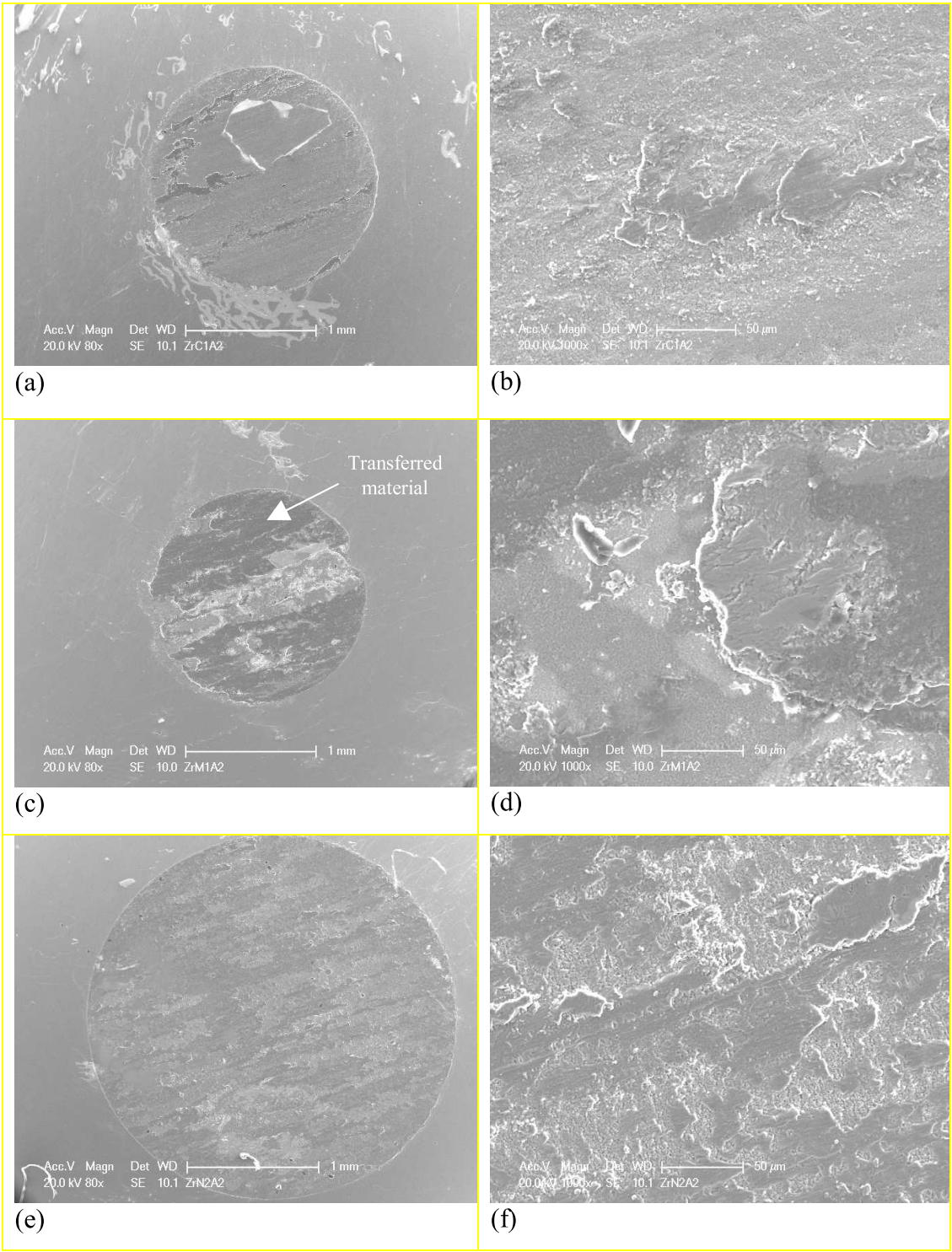

Fig. 7.19 SEM images of worn surfaces of zirconia ball slid against (a-b) the Armacor C coating, (c-d) the Armacor M coating and (e-f) the SHS7170 coating under a load of 70 N at low magnification and higher magnification, respectively.

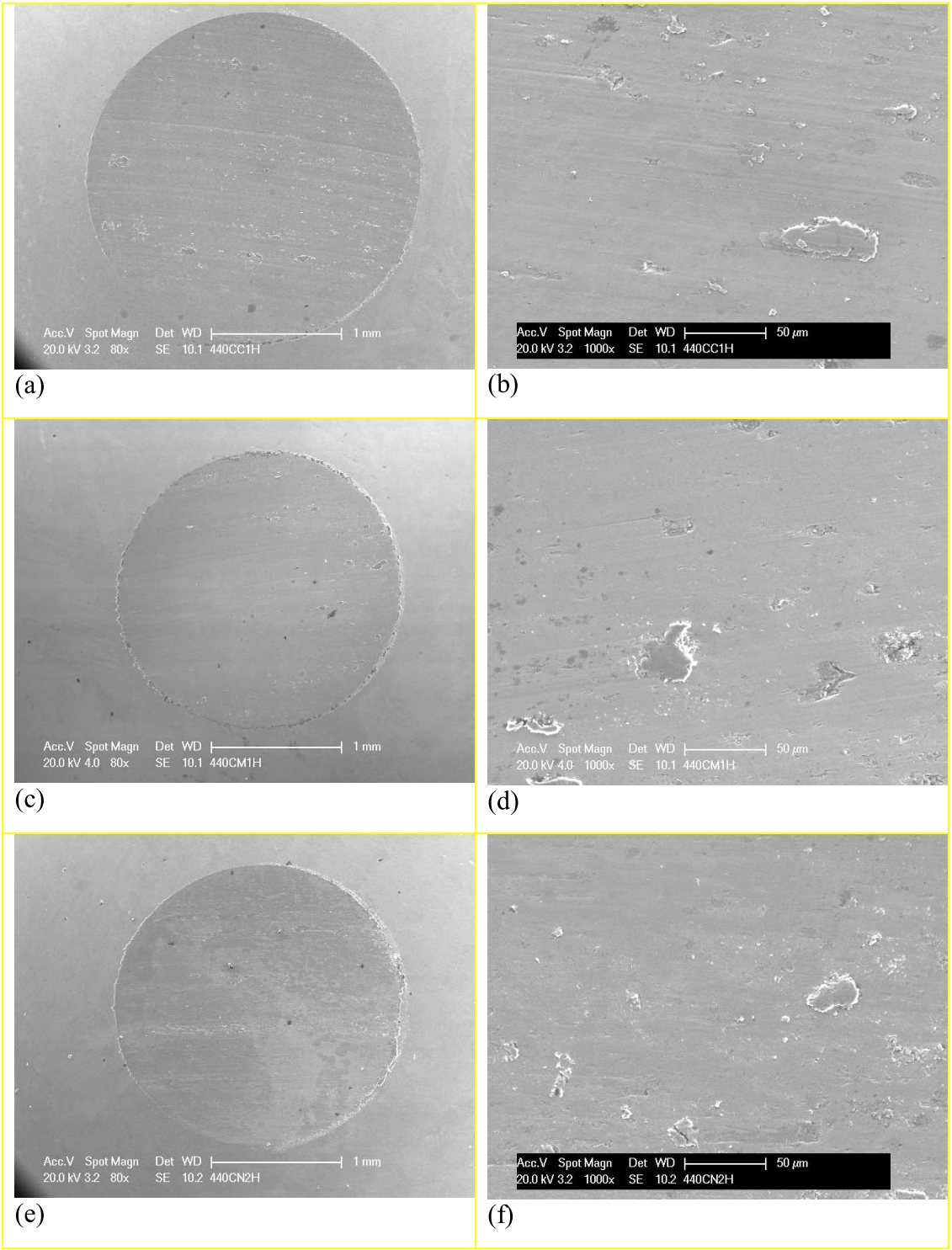

Fig. 7.20 SEM images of worn surfaces of 440C ball slid against (a-b) the Armacor C coating, (c-d) the Armacor M coating and (e-f) the SHS7170 coating under a load of 70 N at low magnification and higher magnification, respectively.

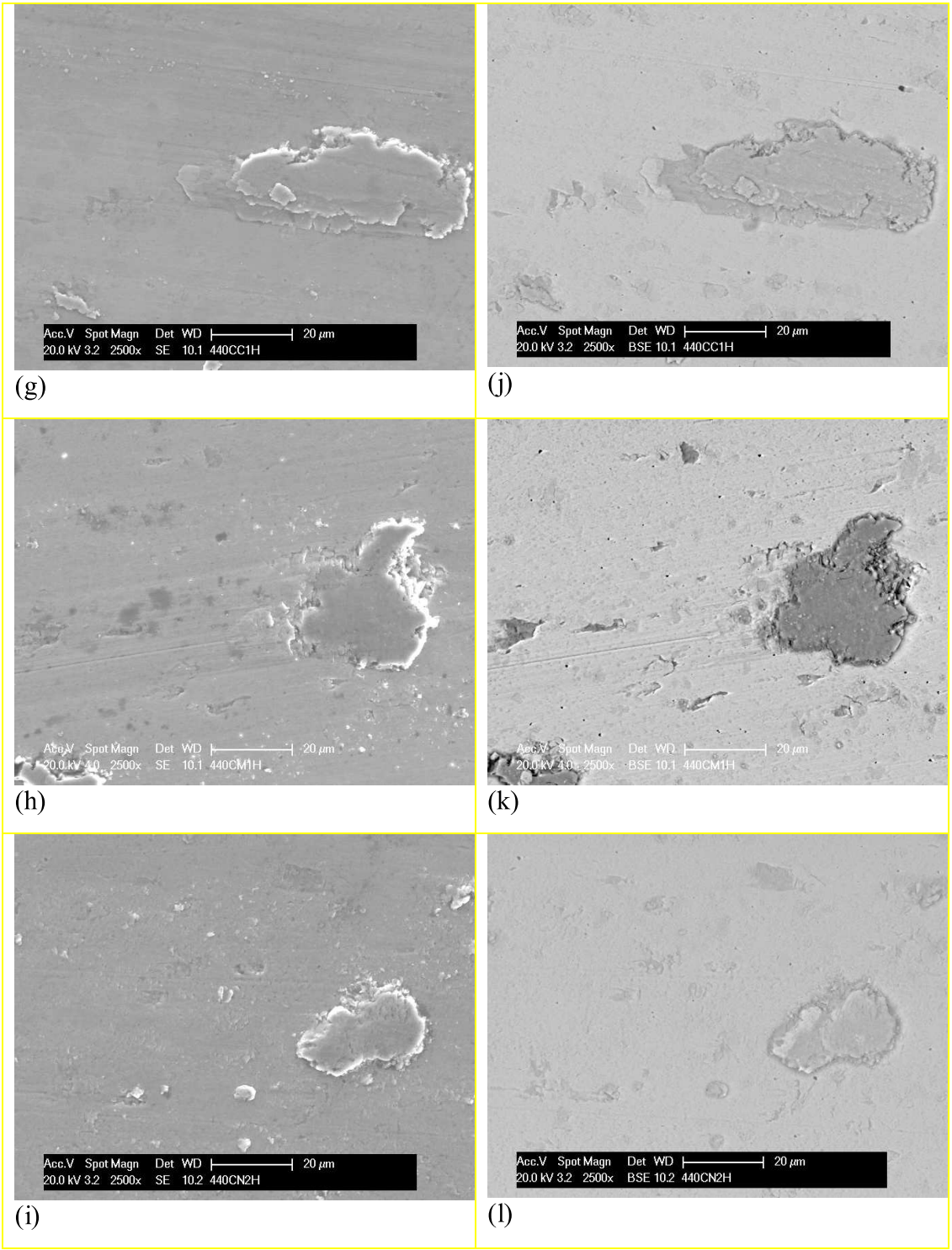

Fig. 7.20 (cont.) (g)-(i) higher magnification SE-SEM images and (j)-(l) BSE-SEM image of wear scars in Fig. 7.24(b), (d) and (f), respectively.

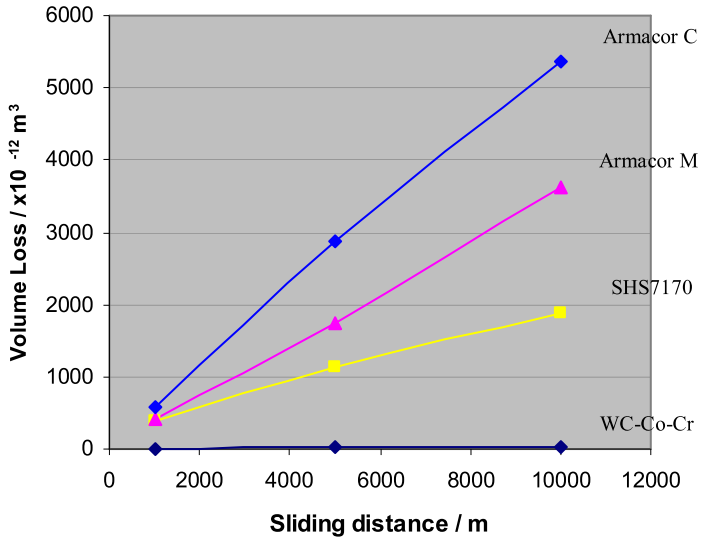

Fig. 7.21 Wear volume loss of the coatings tested against alumina ball under a load of 23.3 N with sliding distances.

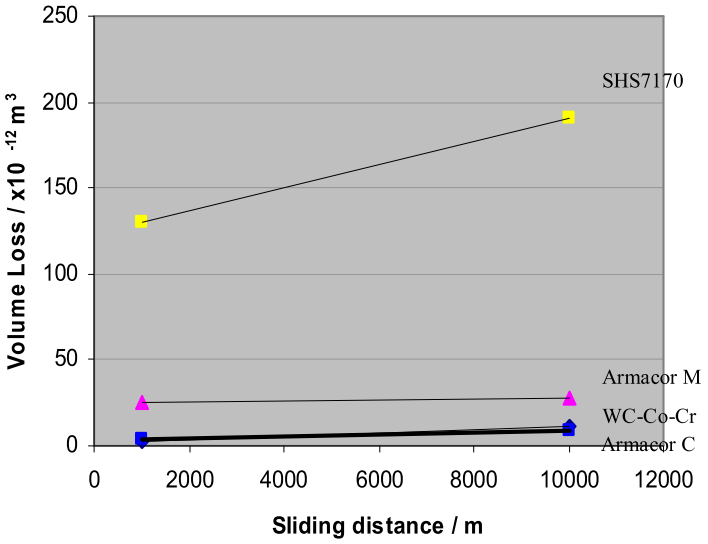

Fig. 7.22 Wear volume loss of alumina ball tested under a load of 23.3 N with sliding distances.

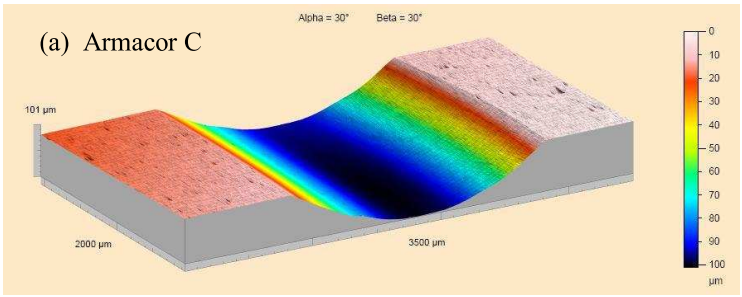

Depth = 93 µm
Width = 1.98 mm
Sliding distance 10,000 m

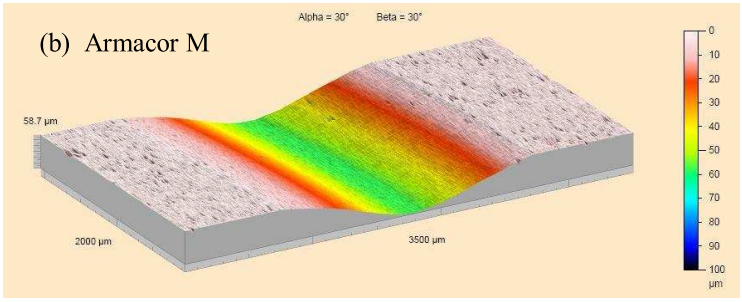

Depth = 57 µm
Width = 2.0 mm
Sliding distance 10,000 m

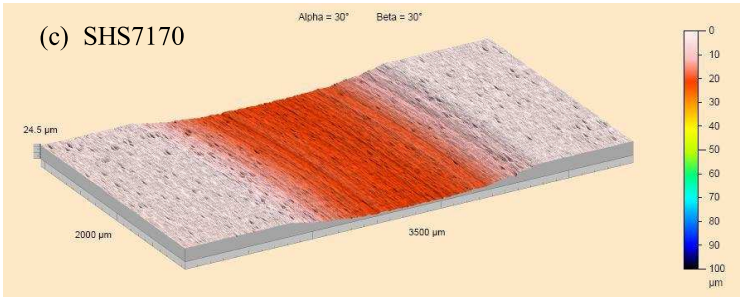

Depth = 22 µm
Width = 2.0 mm
Sliding distance 10,000 m

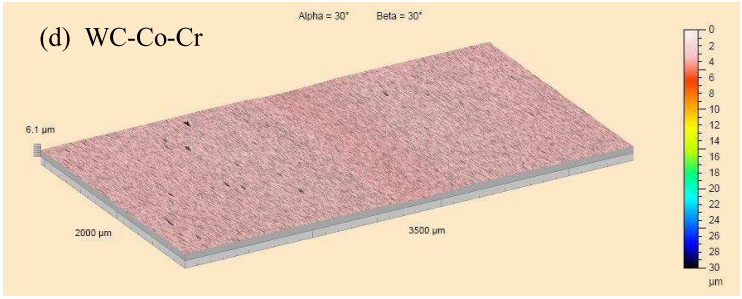

Depth = 1.96 µm
Width = 0.7 mm
Sliding distance 10,000 m

Fig. 7.23 Topology of the coatings (a) Armacor C, (b) Armacor M, (c) SHS7170 and (d) WC-Co-Cr coating following sliding wear test against alumina ball at load 23.3 N for sliding distance 10,000 m.

Chapter 8

Discussion: Microstructure of powders and coatings & their wear performance

8.1 Introduction

Firstly, the three commercially available gas atomised powders (Armacor M, Armacor C and Nanosteel SHS7170) based on the Fe-Cr-B system and a specially designed gas atomised powder, KC1 based on the Fe-Cr-B-C system will be discussed in terms of the microstructure of different size of powder particles and explanations of the differences in microstructure in relation to their compositions will be considered. In the sections which follow, the development of the coating microstructure will be explained and its response to elevated temperature exposure will be analysed; comparisons between the behaviour of powder and coatings will also be made. Furthermore, the DSC results will be considered and the activation and transformation energies assessed. In the final section, the ball-on-disc sliding wear performance of the three Fe-Cr-B based alloy coatings (Armacor M, Armacor C and Nanosteel SHS7170) and a commercially available wear resistant WC-Co-Cr cermet coating will be discussed and related to the coating microstructure.

8.2 Comparison of powder structures

8.2.1 Armacor M and Armacor C

In the Armacor M powder, XRD (Fig.4.3) and SEM (Fig. 4.4) analysis of powder particles showed that they consisted of $(Fe_{1.1}Cr_{0.9})B_{0.9}$ needles in an iron matrix. The large powder particles (Fig. 4.4(d)) contained larger boride needles (~ 3 μm in width) compared to that of the smaller powder particles (~ 2 μm in width) as shown in Fig. 4.4(c). The crystal structure of the Fe phase in these particles is body centred cubic with a lattice parameter $a_o \approx 0.2866$ nm, close to that of pure Fe ($a_o = 0.2886$ nm). The boride phase $(Fe_{1.1}Cr_{0.9})B_{0.9}$ found in this study is different from that of the Armacor M powders reported by Dent et al. (1997). They reported that the Armacor M powder (with compositions Fe-balance, 42.0%Cr-2.2%Si-6.1%B in wt.%) contained α-Fe, Fe(Cr) solid solution matrix phase and Cr-rich metal boride $Cr_{1.65}Fe_{0.35}B_{0.96}$. This suggests that the alloy composition is different giving different borides. In addition, another possible explanation is that the boride phase $(Fe_{1.1}Cr_{0.9})B_{0.9}$ formed in the present study could be formed at lower cooling rate during gas atomisation process (i.e. different gas flow rates). As a result the boride phase was formed at lower temperature where the solubility of Cr is limited (less than 16 at.%) (Yijian and Jian, 1991; Goldfarb et al, 1995) and the boride M_2B may exist in the form of $(Fe_{1.1}Cr_{0.9})B_{0.9}$ rather than $Cr_{1.65}Fe_{0.35}B_{0.96}$.

Similar features of microstructure can be observed in the Armacor C powder, XRD (Fig. 4.20) and SEM (Fig. 4.21) of powder particles showed a two-phase structure which consisted of boride needles in an iron-based matrix (Figs. 4.20 and 4.21). The boride was identified as M_2B type, which could be either $(Fe_{1.1}Cr_{0.9})B_{0.9}$ or $(Cr_{1.65}Fe_{0.35})B_{0.96}$. The overlap of peak on the XRD pattern seems that it is not

possible to identify the boride phase with certainty. This is consistent with the work reported by Manna et al. 2008 that the Armacor C powder of composition Fe-32.0Cr-19.0Ni-9.0Co-4.0Mo-2.4Cu-4.0B-0.12C-1.4Si in wt.%, contained an austenite matrix phase and boride ($Cr_{1.65}Fe_{0.35}B_{0.96}$), but the boride $(Fe_{1.1}Cr_{0.9})B_{0.9}$ was not found in their work.

Considering the different sizes of the powder particles, the large powder particles, Fig. 4.21(d), contained larger boride needles (~ 1 μm in width) compared to that in the small powder particles (~ 0.5 μm in width) in Fig. 4.21(c). The crystal structure of the Fe phase in these particles is face centred cubic with a lattice parameter $a_o \approx$ 0.35922 nm. This is thought to form due to the presence of ~ 20% Ni in the alloy, leading to stabilisation of fcc γ-Fe phase at room temperature (or inhibition of the fcc γ-Fe → bcc α-Fe transformation).

It is noticed that the boride grain sizes in the Armacor M powder are quite considerably larger than those in the Armacor C powder particles. The difference between the boride size in the Armacor M and Armacor C could be due to the difference in composition of the samples. The boron content in the Armacor M powder is 22 at% which is significantly greater than that in the Armacor C powder (15.4 at%). It is well known that the addition of metalloid elements (eg. boron) to the alloy increases the ability of the alloy to form the amorphous structure. However, a high level of chromium (35.9 at%) and boron (22.0 at%) in both powders, led to the formation of primary boride phase during gas atomisation. The larger boron content of the Armacor M powder would tend to precipitate a larger fraction of primary boride phase. The smaller needle size in smaller diameter particles is due to the fact

that the powder cooling rate increases as the diameter decreases. In powder of 50 μm diameter the cooling rate is likely to be ~ 10^3 K/s but in 5 μm particles it is expected to be ~ $5x10^3$ K/s. The results obtained from DSC scan (Fig. 4.5) and SEM (Fig. 4.6) of the solidified Armacor M powder which related to Fe-B and Cr-B phase diagrams confirms this solidification behaviour.

The Armacor M sample has an eutectic-like solidification behaviour with a single exothermic peak during cooling of the melt as proposed:

$$L \longrightarrow \alpha - Fe + (Fe_{1.1}Cr_{0.9})B_{0.9}$$

which starts at 1286°C and ends at 1241°C,

which is different from that of the Armacor C sample (which exhibits off-eutectic behaviour).

$$L \xrightarrow{1226C^\circ} L + \text{boride} \xrightarrow{\sim 1210C^\circ} L + \text{boride} + (\gamma - Fe)$$

$$\xrightarrow{1174C^\circ} L + \text{boride} + (\gamma - Fe) + \text{white phase}$$

where boride is M_2B, either $(Fe_{1.1}Cr_{0.9})B_{0.9}$ or $(Cr_{1.65}Fe_{0.35})B_{0.96}$

However, the solidification behaviour at high cooling rate in gas atomisation could well be different from that seen at 20 K/min in DSC analysis.

8.2.2 SHS7170

For SHS7170 powder, the XRD trace from the powder particles showed that they consisted of boride phase $(Fe_{1.1}Cr_{0.9})B_{0.9}$ and an iron matrix phase (Figs. 5.3). The crystal structure of the Fe phase in these particles is body centred cubic with a lattice parameter $a_o \approx 0.28664$ nm similar to that of the Armacor M powder. However, a

different structure can be observed in small powder particles and large powder particles. Small powder particles show a single phase structure, while large powder particles shown a two-phase structure with boride needles embedded in the Fe matrix phase. The DSC analysis of the different size of SHS7170 powder (Fig. 5.5(c)) at heating rate 20K/min indicated that smaller particles had a higher proportion of amorphous phase and this confirms that the featureless structure of small particles is typically an amorphous structure. The evidence of amorphous formation as a function of particle size has been reported in the work of Branagan et al. (2002). It could be therefore indicated that the boride peaks observed in the XRD of the powder sample (Fig. 5.3) could be from the boride phase in the larger powder particle. As noted previously, smaller particles cool at a higher rate which will tend to encourage amorphous phase formation instead of crystallization.

Considering the solidification sequence at a low cooling of 20 K/min in the DSC the solidification sequence as proposed in chapter 5:

$$L \xrightarrow{1148C^\circ} L + (Fe_{1.1}Cr_{0.9})B_{0.9} \xrightarrow{\sim 1130C^\circ} L + (Fe_{1.1}Cr_{0.9})B_{0.9} + M_{23}C_6$$

$$\xrightarrow{\sim 1120C^\circ} (Fe_{1.1}Cr_{0.9})B_{0.9} + M_{23}C_6 + (\alpha - Fe + \alpha' - Fe)$$

(Where the α and α′ form in a eutectic reaction but are of different composition).

The microstructure of the slowly solidified SHS7170 powder consists of four phase structure (including $M_{23}C_6$ carbide type). However, this $M_{23}C_6$ carbide could not be observed in the as-received powder, this is thought to be due to the effect of the high cooling rate during gas-atomised process and thus leading to suppression of precipitation of $M_{23}C_6$.

Additionally, the SHS7170 powder sample show a high undercooling during solidification from the melt (Fig. 5.12), indicating a lower critical cooling rate for amorphous phase formation of the SHS7170 sample compared to those of the Armacor M (Fig. 4.5) and Armacor C (Fig. 4.22) powders.

8.2.3 KC1

From the knowledge and understanding of the effect of composition on the amorphous phase formation, a specially designed gas atomised powder, KC1, which was based on Fe-Cr-B-C system was made in order to obtain a larger fraction of amorphous phase. A similar alloy has previously been reported to be one of high GFA, but it is the form of a melt spun ribbon (Pang et al., 2002).

The results have shown that KC1 powder particles of all sizes were fully amorphous as analysed by XRD and SEM. Both of small powder particles and large powder particles showed only a single phase structure which is typically an amorphous structure and this indicated a high ability of material to form amorphous phase.

The strong glass forming ability of KC1 sample is thought to result from meeting the three empirical rules for achieving high GFA, proposed by Ma and Inoue (1999), in which (i) a multi-component alloy system should consist of more than three constituent elements, (ii) the main constituent elements should have a significant difference in atom size ratios above 12% and (iii) negative heats of mixing among the main constituent elements. These are in agreement with the work reported by Scruggs (1998) and Branagan (2004). Considering, the present alloy (KC1 powder) based on Fe-Cr-B-C system, as the base composition of $Fe_{40.1}Cr_{16.79}Mo_{17.2}$

$B_{10}C_{15}Si_{0.9}$ and having atomic ratios above 12%, the atomic radius (in Å) of the elements decreases in the order Mo(1.36) > Cr(1.25) > Fe (1.24) > Si(1.15) > B(0.82) > C(0.77) and atomic pairs with large negative heats of mixing (e.g. Fe-Mo (-2 kJ mol^{-1}), Mo-B (-34 $kJmol^{-1}$), Cr-B (-26 $kJmol^{-1}$), Fe-B (-26 $kJmol^{-1}$)), thus this alloy satisfies the three empirical rules for achieving high glass forming ability (Ranganatan, 2007).

8.3 Comparison of coating and powder structures

The microstructure formation of the as-sprayed coatings shown in Fig. 4.11 (Armacor M), Fig. 4.28 (Armacor C), Fig. 5.16 (SHS7170) and Fig. 6.17 (KC1) are typical of that observed in HVOF deposits of metallic alloys produced by this gun system (Zhang et al., 2003; Kong et al., 2005) in which the coating comprised essentially of a partially or completely melted powder particles which form splat layers upon impact with the substrate.

8.3.1 Armacor M & Armacor C

The XRD trace from the as-sprayed Armacor M coating (Fig. 4.11) shows the presence of a bcc phase with a lattice parameter close to α-Fe (JCPDS file # 006-0696) and the boride phase of $(Fe_{1.1}Cr_{0.9})B_{0.9}$ (JCPDS file # 072-1073). The α-Fe peaks are significantly broadened as compared with those of the as-received powder. There is no evidence for an oxide phase being present. This is as expected since in the Met-Jet II (a liquid fuel (kerosene) HVOF system), the powder is introduced into the nozzle where the gas velocities are high and the gas temperatures relatively low. As a result the coating contains a low level of oxide content since particles are not significantly overheated. In contrast, in the Armacor M coating deposited by the Top

Gun system (Dent et al., 1997) the powder experienced a higher temperature as powder is fed into the combustion chamber and the coating contained a higher content of oxide inclusions.

A SEM-BSE image of a cross-section of a coating (Fig. 4.12(a)) shows that the as-deposited coating exhibits characteristic lamellar microstructures, with the splat layers parallel to the substrate surface and also a proportion of unmelted or partially melted particles with a near spherical shape. A near-spherical region correspond to an original powder particle judging from the size of the boride phase within it and such particles are either unmelted or only heated just above their onset of melting temperature whereas a lamellar splat like features (Fig. 4.12(a) and (b)) with fine scale borides, indicate near complete melting of the original particle and the re-precipitation of borides.

TEM images of the as-sprayed Armacor M coating and associated diffraction patterns with a combination of diffuse rings and elongated spots (Fig. 4.13) again confirm that the sample was composed of both amorphous and crystalline regions. The diffuse ring is indicative of an amorphous phase whilst the elongated spots indicate a crystalline phase. The streaking is due to the phase having closely spaced faulted lattice planes.

In contrast, the XRD trace of the as-sprayed Armacor C coating Fig. 4.28(c) shows the presence of a fcc phase with a lattice parameter close to γ – Fe (JCPDS file # 047-1405) and the boride phase of either $(Fe_{1.1}Cr_{0.9})B_{0.9}$ or $(Cr_{1.65}Fe_{0.35})B_{0.96}$. In addition, there has been a significant increase in the proportion of the amorphous

phase as shown by a broader diffraction halo around $2\theta = 39 – 48°$ as compared with that of the as-received powder, indicating a larger proportion of an amorphous or nanocrystalline structure in the coating. This is thought to be due to dissolution of B from the boride in the Fe-rich melt during spraying which promotes the formation of an Fe-B rich amorphous phase together with a supersaturated γ – Fe solid solution following the high cooling of the sprayed particles. Splats are estimated to cool at 10^6–10^7 K/s as compared with ~10^3 K/s for gas atomisation.

BSE of the cross-section of the Armacor C coating (Fig. 4.29) showed that the coatings exhibited characteristic lamellar microstructures, with the splat layers parallel to the substrate surface. A near- spherical morphology of unmelted or partially melted particles was also present in the coating. However, porosity of the Armacor C coating is obviously lower than that in the Armacor M coating.

TEM images of the as-sprayed Armacor C coating and associated diffraction patterns with a combination of diffuse rings and spots (Fig. 4.13) indicate that an amorphous and crystalline phase are present in the coating.

The Armacor M coatings shows a high level of hard boride phase as was seen in the powder feedstock. The more rounded morphology of many of the borides indicates some dissolution during spraying. However, dissolution has been limited by the large boride size in the feedstock (providing a low surface area to volume ratio) and many large borides have survived. Compared with the Armacor M coating, the Armacor C coating exhibits a lower volume fraction of borides (and fine grain size) as in the feedstock powder which resulted in a higher level of dissolved boron into a binder

phase. Thus, it could be expected that the Armacor C coating exhibits a higher volume fraction of amorphous phase than that of the Armacor M coating which has less dissolution of the boride phase during deposition.

8.3.2 SHS7170

The partially amorphous, partially crystalline nature of the coatings is clear from the following: (i) the XRD pattern of Fig. 5.15; (ii) the SEM images of Fig. 5.16; (iii) the TEM images of Fig. 5.18 and (iv) the DSC traces of Fig. 5.19. As has been discussed previously (Zhang et al., 2003), coatings deposited by the liquid fuel gun employed here show clear evidence of the impact of partially melted powder particles (generally those of large diameter) which have near-spherical or deformed spherical shapes in the coating and fully melted powder (generally of smaller diameter) which flatten and solidify to give characteristic lenticular splat features in the coating. As seen in Fig. 5.4(b), the larger particles in the original powder possess a two-phase structure of $Fe_{1.1}Cr_{0.9}B_{0.9}$ plates in a matrix of α-Fe and this microstructure is retained in the as-sprayed coating, see Fig. 5.17. Smaller powder particles are apparently heated to a significantly higher temperature in the gas jet, as predicted by numerical modelling studies (Kamnis et al., 2008), become fully melted and, on impact, form lenticular splats which solidify rapidly. The cooling rate of such splats is estimated to be of the order of 10^7 Ks^{-1} (Moreau et al., 1991) and in this high GFA alloy they are thus expected to form an amorphous structure.

A consideration of the structures formed in the original powder particles supports this analysis. It is seen from Figs. 5.3(a), 5.4(a) and 5.5 that a significant fraction was amorphous and it was observed that the maximum diameter of a fully amorphous

particle was ~ 22 μm. Using the well known relationship between powder diameter and cooling rate (Yule and Dunkley, 1994), 22 μm particles of an Fe-based alloy are estimated to cool at around 10^3 to 10^4 Ks^{-1} during their manufacture by gas atomisation. Thus this cooling rate range can be seen to be an estimate for the critical cooling rate for glass formation in the alloy. This is well below the cooling rate of splats and so confirms that splats of fully melted material are likely to be amorphous.

The bright field TEM image of the SHS7170 coating and the SAD pattern with diffuse rings in Fig. 5.18(a) and (b) confirms an amorphous phase present in the coating. However, in some area of the amorphous matrix, the presence of structure with small grains in size ranging from 20-200 nm can be observed as shown in Fig. 5.18(e), and these may be described as microcrystalline or at the smaller size range (<100 nm), nanocrystalline. The nanocrystalline grains were identified as bcc iron-based from the polycrystalline selected area diffraction (SAD) ring pattern shown in Fig. 5.18(f). The relatively small size of these nanocrystalline grains suggests that these could not to have formed directly by nucleation and growth from the melt during thermal spraying (Dent, 2002). It seems more probable that they formed by devitrification or crystallisation of the amorphous matrix due to the reheating effects of the deposition of subsequent impinging splats. Boride precipitation was also apparent within the coating. These are confirmed from the XRD trace from the coating where peaks from a bcc α–Fe cubic and $Fe_{1.1}Cr_{0.9}B_{0.9}$ are marked.

The present observations on HVOF coating formation are consistent with work reported by Branagan et al. (2005) on the same alloy but deposited by wire-arc spraying. Branagan et al. (2001) also observed similar mixed amorphous/crystalline

structures in HVOF and air plasma sprayed coatings using a high GFA alloy of nominal composition $Fe_{63}Cr_8Mo_2Si_1Al_4B_{17}C_5$. In comparison, the present alloy's composition was $Fe_{52}Cr_{19}Si_3Mo_2W_2Mn_2B_{16}C_4$, i.e. of similar B and C levels but richer in Cr (at the expense of Fe) and with W and Mn replacing Al and Si.

8.3.3 KC1

The microstructure of the KC1 coating (Fig. 6.17) consists of a single phase, fully amorphous structure similar to that of the powder structure. Some of the iron and chromium in the molten powder has oxidised during spraying, resulting in a significant level of chromium oxide within the coating. This could be due to the fact that the powder feedstock contained a higher fraction of < 15 μm diameter fine particles than the other alloys. This would lead to more overheat powder particles, a higher degree of oxidation and thus more oxide stringers can be observed in the BSE image of the cross-section of the coating (Fig.6.18d).

The bright field TEM image of the KC1 coating and SAD pattern with diffuse rings in Fig. 6.18 confirms that the KC1 coating consists of a fully amorphous structure. A fully amorphous structure of Fe-Cr-B-C based alloys with a similar composition has been reported previously in the work of Pang et al. (2002) and Kishitake et al. (1996).

8.4 Analysis of DSC data

8.4.1 Armacor M & Armacor C

From the DSC analysis, the amorphous formation in the coatings was identified by comparing the heat of crystallization of amorphous phase (which is proportional to the area under the peak in the DSC scan) in the powder and the coating samples. In the DSC curves obtained from the Armacor M (Fig. 4.5) and Armacor C (Fig. 4.22) powders, there is no evidence of the exothermic peak can be observed suggesting no amorphous phase formation in the powders. However, the exothermic peak can be observed for the Armacor M and Armacor C coatings indicating that amorphous phase has been formed in these coatings. This is thought to be due to partial dissolution of the boride phase into the molten Fe-matrix during spraying. B is known to promote amorphous phase formation and together with the higher cooling rate of splats compared to gas atomised powder will tend to increase amorphous phase formation.

8.4.2 SHS7170

The DSC traces indicate that the amorphous fraction of the coating crystallises in two stages, a main peak at around 645 °C and a smaller secondary peak at ~ 790 °C, depending on the heating rate (see Fig. 5.19, Table 5.2 and 5.5). A comparison with the DSC thermograms for the powder shows similar temperatures for the first crystallisation peak but in the powder the 2nd peak seems to appear at a significantly higher temperature (around 850°C). Furthermore, in the coating the first peak exhibits a distinct shoulder whereas this is absent in the powder traces, compare Figs. 5.5 and 5.19 for powder and coating respectively. Overall, the decomposition pathway appears to follow that suggested by Lu (1996) i.e. in the first step the

amorphous phase crystallises into a primary phase and a residual amorphous phase of different composition. At a higher temperature this residual phase crystallises in a second step into one or more crystalline phases. Such a two stage crystallization process is common in Fe-based amorphous alloys and often leads to nanoscale crystallization products (Pang et al., 2002; Lu, 1996; Chen et al., 2006). The reason for the formation of a pronounced shoulder on the low temperature side of the first DSC peak obtained from coating samples needs to be examined. Such a shoulder was not present on the DSC traces from powder, see Figs. 5.5 and 5.19. The shoulder on the low temperature side is possibly the manifestation of the early crystallization of amorphous material in the coating that was significantly reheated for a short period during successive passes of the spray gun whilst depositing multiple layers. Local reheating would allow the formation of pre-existing crystalline nuclei or relaxation of the amorphous state, as proposed by Graydon et al. (1995), which leads to a portion of the amorphous phase crystallizing at lower temperature. Local reheating during spraying and amorphous phase relaxation could also be the reason for the lower temperature of the second DSC peak in coating samples.

Activation energy is regarded as an important parameter characterizing the crystallization process and for the first peak it was determined to be 375 kJ/mol for the powder and 385 kJ/mol for the coating using the Kissinger method (see chapter 3). The errors associated with the measurements mean that these values should be regarded as essentially the same. For the second peak, the activation energy is lower than for the first peak and is also found to differ somewhat for powder and coating, the values being 333 and 290 kJ/mol, respectively. This difference could also be due to reheating of the coating during spray deposition. Broadly, these activation energies

are in line with values obtained in other multicomponent Fe-based amorphous alloy systems, for example Chen et al. (2006).

Considering now the enthalpies associated with the two crystallization stages, the value obtained for the first stage is 20 Jg^{-1} for the powder and 55 Jg^{-1} for the coating. For the second stage the respective values for powder and coating are 25 and 16 Jg^{-1} respectively. The much larger value for the coating indicates that a much larger portion of amorphous phase formed as a result of spraying the powder. This is consistent with the more pronounced amorphous halo around 2θ = 42-48° of the XRD pattern from the coating, Fig. 5.15. The powder was clearly a mixture of amorphous and crystalline particulate and the largest particle diameter that was amorphous (as assessed by the absence of contrast in the SEM) was ~ 22 μm. In a separate experiment, the powder particle size distribution was measured using a laser diffractometer-based method and form the resultant size distribution it was found that 18 vol.% was below 22 μm in size. This is equivalent to 18 wt.% as all powder particles are assumed to have the same density. Therefore the measured value of 20 Jg^{-1} for the enthalpy of the first crystallization peak of the powder corresponds to a value of approximately 110 Jg^{-1} (i.e. 5.6 $kJmol^{-1}$) for the material, taking account of the fact that only 18 wt.% of the powder was actually in the amorphous state. This is similar to the value of 127 Jg^{-1} reported by Branagan et al. (2001) for related Fe-based amorphous alloys.

As the first crystallization enthalpy of the coating was 55 Jg^{-1} this would suggest that the amorphous fraction in the coating was around 50%. This increase in amorphous fraction occurs because in the thermal spray gun a significant proportion of the

powder is melted and these molten particles give rise to solidified lenticular splats in the coating, as seen in the SEM images of Figs. 6(a) and (b). Splats cool at a sufficiently high rate (around 10^7 Ks^{-1} (Moreau et al., 1991)) to have an amorphous structure and the 50% amorphous fraction measured by DSC arises from these rapidly quenched splats. The unmelted powder particles seen in the coating retain their crystalline structure during spraying. In contrast to this, Branagan et al. (2005) reported that when a coating of the same alloy was produced by wire-arc spraying (with a cored wire) the amorphous fraction was 70%. This is greater than the present HVOF coatings because wire-arc spraying involves converting all the solid feedstock into fully molten droplets which are then expected to become amorphous when they strike the substrate, cool rapidly and solidify; suggesting a 100% amorphous coating could be achieved. The reason that it was only 70% amorphous is probably due to re-heating of the coating during deposition of successive layers leading to recrystallization of the original amorphous phase.

8.4.3 KC1

The results of the DSC heating and cooling scans of the as-received KC1 powder (Fig. 6.13), obtained at a scanning rate of 20K/min, show evidence of glass transition temperature at ~ 616°C (which is not found in the Armacor M, Armacor C and SHS7170) and the onset of crystallisation temperature at ~ 688°C. The solidus temperature, T_m and liquidus temperature, T_l evaluated from the DSC scans were 1137°C and 1359°C. Therefore, the supercooled liquid region $\Delta T_x = (T_x - T_g) = 72$ K and the reduced glass transition temperature (T_g/T_m) and (T_g/T_l) can be determined to be 0.63 and 0.54, indicating a high glass forming ability. These are in agreement with

the values obtained in an Fe-based amorphous alloys reported by Pang et al. (2002) and Farmer et al. (2009), in which $T_g/T_m \sim 0.62$ and $T_g/T_l \sim 0.55$, respectively.

Also, for the KC1 alloy, a similar value of the heat of crystallization has been obtained in the KC1 powder and coating because both are essentially fully amorphous. Furthermore, these values are higher than those of the SHS7170 powder and coating.

A comparison of the activation energy for crystallization and the heat of crystallization obtained from the DSC scans of the as-received powder and the as-sprayed coating for the four samples is shown in Table 8.1.

Table 8.1 The activation energy E_p and enthalpy ΔH (kJ mol^{-1}) for the crystallisation events obtained from the DSC scans of the as-received powder and the as-sprayed coating for the four samples (using the main peak, P_1)

Sample Type	$E_{p1\ powder}$ kJ mol^{-1}	$\Delta H_{p1\ powder}$ kJ mol^{-1}	$E_{p1\ coating}$ kJ mol^{-1}	$\Delta H_{p1\ coating}$ kJ mol^{-1}
Armacor M	-	-	280	1.12
Armacor C	-	-	225	2.10
SHS7170	375	1.09	385	2.64
KC1	377	5.15	351	4.95

These E_a and ΔH values are in good agreement with other Fe-based amorphous alloys (Chen et al., 2006), implying that the as-sprayed SHS7170 and KC1 coatings exhibit a high thermal stability which therefore means more resistance to crystallization of an amorphous phase formed in the coating. The fraction of amorphous phase in the coatings decreases in the order KC1 >> Nanosteel SHS7170 > Armacor C > Armacor M. These are in agreement with the results of XRD, SEM and TEM that the as-sprayed Armacor M, Armacor C and Nanosteel SHS7170

coatings are a mixture of amorphous and crystalline phases, whereas the as-sprayed KC1 coating is composed of only an amorphous phase.

8.5 Microstructural and microhardness changes during heat treatment

8.5.1 Armacor M & Armacor C

In the Armacor M powders and coatings, heat treatments the samples up to a temperature of 925°C for 1 hour caused no changes to the phases present in the coatings (see XRD traces in Figs. 4.8 and 4.16). The samples show the presence of a bcc Fe matrix phase and the boride phase $(Fe_{1.1}Cr_{0.9})B_{0.9}$ which are similar to those of the as-received powder and as-sprayed coating. However, it is interesting to note that the heat treated coating samples at 750°C for 1 hour, led to microstructural change in which fine boride precipitates can be observed as shown in Fig. 4.17(d). These then became larger at a temperature of 925°C whereas in the powder samples no precipitates can be seen.

Similarly, in the Armacor C powders and coatings, heat treatment of the samples up to a temperature of 925°C for 1 hour again caused no changes to the phases present in the coatings as seen in the XRD traces in Figs. 4.25 and 4.33 and the SEM images in Figs. 4.21 and 4.26. In comparison to the Armacor C powders, a microstructural change, however, can be seen in Fig. 4.34(d) of the coatings following heat treatment at 750°C for 1 hour, fine precipitates within the fully melted region can be observed. This suggests crystallisation of an amorphous matrix occurred in this region and

precipitates became larger at a temperature of 925°C (see Fig. 4.34(f)). These correspond to the XRD peaks as shown in Fig. 4.33.

The hardness of the Armacor M and Armacor C coatings, containing boron decreased when annealed at temperatures of 750°C or higher. The as-sprayed Armacor M coating showed a high hardness (~11.1 GPa) whereas the as-sprayed Armacor C coating has a moderate hardness (~8.5 GPa). The greater hardness of the Armacor M coating is due to the presence of a greater proportion of the boride phase in the coating. However, after annealing at temperature 550-925°C, both the annealed Armacor M and Armacor C coating samples exhibited lower hardness than those of the as-sprayed conditions. This is thought to be due to crystallisation of the matrix and/or precipitation of a boride (M_2B) phase. Similar results have been shown in the work reported by Kim et al. (1999b) for the HVOF-sprayed Armacor M coating following heat treatment at temperatures of 700°C, 800°C, 900°C and 1000°C. They also found that there was no change in phase after heat treatment and the hardness decreased as compared to that of the as-sprayed coating.

8.5.2 SHS7170

Heat treatment temperatures were selected to be: (i) below the first crystallization peak at 550 °C; in between the first and second peaks at 650 and 750 °C; and (iii) well above the second crystallization peak at 925 °C. It is evident from Figs 5.7, 5.9, 5.21 and 5.22 that phase changes and microstructural evolution proceed in a similar manner in powders and coatings. Annealing for 60 minutes at 550 and 650 °C produced no new phases that could be detected in the XRD diffractorgrams. The main difference between these two heat annealing temperatures was the appearance

of more pronounced boride and α-Fe peaks particularly in the coating. Therefore this suggests that the primary crystallization stage at ~ 640 °C involves decomposition of the amorphous phase into these two phases with a residual amorphous phase which decomposes at a higher temperature. Annealing at 750 °C for 60 minutes led to the first appearance of the $M_{23}C_6$ phase in both powder and coating samples. The $M_{23}C_6$ peaks became much stronger and sharper following annealing at 925 °C. This suggests that the main change in the second stage of crystallization was the precipitation of the carbide phase and α-Fe and that most of the boride phase was produced in the first crystallization reaction.

The main microstructural change as a result of annealing was the formation of a nanoscale mixture of crystalline phases, i.e. and nanoscale composite, from fully amorphous regions. This is seen most clearly in Fig. 5.9(c) showing a fine powder particle annealed at 750 °C and in Fig. 5.22(d) (region F) showing a splat region of a coating. In coarser powder particles, nanoscale precipitates also formed following annealing at 750 °C in between the boride plates. The main effect of annealing a coating at 925 °C was to produce a significantly coarser precipitate distribution as seen in Fig 5.22(f) where both F and P regions of a coating display micron sized precipitate features as opposed to the nanoscale features seen following annealing at 750 °C. Following annealing at 925 °C, similar precipitate distributions were found in fine and coarse gas atomised powder particles.

The coatings exhibit a hardening response which depends on heat treatment time and temperature. The hardness in the as-sprayed coating is 9.2 GPa and this is increased to a maximum of 11.8 GPa after heat treatment at 750 °C and a maximum of 12.5

GPa after heat treatment at the lower temperature of 650 °C. These are comparable to the hardness values in the range of 11.55-12.68 GPa obtained in Fe-Cr-B based alloy coating (with composition of $Fe_{49.7}Cr_{17.7}Mn_{1.9}Mo_{7.4}W_{1.6}B_{15.2}C_{3.8}Si_{2.4}$ (in at %)), following heat treatment at 700°C for 10 minutes (Branagan et al., 2006). However, this is less than the values 16.2 GPa obtained in the Fe-Cr-B based alloy as-spun ribbons after heat treatment at 700°C (Branagan and Tang, 2002). It is clear that devitrification of the amorphous phase is the main reason for the increase in hardness seen initially. This devitrification will lead to nanoscale α-Fe grains and nanoscale boride/carbide precipitates. It has also been suggested (Zhong et al., 1997) that compositional changes to the residual amorphous phase can also have an important hardening effect. The higher peak hardness occurs at a lower annealing temperature even though carbide/boride precipitation is more pronounced at the higher temperature. Therefore, it is evident that the relationships between microstructural changes and microhardness are complex and that further work is needed to clarify this behaviour. With longer annealing times, the hardness begins to decrease at both the annealing temperatures. It is observed that grain and precipitate coarsening occurs with increased holding time and it is likely that solid solution strengthening of the α-Fe phase through solute supersaturation also starts to diminish. Both of these factors could account for the decreasing hardness. The presence of a high fraction of high diffusivity grain boundary paths would greatly speed up the process of loss of supersaturation. The fact that loss of hardness occurs much sooner at higher temperatures could suggest it is mainly due to diffusion of transition elements e.g. Cr, Mo, W, which are substitutional atoms, and is not principally a result of loss of supersaturation of interstitial B and C which are mobile even at low temperatures.

8.5.3 KC1

In the KC1 powder and coating samples, heat treatments up to a temperature of 650°C for 1 hour caused no microstructural change in the corresponding XRD traces (Figs. 6.7 and 6.22). However, following heat treatment at 750°C, the presence of a number of new peaks in the XRD trace was identified along with a reduction in the intensity of the amorphous haloes present (Fig. 6.7(d) powder and 6.22(e) coating. The XRD traces for the powder and coating heat treated at 925°C show peaks indexed to the α-Fe and precipitation of a borocarbide $M_{23}(C,B)_6$, carbide M_6C and boride Mo_2FeB_2.

SEM investigations of both the KC1 powder and the coating heat treated at 925°C showed a very fine structure of precipitation of a borocarbide $M_{23}(C,B)_6$, carbide M_6C and boride Mo_2FeB_2 which had precipitated within the amorphous phase (Figs. 6.11 and 6.24). The formation of α-Fe, borocarbide $M_{23}(C,B)_6$ and eta carbide M_6C type has been previously observed following heat treatment of thermally sprayed Fe-10Cr-10Mo-(C,B) coatings (Kishitake et al., 1996), whereas the formation of boride Mo_2FeB_2 type (or M_3B_2 where M is Mo and Fe) in the present study has been previously found in the work reported by Yijian and Jian (1991) for the melt-quenched $Fe_{70}Cr_{18}Mo_2Si_1B_9$ ribbon following annealing at temperatures between 700-1150°C.

It should be noted that the KC1 sample only showed microstructural change at a higher temperature (>750°C) than those of the Armacor M, Armacor C as well as the SHS7170. This is thought to be due the higher thermal stability of the amorphous phase in the KC1 sample (higher values of the glass transition temperature T_g, onset

of crystallization temperature T_x , peak temperature T_P, enthalpy of crystallisation ΔH and the activation energy of reaction E_a, the higher thermal stability of amorphous phase).

Moreover, a significant change in the hardness of the sample was found in the as-deposited KC1 coating following heat treatment at 750°C, the peak hardness of the sample increased and reached at a value of 13.2 GPa and exhibits the highest hardness of all these annealed coatings studied in the present work. This is comparable to the hardness values in the range of 11.8-13.7 GPa obtained in Fe-Cr-(B,C) based alloy coating following heat treatment at 873K (600°C) for 1 hour (Kishitake et al.,1996). The greater hardness of the KC1 coatings after heat treatment could be due to the presence of a very fine mixed structure of α-Fe, carbide, borocarbide and/or boride by decomposition of the amorphous phase in the coating. The difference of the hardness between SHS7170 and KC1 coatings is thought to be partially due to the difference of a volume fraction of amorphous phase which can be then devitrified into a very fine multiphase structure.

8.6 Wear performance of coatings

8.6.1 Wear rates and mechanisms

The wear of the Fe-Cr-B based alloys did not obey the Archard wear equation (Hutchings, 1992) which predicts a direct correlation between hardness and wear rate. A better correlation was found between wear and the microstructure of the coatings which in turn effects their properties.

Table 7.1 presents the hardness of the coatings which decreases in the order WC-Co-Cr > Armacor M > SHS7170 > Armacor C. The Armacor M coating consists of a larger volume fraction of hard boride phase (64 %) compared to that of the SHS7170 coating (35 %) and the Armacor C coating (37 %). For the WC-Co-Cr coating the carbide fraction was ~ 67 %. As a result, the Armacor M coating has higher value of the hardness than the other boride coatings. The fracture toughness of the four coatings decreases in the order WC-Co-Cr > SHS7170 > Armacor M > Armacor C (see Table 7.1). The fracture toughness of the WC-Co-Cr coating in the present study is in agreement with the work reported previously by Deng (2007).

8.6.1.1 Wear of Armacor C and M coatings

The wear performance of the Armacor C coating was particular poor. The wear rate of the Armacor C coating is higher than that of the Armacor M coating as shown in Figs. 7.2 and 7.21. This is as expected since the Armacor C coating has both a lower hardness and lower fracture toughness than that of the Armacor M coating (see Table 7.1).

At high loads, both the Armacor C and Armacor M coatings exhibit high wear rates compared to those of the other coatings (SHS7170 and WC-Co-Cr) investigated in this study. This is thought to be due to lower fracture toughness of the Armacor C and Armacor M coatings compared to those of SHS7170 and WC-Co-Cr coatings as shown in Table 7.5.

SEM images of the Armacor C and Armacor M coating surfaces following sliding wear show extensive material loss and sub-surface cracking within the coatings (Figs. 7.4-7.5, Fig. 7.7 and Figs. 7.8-7.9). The wear scars on the coatings show the features of abrasive wear, adhesive wear, and plastic deformation. However, abrasive wear seemed to dominate the wear process at the highest load 70 N. The wear scars generated under the highest load of 70 N were deeper than those produced at lower loads with more severe subsurface cracking running along splat boundaries indicating more severe abrasive wear, possibly due to higher stress at the contact area (between the ball and the coating).

The Armacor C and the Armacor M coatings following sliding against an alumina ball generated a friction coefficient $\mu \sim 0.4$-0.6 across the range of all applied loads. In contrast, the Armacor C and Armacor M coatings following sliding against zirconia and 440C steel balls exhibited a relatively low friction coefficient ($\mu \sim 0.2$ at the low loads of 5.8-11.7 N and $\mu \sim 0.5$ at the higher loads of 46.6-70 N), which could be due to their self-lubricating nature. Observations of the wear scars on the alumina and zirconia balls following sliding against the Armacor C and Armacor M coating show a small amount of transferred material, even for the 440C steel counterface indicating a low adhesion of wear debris, thus resulting in a low friction

coefficient as indicated. However, the Armacor C coating following sliding against 440C steel ball at the highest load of 70 N generated a high coating wear rate associated with a high coefficient of friction and thus resulting in the high wear rate of the ball as shown in Fig. 7.2(c).

It is interesting to note that the Armacor C coating following sliding against 440C steel ball at the low loads of 23.3 N (Fig. 7.2(c)) generated a low coating wear in comparison to the Armacor M and the SHS7170 coatings. This is thought to be due to a formation of larger patches of oxide-based transferred material on the top of the worn surface (see Fig. 7.8(c-d) and that can act as a protective layer resulting in a low wear rate of the coating.

8.6.1.2 Wear of SHS7170 coating

The wear rate of the SHS7170 coating following sliding against the ceramic ball (alumina and zirconia) is lower than those of the Armacor C coating as shown in Fig. 7.2. This could be due to the fact that the SHS7170 coating has higher hardness than that of the Armacor C coatings. However, the hardness of the SHS7170 coating was lower than that of the Armacor M coating, but the SHS7170 coating exhibited better sliding wear performance. The specific wear rate of the SHS7170 coating (7.489 x 10^{-15} $m^3N^{-1}m^{-1}$) was comparable to those of the HVOLF conventional WC-12wt%Co coating (1.465 x 10^{-15} $m^3N^{-1}m^{-1}$) measured under similar conditions (Sudaprasert et al., 2003). The measured wear rate (<10^{-7} mm^3/Nm) of the SHS7170 coating with no brittle cracking, clearly indicates the occurrence of a mild wear regime.

In the wear test with the SHS7170 coating against the alumina ball, a relatively high friction coefficient is observed. This is comparable to the friction coefficient obtained for the ball-on-disk testing of ceramic/ceramic under unlubricated sliding conditions (M.S.-Suh, 2008) for example in the case of ZrO_2 disk and Al_2O_3 ball, the coefficient of friction is in the range of 0.6-0.8. The high value of the friction coefficient was thought to be due to the formation and localized delamination of a transfer layer when rubbing against the counterfaces.

However, the SHS7170 coating following sliding against the 440C steel ball generated a high wear rate with a relatively high coefficient of friction (especially at the low load of 46.6 N) compared to that of the Armacor C coating as show in Fig. 7.2(c). This could be due to the SHS7170 coating having a good adhesion to the ball surface during sliding wear process.

8.6.1.3 Wear of WC-Co-Cr coating

Although, the hardness of WC-Co-Cr coating was similar to that of the Armacor M coating, the WC-Co-Cr coating exhibited better sliding wear performance. The greater wear resistance of the WC-Co-Cr coating could be due to a number of factors including the fact that the WC-Co-Cr coating has higher fracture toughness than that of the Armacor M coating as shown in Table 7.1. Additionally, the WC-Co-Cr coating gives a lower wear rate with an alumina ball surface as shown in Fig. 7.21, implying that the WC-Co-Cr coating with a combination of high hardness and high fracture toughness exhibits superior sliding wear resistance to that of the Fe-Cr-B based alloy coatings studied in this work.

8.6.2 The effect of counterfaces on wear

The wear scars on the alumina and zirconia counterfaces show the features of abrasive wear, adhesive wear, and plastic deformation. Adhesive wear seemed to dominate the wear process at the highest load 70 N. Those wear scars were wider and/or deeper corresponding to their higher wear factors. The wear scars generated under the highest load of 70 N were wider and rougher than those produced at lower loads with larger patches of oxidised material transferred from coating to ball implying more severe adhesive wear, possibly due to higher temperature at the contact area.

For all coatings, the wear rate with ceramic balls (alumina and zirconia balls) is several times higher than that with the 440C steel balls (Fig. 7.3). This is accounted for by two factors, namely surface morphology and hardness. The ceramic balls (alumina and zirconia) are significantly harder than the coating and wear to form a rough fractured surface whereas the steel 440C ball has lower hardness than those of the ceramic balls. Therefore, the steel 440C ball gives rise to much lower rates of coating wear than that of ceramic balls and as such, there is little evidence of a ploughing component to wear.

In the sliding wear tests of the coatings slid against alumina ball as a function of sliding distance at a load of 23.3 N, the fracture of the alumina ball was minimized, thus the results of the wear resistance of the amorphous/crystalline coating with essentially higher fracture toughness as expected from the SHS7170 coating can be more pronounced in this condition.

Figs. 7.2(a)-7.2(c) show the results of wear rates of the coating when slid against three counterfaces; alumina ball, zirconia ball and steel 440C ball. It is notable that at high load of 70 N, the wear rates of the zirconia ball slid against SHS7170 coating are extensively higher than those of an alumina ball and 440C steel ball when tested against SHS7170 coating. This is not surprising, since the fact that the thermal conductivity of zirconia ball (2.15 W/mK) is poor compared to that of an alumina ball (6.9 W/mK) and a steel 440C ball (24.2 W/mK). In general zirconia had a high adiabatic character, so that the heat generated by friction was not lost to the surroundings, and the contact areas reached higher temperatures (Suh et al., 2008). At contact areas between the surface asperities, the contact temperature could be high enough to thermally activate the phase transformation of the tetragonal to monoclinic phase with the associated volume increase (~ 4%) leading to extensive microcracking that can have a detrimental effect on the wear properties of zirconia (Rainforth, 1993; Vleugels et al., 2002; Basu et al., 2004).

Similarly, alumina balls, when slid against the SHS7170 coatings, suffered severe wear at a high contact load of 70 N. This is consistent with the work reported by Dey et al. (2009) which argued that alumina shows a transition from a mild wear to severe wear under a high load. Wear of alumina can be increased with increasing temperature up to 400 C°, with the exception of alumina softening at 600 C° and its wear mechanism was dominated by adhesive wear mechanism (Ming & Li, 1993).

In contrast, the 440C balls did not suffer severe wear under these particular sliding conditions, but showed superior wear behaviour to those of the ceramic counterfaces. The wear rates of the 440C balls when slid against the three coating types; Armacor

C, Armaocr M and SHS7170 seems to be more similar to the wear rates of the coatings. The superior wear behaviour of the 440C ball would be due to its higher thermal conductivity as well as ductility, fracture toughness and hardness.

In comparison, the WC-Co-Cr coating when slid against the alumina ball shows a low wear rate of both the coating and the ball. It is suggested that the temperature at the areas of contact of the coating and the ball were not high enough to cause a transition from a mild wear to severe wear of the alumina ball in such areas. This could be due to the high thermal conductivity of the cermet WC-Co-Cr coating (~ 84 W/mK for WC) which led to more rapid heat transfer during the sliding wear test and lowering the temperature at the contacting interface.

8.6.3 The factors controlling wear

There may be two main factors controlling wear of the coatings studied in the present work; crack propagation along splat boundaries and oxidative wear. In most cases, crack propagation along splat boundaries of the coatings during dry sliding wear test can be observed. The wear scars on both the SHS7170 coatings and counterface materials surfaces show film oxide layers formed on the surfaces during the sliding wear tests under dry contact conditions. This indicates that oxidational wear has occurred. This is in agreement with several authors who have demonstrated that the wear behaviour of the metallic glasses appears to be dominated by the development of oxide layers on the sliding surfaces (Anis et al., 1994; Prakash et al., 2000; Moreton and Lancaster, 1985). They indicated that protective oxides formed can act as a barrier between the real areas of contact and can support the load during sliding wear, thus lowering the wear rate. However, the formation of an oxide layer can have

a detrimental as well as a beneficial effect on wear mechanism. When these oxide layers reach a critical thickness, normally about 1 to 3 μm, they then break up and appear as wear particles which may accelerate the wear rate (Quinn, 1983; Hucthings, 1992).

This indicates that the microstructure of the coatings have a strong influence on the wear behaviour. The SHS7170 coating consists of a larger proportion of an amorphous phase than that of the Armacor C and Armacor M coatings and thus exhibits higher wear resistance. Models for wear behaviour of these three Fe-Cr-B based alloy coatings are shown in Figs. 8.1a-b. Particularly, the sliding wear mechanism of the SHS710 coating was drawn in Fig. 8.2 for low and high wears of the coating. As discussed previously in the section 8.3, the SHS7170 coating consists of a large fraction of amorphous phase and boride phase. At a low load, the SHS7170 coating shows film oxide layers formed on the surface during sliding wear tests under dry contact conditions (Fig. 8.2) and that acts as a barrier between the real areas of contact between the coating and the ball and that giving a low wear rate. In contrast, at a high load, the rate of material removal is higher than the rate of the oxide formation on the surface of the coating resulting in a high wear rate.

8.7 Summary

As discussed above, it can be seen that coating performance is strongly dependent on the coating microstructure, which in turn is dependent on the characteristics of the starting powder from which the coating is formed and spray process parameters employed. Thus in terms of producing amorphous alloy coatings, it is therefore necessary to consider several factors including: i) the glass forming ability (GFA) of the alloys, ii) the presence of amorphous and/or crystalline structure in the original starting powder as well as iii) the spraying parameters employed which influence the crystallisation of amorphous phases in the coating due to reheating effects as incremental layers are added by rastering the spray gun over the substrate to build up a thick deposit.

For sliding wear-resistant Fe-Cr-B coatings, the microstructure of the coatings becomes an important factor and needs to be considered. In this work the SHS7170 coating consisting of boride precipitates and a larger proportion of an amorphous phase exhibits higher sliding wear resistance, compared with that of the Armacor C and Armacor M coatings. However, the wear resistance of the SHS7170 coating was not better than that of the WC-Co-Cr coating. The greater wear resistance of the WC-Co-Cr coating was believed to be due to a combination of high hardness and high fracture toughness. Thus, improvements in the Fe-Cr-B based alloy coatings in the present work will need to be further investigated in various wear conditions and environments in order to assess the suitability of applying amorphous/crystalline coatings to parts of engineering surface applications requiring high wear resistance.

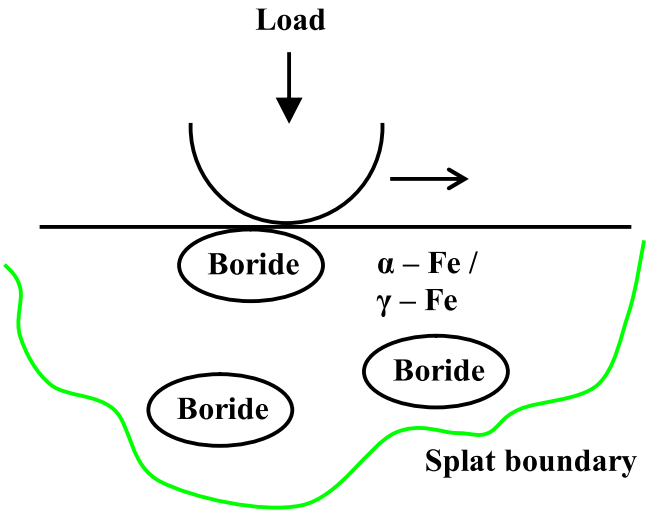

(a)

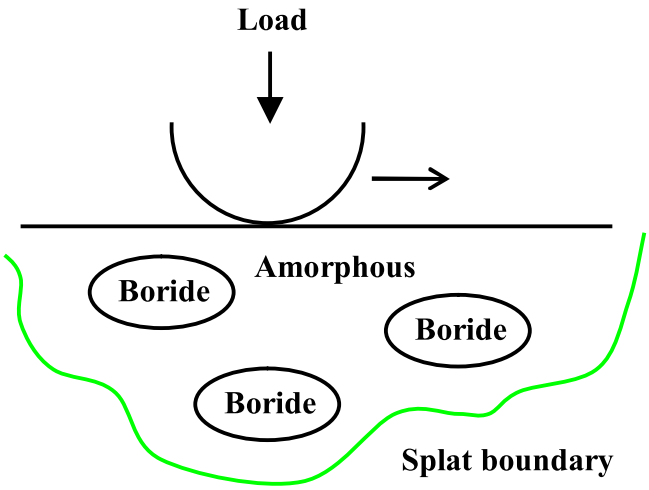

(b)

Figs. 8.1 Models of the microstructure of (a) the Armacor M and the Armacor C coatings, (b) the SHS7170 coating.

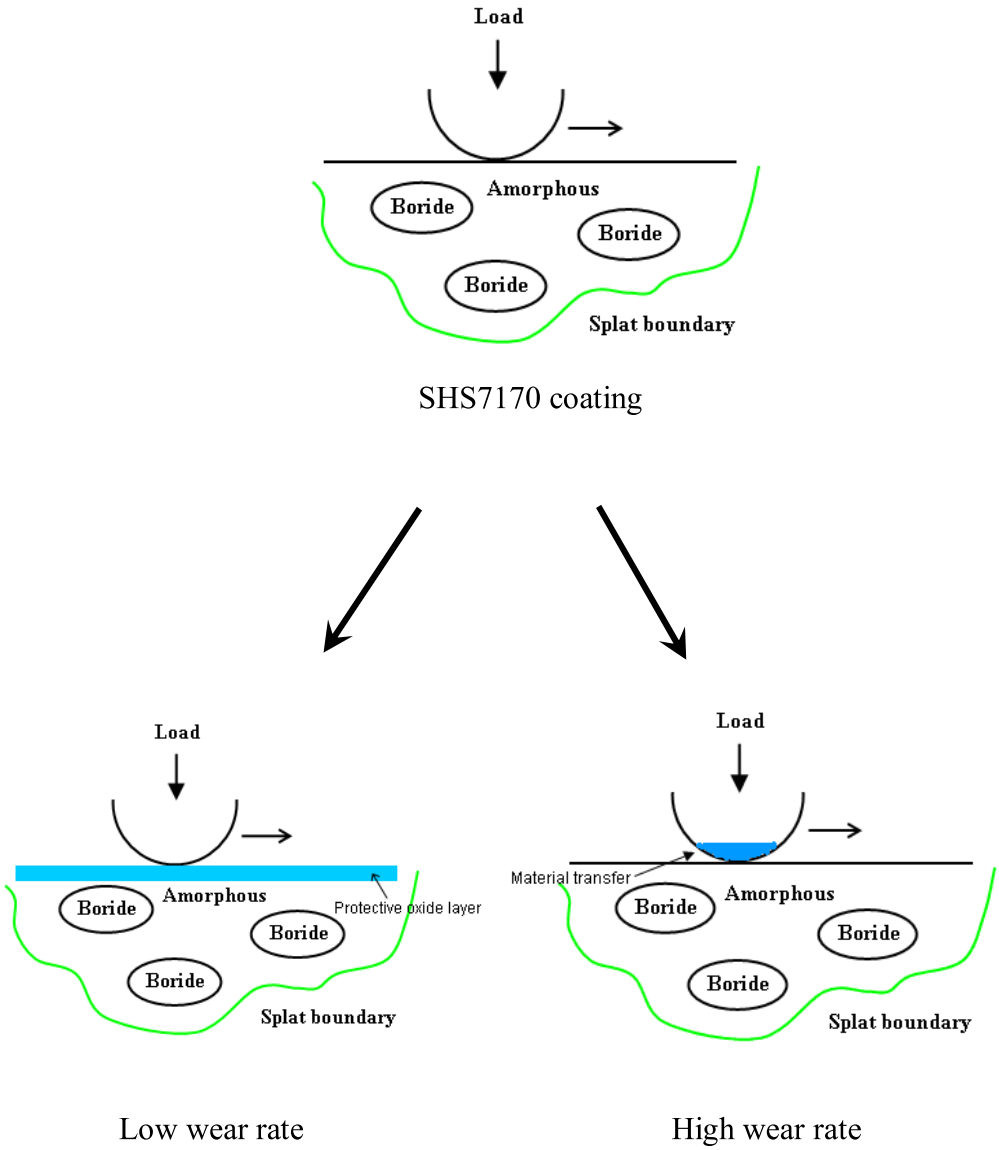

Fig. 8.2 Low/ high wear in the SHS7170 coating.

Chapter 9

Conclusions

9.1 Microstructure evolutions in powders and coatings

High velocity oxy-fuel (HVOF) thermal spraying was used to deposit coating of multi-component Fe-Cr-B based alloys containing boron and/or carbon, approximately 300 μm thick on a mild steel substrate.

The results show that the Armacor M and SHS7170 coatings are composed of amorphous phases and boride phases, such as $(Fe_{1.1}Cr_{0.9})B_{0.9}$, and Cr_2B and α-Fe bcc cubic structure. The Armacor C coating is composed of either boride $(Cr_{1.65}Fe_{0.35})B_{0.96}$ or $(Fe_{1.1}Cr_{0.9})B_{0.9}$ phase and γ-Fe fcc cubic structure, whereas the KC1 coating is composed of only an amorphous phase as well as an oxide phase formation are also present.

The volume fraction of an amorphous phase has been investigated by DSC analysis and the results show that the volume fraction of an amorphous phase in the coatings are in the order of KC1> SHS7170 > Armacor C > Armacor M.

The thermal stability and crystallization behaviour of the powders and the coatings were investigated by DSC and XRD techniques. A comparison of the results of XRD and DSC measurements shows that crystallization in the samples is one stage for the

Armacor M and the Armacor C coatings, whereas two stage processes occurred in the SHS7170 and KC1 coatings.

The amorphous phase in these coatings crystallises on annealing at about 600-700°C and the crystallisation temperatures depend on the content of solute elements (ie. boron and carbon). Thermal stability of the amorphous phase containing boron and carbon is higher than those phases containing only boron.

The apparent activation energies for reactions were calculated from DSC data using various peak shift equations. The apparent activation energies of reaction for the as-sprayed SHS7170 and KC1 coatings containing boron and carbon are higher (~ 350-385 kJ/mol) than those of the Armacor M coating (280 kJ/mol) and the Armacor C coatings (225 kJ/mol) containing boron.

All coatings were heat treated at a range of temperatures up to 925°C for 1 hour. Heat treatment of the SHS7170 and KC1 coatings, at 750°C resulted in the crystallization of matrix phase and precipitation of carbide and/or borocarbide or boride phase type and also had affects on the coating integrity and hardness. The heat treatment of the KC1 coating at temperatures as low as 650°C resulted in improvements in hardness of up to 13.2 GPa which is the highest hardness of all samples studied in this test. Whereas, in the Armacor M and the Armacor C coatings, there is no evidence of improvements in the hardness after heat treatment, but a decrease in hardness was observed which could be due to crystallisation of the amorphous matrix and/or precipitation of the boride phase present in the coatings.

A formation of a very fine mixed structure of α-Fe and carbide, borocarbide, or boride by decomposition of the amorphous phase in the KC1 coating, bringing about a hardness of (~12.4-13.2 GPa). The KC1 coating retain a hardness of more than (~11.3 GPa), even on annealing at temperatures of 750°C or higher.

9.2 Wear behaviour of coatings

Wear resistance of the three coatings (SHS7170, Armacor C and Armacor M) was investigated by unlubricated sliding wear (ball-on-disc). The SHS7170 coating, containing a large proportion of amorphous phase exhibits the best sliding wear resistance of all these three Fe-Cr-B based alloy coatings studied in this test.

The Armacor M coating consists of a larger volume fraction of hard boride phase compared to the Armacor C and thus leading to high value of the hardness. The fracture toughness of the four coatings decreases in the order WC-Co-Cr > SHS7170 > Armacor M > Armacor C.

The hardness of SHS7170 coating was lower than that of the Armacor M coating, but the SHS7170 coating exhibited better sliding wear performance. This is thought to be due to the other factor including the fact that the SHS7170 coating consists of a larger proportion of an amorphous phase than that of the Armacor C and Armacor M coatings and thus exhibits higher fracture toughness as can be seen from the high wear rates of the ceramic balls.

The coatings with a combination of high hardness and high fracture toughness exhibits superior sliding wear. Thus, the improvement of the Fe-Cr-B based alloy coating in the present work will be need to be further investigated in various wear conditions and environments in order to find out the possibility of applying amorphous/crystalline coatings to parts of engineering surface applications requiring high wear resistance.

Future Work

1) To investigate the wear resistance, fracture toughness and corrosion resistance as following heat treatment of the Fe-Cr-B coatings and compared with those of the wear resistant cermet WC-Co coatings.

2) To produce amorphous materials in the form of coating by using the materials that have been developed (a locally designed powder, KC1 with a relatively high glass-forming ability (GFA) and thus such materials can provide a sufficiently high cooling rate to form a fully amorphous coating.

3) To investigate the relationship between the microstructural evolution and the mechanical and chemical properties in particular wear conditions and compare with those of a commercially available Fe-Cr-B based alloy coating as well as the competitive HVOF WC-Co coatings.

4) TEM investigation of microstructure at peak hardness.

References

1. Anis, M., Rainforth, W. M. and Davies, H. A. (1994). "Wear behaviour of rapidly solidified $Fe_{68}Cr_{18}Mo_2B_{12}$ alloys." *Wear*, 172(2), 135-145.
2. Archard, J.F. (1953). "Contact and rubbing of flat surfaces." *Journal of Applied Physics*, 24, 8, 981-988.
3. Baker, H. (1992). Alloy phase diagrams, In: *ASM Handbook Vol.3*, ASM International, Ohio, 2, 81.
4. Bansal, N. P. and Zhu, D. (2005). "Thermal conductivity of zirconia-alumina composites." *Ceramics International*, 31(7), 911-916.
5. Basu, B., Vleugels, J. and Biest, O. V. D. (2004). "Transformation behaviour of tetragonal zirconia: role of dopant content and distribution." *Materials Science and Engineering A*, 366(2), 338-347.
6. Basu, S.K., Sengupta, S.N. and Ahuja, B.B. (2005). *Fundamentals of Tribology*. Prentice-Hall of India, Private Limited, New Delhi.
7. Bayer, R.G. (2004). *Mechanical wear fundamentals and testing*. 2nd ed., Revised and Expanded, Marcel Dekker, Inc., New York.
8. Berger, L.M., Vuoristo, P., Mantyla, T. and Gruner, W. (1998). "A study of oxidation behaviour of WC-Co, CrC-NiCr and TiC-Ni based", Materials in Thermal Spray processes, 15th International Thermal Spray Conference, Nice, France, May, 75-82.
9. Bondar, A. (2008). Boron-Chromium-Iron. In iron systems: phase diagrams, crystallographic and thermodynamic data, Materials Science International Services GmbH, 800749, 70507 Stuttgart, Germany.
10. Bowden, F.P. and Tabor, D. (1964). *The Friction and lubrication of Solids*, Part I. Oxford Claredon Press.
11. Branagan, D.J., Swank, W.D., Haggard, D.C. and Fincke, J.R. (2001). "Wear-resistant amorphous and nanocomposite steel coatings." *Metallurgical and Materials Transactions A-Physical Metallurgy and Materials Science*, 32(10), 2615-2621.

12. Branagan, D. J. and Tang, Y.L. (2002). "Developing extreme hardness (>15 GPa) in iron based nanocomposites." *Composites Part A-Applied Science and Manufacturing,* 33(6), 855-859.
13. Branagan, D. J. (2004). Bechtel BWXT Idaho, LLC. "Methods of Forming Hardened Surfaces." *US Patent* No.6767419.
14. Branagan, D.J., Breitsameter, M., Meacham, B.E. and Belashchenko, V. (2005). "High-performance nanoscale composite coatings for boiler applications." 14(2), 196-204.
15. Branagan, D.J., Marshall, M.C. and Meacham, B.E. (2006). "Wear and corrosion resistant amorphous / nanostructured steel coatings for replacement of electrolytic hard chromium." *ITSC 2006*, US.
16. Brown, M.E. (1988) or (2001). *Introduction to thermal analysis: Techniques and applications*. Kluwer Academic Publishers.
17. Brydson, R. (2001). *Electron energy loss spectroscopy*. BIOS Scientific Publishers Ltd.
18. Busch, R. (2000). "The thermophysical properties of bulk metallic glass-forming liquids." *JOM*, *Journal of the Minerals, Metals and Materials Society,* 52(7), 39-42.
19. Champness, P.E. (2001). *Electron diffraction in the transmission electron microscope*. Oxford, BIOD Scientific Publishers Ltd.
20. Chen, Q.J., Fan, H.B., Shen, J., Sun, J.F. and Lu, Z.P. (2006). "Critical cooling rate and thermal stability of Fe-Co-Zr-Y-Cr-Mo-B amorphous alloy." *Journal of Alloys and Compounds*, 407(1-2), 125-128.
21. Cowlam, N. and Carr, G. E. (1985). "Magnetic and structural properties of Fe-B binary metallic glasses I: Variation of magnetic moment with composition." *Journal of Physics F: Metal Physics*, 15(5), 1109-1116.
22. Cullity, B.D. and Stock, S.R. (2001). *Elements of X-ray diffraction*. 3rd ed., Upper Saddle River, New Jersey, Prentice Hall.
23. Cutler, R.A. (1991) Engineering properties of borides, *Engineeing Materials Handbook: Ceramic and Glasses*, 4, 787-803.
24. Davis, J.R. (2001). *Surface engineering for corrosion and wear resistance*. ASM International, Materials Park, Ohio.
25. Davis, J.R. (2004). *Handbook of Thermal Spray Technology*. Thermal Spray Society and ASM International, Ohio.

26. Deng, C., M. Liu, M., Wu, C., Zhou. K. and Song, J. (2007). "Impingement resistance of HVAF WC-based coatings." *Journal of Thermal Spray Technology*, 16(5-6), 604-609.
27. Degnan, C.C. and P.H. Shipway. (2002). "Influence of reinforcement volume fraction on sliding wear behaviour of SHS derived ferrous based metal matrix composite." *Materials Science and Technology*, 18(10), 1156-1162.
28. Dent, A.H., Horlock, A.J., McCartney, D.G. and Haris, H.J. (1997) *In*: Berndt, C.C. ed. *Thermal Spray*: *A United Forum for Scientific and Technological Advances.* Indianapolis, Indiana, USA, 917-923.
29. Dent, A., Horlock, A., McCartney, D. and Harris, S. (1999). "The corrosion behavior and microstructure of high-velocity oxy-fuel sprayed nickel-base amorphous/nanocrystalline coatings", *J. Therm. Spray Technol.*, 8(3), 399-404. (Ni-Cr-B)
30. Dey, A. K. and Biswas, K. (2009). "Dry sliding wear of zirconia-toughened alumina with different metal oxide additives." *Ceramics International*, 35(3), 997-1002.
31. Ding, Y. (2009). Effects of elevated temperature exposure on the microstructural evolution of Ni(Cr)-Cr3C2 coated 304 stainless steel, Ph.D. Thesis, University of Nottingham, UK.
32. Dumitru, G., Romano, V., Weber, H. P., Haefke, H., Gerbig, Y. and Pflüger, E. (2000). "Laser microstructuring of steel surfaces for tribological applications." *Applied Physics A: Materials Science & Processing*, 70(4), 485-487.
33. Edrisy, A., Perry, T. and Alpas, A.T. (2005). "Wear mechanism maps for thermal-spray steel coatings." *Metalllurgical and Materials Transactions A,* 36(10), 2737-2750.
34. Farmer, J., Choi, J.S., Saw, C., Haslam, J., Day, D., Hailey, P., Lian, T., Rebak, R., Perepezko, J., Payer, J., Branagan, D., Beardsley, B., D'amato, A. and Aprigliano, L. (2009). "Iron-based amorphous metals: High-performance corrosion-resistant material development." *Metallurgical and Materials Transactions A*, 40(6), 1289-1305.
35. Fincke, J.R., Swank, W.D. and Haggard, D.C. (1994)."Comparison of the characteristics of HVOF and plasma thermal spray." *Proceedings of the 7th*

National Thermal Spray Conference, 20-24 June, Boston, Massachusetts, 325-330.

36. Fu, X.Y. and Rigney, D.A. (1999). Bulk metallic glasses. *In*: Inoue, A. et al. eds. *MRS Symposium Proceedings*, Warrendale, PA, Materials Research Society, 554, 437-442.
37. Galvanetto, E., Borgioli, F., Bacci, T. and Pradelli, G. (2006). "Wear behaviour of iron boride coatings produced by VPS technique on carbon steels." *Wear,* 260(7-8), 825-831.
38. Gautier, P. and Kato, K. (1993). "Wear mechanisms of silicon nitride, partially stabilized zirconia and alumina in unlubricated sliding against steel." *Wear.* 162-164, 305-313.
39. Gigolotti, J.C.J., Chad, V.M., Faria, M.I.S.T., Coelho, G.C., Nunes, C.A. and Suzuki, P.A. (2008). "Microstructural characterization of as-cast Cr-B alloys." *Materials Characterization*, 59(1), 47-52.
40. Gloriant, T. and Greer, A.L. (1998). "Al-based nanocrystalline composites by rapid solidification of Al-Ni-Sm alloys." *Nanostructured Materials*, 10(3), 389-396.
41. Goldfarb, I., Kaplan, W.D., Ariely, S. and Bamberger, M. (1995). "Fault-induced polytypism in $(Cr, Fe)_2B$." *Philosophical Magazine A,* 72(4), 963-979.
42. Graydon, J. W., Thorpe, S. J. and Kirk, D. W. (1995). "Effect of composition on the formation and thermal stability of $Ni_{72}(Mo,Co)_8B_{20}$ metallic glass." *Acta Metallurgica et Materialia*, 43(4), 1363-1373.
43. Greer, A.L., Zhong, Z.C., Jiang, X.L., Rutherford, K.L. and Hutchings, I.M. (1997). "Al-Y-Ni nanophase composites by devitrification-microstructure, hardness and abrasive wear resistance." *In*: Ma, E., Fultz, B., Shull, R., Morral, J. and Nash, P., (eds.) Chemistry and Physics of Nanostructures and Related Non-Equilibrium Materials. *Minerals, Metals, & Materials Society,* Warendale, PA, TMS, 3-12. ISBN 873393538. http://publications.eng.cam.ac.uk/10973/
44. Greer, A.L. (2001a). "Metallic Glasses." *Encyclopedia of Materials: Science and Technology*, *In*: Buschow, K.H.J., Cahn, R.W., Flemings, M.C., Ilschner, B., Kramer, E.J., Mahajan, S. and Veyssière, P. eds., Vol.6, Oxford, Elsevier, 5529-5537.

45. Greer, A.L. (2001b). "Partially or fully devitrified alloys for mechanical properties." *Materials Science and Engineering A*, 304-306, 68-72.
46. Greer, A.L. and Myung, W.N. (2001c). "Supercooled liquid, bulk glassy, and nanocrystalline states of alloys." *In*: Dauskrdt, R.H. et al., eds. *MRS Symposium Proceedings*, Warrendale, PA, Materials Research Society, 644, L10.4.1-L10.4.12.
47. Greer, A.L., Rutherford, K.L. and Hutchings, I.M. (2002). "Wear Resistance of Amorphous Alloys and Related Materials." *International Materials Reviews*, 47(2), 87-112.
48. Guilemany, J. M., Miguel, J. M., Vizcaíno, S., Lorenzana, C., Delgado, J. and Sánchez, J. (2002). "Role of heat treatments in the improvement of the sliding wear properties of Cr3C2-NiCr coatings." *Surface and Coatings Technology*, 157(2-3), 207-213.
49. Hammond, C. (2001). *The basics of crystallography and diffraction*. 2nd ed., Oxford Press.
50. Harvey, D. (1996). "The tough truth - Wear-resistant coatings using high velocity oxyfuel." *Industrial Lubrication and Tribology*, 48(2), 11-16.
51. Herman, H. and Sampath, S. (1996) Thermal spray coatings, In: Stern K.H. (ed), Metallurgical and ceramic protective coatings, London, Chapman & Hall, 274-289.
52. Hutchings, I.M. (1992). *Tribology: Friction and Wear of Engineering Materials*. London: Edward Arnold.
53. Inoue, A. (1988). *Bulk Amorphous Alloys*. Trans Tech Publications Ltd, Zuerich.
54. Inoue, A. (1997). Bulk amorphous alloys with soft and hard magnetic properties. Materials Science and Engineering A, 226-228, 357-363.
55. Inoue, A., Zhang, T. and Takeuchi, A. (1997). Bulk amorphous alloys with high mechanical strength and good soft magnetic properties in Fe--TM--B (TM = IV--VIII group transition metal) system. Applied Physics Letters, 71(4), 464-466.
56. Inoue, A. (2000). "Stabilization of metallic supercooled liquid and bulk amorphous alloys." *Acta Materialia*, 48(1), 279-306.

57. Inoue, A. and Wang, X.M. (2000). Bulk amorphous FC20 (Fe-C-Si) alloys with small amounts of B and their crystallized structure and mechanical properties. Acta Materialia, 48(6), 1383-1395.
58. Jones, M. (2002). "Properties of HVOF sprayed TiC and TiB_2 - based cermet coatings." *PhD thesis*, The University of Nottingham, Nottingham, UK.
59. Johnson, W.L. (1990). Metallic Glasses. In: *Properties and selection: Nonferrous alloys and special purpose materials*, ASM Handbook, Vol.2, 10th ed., ASM International, Ohio, 804-821.
60. Kamal, S., Jayaganthan, R. and Prakash, S. (2009). "High temperature oxidation studies of detonation-gun-sprayed Cr3C2-NiCr coating on Fe- and Ni-based superalloys in air under cyclic condition at 900 °C." *Journal of Alloys and Compounds*, 472(1-2), 378-389.
61. Kato, K. and Adachi, K. (2002). "Wear of advanced ceramics." *Wear*, 253(11-12), 1097-1104.
62. Kaur, M., Singh, H. and Prakash, S. (2008). "A survey of the literature on the use of high velocity oxy-fuel spray technology for high temperature corrosion and erosion-corrosion resistant coatings." *Anti-Corrosion Methods and Materials,* 55(2), 86-96.
63. Kaur, M., Singh, H. and Prakash, S. (2009). "High-Temperature Corrosion Studies of HVOF-Sprayed Cr3C2-NiCr Coating on SAE-347H Boiler Steel." *Journal of Thermal Spray Technology*, 18(4), 619-632.
64. Kim, H.J., Grossi, S. and Kweon, Y.G. (1999). "Wear performance of metamorphic alloy coatings." *Wear*, 232(1), 51-60.
65. Kim, H.J., Grossi, S. and Kweon, Y.G. (1999), "Characterization of Fe-Cr-B based coatings produced by HVOF and PTA processes", *Metals and Materials International*. **5**(1), 63-72.
66. Kim, Y.S., Kim, K.T., Kim, B.T and Bae, J II. (2007). "Microstructure and wear behaviour of thermally sprayed Fe-based amorphous coating." *Key Engineering Material*, 353-358, 848–851.
67. Kishitake, K., Era, H. and Otsubo, F. (1996). "Characterization of plasma sprayed Fe-10Cr-10Mo-(C,B) amorphous coatings." *Journal of Thermal Spray Technology,* 5(2), 145-153.
68. Kissinger, H.E. (1957). "Reaction kinetics in differential thermal analysis." *Analytical Chemistry*, 29(11), 1702-1706.

69. Koiprasert, H., Dumrongrattana, S. and Niranatlumpong, P. (2004). "Thermally sprayed coatings for protection of fretting wear in land-based gas-turbine engine." *Wear*, 257(1-2), 1-7.
70. Kong, C.J., Brown, P.D., Harris, S.J. and McCartney, D.G. (2005). "The microstructures of a thermally sprayed and heat-treated Al-20wt%Sn-3wt%Si alloy." *Materials Science and Engineering A,* 403(1-2), 205–214.
71. Krepski, R.P. (1993), *Thermal Spray Coating Applications in the Chemical Process Industries*, NACE International.
72. Laul, K. and Dorfman, M. (2000). "New chromium carbide-nickle chrome materials for high temperature wear applications", Thermal Spray: Surface Engineering via Applied Research, ASM International, Ohio, USA, 561-566.
73. Li, S. and Wang, Y. (1991). "Wear resistance of amorphous cobalt-based alloys." *Wear*, 147, 275-284.
74. Liao, P.K. and Spear, K.E. (1986). "The B-Cr (Boron-Chromium) system." *Journal of Phase Equilibria*, 7(3), 232-237.
75. Liao, P.K. and Spear, K.E., Boron-iron binary phase diagram, Binary Alloy Phase Diagrams, 351-356.
76. Liao, H., Normand, B. and Coddet, C. (2000). "Influence of coating microstructure on the abrasive wear resistance of WC/Co cermet coatings." *Surface and Coatings Technology*, 124(2-3), 235-242.
77. Liu, X.Q., Zheng, Y.G., Chang, X.C., Hou, W.L., Wang, J.Q., Tang, Z. and Burgess, A. (2009). "Microstructure and properties of Fe-based amorphous metallic coating produced by high velocity axial plasma spraying." *Journal of Alloys and Compounds*, 484(1-2), 300-307.
78. Lotfi, B., Shipway, P. H., McCartney, D. G. and Edris, H. (2003). "Abrasive wear behaviour of Ni(Cr)-TiB2 coatings deposited by HVOF spraying of SHS-derived cermet powders." *Wear*, 254(3-4), 340-349.
79. Lu, K. (1996). "Nanocrystalline metals crystallized from amorphous solids: nanocrystallization, structure, and properties." *Materials Science and Engineering: R: Reports*, 16(4), 161-221.
80. Ludema, K.C. (1992). Wear, *In*: *Friction, Lubrication, and Wear Technology*, Metals Handbook, Vol.18, ASM International, Ohio.
81. Ma, L. and Inoue, A. (1999). "On glass-forming ability of Fe-based amorphous alloys." *Materials Letters*, 38(1), 58-61.

82. Manna, I., Chattopadhyay, P.P., Banhart, F., Croopnick, J. and Fecht, H.J. (2008). "Microstructural evolution of wear-resistant FeCrB and FeCrNiCoB coating alloys during high-energy mechanical attrition." *Wear*, 264(11-12), 940-946.
83. Massalski, T.B. (1990). Binary alloy phase diagrams. 2nd edition. Materials Park, OH: ASM International, 3 volumes.
84. McHennry, M.E., Matthew, A.W. and David, E.L. (1999). "Amorphous and nanocrystalline materials for applications as soft magnets." *Progress in Materials Science*, 44, 291-433.
85. Mellor, B.G. (2006) Surface coatings for protection against wear, Woodhead Publishing Limited. Cambridge England.
86. Ming-Chang, J. and Li-Yung, Y. (1993). "Environmental effects on wear behaviour of alumina." *Wear*, 161(1-2), 111-119.
87. Miyoshi, K. and Buckley, D.H. (1986). "Microstructure and surface chemistry of amorphous alloys important to their friction and wear behaviour." *Wear*, 110, 295-313, ISSN 0043-1648.
88. Moreau, C., Cielo, P., Lamontagne, M., Dallaire, S., Krapez, J.C. and Vardelle, M. (1991). "Temperature evolution of plasma-sprayed niobium particles impacting on a substrate." *Surface & Coatings Technology*, 46(2), 173–187.
89. Moreton, R. and Lancaster, J.K. (1985). "The friction and wear behavior of various metallic glasses." *Journal of Materials Science Letters*, 4(2), 133-137.
90. Murthy, J.K.N. and B. Venkataraman (2006). "Abrasive wear behaviour of WC-CoCr and Cr3C2-20(NiCr) deposited by HVOF and detonation spray processes." *Surface and Coatings Technology*, 200(8): 2642-2652.
91. Neale, M.J. and Gee, M. (2000). *Guide to Wear Problems and Testing for Industry*, Bury St Edmunds, UK.
92. Ni, N.S., Liu, X.H., Chang, W.L., Liu, H.W. and Wang, J.Q. (2009). "High performance amorphous steel coating prepared by HVOF thermal spraying." *Journal of Alloys and Compounds*, 467(1-2), 163-167.
93. Pang, S.J., Zhang, T., Asami, K. and Inoue, A. (2002a). "Bulk glassy Fe-Cr-Mo-C-B alloys with high corrosion resistance." *Corrosion Science*, 44(8), 1847-1856.

94. Pang, S.J., Zhang, T., Asami, K. and Inoue, A. (2002b). "Formation of bulk glassy Fe75-x-yCrxMoyC15B10 alloys and their corrosion behavior." *Journal of Materials Research*, 17(3), 701-704.
95. Pang, S.J., Zhang, T., Asami, K. and Inoue, A. (2002c). "Synthesis of Fe-Cr-Mo-C-B-P bulk metallic glasses with high corrosion resistance." *Acta Materialia*, 50(3), 489-497.
96. Pawlowski, L. (1995). *The science and engineering of thermal spray coatings*. John Wiley & Sons, Chichester.
97. Poorman, R.M., Sargent, H.B. and Lamprey, H. (1955). "Method and apparatus utilizing detonation waves for spraying and other purposes." *US Patent* 2 714 553.
98. Prakash, B. and Hiratsuka, K., (2000). "Sliding wear behaviour of some Fe-, Co- and Ni-based metallic glasses during rubbing against bearing steel." *Tribology Letters*, 8, 153-160.
99. Qu, J., Blau, P. J., Watkins, T. R., Cavin, O. B. and Kulkarni, N. S. (2005). "Friction and wear of titanium alloys sliding against metal, polymer, and ceramic counterfaces." *Wear*, 258(9), 1348-1356.
100. Quinn, T.F.J. (1983a). "Review of oxidational wear: Part I: The origins of oxidational wear." *Tribology International*, 16(5), 257-271.
101. Quinn, T.F.J. (1983b). "Review of oxidational wear Part II: Recent developments and future trends in oxidational wear research." *Tribology International*, 16(6), 305-315.
102. Quinn, T.F.J., Sullivan, J.L. and Rowson, D.M. (1984). "Origins and development of oxidational wear at low ambient temperatures." *Wear*, 94(2), 175-191.
103. Quinn, T.F.J. and Winer, W.O. (1985). "The thermal aspects of oxidational wear." *Wear*, 102(1-2), 67-80.
104. Rabinowicz, E., Dunn, L.A. and Russell, P.G. (1961) "A study of abrasive wear under three-body conditions.", *Wear*, 4, 345-355.
105. Rabinowicz, E. (1965). *Friction and wear of materials*. Wiley and Sons, New York.
106. Rainforth, W.M. and Stevens, R. (1993). "A transmission electron microscopy study of wear of magnesia partially stabilized zirconia." *Wear*, 162-164, 322-331.

107. Ranganathan, S., Makaya, A., Fredriksson, H., and Savage, S. (2007). "Rapid solidification behavior of Fe-Cr-Mn-Mo-Si-C alloys." *Metallurgical and Materials Transactions B-Process Metallurgy And Materials Processing Science*, 38(6), 917-926.

108. Rickerby, D.S. and Matthews, A. (1991). *Advanced Surface Coatings: A Handbook of Surface Engineering*. New York.

109. Rutherford, K.L. and Hutchings, I.M. (1996). "A micro-abrasive wear test, with particular application to coated systems." *Surface Coating Technol*ogy, 79, 231-239.

110. Sahraoui, T., Fenineche, N.E., Montavon, G. and Coddet, C. (2003). "Structure and wear behaviour of HVOF sprayed Cr_3C_2–NiCr and WC-Co coatings." *Materials and Design,* 24(5), 309-313.

111. Schneider, K.E., Belashchenko, V., Dratwinski, M., Siegmann, S. and Zagorski, A. (2006). *Thermal spraying for power generation components*. Wiley-Vch.

112. Scruggs, D.M. (1988). Dresser Industries,Inc. "Materials transformable from the nonamorphous to the amorphous state under frictional loadings." *US Patent*, No.4725512.

113. Shen, T.D. and Schwarz, R.B. (2001). "Bulk ferromagnetic glasses in the Fe-Ni-P-B System." *Acta Materialia*, 49(5), 837-847.

114. Shipway, P.H. (1999). "The role of test conditions on the microabrasive wear behaviour of soda-lime glass." *Wear*, 233-235, 191-199.

115. Shipway, P.H. (2006). "The range of surface coating methods." In *Surface coatings for protection against wear* (ed. Mellor, B.G.), Woodhead Publishing Ltd., Cambridge, England.

116. Shmyreva, T. and Knapp, J. (2003). "Nano-amorphous coatings for medical instruments." *Proceedings of the materials & Processes for Medical Devices Conference*, September.

117. Sidhu, T.S., Prakash, S. and Agrawal, R.D. (2005). "Studies on the properties of high-velocity oxy-fuel thermal spray coatings for higher temperature applications." *Materials Science*, 41(6), 805-823.

118. Sidhu, H.S., Sidhu, B.S. and Prakash, S. (2010). "Wear characteristics of Cr3C2-NiCr and WC-Co coatings deposited by LPG fueled HVOF", *Tribology International*, 43(5-6), 887-890.

119. Smith, R.W. and Knight, R. (1995). "Thermal spraying I: Powder consolidation from coating to forming." *Journal of Materials,* 47(8), 32-39.

120. So, H. (1995). "The mechanism of oxidational wear." *Wear*, 184(2), 161-167.

121. So, H., Yu, D. S. and Chuang, C. Y. (2002). "Formation and wear mechanism of tribo-oxides and the regime of oxidational wear of steel." *Wear*, 253(9-10), 1004-1015.

122. Somaraju, K.R.C., Srinivasarao, D., Sivakumar, D., Sen, D., Rao, G.V.N. and Sundararajan, G. (2000). "The influence of powder characteristics on the properties of detonation sprayed CrC-25NiCr coatings", Thermal Spray: Surface Engineering via Applied Research, ASM International, Ohio, USA, 309-316.

123. Sturgeon, A.J. (1993). "Thermal spray technology." *Materials Word*, June, 351-354.

124. Sudaprasert, T., Shipway, P. H., and McCartney, D. G. (2003). "Sliding wear behaviour of HVOF sprayed WC-Co coatings deposited with both gas-fuelled and liquid-fuelled systems." *Wear*, 255, 943-949.

125. Suh, N.P. (1973). "The delamination theory of wear", *Wear*, 25, 111-124.

126. Suh, N.P. (1986). *Tribophysics*. Prentice Hall, Englewood Cliffs.

127. Tylczak, J.H. (1992) Abrasive wear, In: Henry, S.D. (ed), *ASM Handbook*, 10th ed, vol.18, Ohio: ASM International, pp. 184-190.

128. Veshchunov, M.S. and Hofmann, P. (1995). "Modelling of the interactions between B_4C and stainless steel at high temperatures." *Journal of Nuclear Materials*, 226(1-2), 72-91.

129. Vleugels, J., Basu, B., Kumar Hari, Vitchev, R.G. and Van Der Biest, O. (2002). "Unlubricated Fretting Wear of TiB_2-containing composites against bearing steel." *Metalllurgical and Materials Transactions A*, 33A, 3847-3859.

130. Walsh, P.N., Quets, J.M., and Tucker, R.C. (1995). "Coatings for the protection of turbine blades from erosion." *Journal of Engineering for Gas Turbines and Power*, 117(1), 152-155.

131. Wang, J.G., Choi, B.W. and Nieh, T.G. and Liu, C.T. (2000). "Nano-scratch behavior of a bulk Zr-10Al-5Ti-17.9Cu-14.6Ni amorphous alloy." *Journal of Materials Research*, 15(4), 913-922.

132. Watt, I.M. (1997). *The principles and practice of electron microscopy*. 2nd ed., Cambridge University Press.

133. Weston, D.P., Shipway, P.H., Harris, S.J. and Yellop, J. (2009). Swindell & Pearson Ltd, UK. "Surface coating." International Publication Number WO 2009/130450 A1.

134. Whang, S.H. and Giessen, B.C. (1982). *Proceedings of the 4th International Conference on Rapidly Quenched Metals. In*: Masumoto, T. and Suzuki, K. eds., 2, 1403-1406.

135. Williams, D.B. and Carter, C.B. (1996). *Transmission electron microscopy – a textbook for materials science*. Plenum Press.

136. Wirojanupatump, S., Shipway, P.H. and McCartney, D.G. (2001). "The influence of HVOF powder feedstock characteristics on the abrasive wear behaviour of CrxCy-NiCr coatings." *Wear*, 249(9), 829-837.

137. Wong, C.J and Li, J.C.M. (1984). "Wear behavior of an amorphous alloy." *Wear*, 98, 45-61.

138. Wood, R.J.K. (2006). "Understanding surface wear in engineering materials." In *Surface coatings for protection against wear* (ed. Mellor, B.G.), Woodhead Publishing Ltd., Cambridge, England.

139. Wood, R.J.K. (2010) "Tribology of thermal sprayed WC-Co coatings." *International Journal of Refractory Metals and Hard Materials*, 28(1), 82-94.

140. Wu, Y.P., Lin, P.H., Wang, Z.H. and Li, G.Y. (2009). "Microstructure and microhardness characterization of a Fe-based coating deposited by high-velocity oxy-fuel thermal spraying." *Journal of Alloys and Compounds*, 481(1-2), 719-724.

141. Yang, Q., Senda, T. and Ohmori, A. (2003). Effect of carbide grain size on microstructure and sliding wear behavior of HVOF-sprayed WC-12% Co coatings. *Wear*, 254(1-2), 23-34.

142. Yang, Q., Senda, T. and Hirose, A. (2006). "Sliding wear behavior of WC-12% Co coatings at elevated temperatures." *Surface and Coatings Technology*, 200(14-15), 4208-4212.

143. Yijian, L., Jian, H., Chunyong, J. and Quanqin, Y (1990). "Change of boride in $Fe_{70}Cr_{18}Mo_2Si_1B_9$ with thermal treatment." *Acta Metallurgiga Sinica (English Edition)*, 3(3), 185-190.

144. Yijian, L. and Jian, H. (1991). "Borides in microcrystalline Fe-Cr-Mo-B-Si alloys." *Journal of Materials Science*, 26(10), 2833-2840.

145. Zhang, D., McCartney, D.G. and Harris, S.J. (2003). "Microstructure formation and corrosion behaviour in HVOF-sprayed inconel 625 coatings." *Materials Science and Engineering A*, 344(1-2), 45–56.

146. Zhong, Z.C., Jiang, X.Y. and Greer, A.L. (1997). "Microstructure and hardening of Al-based nanophase composites." *Materials Science and Engineering A*, 226-228, 531-535.

Appendix

Standard JCPDS Files

Pattern : 01-085-1410 ***Radiation =*** 1.540598 ***Quality :*** Calculated

Fe

Iron
Iron

Lattice : Body-centered cubic
S.G. : Im-3m (229)

a = 2.88600

Z = 2

Mol. weight = 55.85
Volume [CD] = 24.04
Dx = 7.716
Dm = 7.870
I/Icor = 10.81

ICSD collection code: 064795
Remarks from ICSD/CSD: REM M PDF 6-696.
Test from ICSD: Calc. density unusual but tolerable.
Test from ICSD: No R value given.
Test from ICSD: At least one TF missing.
Additional pattern: See PDF 6-696.
Data collection flag: Ambient.

Swanson, H.E., Tatge, E., Natl. Bur. Stand. (U.S.), Circ. 539, volume 539, page 4 (1955)
Calculated from ICSD using POWD-12++ (1997)

Radiation : CuKa1
Lambda : 1.54060
SS/FOM : F3=1000(0.0001,3)

Filter : Not specified
d-sp : Calculated spacings

2th	*i*	*h*	*k*	*l*
44.354	999	1	1	0
64.528	116	2	0	0
81.656	176	2	1	1

Pattern : 00-006-0696 **Radiation =** 1.540598 **Quality :** High

Fe

Iron
Iron, syn
Also called: ferrite

Lattice : Body-centered cubic
S.G. : Im3m (229)

a = 2.86640

Z = 2

Mol. weight = 55.85
Volume [CD] = 23.55
Dx = 7.875

Color: Gray, light gray metallic
General comments: Total impurities of sample <0.0013% each metals and non-metals.
Temperature of data collection: Pattern taken at 25 C.
Sample preparation: The iron used was an exceptionally pure rolled sheet prepared at the NBS, Gaithersburg, MD, USA., [Moore, G., *J. Met.*, **5** 1443 (1953)]. It was annealed in an H2 atmosphere for 3 days at 1100 C and slowly cooled in a He atmosphere.
General comments: γ-Fe (fcc)=(1390 C) δ-Fe (bcc).
General comments: Opaque mineral optical data on specimen from Meteorite: RR_2R_e= 57.7, Disp.=16, VHN=158 (mean at 100, 200, 300), Color values=.311, .316, 57.9, Ref.: IMA Commisssion on Ore Microscopy QDF.
Additional pattern: See ICSD 64795 (PDF 85-1410).
Data collection flag: Ambient.

Swanson et al., Natl. Bur. Stand. (U.S.), Circ. 539, volume IV, page 3 (1955)

CAS Number: 7439-89-6

Radiation : CuKa1
Lambda : 1.54050
SS/FOM : F6=225(0.0044,6)

Filter : Beta
d-sp : Not given

2th	*i*	*h*	*k*	*l*
44.674	100	1	1	0
65.023	20	2	0	0
82.335	30	2	1	1
98.948	10	2	2	0
116.390	12	3	1	0
137.143	6	2	2	2

Pattern : 00-047-1405 ***Radiation =*** 1.540598 ***Quality :*** Indexed

$Fe_{0.64}Ni_{0.36}$

Iron Nickel

Lattice : Face-centered cubic

S.G. : Fm3m (225)

a = 3.59220

Z = 4

Mol. weight = 56.87

Volume [CD] = 46.35

Dx = 8.150

Sample preparation: Formed by mechanical alloying of bimetallic layers.
Data collection flag: Ambient.

Samvel'yan, R., Abovyan, E., Agbalyan, S., Manukyan, N., Sakanyan, M., Soviet Powder Metall. and Met. Ceramics, volume 30, page 606 (1991)

Radiation : CoKa

Lambda : 1.79020

SS/FOM : F5= 43(0.0230,5)

Filter : Monochromator crystal

d-sp : Diffractometer

2th	*i*	*h*	*k*	*l*
43.605	100	1	1	1
50.795	49	2	0	0
74.679	25	2	2	0
90.633	20	3	1	1
95.907	7	2	2	2

Pattern : 00-038-1399 ***Radiation =*** 1.540598 ***Quality :*** High

Cr_2B

Boron Chromium

Lattice : Face-centered orthorhombic

S.G. : Fddd (70)

Mol. weight = 114.80

Volume [CD] = 463.23

a = 7.40900

b = 14.71180

c = 4.24980

a/b = 0.50361

c/b = 0.28887

Z = 16

Dx = 6.584

Sample source or locality: The sample was from Cerac, Incorporated, Milwaukee, Wisconsin, USA.
Temperature of data collection: The mean temperature of data collection was 25.7 C.
Color: Gray
Additional pattern: To replace 18-380 (1).
Polymorphism: Bertaut and Blum (2) reported a tetragonal form.
Structure: Guy and Uraz (3) studied the unit cell and space group.
Analysis: Spectroscopic analysis result shows Al 0.06%, Ca 0.05%, Fe 0.4%, Mg 0.2%, Mn 0.01%, Ni 0.01%, Si 0.07%, and Zr 0.3%.
Data collection flag: Ambient.

Wong-Ng, W., McMurdie, H., Paretzkin, B., Hubbard, C., Dragoo, A., NBS (USA)., ICDD Grant-in-Aid (1987)

CAS Number: 12006-80-3

Radiation : CuKa1

Lambda : 1.54060

SS/FOM : F30= 66(0.0094,49)

Filter : Monochromator crystal

d-sp : Diffractometer

Internal standard : Si W

2th	*i*	*h*	*k*	*l*
24.189	9	0	4	0
24.887	7	1	1	1
30.307	14	1	3	1
39.140	57	1	5	1
42.746	55	3	1	1
44.334	100	0	2	2
46.354	16	3	3	1
49.135	5	4	0	0
49.378	7	2	0	2
49.538	10	0	8	0
49.883	38	1	7	1
52.950	2	3	5	1
55.503	19	4	4	0
55.734	26	2	4	2
62.048	2	1	9	1
70.276	1	1	3	3
72.375	5	4	8	0
72.565	8	2	8	2
72.796	5	3	9	1
75.120	10	5	5	1
75.532	5	1	5	3
77.949	11	3	1	3
78.489	5	6	2	0
78.815	14	4	6	2
79.110	3	0	10	2
80.531	2	3	3	3
82.809	4	5	7	1
83.212	6	1	7	3
85.625	10	3	11	1
92.347	8	6	0	2
92.899	4	5	9	1

Pattern : 01-072-1073 ***Radiation =*** 1.540598 ***Quality :*** Calculated

$Fe_{1.1}Cr_{0.9}B_{0.9}$

Iron Chromium Boron

Lattice : Face-centered orthorhombic
S.G. : Fddd (70)

a = 14.57000
b = 7.32000
c = 4.22000
a/b = 1.99044
c/b = 0.57650

Z = 16

Mol. weight = 117.96
Volume [CD] = 450.07
Dx = 6.963
I/Icor = 2.66

ICSD collection code: 016554
Remarks from ICSD/CSD: REM REF.
Test from ICSD: At least one TF implausible.
Temperature factor: ITF
Data collection flag: Ambient.

Brown, B.E., Beerntsen, D.J., Acta Crystallogr., volume 17, page 448 (1964)
Calculated from ICSD using POWD-12++ (1997)

Radiation : CuKa1
Lambda : 1.54060
SS/FOM : F30=143(0.0054,39)

Filter : Not specified
d-sp : Calculated spacings

2th	i	h	k	l
24.418	133	4	0	0
25.093	127	1	1	1
27.246	1	2	2	0
30.582	130	3	1	1
39.515	664	5	1	1
43.244	999	1	3	1
44.677	778	2	0	2
44.752	901	6	2	0
46.865	287	3	3	1
49.845	88	0	4	0
*49.845	88	0	2	2
50.042	56	8	0	0
50.410	397	7	1	1
53.539	8	5	3	1
56.261	350	4	4	0
*56.261	350	4	2	2
62.716	33	9	1	1
68.033	5	1	5	1
68.129	6	1	1	3
69.101	1	2	4	2
69.367	1	10	2	0
70.770	11	3	5	1
70.865	10	3	1	3
73.317	105	8	4	0
*73.317	105	8	2	2
73.667	37	9	3	1
76.118	78	5	5	1
76.211	76	5	1	3
76.421	45	11	1	1
78.735	169	1	3	3
*78.735	169	12	0	0
79.612	89	2	6	0
79.756	160	6	4	2
79.954	129	10	0	2
81.338	38	3	3	3
83.930	76	7	5	1
84.020	74	7	1	3
86.697	90	11	3	1
89.918	1	6	6	0

Pattern : 00-035-1180 ***Radiation =*** 1.540598 ***Quality :*** Not indexed

$Cr_{1.65}Fe_{0.35}B_{0.96}$

Boron Chromium Iron

Lattice : Face-centered orthorhombic
S.G. : Fddd (70)

a = 14.58300
b = 7.37900
c = 4.24500
a/b = 1.97628
c/b = 0.57528

Z = 16

Mol. weight = 115.72
Volume [CD] = 456.80
Dx = 6.730

General comments: Boride particles were chemically extracted from a steel matrix.
Data collection flag: Ambient.

Padilha, A., Schanz., J. Nucl. Mater., volume 95, page 229 (1980)

Radiation : CuKa1
Lambda : 1.54051
SS/FOM : F10= 5(0.0620,35)

Filter : Monochromator crystal
d-sp : Guinier
Internal standard : Si

2th	i	h	k	l
24.265	30	4	0	0
39.259	20	5	1	1
42.931	70	1	3	1
44.416	85	2	0	2
46.510	20	3	3	1
49.613	10	0	2	2
50.079	20	8	0	0
55.881	100	4	4	0
*55.881	100	4	2	2
75.515	40	5	5	1
78.153	60	1	3	3

Pattern : 00-005-0721 ***Radiation =*** 1.540598 ***Quality :*** Indexed

$(Cr,Fe,W,Mo)_{23}Fe_{21}(W,Mo)_2C_{12}$

Chromium Iron Tungsten Molybdenum Carbide

Lattice : Face-centered cubic
S.G. : Fm3m (225)

a = 10.62280

Z = 2

Mol. weight = 2880.53
Volume [CD] = 1198.72
Dx = 7.981

General comments: The lattice-dimensions depend on alloy content.
General comments: Material was extracted from Cr/Ni steel.
General comments: Carbon manganese C6 Mn23 isomorphous with the above; pattern virtually identical.
Data collection flag: Ambient.

Goldschmidt., Metallurgia, volume 40, page 103 (1949)

Radiation : CoKa
Lambda : 1.79020
SS/FOM : F20= 28(0.0148,48)

Filter : Not specified
d-sp : Not given

2th	*i*	*h*	*k*	*l*
37.851	80	4	2	0
41.624	60	4	2	2
44.278	100	5	1	1
48.431	60	4	4	0
50.795	60	5	3	1
54.582	60	6	2	0
57.480	40	6	2	2
73.462	60	8	2	0
75.941	80	6	6	0
77.775	60	7	5	1
82.696	60	9	1	1
90.569	100	8	4	4
92.316	40	7	7	1
102.704	60	10	4	0
105.191	60	10	4	2
107.073	20	11	1	1
110.255	20	8	8	0
112.192	100	9	7	1
115.482	20	10	6	0
118.182	20	10	6	2

Pattern : 00-047-1191 ***Radiation =*** 1.540598 ***Quality :*** Indexed

η-Fe_3Mo_3C

Iron Molybdenum Carbide

Lattice : Face-centered cubic
S.G. : Fd3m (227)

a = 11.13550
Z = 16

Mol. weight = 467.37
Volume [CD] = 1380.79
Dx = 8.993

Sample preparation: Prepared by arc melting.
General comments: Least squares refinement used to obtain cell parameter.
Data collection flag: Ambient.

Kimmel, G., Haberman, Z., Israel Inst. of Technology, Technion Haifa, Israel., ICDD Grant-in-Aid (1994)

Radiation : CuKa1
Lambda : 1.54060
SS/FOM : F30= 20(0.0280,53)

Filter : Monochromator crystal
d-sp : Diffractometer
Internal standard : Si

2th	*i*	*h*	*k*	*l*
22.563	2	2	2	0
32.121	8	4	0	0
35.087	20	3	3	1
39.598	40	4	2	2
42.112	100	5	1	1
46.047	33	4	4	0
49.016	6	4	4	2
54.595	4	6	2	2
59.176	7	7	1	1
64.180	8	7	3	1
67.170	1	8	0	0
68.948	9	7	3	3
71.849	33	6	6	0
73.581	10	7	5	1
74.149	2	6	6	2
78.100	3	9	1	1
78.645	2	8	4	2
80.947	1	6	6	4
86.954	15	7	7	1
89.688	6	10	2	0
91.374	9	7	7	3
91.923	2	6	6	6
104.772	4	11	3	1
107.488	7	10	6	0
112.207	11	12	0	0
113.950	7	11	5	1
117.072	7	10	6	4
118.888	1	11	5	3
127.449	1	10	8	2
129.499	9	13	1	1
135.467	20	13	3	1
136.292	1	10	8	4
139.597	6	12	6	2

Pattern : 00-012-0570 ***Radiation =*** 1.540598 ***Quality :*** Not indexed

$Fe_{23}(C,B)_6$

Iron Boron Carbide

Lattice : Face-centered cubic

S.G. : Fm3m (225)

a = 10.59100

Z = 4

Mol. weight = 1352.94

Volume [CD] = 1187.98

Dx = 7.564

Unit cell: Stadelmaier, Gregg found for Fe23 B3 C3, a=10.594 (C rich) to a=10.62 (B rich), Cr23 C6 type structure, ideal composition not included in the homogeneous range at 800 C. [*Metall.*, **17** 412 (1963)].
Unit cell: Reference reports: a=10.62.
General comments: Cell parameter generated by least squares refinement.
Data collection flag: Ambient.

Carroll et al., Nature (London), volume 174, page 978 (1954)

Radiation : CoKa

Lambda : 1.79020

SS/FOM : F26= 10(0.0620,44)

Filter : Not specified

d-sp : Not given

2th	*i*	*h*	*k*	*l*
27.974	1	3	1	1
29.209	1	2	2	2
33.876	5	4	0	0
37.984	40	4	2	0
41.765	35	4	2	2
44.439	100	5	1	1
48.596	20	4	4	0
50.917	30	5	3	1
51.753	15	6	0	0
54.794	1	6	2	0
57.052	5	5	3	3
57.756	10	6	2	2
63.396	1	6	4	0
71.092	5	8	0	0
73.729	10	8	2	0
76.228	25	8	2	2
78.153	15	7	5	1
81.255	5	8	4	0
83.044	9	9	1	1
87.790	3	9	3	1
90.783	15	8	4	4
92.653	10	7	7	1
103.187	3	10	4	0
105.642	1	10	4	2
107.546	5	11	1	1
112.691	10	9	7	1

Pattern : 00-018-0839 ***Radiation =*** 1.540598 ***Quality :*** Not indexed

Mo_2FeB_2

Boron Iron Molybdenum

Lattice : Tetragonal
S.G. : P4/mbm (127)

a = 5.77500
c = 3.14500

Z = 2

Mol. weight = 269.35
Volume [CD] = 104.89
Dx = 8.528

General comments: Higher angle intensities enhanced by absorption.
Unit cell: Reference reports: a=5.782, c=3.148.
General comments: Cell parameters generated by least squares refinement.
Data collection flag: Ambient.

Rieger et al., Monatsh. Chem., volume 95, page 1502 (1964)

Radiation : CrKa
Lambda : 2.29090
SS/FOM : F19= 6(0.1130,28)

Filter : Not specified
d-sp : Not given

2th	*i*	*h*	*k*	*l*
28.401	50	0	0	1
31.127	20	2	0	0
34.813	80	2	1	0
36.071	50	1	1	1
42.507	100	2	0	1
44.324	50	2	2	0
45.474	100	2	1	1
49.991	60	3	1	0
57.559	5	3	2	0
58.642	50	0	0	2
66.709	60	4	1	0
68.883	20	3	3	0
69.999	60	2	1	2
71.842	20	4	0	1
73.197	20	4	2	0
73.997	100	4	1	1
76.156	100	3	3	1
80.434	100	3	1	2
83.660	10	4	3	0

Pattern : 00-024-0512 **Radiation =** 1.540598 **Quality :** Deleted

$Fe^{+2}Cr_2O_4$

Iron Chromium Oxide
Chromite, syn

Lattice : Face-centered cubic
S.G. : Fd-3m (227)

a = 8.36400

Z = 8

Mol. weight = 223.84
Volume [CD] = 585.12
Dx = 5.082

2th	i	h	k	l
30.210	40	2	2	0
35.641	100	3	1	1
37.201	15	2	2	2
43.232	35	4	0	0
53.615	5	4	2	2
57.168	40	5	1	1
62.775	45	4	4	0

Deleted and rejected by: Deleted by Berry letter of February 22, 1974.
General comments: Extracted from 2% Cr containing alloy.
Analysis: Chemical analysis (by activation 40% Cr2 O3.
General comments: For comparison with synthesized specimen see Iwamoto, Adachi., *Trans. I.S.I.J.*, 9 59 (1969).
Structure: Spinel structure chrome content indicates composition Fe0.94 + 2 Fe0.85 +3 Cr1.2 O4 to Fe1.57 3 Cr1.1 O4.
Color: Red
Data collection flag: Ambient.

Adachi, Iwamoto., Trans. Iron Steel Inst. Japan, volume 6, page 188 (1966)
Tetsu to Hagane (Iron and Steel), volume 50, page 2302 (1964)

Radiation : CrKa
Lambda : 2.28970
SS/FOM : F7= 22(0.0360,9)

Filter : Not specified
d-sp : Not given